PROBING NONEQUILIBRIUM DYNAMICS IN TWO DIMENSIONAL QUANTUM GASES

by

Cheng-An Chen

A Dissertation

Submitted to the Faculty of Purdue University

In Partial Fulfillment of the Requirements for the degree of

Doctor of Philosophy

Department of Physics and Astronomy

West Lafayette, Indiana

December 2021

THE PURDUE UNIVERSITY GRADUATE SCHOOL
STATEMENT OF COMMITTEE APPROVAL

Dr. Chen-Lung Hung, Chair

Department of Physics and Astronomy

Dr. Christopher H. Greene

Department of Physics and Astronomy

Dr. Ruichao Ma

Department of Physics and Astronomy

Dr. Sergei Khlebnikov

Department of Physics and Astronomy

Approved by:

Dr. Gabor A. Csathy

ACKNOWLEDGMENTS

I would like to thank my advisor Professor Chen-Lung Hung for his guidance. Chen-Lung is a very special advisor in a way that he is always there when students need help, and over these years I am always amazed everyday by his sharp sense of physics, unlimited ideas, and tireless working. I am very fortunate to have the privilege to work with him.

I would like to thank our postdoctoral fellow (2016–2018) Dr. May E. Kim. May has been super helpful and always bringing positive energy ($E \gg 0$) ever since. I especially appreciate her effort to bring everything and everyone together in the lab. Working in a startup lab is hard, and it would not be successful without her.

I would like to thank many people who helped me with my research work. Ting-Wei Hsu is the electronics guru, his excellent ability of designing and building circuits benefits our group a lot. Bruce Edleman helped me to build a really nice and critical laser, and Wuxiucheng Wang spent so much time helping me to build the complicated computer control. Wenjun Zhang helped me to characterize the new microscope objective and his codes of imaging calibration have been used all the time.

I would also like to thank everyone in Purdue AMO theoretical groups: Professor Greene group, Professor Robicheaux group, Professor Zhou group, as well as our collaborators Professor Kruczenski group and Professor Khlebnikov group. I want to thank every one of them for fruitful discussions and answering my questions. I also thank many people in the department: Sandy, Janice, Kasey, Kristin, James, and Tom in the PRIME lab.

I would like to thank Trang, Jeremy, Andres, Adeel, Kevin, Keiichiro, Akhil, Chun-Chia, Panpan, Ya-Ting, and many other friends. Thank you for being with me and caring for me during my entire PhD, I would not be able to finish it without you. Adeel, we all miss you.

And last but not least I would like to thank my former supervisors Dr. Yu-Ju Lin and Dr. Ming-Shien Chang. December 2021 marks the tenth anniversary since I joined their rubidium BEC experiments and began my AMO journey. I would not have come to the US for the doctoral degree without their encouragement.

TABLE OF CONTENTS

LIST OF TABLES

LIST OF FIGURES

ABSTRACT

Probing nonequilibrium dynamics in a trapped, inhomogeneous atomic quantum gas can be a challenging task because coexisting mass transport and spreading of quantum correlations often make the problem intractable. By removing density inhomogeneity in an atomic quantum gas and employing local control of chemical potential as well as interaction parameters, it is possible to perform quasi-particle control, initiate and probe collective quantum dynamics without or with a controlled mass flow. We report our experimental results toward quasi-particle control and nonequilibrium dynamics in a homogeneous two-dimensional quantum gas.

1. INTRODUCTION

1.1 Toward designer quantum simulator

Quantum simulations have been prosperously studied for quantum physics in the past decade. [1]–[5]. A quantum simulator typically consist of quantum particles that evolve under a specific Hamiltonian with proper control of a set of system parameters, allowing us to simulate the quantum physics such as quantum phases and quantum many-body dynamics, which can be found in other many-body systems governed by similar Hamiltonians. Quantum simulator is a prominent application for quantum information and quantum communication with the great potential to solve classical intractable problems. Several potential platforms have recently demonstrated theoretically and experimentally the basic functionality of quantum simulation applied to investigate quantum phase transitions, quantum entanglement, quantum magnetism, quantum spin model, and other related quantum mechanics [6]–[13]. A configurable quantum simulator could be realized in different quantum systems, such as atoms in optical lattices [14], [15], atoms in arrays of cavities [16]–[18], arrays of trapped ions [19]–[21], superconducting circuits [22], [23], electrons in quantum dots [24]–[26], arrays of laser-excited Rydberg atoms [27]–[29], NV centers in diamond [30], [31], and many more. The goals of such simulators is to tackle the difficult computational tasks that are inefficient or unsolvable on today's semiconductor based computers. Although the capability of classical supercomputers has been pushed to new records by taking advantage of customized tensor networks and specialized algorithms [32] backed by a huge amount of new generation CPU (central processing unit) and GPU (graphics processing unit), quantum simulators still show strong primacy [33], [34].

Ultracold atoms have been shown remarkable capability of accessing quantum many-body problems that could emulate statistical physics, quantum chemistry, condensed matter physics, and high-energy physics [35]. Over the past decades, quantum control of light and matter in atomic, molecular and optical (AMO) physics has reached an astonishing level [36], [37]. The highly tunable and flexible controllability and new tools of probing cast ultracold atoms as a promising candidate of *analog* quantum simulators [38]–[40]. Single- and many-body Hamiltonians of ultracold quantum gases and their Hamiltonians can be

precisely engineered, and the resulting dynamics can be closely monitored [28], [41], [42]. In particular, the active developments of optical lattices, optical tweezers and atomic interaction controls have opened up the possibility to realize analog quantum simulators from weakly to strongly correlated many-body systems, and paved a way to the exploration of previously inaccessible out-of-equilibrium dynamics of quantum systems [43] and possible explanation of high-temperature superconductivity [44], [45], quantum phase transitions from a superfluid to a Mott insulator [46], [47], and also for exotic quantum matters [48]–[51]. These developments enable the visionary ideas of Feynman [52], [53], who was one of the first people conceived a universal quantum simulator in the future [54], [55].

To design such quantum simulators with ultracold bosonic atoms, we begin with a many-body Hamiltonian H acting on the total wavefunction $\Psi(\mathbf{r}_1, \mathbf{r}_2, \mathbf{r}_3, \ldots \mathbf{r}_N)$ of N identical bosons with two-body interaction, where $\mathbf{r}_\mathrm{i}$ is the coordinate of the i-th boson. The Hamiltonian of the system in pseudopotential interaction model and in the dilute limit is

$$H = \sum_{\mathrm{i}=1}^{N} \left(-\frac{\hbar^2}{2m} \frac{\partial^2}{\partial \mathbf{r}_\mathrm{i}^2} + V(\mathbf{r}_\mathrm{i}) \right) + \sum_{\mathrm{i}<\mathrm{j}} g\delta(\mathbf{r}_\mathrm{i} - \mathbf{r}_\mathrm{j}) \tag{1.1}$$

where m is the mass of a single boson, $\hbar = \frac{h}{2\pi}$ and h is the Planck constant, $V(\mathbf{r})$ is the external potential at position $\mathbf{r}$, g is the interatomic interaction parameter (Sec. 1.3), and $\delta(\mathbf{r})$ is the Dirac delta-function.

While the external potential $V(\mathbf{r}_\mathrm{i})$ can be precisely designed through an optical dipole potential, such as optical lattices [14], [46], [56] or optical tweezers, the interaction term $g = \frac{4\pi\hbar^2 a_s}{m}$, is also widely studied by utilizing collisional resonances. For instance, the Feshbach resonances in cold collisions [57], [58], where the total energy of two approaching atoms in an energetically open channel is magnetically tuned to resonate with a bound state in a closed channel [59]. In the presence of the Feshbach resonances where the open and the close channels are strongly coupled, the interaction strength between two atoms is greatly modified (detailed in Chapter 1.3). As a result, a many-body system could exhibit exotic dynamics when the interacting particles in such a system are out of equilibrium. In addition to the global change of interaction by magnetic field, optical means of interaction tuning

offer advantages over magnetic Feshbach resonances, e.g. high-resolution spatial control and high-speed temporal control of the interaction strength [60], [61].

With the ability to engineer Hamiltonians dynamically via optical tuning, we can design desired quantum simulation in an ultracold atomic system. Optical field control creates designer interactions as well as external potentials with high resolution in position, momentum, and time, offering a much richer palette for wide applications and opens many new research fields [62]–[64]. For example, studies of nonequilibrium thermodynamics of strongly interacting gases via spatial-temporal control of chemical potential [65], [66], space-time matrices of analog black hole by dynamically changing sound speed in a superfluid [67], [68], quantum phase transitions and quantum critical transport cooperating with optical lattices [69]–[71]. Therefore, optical interaction tuning methods are of great interest.

Upon the unprecedented capability of engineering the Hamiltonians with ultracold atoms, various experimental approaches have been attempted to extract sensitive information of near or nonequilibrium density fluctuations and their spatial correlations, which is critical for revealing statistical dynamics and collective behaviors in a many-body system. There are a few key ingredients required to tackle the challenging task: a monolayer of two-dimensional (2D) quantum gas, where the degree of freedom is kinetically frozen to its motional ground state along the probing direction. Unlike 3D samples whose only bulk properties along the probing axis are measured, dynamics and related physics of 2D samples manifest on one plane, therefore the precise in-trap atomic density distribution can be preserved and probed by performing *in situ* absorption imaging at a time. In addition to 2D, a homogeneous sample is also essential for studying equilibrium and nonequilibrium dynamics without extra mass gradient set in, and helps to access certain physics that require large samples of the same phases, or of interference between nontrivial phases. The homogeneity of samples not only removes undesired particle flow, but also gives rise to a better control of chemical potentials globally and locally – a key to unlock nonequilibrium dynamics.

Equilibrium properties of two-dimensional Bose gases have been previously studied [12], [72]–[80]. In most of preceding experiments, a 3D Bose-Einstein condensate is converted into a 2D gas either by loading atoms into a one-dimensional optical lattices formed by an attractive dipole beam [81]–[83], or by compressing the BEC along one direction using a

repulsive Hermite-Gaussian HG_{01} beam [84]. The caveat of these two methods is that they still inevitably introduce trap inhomogeneity in the plane of the 2D gas, thus even in the equilibrium the atomic density is not homogeneous. Such inhomogeneous samples obstruct precise explorations of quantum criticality and quantum critical dynamics in low dimensions [85], [86], where the sample homogeneity is crucial. Besides, in the case of attractive dipole potential, atoms are locally trapped in the optical intensity maximum, resulting in the vulnerability to the optical power fluctuations. For repulsive Hermite-Gaussian potential, it is in general difficult to engineer a very tight trap due to the diffraction limit of the laser beam, and often requires more optical power to fully compress atoms to 2D regime as well.

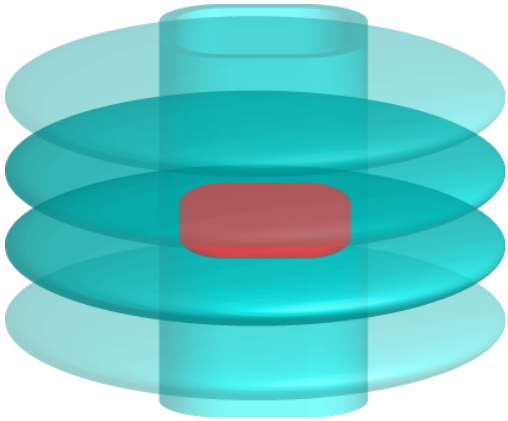

Figure 1.1. Schematic diagram of the box potential. Cyan: blue-detuned repulsive laser, Maroon: trapped 2D gas.

We have implemented a novel technique to solve these problems. In our state-of-the-art quantum gas apparatus, two oblate blue-detuned repulsive lasers interfere to form a one-dimensional optical lattice. Ultracold atoms are trapped in a single dark fringe due to the repulsive dipole force (Fig. 1.1). As a result, the trap potential is homogeneous and less sensitive to optical power instability. Since atoms are located at an optical intensity minimum, they scatter less photons so that the lifetime is also longer than those in the red-detuned attractive trap [87]. Similarly, the horizontal confinement is also formed by a blue-detuned repulsive potential, where a digital micromirror device (DMD) selectively reflects the laser profile as a designated pattern that is projected onto the atoms. We project the horizontal trapping beam through a high-resolution microscope objective which focuses

on the 2D plane. The tightly focused blue-detuned repulsive beam not only makes a flat 'box' trap along with the vertical lattice, but also creates the sharp boundary of the step-like potential edges. The technical details of our method are described in Chapter 3.2, and similar box-trap schemes have also been reported recently [88], [89].

The information of 2D gases can be probed by either time-of-flight (TOF) or *in situ* imaging [90], [91] methods. The time-of-flight procedure begins by abruptly switching off the confinement to atomic samples, allowing the sample to expand for a variable time, followed by the absorption imaging or phase-contrast imaging to measure the density profile of the sample. Although the phase coherence and the momentum distribution of quantum gases can be revealed in this way, the time-of-flight method only obtains the bulk properties of samples, i.e. the phase and momentum information from the interference of the whole sample. In contrast to the time-of-flight measurement where close comparison with theoretical calculations and non-trivial transformations are required to reconstruct the spatial distribution [65], [92]–[94], an *in situ* image is a 'sanp-shot' picture of an atomic sample along the confined and reduced axis, the dynamics is resolved from the atomic density distribution (Fig. 1.2). Because the thickness along the line-of-sight of the probing is negligible, 2D *in situ* imaging reserves the integrity of the information.

The dissertation is organized as follows: in the next Section 1.2, I continue to show more intriguing properties of our platform – two-dimensional homogeneous Bose gases, and signify the importance and necessity of our choice. In Section 1.3, I introduce the atomic interaction of the Feshbach resonances originating from the collisions of cold atoms. With interacting bosons, it will arrive the energy dispersion of microscopy quasi-particles by Bogoliubov theory in Section 1.4.1, followed by the discussion of the pair-correlation between quasi-particles via the pair-correlation function and the structure factor in Section 1.4.2. In Chapter 2, I depict our versatile apparatus for quantum gas experiments part by part, followed by Chapter 3 describing the experimental procedures including the laser cooling techniques and the steps toward sample preparation.

In Chapter 4, we study universal nonequilibrium dynamics of two-dimensional atomic Bose gases quenched from repulsive to attractive interactions. We observe the manifestation of modulational instability that, instead of causing collapse, fragments a large two-

dimensional superfluid into multiple wave packets universally around a threshold atom number necessary for the formation of Townes solitons. We experimentally realize the first demonstration of matter-wave Townes solitons, as well as arguably the first Townes solitons on all platforms. In Chapter 5, we achieve near-deterministic generation of two-dimensional matter-wave Townes solitons, and a precision test on scale invariance in attractive 2D Bose gases. We confirm scale invariance by inducing a shape-controlled modulational instability in an elongated 2D matter-wave to create an array of isolated solitary waves of various sizes and peak densities. In Chapter 6, we report observation of quasiparticle pair-production by a modulational instability and present a 'homodyne' detection between ground state atoms and quasiparticles of opposite momenta. We confirm quantum entanglement between interaction quench-induced quasiparticles by observing to oscillate below a quantum limit set by the Peres-Horodecki separability criterion of continuous-variable states.

In Chapter 7, I describe the recent important upgrade of our apparatus, and further detail our state-of-the-art quantum gas machine. In Chapter 8, I conclude my graduate work and lay out some of our primary projects regarding probing nonequilibrium dynamics in two-dimensional quantum gases.

1.2 Two-dimensional homogeneous Bose gases

In this section I present some features of our quantum simulation platform: the two-dimensional homogeneous Bose quantum gases. Two-dimensional (2D) Bose gases exhibit intriguing thermodynamic properties [80], [82], [84], [95]–[101]. For instance, a non-interacting ideal 2D gas does not have Bose-Einstein condensate (BEC) transition. This can be observed from the equation of state derived from the Bose distribution function [102],

$$n_{th}(\mu, T) = \int \frac{d^2p}{(2\pi\hbar)^2} \frac{1}{\exp\left[\beta(p^2/2m - \mu)\right] - 1} = -\lambda_{dB}^{-2} \ln\left(1 - \mathrm{e}^{\beta\mu}\right) \tag{1.2}$$

here m is the mass of the boson, $\hbar = \frac{h}{2\pi}$ and h is the Planck constant, $\lambda_{dB} = \frac{h}{\sqrt{2\pi m k_B T}}$ is the thermal de Broglie wavelength, k_B is the Boltzmann constant, T is the temperature, $\beta = \frac{1}{k_B T}$, and μ is the chemical potential. We find when $\mu \to 0, n_{th} \to \infty$, suggesting that no atom could accumulate in the ground state. In a weakly interacting 2D Bose gas where the most experiments are relevant to, one of the fascinating signatures is that the density fluctuations are greatly suppressed at low temperatures. It can be estimated as follows: first, the scattering process between atoms is still approximately 3D, therefore the interaction energy is given by

$$E_{\text{int}} = \frac{g}{2} \int n^2(\mathbf{r}) d\mathbf{r} \tag{1.3}$$

where g is the parameter of interaction strength, $n(\mathbf{r})$ is the local atomic density at position $\mathbf{r}$. As Chapter 1.3 will describe, the 3D interaction strength $g = \frac{4\pi^2\hbar^2}{m} a_s$ depends on the s-wave scattering length a_s, a dimensionless coupling constant $\tilde{g}_{2D} = \frac{m}{\hbar^2} g$ for 2D can be expressed as [103]

$$\tilde{g}_{2D} = \frac{\sqrt{8\pi} a_s}{l_z} \tag{1.4}$$

where l_z is the harmonic oscillator length along the axis where the gas is tightly confined to the vibrational ground state, thus dynamics in this direction can be considered kinetically

frozen. In an infinite uniform 2D Bose gases, one can estimate the interaction energy by the mean-field approximation $n(\mathbf{r}) = n$

$$E_{\text{int}} = \frac{g}{2}\int n^2(\mathbf{r})d\mathbf{r}^2 \simeq \frac{g}{2}L^2\langle n^2(\mathbf{r})\rangle = \frac{\hbar^2}{2m}n\tilde{g}_{2D}N \tag{1.5}$$

where L is the length and N is the total number of particles. If the average density $\langle n^2(\mathbf{r})\rangle$ is fixed, then minimizing the interaction energy is equivalent to minimizing the density fluctuations. In the low temperature $T \approx 0$ limit, the minimum energy of causing density fluctuations can be estimated by thermodynamics, in which adding a single particle to the system increases the interaction energy by

$$\frac{\partial E_{\text{int}}}{\partial N} = ng = \frac{\hbar^2}{m}n\tilde{g}_{2D} \tag{1.6}$$

where $ng \gg k_B T$ when $T \to 0$ suggests that any density fluctuations are strongly suppressed with the dependence of the interaction strength $\tilde{g}_{2D} \propto g$.

Although the density fluctuations are suppressed at sufficiently low T, the phase fluctuations are not. In addition to the density fluctuations, another source of phase fluctuations are vortices. It was pointed out by Kosterlitz and Thouless [104], [105] that the phase transition (BKT-transition) from the normal gas to the superfluid is continuous at a critical temperature T_{BKT} due to the 'quasi-long-range order', and there is no true 'long-range order' on either side . In contrast to other phase transitions such as Bose-Einstein condensate [106], thermodynamics properties change smoothly across the BKT-transition [107], [108].

In a simple macroscopical picture, a weakly interacting 2D Bose gas can be described by the wave function $\psi = \sqrt{n}\mathrm{e}^{\mathrm{i}\theta}$, where n is the density and θ is the phase. Assuming a superfluid has density $n_s \approx n$ at low temperature, θ varies by a multiple of $2\boldsymbol{\pi}$ around an isolated single vortex where the superfluid density vanishes at the core. The size of the vortex is the healing length ξ, which is on the length scale of interaction so the presence of vortices does not violate the fact that the density fluctuations are suppressed. The velocity field $\mathbf{v} = \frac{\hbar}{m}\nabla\theta \propto \frac{\hbar}{mr}$ and its angular momentum is quantized $\hbar$ for each vortex core. The

kinetic energy cost of adding a single vortex to the ground state atoms is given by [105], [109]

$$E = \frac{1}{2}\int_{\xi}^{R\to\infty} n_s \left(\frac{\hbar}{mr}\right)^2 = \frac{\hbar^2\pi}{m}\ln\left(\frac{R}{\xi}\right) \tag{1.7}$$

The entropy of a single vortex can be calculated by the number of vortices of radius ξ that can be added to different locations in a region of radius R

$$S = k_B \ln\left(\frac{\pi R^2}{\pi\xi^2}\right) = 2k_B \ln\left(\frac{R}{\xi}\right) \tag{1.8}$$

One can get the free energy $F = E - TS$ of vortices:

$$F = \frac{k_B T}{2}(n_s\lambda_{dB}^2 - 4)\ln\left(\frac{R}{\xi}\right) \tag{1.9}$$

Thus the free energy of adding or removing a vortex changes sign at $n_s\lambda_{dB}^2 = 4$. For $n_s\lambda_{dB}^2 > 4$, the free energy F is positive, so the superfluid is stable against the appearance of a free vortex. On the other hand, for $n_s\lambda_{dB}^2 < 4$, F is negative, suggesting that the instability takes places, and the presence of each free vortex reduces n_s and amplifies the further creations of free vortices. This avalanche effect eventually renders the superfluid density n_s to zero, therefore the superfluid in 2D is unstable at $0 < n_s < \frac{4}{\lambda_{dB}^4}$. The superfluid density discontinuity occurs at the BKT-transition temperature

$$T_{BKT} = \frac{\hbar^2\pi n_s}{2k_B m} \tag{1.10}$$

Below the transition temperature T_{BKT}, vortices can only form in pairs of opposite circulations instead of single free vortices. Near the BKT-transition, the density of vortex pairs increases and the average size of a pair of vortex diverges. However this result alone only tells us whether the superfluid density discontinues at T_{BKT}, rather than allows us to obtain the value of T_{BKT} for a many-body system. Calculating the actual value of T_{BKT} in a practical system in terms of n and $\tilde{g}_{2D}$ is difficult, because near the transition the interplay between the superfluid density n_s and n is complicated due to the short-distance physics. In

weakly interacting systems $\tilde{g}_{2D} \ll 1$, the value for the critical phase-space density is given by analytical and numerical calculations [96]–[98]

$$D_c = \ln\left(\frac{C}{\tilde{g}_{2D}}\right) \tag{1.11}$$

where the dimensionless constant $C = 380 \pm 3$ is numerically calculated by Monte-Carlo simulations. In the experimental regime we explore so far where $\tilde{g}_{2D} \approx 0.05 - 0.5$, the critical phase-space density $D_c \approx 3 - 6$, and typically the phase-space density of our ultracold 2D samples is $\gg 60$.

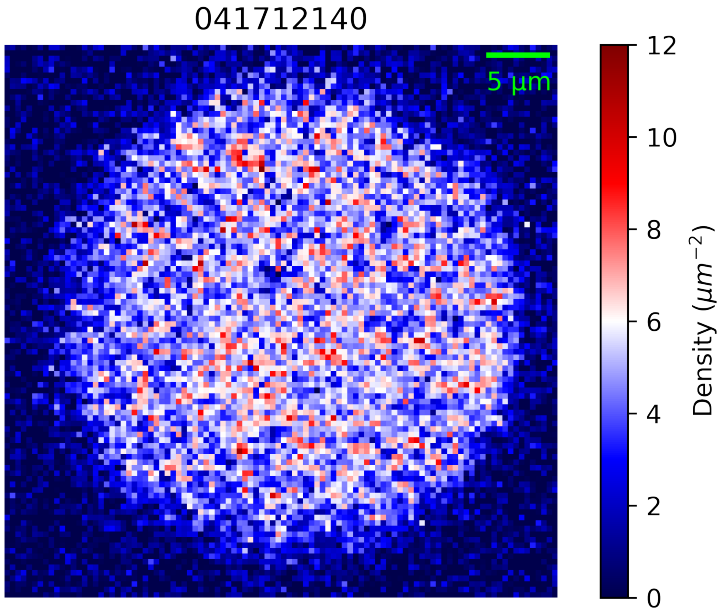

Figure 1.2. Single shot *in situ* absorption image of a 2D quantum gas.

1.3 Feshbach resonance

In this section I review the physical origin of Feshbach resonances in cold atom collisions. One of the reasons we choose cesium quantum gas as our experimental platform is that cesium has widely tunable atomic interaction via magnetic Feshbach resonances. Below I derive the s-wave scattering length a_s as a function of the magnetic field B, leading to an essential interaction parameter in many-body physics.

1.3.1 s-wave scattering

In a general scattering problem [110], an incident wavefunction is characterized by a wavevector $\mathbf{k}$ along a defined axis z

$$\phi_{\text{in}} = \mathrm{e}^{\mathrm{i}kz},\ \phi_{\text{sc}} = \frac{f(\theta)\mathrm{e}^{\mathrm{i}kr}}{r} \tag{1.12}$$

where k is the wave number, r is the radius of the scattered wave, and $f(\theta)$ is the partial-wave amplitude. The scattering cross section is given by

$$\sigma = \int |f(\theta)|^2 d\Omega \tag{1.13}$$

where Ω is the solid angle that particles pass through. At far field (large r), the interference of incident and scattered waves is

$$\phi_{r\to\infty} = \phi_{\text{in}} + \phi_{\text{sc}} = \mathrm{e}^{\mathrm{i}kz} + \frac{f(\theta)\mathrm{e}^{\mathrm{i}kr}}{r} \tag{1.14}$$

and the solution to the spherical Schrödinger's equation with central potential $V(r)$ is

$$\phi_{r\to\infty} = \left(\sum_{l=0}^{\infty} C_l P_l(\cos\theta)\right) \frac{1}{kr} \sin\left(kr - \frac{l\pi}{2} + \delta_l\right) \tag{1.15}$$

where P_l is the Legendre polynomials with the angular momentum quantum number l, C_l is the expansion coefficient, and δ_l is the phase shift during the scattering. One can expand e^{ikz} and equate coefficients on both sides

$$f(\theta) = \frac{1}{k}\sum_{l=0}^{\infty}(2l+1)e^{i\delta_l}\sin\delta_l P_l(\cos\theta) \tag{1.16}$$

For cold collisions of low energy particles such as ultracold atoms, only $l = 0$ or s-wave scattering is allowed for particles to reach short distance r , so the wave function is essentially

$$\phi_{r\to\infty} = \frac{C_0}{kr}\sin(kr - \delta_0) \tag{1.17}$$

which suggests that

$$f = \frac{1}{k}e^{i\delta_0}\sin\delta_0 = \frac{1}{k}\frac{\sin\delta_0}{\cos\delta_0 - i\sin\delta_0} = \frac{1}{k\cot\delta_0 - ik} \tag{1.18}$$

The s-wave scattering length a_s is defined as

$$a_s = -\lim_{k\to 0}\frac{\tan\delta_0(k)}{k} \tag{1.19}$$

and the limit of the total scattering cross section at $k \to 0$ is given by

$$\sigma = 4\pi\lim_{k\to 0}\left|\frac{1}{k\cot\delta_0 - ik}\right|^2 = 4\pi a_s^2 \tag{1.20}$$

1.3.2 Feshbach resonances in cold collisions

In the case of neutral atoms where the long-range interaction is absent, two atoms can still form a weakly bound molecule by van der Waals force. Qualitatively speaking, in a short distance the van der Waals potential becomes larger than the collision energy when two atoms are approaching, thus the scattering wavefunction oscillates rapidly. On the contrary, at long distance the wavefunction asymptotically approaches the free atom form, the oscillations of the wavefunction are on the length scale of the de Broglie wavelengths of

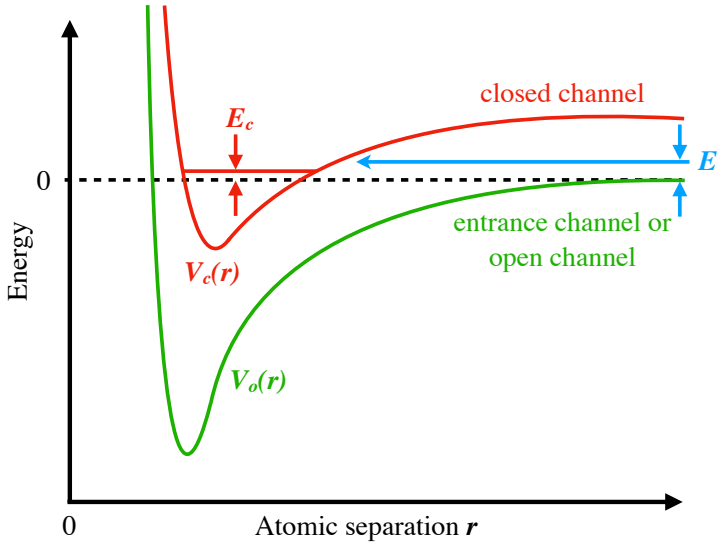

Figure 1.3. Basic two-channel model for a Feshbach resonance. [59]

two colliding atoms, leading to the threshold behavior between the short- and long-distance forms of the wavefunction [111]–[113], giving rise to the Feshbach resonances.

The Feshbach resonances can be better understood from the two-channel picture when two atoms are approaching each other: an open channel V_o has an asymptotic form of zero energy at long distance, and a closed channel V_c exhibiting a bound state of diatomic molecule (Fig. 1.3). For two ground-state alkali atoms, the exchange of total spin S results in two potentials of interatomic interaction: $\mathbf{S} = 1$ triplet (open channel) and $\mathbf{S} = 0$ singlet (closed channel).

The two colliding atoms scatter off each other in the open channel V_o with a fixed phase shift if there is no coupling between the singlet (closed channel) and the triplet (open channel) potentials. On the other hand, the hyperfine interaction $V_{\rm hf}$ has off-diagonal terms in the total electronic spin $\mathbf{S} = \mathbf{s}_1 + \mathbf{s}_2$ of the two atoms **1** and **2**, hence couples singlet (closed channel) and triplet (open channel) potentials

$$\begin{aligned} V_{\rm hf} &= a_{\rm hf}(\mathbf{s}_1 \cdot \mathbf{i}_1 + \mathbf{s}_2 \cdot \mathbf{i}_2) \\ &= \frac{a_{\rm hf}}{2}\mathbf{s}(\mathbf{i}_1 + \mathbf{i}_2) + \frac{a_{\rm hf}}{2}(\mathbf{s}_1 - \mathbf{s}_2)(\mathbf{i}_1 - \mathbf{i}_2) \\ &= V_{\rm hf}^{+} + V_{\rm hf}^{-} \end{aligned} \tag{1.21}$$

where $a_{\rm hf}$ is the hyperfine constant and $\mathbf{i}_{1(2)}$ are the nuclear spins of the colliding atoms $\mathbf{1}(\mathbf{2})$. The off-diagonal terms of $V_{\rm hf}^{-}$ couple singlet and triplet states. From a qualitative picture, the operator $\mathbf{s}_1 - \mathbf{s}_2$ is anti-symmetric with both $\mathbf{1}$ and $\mathbf{2}$ atoms, therefore couples symmetric (triplet) electronic spin states to anti-symmetric (singlet) states. As a result, $\mathbf{s}_1 - \mathbf{s}_2$ is fully off-diagonal in the singlet/triplet basis, also suggesting that coupling matrix elements are on the order of unity, and $V_{\rm hf}^{-}$ has matrix elements on the order of $a_{\rm hf}$. An external magnetic field can lift the degeneracy of triplet potentials by Zeeman shift and vary the triplet potential with respect to the singlet potential, thus induces a weak singlet-triplet coupling and acquires a sudden phase shift during the scattering.

The Schrödinger equation of two-channel s-wave coupling picture is given by [114]

$$\begin{bmatrix} -\frac{\hbar^2}{2\mu}\frac{d^2}{dr^2} + V_c(r) & W(r) \\ W(r) & -\frac{\hbar^2}{2\mu}\frac{d^2}{dr^2} + V_o(r) \end{bmatrix} \begin{bmatrix} \psi_1 \\ \psi_2 \end{bmatrix} = E \begin{bmatrix} \psi_1 \\ \psi_2 \end{bmatrix} \tag{1.22}$$

where ψ_1 and ψ_2 are the total wavefunctions of closed and open channels, respectively. $W(r)$ is the coupling between two channels, and μ is the reduced mass of two atoms. For the wavefunction of each channel

$$\left[-\frac{\hbar^2}{2\mu}\frac{d^2}{dr^2} + V_c(r)\right]\psi_b = E_b\psi_b, \tag{1.23}$$

$$\left[-\frac{\hbar^2}{2\mu}\frac{d^2}{dr^2} + V_o(r)\right]\psi_E = E\psi_E \tag{1.24}$$

where $|\psi_b\rangle$ is the bound state in the close channel and its eigen-energy is E_b, and ψ_E is the energy of the scattering state in the open channel

$$\psi_E(r \to \infty) = \sqrt{\frac{2\mu}{\pi\hbar^2 k}}\sin(kr + \delta_0) \tag{1.25}$$

here $\hbar k = \sqrt{2\mu(E - V_o(r \to \infty))}$ is the momentum of a free atom. From the Taylor expansion of Eq. 1.19

$$k\cot\delta_0(k) = -\frac{1}{a_{\rm bg}} + \frac{1}{2}r_{\rm eff}k^2 + \mathcal{O}\left(k^4\right) \tag{1.26}$$

where a_{bg} is the background scattering length and r_{eff} is the effective range of potential $V_o(r)$ [110], [115]. In the cold collision regime $k \to 0$, the phase shift $\delta_0 \approx -ka_{\text{bg}}$. The off-diagonal term $W(r)$ in the Hamiltonian couples the two channels, so the bound state and the scattering state are dressed or mixed by the interaction, and the scattering phase acquires a resonant shift due to the bound state embedded in the scattering continuum $\delta = \delta_0 + \delta_{\text{res}}$, where δ_{res} has the Breit-Wigner distribution as

$$\delta_{\text{res}} = -\arctan\left(\frac{\Gamma(E_c)/2}{E - E_c - \delta_E(E_c)}\right) \tag{1.27}$$

where $\Gamma(E_c)$ is the width of the resonance, and $\delta_E(E_c)$ is the energy shift near the resonant energy position E_c, leading to

$$\Gamma = 2\pi|\langle\psi_b|W|\psi_E\rangle|^2 \tag{1.28}$$

$$\delta E = \langle\psi_b|W\hat{G}W|\psi_b\rangle \tag{1.29}$$

The scattering Schrödinger equation is given by

$$G(r,r')\left[E + \frac{\hbar^2}{2\mu}\frac{d^2}{dr^2} - V_o(r,r')\right] = \delta(r,r') \tag{1.30}$$

where $\hat{G}$ is the Green's function. The acquired resonant phase shift is $\delta_{\text{res}} \approx \pi$ when energy E changes across a resonance over a range of Γ. In the low energy limit $E_c \approx E = 0$, as a result, the width of the resonance is independent from the incoming collision energy

$$\Gamma_0 = \frac{\Gamma}{2ka_{\text{bg}}},\ (k \to 0) \tag{1.31}$$

and the s-wave scattering length is defined by

$$a_s = \lim_{k\to 0} -\frac{\tan\delta_0 + \delta_{\text{res}}}{k} = a_{\text{bg}}(1 + \frac{\Gamma_0}{-E_0}) \tag{1.32}$$

In a magnetic Feshbach resonance, the magnetic moment of the separated atoms μ_a and the magnetic moment of the bound state in the closed channel μ_c are different. When an external magnetic field is applied, the energy difference can vary

$$\Delta E = (\mu_a - \mu_c)(B - B_0) \tag{1.33}$$

where B_0 is the resonant magnetic field, at which $\Delta E = 0$. The scattering length near a magnetic Feshbach resonance is then

$$a_s = a_{\text{bg}} \left(1 + \frac{\Delta B}{B - B_0}\right) \tag{1.34}$$

where $\Delta B = \Gamma_0/(\mu_a - \mu_c)$ is the width of the resonance in the magnetic field. In our cesium quantum gas platform, the scattering length a_s is widely tunable in the range from $\approx -2000\ a_0$ to $\approx +1000\ a_0$ within the external magnetic field 0 – 60 G (Appendix A). Alternatively, two-channel coupling can be achieved by optical means, leading to optical Feshbach resonances [63], [64]. In such resonances, a photoassociation laser drives a transition of atoms from the scattering continuum to a molecular bound state. For cases in the absence of accessible magnetic resonances, optical Feshbach resonances are particularly prominent and useful, whereas inelastic light-induced collisions and the associated atom loss could pose fundamental limitations.

If other open channels and inelastic collisions are present, the phase shift can be recast as $\delta_0 \to -k\tilde{a}_s$ for $k \to 0$ in terms of a complex scattering length $\tilde{a}_s = a_s - \mathrm{i}b$, where a and b are real. A decay rate $\gamma/\hbar$ is added to account for all available loss channels

$$\tilde{a}_s = a_s - \mathrm{i}b = a_{\text{bg}} \left(1 + \frac{\Gamma_0}{-E_0 + \frac{\mathrm{i}\gamma}{2}}\right) \tag{1.35}$$

For magnetic Feshbach resonances, γ can be zero or small enough to be ignored if a proper channel is chosen, whereas in the cases of optical resonances, there are always collisional

losses γ associated with the decay from the excited molecule state. The complex scattering length at laser frequency ν is

$$\tilde{a}_s = a_{\rm bg}\left(1 + \frac{\Delta\nu}{\nu - \nu_0 + \frac{i\gamma}{2h}}\right) \tag{1.36}$$

where ν_0 is the resonant frequency, $\Delta\nu = \Gamma_0/h$ is the width of optically induced resonance. In either magnetically or optically tunable resonances, with the presence of bound state decay,

$$a_s = a_{\rm bg} + a_{\rm res}\left(\frac{\gamma E_0}{E_0^2 + (\frac{\gamma}{2})^2}\right) \tag{1.37}$$

where $a_{\rm res} = a_{\rm bg}\Gamma_0/\gamma$ is the resonant length parameter, and the accompanied collisional loss is given by

$$b = \frac{a_{\rm res}}{2}\frac{\gamma^2}{E_0^2 + (\frac{\gamma}{2})^2} \tag{1.38}$$

This leads to the maximum tunable range of the scattering length $a_{\rm bg} \pm a_{\rm res}$ at $E_0 = \pm\gamma/2$, while $b = a_{\rm res}$. Resonances with $a_{\rm res} \ll |a_{\rm bg}|$ only allow the scattering length to change in a relatively small range yet b is relatively large, resulting in large inelastic loss rate; whereas with $a_{\rm res} \gg |a_{\rm bg}|$, losses can be reduced by choosing a large detuning, and the scattering length can change in a range of $a_s - a_{\rm bg} = -a_{\rm res}(\gamma/E_0)$ when $E_0 \gg \gamma$, given that

$$\frac{b}{|a - a_{\rm bg}|} = \frac{\gamma/E_0}{2} \ll 1 \tag{1.39}$$

In our experiment, the cesium quantum gases are produced in the lowest energy ground state, $|F = 3, m_f = 3\rangle$ (Fig. 2.3), in which at low temperatures the inelastic two-body collisional losses are typically suppressed [116]. Due to a broad Feshbach resonance located at $B \approx -12$ G (Fig. A), the elastic collisions [106] thus the s-wave scattering length varies smoothly at low magnetic fields [117]. In the next section, we briefly introduce an alternative optical Feshbach tuning scheme that employs magnetic Feshbach resonances and light shifts for the spatial control of the atomic interaction.

1.3.3 Optical Feshbach tuning

Closed channel and open channel coupling can be tuned by optical means, giving rise to optical Feshbach resonances [60], [62], [118]–[122]. For instance, optical coupling via EIT (electromagnetically induced transparency)-scheme [63], [64], [123]. However, employing optical Feshbach resonance often suffers from short lifetimes on the time scale of milliseconds by the decay of molecular bound states. This could hinder the studies of quantum gases in equilibrium or requiring critical time scales of dynamics. In addition, varying the interaction from optical Feshbach resonance often imposes a different light shift. The light shift could result in a dipole force with which the observed dynamics is perturbed when the light intensity and accompanying interaction strength are modulated spatially. Recently, Clark et al. (2015) [124] implemented a scheme for optical control of interaction strength while the quantum gas remains a long life time, and the induced dipole potential is negligible. By using a far-detuned laser to only light shift molecular bound states near a magnetic Feshbach resonance, the interaction strength can be optically tuned. The large detuning from all transitions sufficiently reduces the light scattering and atom loss for the quantum gas. Furthermore, the laser operates at a magic wavelength to compensate for the atomic dipole potential, and chemical potential can also be fine tuned at the illuminated region by adjusting the wavelength slightly detuned from the magic wavelength. It may allow us to induce synthetic mass flow or eliminate the chemical potential shift due to atom loss under long-term off-resonance photon scattering. In Section 8.2.1, we propose a similar scheme for realizing the local atomic interaction control.

1.4 Weakly interacting Bose gases

In this section I give an overview of interacting particles in ultracold Bose gases. In our experiments, we measure the atomic density fluctuations which manifest the quasiparticles in quantum gases. Below I compute the excitation spectrum from Bogoliubov theory [125] which provides a theoretical framework for weakly interacting Bose gases in the dilute limit, and arrive at the energy dispersion of quasiparticles. We will utilize the energy dispersion in later Chapters.

1.4.1 Bogoliubov theory

Microscopic Hamiltonian for the uniform bosons with contact interaction g is given in terms of creation $\hat{\psi}^\dagger(\mathbf{r})$ and annihilation $\hat{\psi}(\mathbf{r})$ operators [106]

$$\hat{H} = \int d\mathbf{r} \left[-\hat{\psi}^\dagger(\mathbf{r}) \frac{\hbar^2}{2m} \nabla^2 \hat{\psi}(\mathbf{r}) + V(\mathbf{r}) \hat{\psi}^\dagger(\mathbf{r}) \hat{\psi}(\mathbf{r}) + \frac{g}{2} \hat{\psi}^\dagger(\mathbf{r}) \hat{\psi}^\dagger(\mathbf{r}) \hat{\psi}(\mathbf{r}) \hat{\psi}(\mathbf{r}) \right] \tag{1.40}$$

where $\hbar$ is reduced Planck constant, m is the mass of a particle, and V is the external potential. The strength of contact interaction g is proportional to the s-wave scattering length a_s given by (Sec. 1.3)

$$g = \frac{4\pi\hbar^2 a_s}{m} \tag{1.41}$$

When most atoms microscopically occupy in the ground state of a condensate with the presence of quantum fluctuations

$$\hat{\psi}(\mathbf{r}) = \psi(\mathbf{r}) + \delta\psi(\mathbf{r}) \tag{1.42}$$

For a uniform gas of N interacting bosons occupying the volume V, the creation and annihilation operators can be expanded by the plane waves in momentum states $\mathbf{p}$

$$\hat{\psi}(\mathbf{r}) = \frac{1}{\sqrt{V}} \sum_{\mathbf{p}} \hat{a}_{\mathbf{p}} e^{i\mathbf{p}\cdot\mathbf{r}/\hbar} = \frac{\sqrt{V}}{(2\pi\hbar)^3} \int \hat{a}_{\mathbf{p}} e^{i\mathbf{p}\cdot\mathbf{r}/\hbar} d\mathbf{p} \tag{1.43}$$

where $\hat{a}_{\mathbf{p}}^{(\dagger)}$ is the annihilation (creation) operator for a single particle state of a plane wave with momentum $\mathbf{p}$ and

$$\hat{a}_{\mathbf{p}}^{(\dagger)} = \frac{1}{\sqrt{V}} \int \hat{\psi}^{(\dagger)}(\mathbf{r}) \mathrm{e}^{-\mathrm{i}\mathbf{p}\cdot\mathbf{r}/\hbar} d\mathbf{r} \tag{1.44}$$

The Hamiltonian becomes

$$\hat{H} = \sum_{\mathbf{p}} \frac{p^2}{2m} \hat{a}_{\mathbf{p}}^{\dagger} \hat{a}_{\mathbf{p}} + \frac{g}{2V} \sum_{\mathbf{p},\mathbf{p}',\mathbf{q}} \hat{a}_{\mathbf{p}+\mathbf{q}}^{\dagger} \hat{a}_{\mathbf{p}'-\mathbf{q}}^{\dagger} \hat{a}_{\mathbf{p}'} \hat{a}_{\mathbf{p}} \tag{1.45}$$

The creation operator $\hat{a}_{\mathbf{p}}^{\dagger}$ and the annihilation operator $\hat{a}_{\mathbf{p}}$ that create and destroy bosons in the momentum states $\mathbf{p}$ obey the Bose commutation relations

$$[\hat{a}_{\mathbf{p}}, \hat{a}_{\mathbf{p}'}^{\dagger}] = \delta_{\mathbf{p},\mathbf{p}'},\ [\hat{a}_{\mathbf{p}}, \hat{a}_{\mathbf{p}'}] = 0,\ [\hat{a}_{\mathbf{p}}^{\dagger}, \hat{a}_{\mathbf{p}'}^{\dagger}] = 0 \tag{1.46}$$

Assuming that the lowest ground state is macroscopically occupied by N_0 particles of the condensate, one can treat quantum fluctuations in the unperturbed system

$$\hat{a}_0^{\dagger}|N_0 = \sqrt{N_0+1}|N_0+1\rangle,\ \hat{a}_0|N_0 = \sqrt{N_0}|N_0-1\rangle \tag{1.47}$$

Therefore, $\hat{a}_0$ and $\hat{a}_0^{\dagger}$ can be replaced by $\sqrt{N_0}$. Since $\delta\hat{\psi}(\mathbf{r})$ is small, the Hamiltonian can be rewritten in the second quantization form as

$$\hat{H} = \frac{N_0^2 g}{2V} + \sum_{\mathbf{p}(\mathbf{p}\neq 0)} (\frac{p^2}{2m} + 2n_0 g) \hat{a}_{\mathbf{p}}^{\dagger} \hat{a}_{\mathbf{p}} + \frac{n_0 g}{2} \sum_{\mathbf{p}(\mathbf{p}\neq 0)} (\hat{a}_{\mathbf{p}}^{\dagger} \hat{a}_{-\mathbf{p}}^{\dagger} + \hat{a}_{\mathbf{p}} \hat{a}_{-\mathbf{p}}) \tag{1.48}$$

where $n_0 = N_0/V$ is the density of particles in the zero momentum state. The operator for the total particle number is given by

$$\hat{N} = \sum_{\mathbf{p}} \hat{a}_{\mathbf{p}}^{\dagger} \hat{a}_{\mathbf{p}} = N_0 + \sum_{\mathbf{p}(\mathbf{p}\neq 0)} \hat{a}_{\mathbf{p}}^{\dagger} \hat{a}_{\mathbf{p}} \tag{1.49}$$

when the total number of particles is conserved. The Hamiltonian is recast after replacing $\hat{N}$ by its expectation value and $n = N/V$

$$\hat{H} = \frac{1}{2}ngN + \sum_{\mathbf{p}} \frac{p^2}{2m}\hat{a}^\dagger_{\mathbf{p}}\hat{a}_{\mathbf{p}} + \frac{1}{2}ng \sum_{\mathbf{p}(\mathbf{p}\neq 0)} (2\hat{a}^\dagger_{\mathbf{p}}\hat{a}_{\mathbf{p}} + \hat{a}^\dagger_{\mathbf{p}}\hat{a}^\dagger_{-\mathbf{p}} + \hat{a}_{\mathbf{p}}\hat{a}_{-\mathbf{p}}) \tag{1.50}$$

The last summation in the equation above represents two atoms in the condensate that are scattered to momentum states $\pm\mathbf{p}$ due to the interaction. The Hamiltonian can be diagonalized by performing a canonical transformation, known as the Bogoliubov transformation,

$$\hat{a}_{\mathbf{p}} = u_p\hat{b}_{\mathbf{p}} + v_{-p}\hat{b}^\dagger_{-\mathbf{p}} \tag{1.51}$$

$$\hat{a}^\dagger_{\mathbf{p}} = u_p\hat{b}^\dagger_{\mathbf{p}} + v_{-p}\hat{b}_{-\mathbf{p}} \tag{1.52}$$

and the operators obey the commutation relations

$$[\hat{a}, \hat{a}^\dagger] = [\hat{b}, \hat{b}^\dagger] = 1,\ [\hat{a}, \hat{b}^\dagger] = [\hat{b}, \hat{a}^\dagger] = [\hat{a}, \hat{b}] = [\hat{a}^\dagger, \hat{b}^\dagger] = 0 \tag{1.53}$$

thus a constraint for two parameters u and v is

$$u_p^2 - v_{-p}^2 = 1 \tag{1.54}$$

to make the non-diagonal terms vanish, one requires

$$\frac{ng}{2}(u_p^2 + v_{-p}^2) + \left(\frac{p^2}{2m} + ng\right) u_p v_{-p} = 0 \tag{1.55}$$

thus the solutions of u and v can be parameterized as

$$u_p = \cosh\theta_p,\ v_{-p} = \sinh\theta_p \tag{1.56}$$

leading to

$$\coth 2\theta_p = -\frac{\frac{p^2}{2m} + ng}{ng} \tag{1.57}$$

from which two coefficients u and v can be uniquely determined as

$$u_p, v_{-p} = \pm\sqrt{\left(\frac{\frac{p^2}{2m}+ng}{2\epsilon(p)} \pm \frac{1}{2}\right)} \tag{1.58}$$

where $\epsilon(p)$ is the energy dispersion of the Bogoliubov excitation spectrum, one arrives

$$\epsilon(p) = \sqrt{\frac{p^2}{2m}\left(\frac{p^2}{2m}+2ng\right)} \tag{1.59}$$

The Hamiltonian is finally diagonalized

$$\hat{H} = \epsilon_0 + \sum_{\mathbf{p}(\mathbf{p}\neq 0)} \epsilon(p)\hat{b}^\dagger_{\mathbf{p}}\hat{b}_{\mathbf{p}} \tag{1.60}$$

where ϵ_0 is the ground-state energy with interaction

$$\epsilon_0 = \frac{1}{2}ngN + \frac{1}{2}\sum_{\mathbf{p}(\mathbf{p}\neq 0)}\left[\epsilon(p) - ng - \frac{p^2}{2m} + \frac{mn^2g^2}{p^2}\right] \tag{1.61}$$

In the Bogoliubov picture, a real particle $\hat{a}_{\mathbf{p}}$ is described as the superposition of the forward $u_p\hat{b}_{\mathbf{p}}$ and backward $v_p\hat{b}^\dagger_{-\mathbf{p}}$ counter-propagating quasiparticles. For small momenta $p \ll \sqrt{mng}$, the Bogoliubov dispersion is well approximated by the linear phonon-like dispersion form

$$\epsilon(p) = pc \tag{1.62}$$

where $c = \sqrt{\frac{ng}{m}}$ is the speed of sound. In this regime, a real particle is represented by the coherent superposition of forward and backward propagating quasiparticles $\hat{a}_{\mathbf{p}} = u_p\hat{b}_{\mathbf{p}} + v_{-p}\hat{b}^\dagger_{\mathbf{p}} \approx u_p(\hat{b}_{\mathbf{p}} + \hat{b}^\dagger_{-\mathbf{p}})$ where $|u_p| \approx |v_{-p}| \approx \sqrt{\frac{mc}{2p}} \gg 1$. On the other hand, in the limit $p \gg \sqrt{mng} = mc$, $|u_p| \approx 1$ and $|v_{-p}| \approx 0$, a quasiparticle $\hat{b}_{\mathbf{p}}$ is indistinguishable from a real particle $\hat{a}_{\mathbf{p}}$, i.e. $\hat{a}_{\mathbf{p}} \sim \hat{b}_{\mathbf{p}}$, and the Bogoliubov dispersion becomes the free-particle form

$$\epsilon(p) = \frac{p^2}{2m} + ng \tag{1.63}$$

The transition between the phonon regime and the free particle regime occurs near $\frac{p^2}{2m} = ng$, where the characteristic length $\xi = \hbar/p$ is given by

$$\xi = \sqrt{\frac{\hbar^2}{2mng}} = \frac{1}{\sqrt{2}}\frac{\hbar}{mc} \tag{1.64}$$

which is also known as the 'healing length' – the length scale where the density and phase fluctuations in the condensate are suppressed by the contact interactions.

The average number of atoms with momentum p can be calculated by Bogoliubov transformation

$$N_p \equiv \langle \hat{a}_p^\dagger \hat{a}_p \rangle = |v_{-p}|^2 + |u_p|^2 \langle \hat{b}_p^\dagger \hat{b}_p \rangle + |v_{-p}|^2 \langle \hat{b}_{-p}^\dagger \hat{b}_{-p} \rangle - u_p v_{-p} (\langle \hat{b}_p^\dagger \hat{b}_p^\dagger \rangle + \langle \hat{b}_p \hat{b}_{-p} \rangle) \tag{1.65}$$

In the eigenstates of the Hamiltonian, $\langle \hat{b}_p \hat{b}_{-p} \rangle = \langle \hat{b}_p \rangle \langle \hat{b}_{-p} \rangle = 0$ and $\langle \hat{b}_p^\dagger \hat{b}_{-p}^\dagger \rangle = \langle \hat{b}_p^\dagger \rangle \langle \hat{b}_{-p}^\dagger \rangle = 0$ for $p \neq 0$. In thermal equilibrium, the number of quasiparticles obeys the Bose-Einstein distribution

$$\langle \hat{b}_p^\dagger \hat{b}_p \rangle = \frac{1}{\mathrm{e}^{\frac{\epsilon(p)}{k_B T}} - 1} \tag{1.66}$$

where k_B is the Boltzmann constant. Therefore, the the number of total particles is

$$\hat{N} \equiv N_0 + \sum_{p \neq 0} N_p = N_0 + \sum_{p \neq 0} |v_{-p}|^2 + \sum_{p \neq 0} (|u_p|^2 + |v_{-p}|^2) \langle \hat{b}_p^\dagger \hat{b}_p \rangle \tag{1.67}$$

$$= N_0 + \sum_{p \neq 0} |v_{-p}|^2 + \sum_{p \neq 0} \frac{|u_p|^2 + |v_{-p}|^2}{\mathrm{e}^{\frac{\epsilon(p)}{k_B T}} - 1} \tag{1.68}$$

The first term N_0 is the number of atoms in the condensate. The second term is the depletion of the condensate by interactions even though quasiparticles are absent, which is also referred to as quantum depletion. The last terms represent the depletion of the condensate due the presence of real excitations. At higher temperatures, the population of quasiparticles increases proportional to T^4, and these extra excitations are referred to as thermal depletion.

1.4.2 Quasiparticle correlation

We have seen aforementioned that in an ultracold interacting gas, quasiparticles can deplete from the ground state atoms in pairs, resulting in density fluctuations. It is natural to ask the correlation between these scattered quasiparticles due to the interaction, because fluctuations and correlations from a nonequilibrium many-body system can reveal thermodynamics or phase transition of a system. In a scattering process, a generalized pair-correlation function, or often refer to as normalized second-order correlation function $g^{(2)}(\mathbf{r}, t)$ can be expressed with dependence of a spatial vector $\mathbf{r}$ and a temporal interval t. It is then easier to visualize a number of qualitative properties by the $g^{(2)}$ function, making it a very useful tool in many practical cases. The advantage of using pair-correlation function $g^{(2)}$ is the full monitoring of spatial and temporal dynamics: $g(\mathbf{r}, t)$ reveals the pair-correlation between a particle in position $\mathbf{r}' + \mathbf{r}$ at time $t' + t$ and the other particle in position $\mathbf{r}'$ at time t', averaged over the distance $\mathbf{r}'$.

We describe the atoms by a Bose field operator $\hat{\psi}(\mathbf{r}, t)$, which satisfies

$$[\hat{\psi}(\mathbf{r}, t), \hat{\psi}^\dagger(\mathbf{r}', t)] = \delta(\mathbf{r} - \mathbf{r}') \tag{1.69}$$

$$[\hat{\psi}(\mathbf{r}, t), \hat{\psi}(\mathbf{r}', t)] = 0 \tag{1.70}$$

We can further omit the time arguments and focus on the spatial correlations if the system is in thermal equilibrium at a certain time. The degree of first-order coherence $g^{(1)}$ and the degree of second-order coherence $g^{(2)}$ are

$$g^{(1)}(\mathbf{r}, \mathbf{r}') = \frac{\langle \hat{\psi}^\dagger(\mathbf{r}) \hat{\psi}(\mathbf{r}') \rangle}{\sqrt{\hat{\psi}^\dagger(\mathbf{r}) \hat{\psi}(\mathbf{r})} \sqrt{\hat{\psi}^\dagger(\mathbf{r}') \hat{\psi}(\mathbf{r}')}} \tag{1.71}$$

$$g^{(2)}(\mathbf{r}, \mathbf{r}') = \frac{\langle \hat{\psi}^\dagger(\mathbf{r}) \hat{\psi}^\dagger(\mathbf{r}') \hat{\psi}(\mathbf{r}') \hat{\psi}(\mathbf{r}) \rangle}{\langle \hat{\psi}^\dagger(\mathbf{r}) \hat{\psi}(\mathbf{r}) \rangle \langle \hat{\psi}^\dagger(\mathbf{r}') \hat{\psi}(\mathbf{r}') \rangle} \tag{1.72}$$

We can see that $g^{(1)}$ represents the phase coherence of the field operator, while $g^{(2)}$ characterizes the spatial separation between two field operators. In the simplest case of ideal Bose gases,

$$g^{(2)}(\mathbf{r},\mathbf{r}') = 1 + |g^{(1)}(\mathbf{r},\mathbf{r}')|^2 \tag{1.73}$$

$$g^{(1)}(\mathbf{r},\mathbf{r}) = 1, \lim_{|\mathbf{r}-\mathbf{r}'|\to\infty} g^{(1)}(\mathbf{r},\mathbf{r}') = 0 \tag{1.74}$$

$$g^{(2)}(\mathbf{r},\mathbf{r}) = 2, \lim_{|\mathbf{r}-\mathbf{r}'|\to\infty} g^{(2)}(\mathbf{r},\mathbf{r}') = 1 \tag{1.75}$$

On the other hand, if a condensate is present, the long-range order leads to significant changes of the correlations functions [126]–[128]

$$g^{(2)}(\mathbf{r},\mathbf{r}') = 1 + |g^{(1)}(\mathbf{r},\mathbf{r}')|^2 - \frac{\hat{\psi}^\dagger(\mathbf{r})\hat{\psi}(\mathbf{r})\hat{\psi}^\dagger(\mathbf{r}')\hat{\psi}(\mathbf{r}')}{\langle\hat{\psi}^\dagger(\mathbf{r})\hat{\psi}(\mathbf{r})\rangle\langle\hat{\psi}^\dagger(\mathbf{r}')\hat{\psi}(\mathbf{r}')\rangle} \tag{1.76}$$

which manifests the boson bunching in quantum statistics.

With the pair-correlation function in mind, we turn to the density observable which relates to the expectation value of Bose field operator $\hat{n}(\mathbf{r}) = \langle\hat{\psi}^\dagger(\mathbf{r})\hat{\psi}(\mathbf{r})\rangle$. In momentum $\mathbf{k}$ space, the Bose field operator can be expanded as

$$\hat{\psi}(\mathbf{r}) = \frac{1}{\sqrt{V}}\sum_{\mathbf{k}} \hat{a}_{\mathbf{k}} \mathrm{e}^{-\mathrm{i}\mathbf{k}\mathbf{r}} \tag{1.77}$$

In a superfluid with macroscopically occupied zero momentum state, the density operator can be approximated by

$$\hat{n}(\mathbf{r}) \approx \frac{N_0}{V} + \frac{1}{V}\sum_{\mathbf{k}\neq 0} \hat{a}_0^\dagger \hat{a}_{-\mathbf{k}} \mathrm{e}^{-\mathrm{i}\mathbf{k}\mathbf{r}} + \hat{a}_0 \hat{a}_{\mathbf{k}}^\dagger \mathrm{e}^{\mathrm{i}\mathbf{k}\mathbf{r}} \tag{1.78}$$

where V is the volume of the gas, N_0 is the atom number in the condensate, approximately equals to the total atom number $N = \bar{n}V = \int \hat{n}(\mathbf{r})d\mathbf{r}$. We can also replace the operators

in the zero momentum state with a number $\hat{a}_0^{(\dagger)} \approx \sqrt{N}$. Therefore, the density fluctuations can be expressed as

$$\delta\hat{n}(\mathbf{r}) = \hat{n}(\mathbf{r}) - \bar{n}(\mathbf{r}) = \frac{1}{V}\sum_{\mathbf{k}\neq 0}\hat{n}_{\mathbf{k}}\mathrm{e}^{\mathrm{i}\mathbf{k}\mathbf{r}} \tag{1.79}$$

then the pair-correlation function can be rewritten in terms of density fluctuations

$$g^{(2)}(\mathbf{r},\mathbf{r}') = \frac{\langle\delta\hat{n}(\mathbf{r})\delta\hat{n}(\mathbf{r}')\rangle}{\langle|\hat{n}(\mathbf{r})|\rangle^2} \tag{1.80}$$

Besides, the Fourier components $\hat{n}_{\mathbf{k}}$ is related to bosonic creation and annihilation operators

$$\delta\hat{n}_{\mathbf{k}} = \hat{a}_0^\dagger\hat{a}_{-\mathbf{k}} + \hat{a}_0\hat{a}_{\mathbf{k}}^\dagger \approx \sqrt{N}(\hat{a}_{\mathbf{k}}^\dagger + \hat{a}_{-\mathbf{k}}) \tag{1.81}$$

Structure factor

The static structure factor is the Fourier transform of the pair-correlation function [129]–[131]

$$S(\mathbf{k}) = \int g^{(2)}(\mathbf{r},\mathbf{r}')\mathrm{e}^{-\mathrm{i}\mathbf{k}\cdot\mathbf{r}}d\mathbf{r} \tag{1.82}$$

$$= \frac{\langle\delta\hat{n}_{\mathbf{k}}\delta\hat{n}_{-\mathbf{k}}\rangle}{N} = \frac{\langle|\delta\hat{n}_{\mathbf{k}}|^2\rangle}{N} \tag{1.83}$$

$$= \frac{1}{N}\sum_{\mathbf{q},\mathbf{q}'}\langle\hat{a}_{\mathbf{q}+\mathbf{k}}^\dagger\hat{a}_{\mathbf{q}}\hat{a}_{\mathbf{q}'-\mathbf{k}}^\dagger\hat{a}_{\mathbf{q}'}\rangle \tag{1.84}$$

where $\hat{a}_{\mathbf{k}}^{(\dagger)}$ is the annihilation (creation) operator of the momentum state $|\mathbf{k}\rangle$, and $\delta\hat{n}_{\mathbf{k}} = \delta\hat{n}_{-\mathbf{k}}^*$ since the density fluctuation is a real number. Consequently $S(\mathbf{k})$ is equivalent to the normalized density fluctuation power spectrum. In a low temperature Bose gas, the static structure factor $S(\mathbf{k})$ is dominated by ground state contributions, replacing $\hat{a}_0^\dagger = \hat{a}_0 \approx \sqrt{N}$ yields

$$S(\mathbf{k}) = \langle\hat{a}_{\mathbf{k}}^\dagger\hat{a}_{\mathbf{k}}\rangle + \langle\hat{a}_{-\mathbf{k}}\hat{a}_{-\mathbf{k}}^\dagger\rangle + \langle\hat{a}_{\mathbf{k}}^\dagger\hat{a}_{-\mathbf{k}}^\dagger\rangle + \langle\hat{a}_{-\mathbf{k}}\hat{a}_{\mathbf{k}}\rangle \tag{1.85}$$

We can further evaluate $S(\mathbf{k})$ in terms of quasiparticle operators $\hat{b}_{\mathbf{k}}^{(\dagger)}$ by using the Bogoliubov theory (1.4.1)

$$\begin{pmatrix} \hat{a}_{\mathbf{k}} \\ \hat{a}_{-\mathbf{k}}^{\dagger} \end{pmatrix} = \begin{pmatrix} \cosh\alpha_{\mathbf{k}} - \sinh\alpha_{\mathbf{k}} \\ -\sinh\alpha_{\mathbf{k}} \cosh\alpha_{\mathbf{k}} \end{pmatrix} \begin{pmatrix} \hat{b}_{\mathbf{k}} \\ \hat{b}_{-\mathbf{k}}^{\dagger} \end{pmatrix} \tag{1.86}$$

where $\alpha_{\mathbf{k}} = \cosh^{-1}\sqrt{\frac{\hbar^2k^2/2m+mc^2}{2\epsilon(\mathbf{k})} + \frac{1}{2}}$, $\epsilon(\mathbf{k}) = \hbar kc\sqrt{1+(\frac{\hbar k}{2mc})^2}$ is the Bogoliubov quasiparticle energy dispersion, and c is the speed of sound. It gives rise to

$$S(\mathbf{k}) = \frac{\hbar^2k^2}{2m\epsilon(\mathbf{k})}\left[\langle\hat{b}_{\mathbf{k}}^{\dagger}\hat{b}_{\mathbf{k}}\rangle + \langle\hat{b}_{-\mathbf{k}}\hat{b}_{-\mathbf{k}}^{\dagger}\rangle + \langle\hat{b}_{\mathbf{k}}^{\dagger}\hat{b}_{-\mathbf{k}}^{\dagger}\rangle + \langle\hat{b}_{-\mathbf{k}}\hat{b}_{\mathbf{k}}\rangle\right] \tag{1.87}$$

At thermal equilibrium, the number of quasiparticles should obey Bose-Einstein distribution, so the static structure factor becomes

$$S(\mathbf{k}) = \frac{\hbar^2k^2}{2m\epsilon(k)}\coth\frac{\epsilon(\mathbf{k})}{2k_BT} \tag{1.88}$$

where k_B is the Boltzmann constant and T is the equilibrium temperature (Fig. 1.4). The static structure factor of a Bose condensate reveals collective and the statistical behaviors of the elementary excitations.

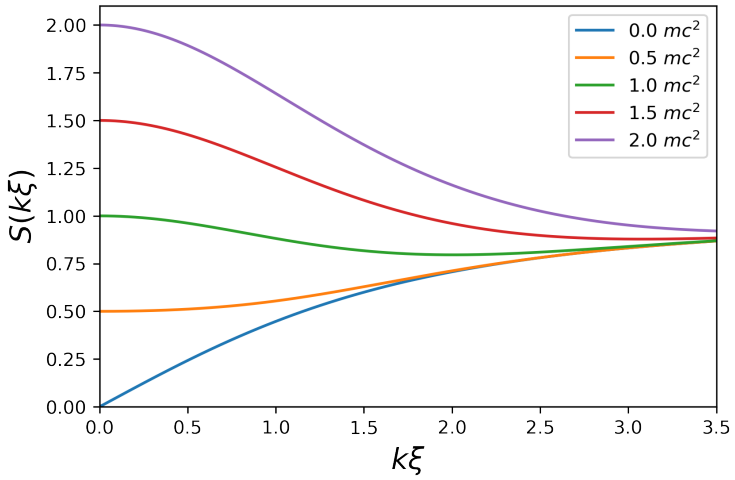

Figure 1.4. Static structure factor S of different temperatures scaled by mc^2, where c is the speed of sound and ξ is the healing length.

Furthermore, the dynamic structure factor is the spatial and temporal Fourier transform of the pair-correlations of the density fluctuations [132]–[134]

$$S(\mathbf{k},\omega) = \frac{V}{2\pi N}\int d\mathbf{r}dt\ \mathrm{e}^{-\mathrm{i}(\mathbf{kr}-\omega t)}\langle\delta\hat{n}(\mathbf{r},t)\delta\hat{n}(0,0)\rangle \tag{1.89}$$

where V is the volume and $\delta\hat{n}(\mathbf{r},t)$ is the density fluctuations in space and time. It can be rewritten in momentum space as

$$S(\mathbf{k},\omega) = \frac{1}{2\pi N}\int dt\ \mathrm{e}^{\mathrm{i}\omega t}\langle\delta\hat{n}_{\mathbf{k}}(t)\delta\hat{n}_{-\mathbf{k}}(0)\rangle \tag{1.90}$$

The dynamic structure factor generally characterizes the spatio-temporal response of the system to perturbations of a source.

2. EXPERIMENTAL SETUP

In this chapter I introduce the main setup of our experimental apparatus. We began our quantum gas project in 2016. The general design idea of the experiment is to build a versatile yet compact quantum gas machine with great efficiency and extensive flexibility. The setup approximately includes four parts: lasers, electronic devices, vacuum chamber, and computer programs; of which we are proud to design and build most parts on our own. The details about a recent upgrade and the full capability of our quantum gas machine will be further elaborated in Chapter 7.

2.1 Laser system

Our lasers consist of four major parts, each of them serves as different functionality in the laser cooling experiment. An external-cavity diode laser provides the light source of a single frequency for a specific atomic transition. The tapered amplifier magnifies the laser power of desired frequencies for multiple purposes. Nd:YAG and Ti:Sapphire lasers are solid-state lasers responsible for single frequency and narrow linewidth applications.

2.1.1 External-cavity diode laser

We have four homemade external-cavity diode lasers (ECDL) for laser cooling, each of them is set to different wavelengths for different electronic dipole transitions. The lasers start with Eagleyard anti-reflective (AR) coated laser diode (P.N.: EYP-RWE-0860-06010-1500-SOT02-0000) mounted on a custom designed laser diode holder, which has a aluminum block of minimum size to reduce the heat capacity. The lasers' currents are controlled by homemade current controllers [135]–[138], and the controller senses the current flowing thru a precision sensing resistor and locks the voltage across the sensing resistor to the voltage setpoint where users set on the front panel via a trimmer resistor. The lasers' temperatures are also stabilized by homemade temperature controllers [139] via thermistor and thermoelectric cooler (TEC) underneath the aluminum laser holder. The thermistor senses the temperature at the holder of the laser diode, and the controller compares the resistances of the thermistor and the

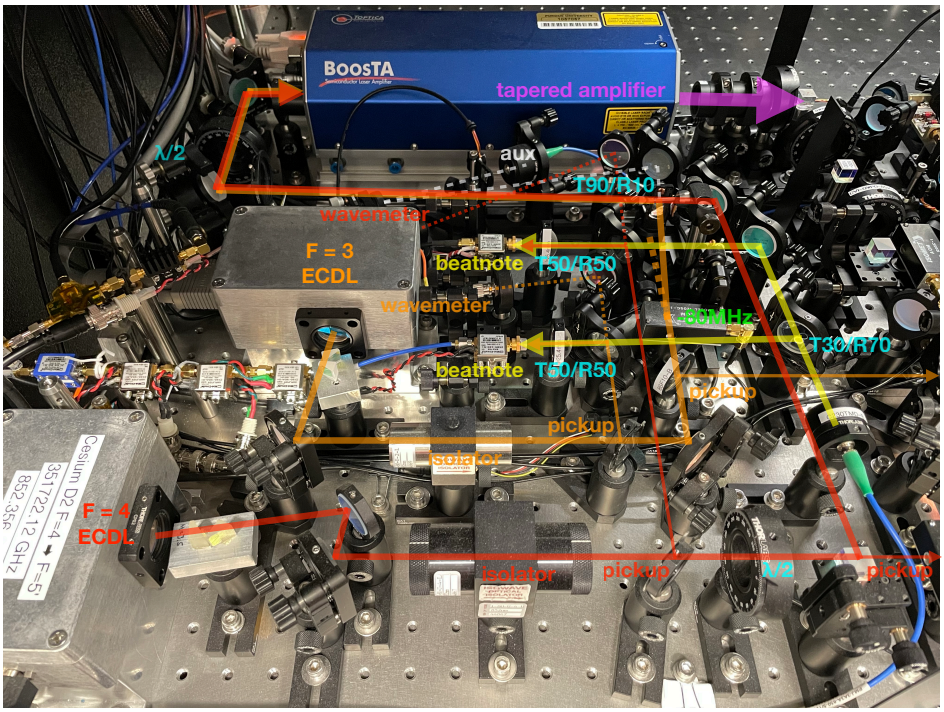

Figure 2.1. Actual optical layout for laser cooling. Red: $F = 4$, Orange: $F = 3$, Yellow: reference laser, Purple: amplified $F = 4 + F = 3$.

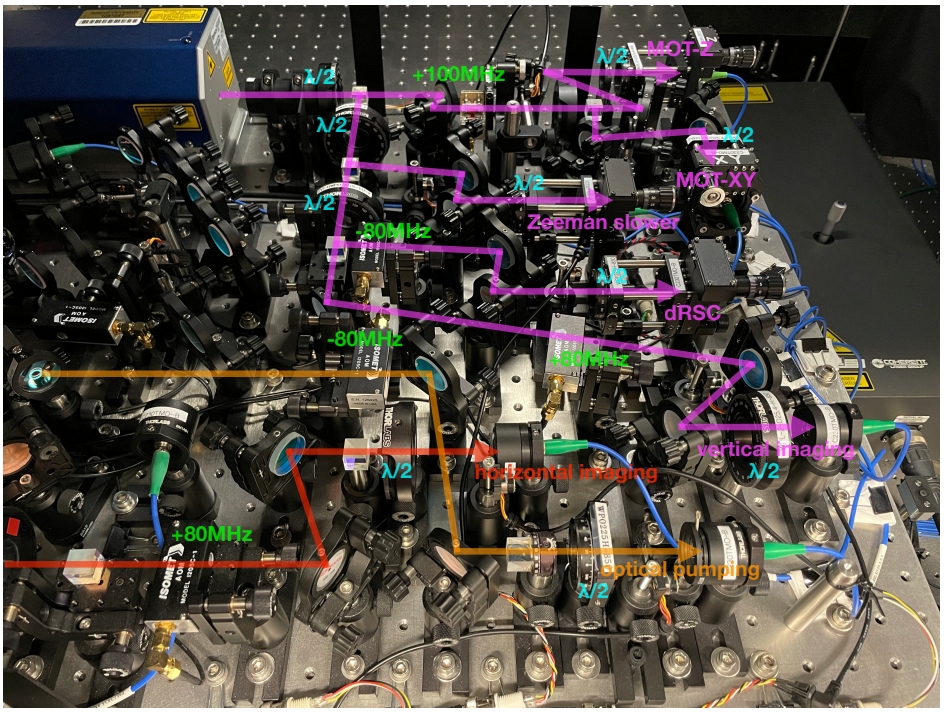

Figure 2.2. Actual optical layout for laser cooling. Purple: tapered amplifier output, Red: $F = 4$ for horizontal imaging, Orange: $F = 3$ for optical pumping.

trimmer resistor set by users, then feed back the error signal to a proportional-integral (PI) servo which controls the current output of the TEC. Since the error is bipolar, i.e. can be positive and negative, the TEC can serve as a cooling or a heating source. Under the TEC, we design a big aluminum block as a heat reservoir for the heat dissipation. The entire setup is then covered by an air-tight hermetically sealed aluminum box.

Our ECDLs are configured as Littrow configuration, where there is a commercial half inch mirror mount holding a holographic grating (Edmund Optics #43-775). We carefully adjust the grating feedback to minimize the lasing threshold current at the desired wavelength, so that the efficiency of the external-cavity is optimized. Once the cavity is well-aligned, the laser beam travels through an anti-reflection coated wedged window mounted on the aluminum laser cover. The wedged window is rotated to avoid any reflected light coming back to the laser diode, and a rubber o-ring is sandwiched between the wedged window and the aluminum laser cover to insulate the possible air flow. Desiccants are placed inside the laser enclosure to keep the humidity low. We have been operating the ECDLs without adjusting the grating for more than six years since they were built and sealed, even after occasional shutdown of the HVAC and humidity control in the lab.

The beam shape coming from a diode laser is usually elliptical due to the geometry of the semiconductor lasing facet on the laser diode. Right after the laser beam goes through the wedged window, we use a prism pair (Thorlabs PS871-B) to reshape the beam to circular-like profile in order to increase the efficiency of the fiber coupling. Nevertheless, the intrinsic astigmatism cannot be improved by the prism pair. Once the beam profile is roughly shaped to the lowest order of transverse electromagnetic modes (TEM_{00}), we send the laser beam into an optical isolator and the following optics.

Reference laser

The reference laser is the central part of the ECDL system as it provides a fixed, stable, and reliable frequency for all other lasers to refer to. We use the modulation transfer spectroscopy [141] to get the frequency difference between the reference laser and a cesium D_2 atomic transition $|F = 4\rangle \rightarrow |F' = 5\rangle$. This differential signal is processed as the error

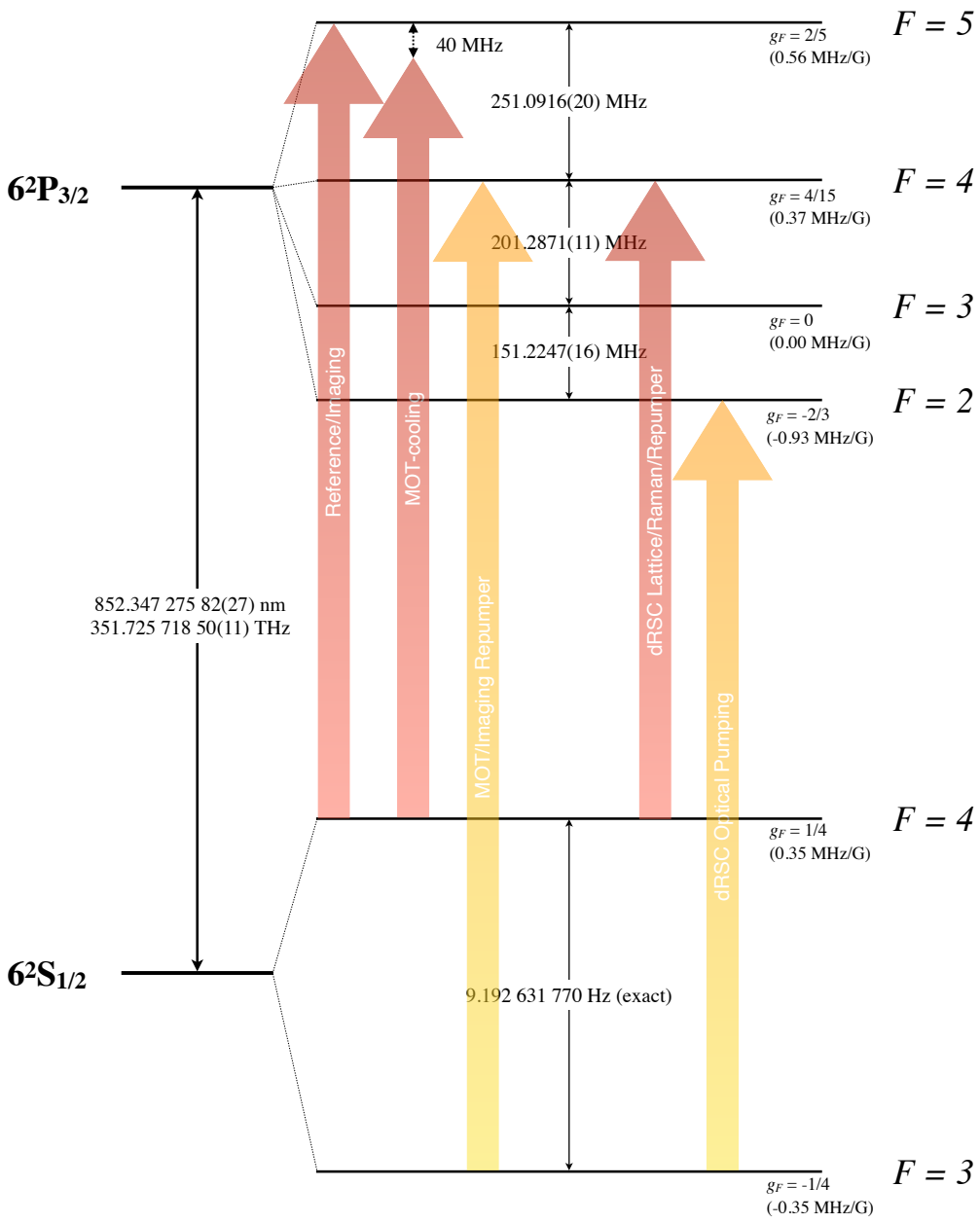

Figure 2.3. Cesium D_2 transition hyperfine structure. [140]

signal for the laser locking, so that the frequency of the reference laser is always locked to the atomic transition. Our reference laser is a homemade ECDL optimized to a large mode-hop free range around 5 GHz. The laser is split into several beam paths, one of them is sent into a cesium vapor cell after it is phase-modulated by an electro-optic modulator (EOM) driven by a commercial Direct Digital Synthesizer (DDS) at 7 MHz. The phase modulation creates differential absorption signals around an atomic transition, thus the strength of the absorption becomes the error signal for the laser frequency lock-in. The major power of the reference is split into two main paths, one is used to phase lock two different lasers in the other experimental apparatus, the second path double-passes through a 250 MHz acousto-optic modulator (AOM), creating a 500 MHz up shift from the original frequency, before being coupled into an optical fiber and sent to the quantum gas apparatus. The 500 MHz frequency up shift is necessary since we are using a phase lock technique to stabilize the frequency of our $F = 4$ laser (described below), and this requires a nonzero beat-note signal. Furthermore, 500 MHz is chosen to match the minimum acceptable frequency for the phase lock chip we are using (Analog Devices ADF4007, detailed below). At the fiber output, the reference laser is divided by a T=70%/R=%30 beam splitter into two beams for locking $F = 3$ and $F = 4$ lasers, respectively.

Cooling laser

Our $F = 4$ laser is built based on the description above. A pick-up glass plate splits a small amount of the light and merges with the reference beam, then sent into a ultra fast GaAs photodetector (HAMAMATSU G4176-03), which features 30 ps response time (Fig. 2.1). The overlapping beams create the beat-note on the photodetector, and the signal is then DC biased 24 V by a bias-tee (Mini-Circuits ZX85-12G-S+) and amplified by two radio frequency (RF) amplifier (Mini-Circuits ZKL-1R5+ and ZFL-500LN). After which the beat-note is sent to the Analog Devices ADF4007 Eval Board (UG-58), where we perform the phase-lock loop (PLL). ADF4007 takes two input signals: one is the beat-note RF signal to be locked, the other is the RF reference signal which is essentially the setpoint of the PLL (Fig. 2.4). ADF4007 has built-in frequency dividers and can be configured to

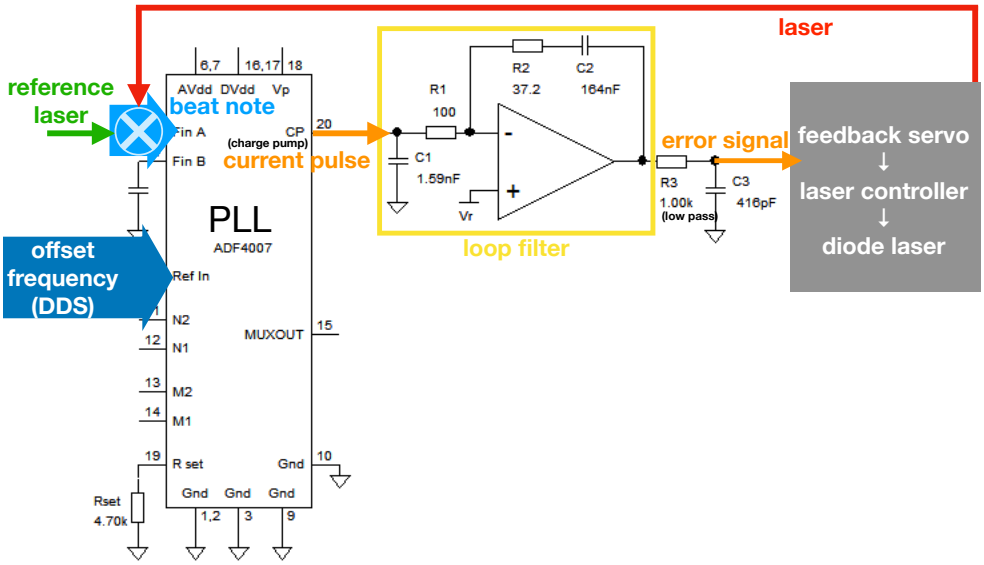

Figure 2.4. Schematic diagram of the phase-locked loop for laser frequency lock.

adopt different phase lock scenarios. In the $F = 4$ laser setup, we choose $\div 32$ as the RF divider and $\div 2$ as the reference divider, so the output of the PLL is always proportional to the difference between beat-note$\div 32$ − reference$\div 2$. We use a commercial Direct Digital Synthesizer (DDS) as the RF reference (Novatech DDS9m). DDS9m has four synchronized RF channels, and the first two channels have the "table mode", which means its frequency sequences can be programmed before the experimental procedure begins. Once the table mode is written into DDS9m's EEPROM, the frequency output follows the external trigger signal and advances to the next setting at the falling edge of each trigger. It is especially useful because cold atom experiments usually require real time synchronization of all lasers.

The original output of ADF4007 Eval Board is a charge pump (CP) essentially generating a series of current pulse width modulations (PWM), we convert these current pulses to analog voltage by a designed loop filter (LF) which is similar to a low-pass filter. The loop filter smooths out the PWM and result in an output voltage proportional to the difference between the input RF and reference RF, this is the error signal we feed into our homemade

PI (proportional-integral) servo. The laser PI servo shifts the error signal by a DC bias, making the zero point as the laser locking point such that the laser is always locked to zero error. The laser PI servo has two output branches that feed to the current driver and the piezo driver of the ECDL.

Repumper laser

Our $F = 3$ laser is very similar to the $F = 4$ laser above, except the detail configurations are different. Once again the pick-up from the repumper is overlapping with the reference beam on the ultra fast photodetector (Fig. 2.1), and the beat-note signal is DC biased by the same bias-tee (Mini-Circuits ZX85-12G-S+) then amplified by three microwave amplifiers (Mini-Circuits ZX60-183A-S+). Since the hyperfine splitting of the cesium ground state is 9.192 GHz, exceeding the maximum frequency that the ADF4007 Eval Board can take, so we further divide the beat-note by a factor of two via a microwave frequency divider (Analog Device EVAL-ADF500EB2Z), it is effectively a PLL device as well. After which we use a microwave high-Q low-pass filter (Mini-Circuits ZLSS-8G-S+) to filter out the interference of $\approx$ 9.1 GHz from other microwave spectroscopy signal, and amplify the beat-note signal (Mini-Circuits ZX60-8008E-S+) to meet the minimum power requirement of the ADF4007. We design a different loop filter for the repumper, and optimize the response time and stability of the PLL, then send the error signal to the repumper's laser PI servo.

2.1.2 Tapered amplifier

The $F = 4$ and $F = 3$ lasers from ECDLs are combined by a T=90%/R=10% non-polarized beam splitter then seeding into the tapered amplifier (Toptica BoosTA), in which the $F = 3$ laser frequency is downshift 80 MHz before combining with the $F = 4$ (Fig. 2.1). We reshape the combined beam by a prism pair for mode matching the TA chip. The TA is operated at current $I = 1400$ mA, and its output is shared among magneto-optical trap (MOT) beams, Zeeman slower beam, dRSC beams, and vertical imaging beam (Fig. 2.2). The residual power from the 90:10 beam splitter is coupled to an auxiliary optical fiber for other uses.

Before sending $F = 4$ and $F = 3$ lasers into the tapered amplifier (TA) for amplifying the optical power, each laser is picked up by 5% (Thorlabs BSF10-B) for other uses. $F = 4$ pick-up is sent through an AOM (up shift 80 MHz) and an optical fiber for the horizontal imaging beam, while $F = 3$ pick-up is sent through another AOM (down shift 80 MHz) and fiber for the optical pumping beam (Fig. 2.2).

2.1.3 dRSC laser

The basis of degenerate Raman sideband cooling (dRSC) will be described in Section 3.1.1. In order to perform dRSC, we need a red-detuned laser serving as the optical lattice beam as well as the two-photon Raman coupling beam. The optical lattices provide the tight traps and resolvable Raman sideband, and the two-photon Raman coupling rate is required to be faster than other possible heating rates such as photon scattering loss. Before September 2021, we used injection lock to amplify the optical power for red-detuned dRSC optical lattices. We built an ECDL as the master laser, and it is free running at the frequency $\approx$ 20 GHz red-detuned from $|F = 4\rangle \rightarrow |F'\rangle$. The master ECDL's grating feedback is carefully aligned so that the mode-hop-free range is maximized. The slave laser is assembled by a high power laser diode (Thorlabs LD852-SE600) without the holographic grating feedback, and it is stably controlled by commercial current and temperature controllers (Thorlabs LDC 240C and TED 200C, respectively). The slave laser is locked by reversely injecting the master laser through an exit port of a two-state optical ioslator to the gain region of the high-power laser diode. Once the slave laser is seeded, then stabilized and locked to a single-mode, narrow linewidth, the output of the slave laser is sent to an AOM (up shift 80 MHz) for intensity control before being coupled into an optical fiber.

In September 2021, we modified the dRSC laser to use the $F = 4$ laser directly. We couple a portion of the laser output from the tapered amplifier to the same optical path described above. The $F = 4$ laser serves as the optical lattice beam, two-photon degenerate Raman transition, and repumper in dRSC. The laser frequency is set to $|F = 4\rangle \rightarrow |F' = 4\rangle$ during the dRSC stage, where the AOM is set to down shift 80 MHz, while the $F = 3$ seeding beam from ECDL to the tapered amplifier is extinguished by an optical shutter. The dRSC

lattice beams have optical power ≈ (25, 12, 12) mW in (x, y, z) directions, respectively. Due to the closer detuning (≈ 9.5 GHz) to the dRSC optical pumping $|F = 3\rangle \rightarrow |F' = 2\rangle$, the magnetic field and the dRSC time are adjusted accordingly to optimize the cooling. Using the $F = 4$ laser from the tapered amplifier greatly reduces the effort to maintain two extra lasers prior to this modification, and significantly improves the stability of the laser system.

2.1.4 Nd:YAG laser

There are two Nd:YAG lasers used in the apparatus. Our optical dipole trap is produced from 1064 nm Nd:YAG laser beams, which are derived from a 25 W master oscillator power amplifier (MOPA) laser (InnoLight Mephisto MOPA). The MOPA output is divided to four paths, shifted by different frequencies via AOMs (Crystal Technology/Gooch & Housego 3110-197) to avoid interference between each other, and then coupled to 2 meter short optical fibers to avoid the stimulated Brillouin scattering (SBS) [142]. All optics are carefully adjusted then firmly secured on the optical table to maintain high stability. Moreover, thick aluminum blocks are placed under the AOMs as thermal heat reservoirs to reduce the temperature drifting. The other 532 nm Nd:YAG laser (Lighthouse Photonics Sprout-G 10) is responsible for pumping the Ti:Sapphire laser (describe below), where a part of laser output is split to two 532 nm AOMs (Gooch & Housego 3080-125) and coupled to two 2 meter fibers respectively.

2.1.5 Ti:Sapphire laser

Since its invention in the 1980s, Ti:Sapphire lasers have been reliable light sources with the capability of wide tunable wavelength. Ti:Sapphire lasers have narrow linewidths and broad mode-hop free range compared to external-cavity diode lasers, thus are suitable for applications requiring different wavelengths commercial laser diodes cannot offer. We use a Ti:Sapphire laser running continuous wave (CW) for different purposes such as optical Feshbach tuning. Our Ti:Sapphire laser is a Coherent MBR 110 pumped by a 532 nm diode-pumped solid-state Nd:YAG laser (Lighthouse Photonics Sprout-G 10), and its wavelength is

very tunable in 700 – 1030 nm with the replacement of the AR coated mirror in the internal optical cavity.

2.2 Magnetic coil

Magnetic coils are responsible for producing magnetic fields according to different experimental stages. In particular, we employ the magnetic Feshbach resonances of cesium for tuning the atomic interaction, thus a low-noise, stable, fast switching magnetic field is required. It is accomplished by a pair of main coils providing the major adjustment of the magnetic field, with the assistance from three pairs of bias coils to null the stray field.

2.2.1 Main coil

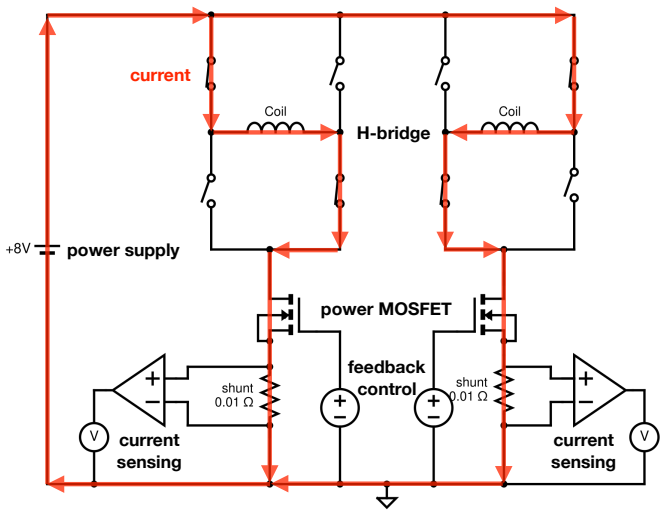

Figure 2.5. Schematic diagram of the H-bridge for reversing main coil current.

The main coil is responsible for the magneto-optical trap (MOT), magnetic levitation, evaporative cooling, and most importantly, the magnetic Feshbach resonance, so the accuracy and stability of the main coil field is crucial. We wind 4 (axial) by 7 (radial) turns for top and bottom coils with AWG 10 enameled square magnet wire (diameter $\approx$ 2.5 mm), sufficient for producing 2.48 Gauss/A in Helmholtz configuration and 0.62 Gauss/cm/A in anti-Helmholtz configuration. Here, we use a high precision 10 mΩ shunt resistor (Canadian

Shunt Industries) and a precision instrumental amplifier (Texas Instruments INA103) to measure the current, comparing it to the voltage provided by the computer control, then feedback to the high current N-channel power MOSFET (IXYS IXFN170N65X2) to control the current flowing through individual coil. The power MOSFET is chosen to have low ON resistance (R_{ON}) such that the most part of voltage/power from the high current power supply (Agilent 6551A, +8 V, 50 A) is dumped to the coil instead of the power MOSFET itself. Moreover, the load line (I_D vs. V_{DS}) of all our operations is well within the safe operating area of the power MOSFET. We later upgraded the high current power supply (Agilent 6673A, 0 – 35 V, 0 – 60 A) set to CV mode of +18 V and 50 A.

The coil driver can drive bidirectional current so that it is flexible to introduce magnetic field gradient and bias at the same time. We design a full H-bridge (Microsemi APTM10HM19FT3G) driven by two commercial isolated dual-channel gate drivers (Texas Instruments UCC21520EVM-286) to reverse the current direction. With four sets of power MOSFET in one full H-bridge package, the current direction of each coil can be switched from one to the other within microseconds (Fig. 2.5). Several high power varistors are installed in parallel with the coils to clamp down the induced voltage caused by the coil inductance during the switching in order to speed up the response of the coil current. The slew rate of the main coil is ≈ 0.1 A/μs, and could be increased by a higher voltage setting from the DC power supply. The eddy current during the switching is compensated by a pre-emphasis circuit added between the computer control analog output and the coil driver input. The pre-emphasis circuit is basically an adder of the control input voltage and several low-pass filtered voltages from the same control. The purpose of the pre-emphasis circuit is to overshot the coil current proportional to the control voltage with an exponential decay, so that the eddy current is canceled by the extra added magnetic field. We calibrate the low-pass filters in the pre-emphasis circuit by radio-frequency (RF) spectroscopy and microwave spectroscopy of the ground state atoms (Appendix C). RF or microwave spectroscopy can precisely measure the magnetic field by converting the resonant frequency to the Zeeman shift via Breit-Rabi formula. We therefore determine two major time scales of the eddy current $\tau \approx 0.3$ ms and 0.5 ms for the low-pass filters.

2.2.2 Bias coil

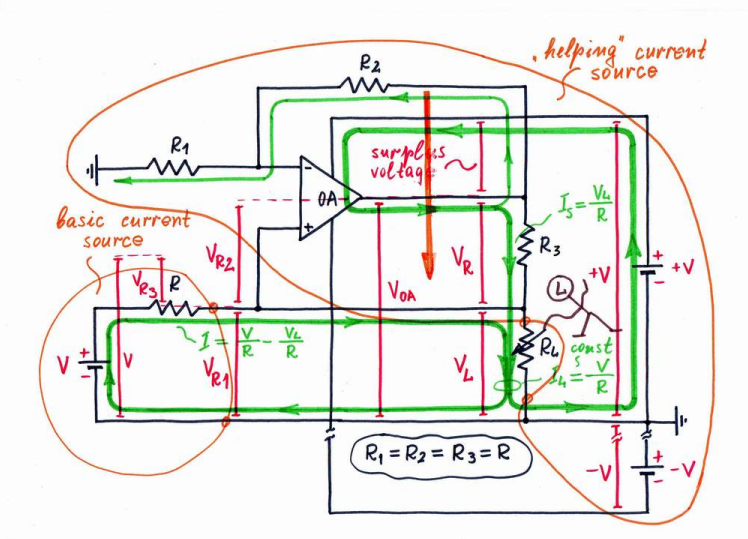

Figure 2.6. Schematic diagram of the Howland current source for the bias coil driver. [143] *CC-BY-SA*

Bias coils, or sometimes referred to as compensation coils, are used to cancel the external stray field as well as providing the principal axis during the degenerate Raman sideband cooling, optical pumping, and imaging. Our bias coil driver uses the idea of Howland current source (Fig. 2.6), in which the current flows through the coil $I_L = \frac{V_L}{R_L}$, where V_L is the output voltage of the power operational amplifier (op-amp, Texas Instruments OPA548) and R_L is the loading resistor we choose. Since the current is independent of the coil, it is stationary when the output voltage and the loading resistor are fixed. Practically the coil inductance would still cause the current ringing, thus in the circuit there is a feedforward design to suppress the induced voltage from the coil switching. A precision sensing resistor is used in the circuit to measure the current and compare it to the voltage from the computer control, then feeds back to the power operational amplifier in the Howland current source. The Howland current source has been widely used in cold atom experiments thanks to its nature of bipolar current driving and self-stabilization, therefore it is indeed possible to replace the main coil driver with the same kind if a proper high-current operational amplifier is available.

2.3 Vacuum system

Vacuum chamber is the vessel of the experiments. Strict ultra-high vacuum (UHV) is necessary for an ultracold atomic experiment, because miscellaneous room-temperature gas molecules will collide with cold atoms and expel them from the trap.

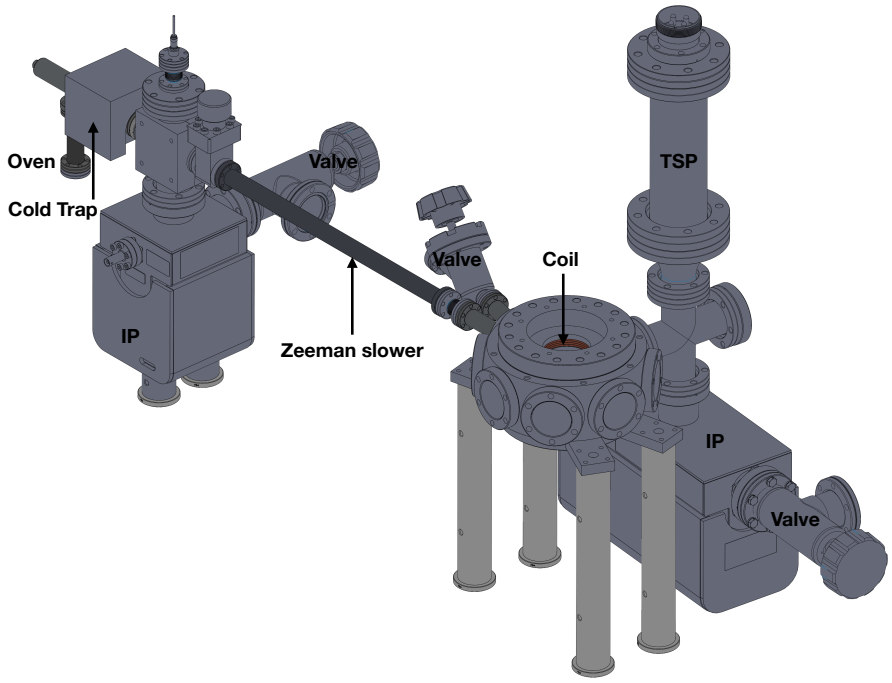

Figure 2.7. CAD drawing of the vacuum chamber with the main coils. IP: ion pump, TSP: titanium sublimation pump.

2.3.1 Design

A 5 grams 99.95% cesium ampule (Sigma Aldrich #239240) is responsible for the cesium source in our experiments. Its glass ampule is opened in an argon glove box and sealed into a nipple with a 1.33" CF all-metal angle valve to prevent any oxidation on the cesium surface before we pump down the chamber to vacuum. Silver-plated copper gaskets are used in all connections to avoid possible attack from hot cesium vapor. This source part is heated to $\approx$ 60 °C and generates $\approx 3\times10^{-5}$ Torr cesium vapor. The vapor is collimated by two skimmers, each of them has a 2 mm diameter aperture at the center. Skimmers are separated by a 3

inches nipple, giving an atomic beam with a solid angle of 0.026 rad. The nipple also serves as a 'cold spot' and is cooled down by a TEC along with the assistance of water cooling on the back. The entire cold spot is capped by a 3D printed box filled with polyurethane (PU) foam to insulate it from the room environment, thus we can cool it down to ≈ 0 °C and reduce the background cesium pressure. Meanwhile the skimmers are heated to ≈ 70 °C to prevent any cesium condensation from clogging the 2 mm aperture.

The collimated cesium vapor then enters the first pumping area, where a 25 L/s titanium ion pump is installed (Gamma Vacuum 25s). The second cold spot is also installed on top of the ion pump as a local temperature minimum, in order to protect the ion pump against long-term cesium poisoning[1]. After the first stage pumping, the cesium atomic beam enters a custom-made Zeeman slower nipple (L = 14 inches, OD = 3/8 inches), which gives the vacuum conductance ≈ 0.17 L/s. The Zeeman slower nipple is connected to a short flexible bellow for the flexibility of atomic beam alignment, then connected to a multi-flange. The multi-flange is designed to merge two 1.33 inches ConFlat (CF) flanges to one 2.75 inches CF flange, and each entrance is pointing to the center of the main chamber as described below. The other 1.33 inches CF flange on the multi-flange is reserved for future use and is terminated by an in-line all-metal valve and a 1.33 inches CF viewport currently.

The main chamber is an all-metal octagon (Kimball Physics MCF600-SphOct-F2C8) which features eight 2.75 inches CF flanges and two 6 inches CF flanges. We install seven 2.75 inches custom AR-coated vacuum viewports on the side (Kurt J. Lesker VPZL-275) and two custom-made recessed viewports on the top and the bottom (MPF A15199-1). The recessed viewports give us the ability to install magnetic coils and the microscope objective closer to the atoms, where the minimum distance from the center of the chamber to the viewport is ≈ 0.5 inches. The main chamber is pumped by a 75 L/s titanium ion pump (Gamma Vacuum 75s) and two titanium sublimation pumps (TSP, Gamma Vacuum G360819 and G360547) together (Fig. 2.7).

[1]↑Gamma Vacuum 25s ion pump failed in an accident on October 5, 2019. A SAES NEXTorr D 200-5 getter pump is attached as a replacement.

2.3.2 Preparation

All vacuum components require careful cleaning and handling. Except the viewports and the all-metal valves, we clean stainless steel components by Alconox → acetone → methanol → isopropanol in ultrasonic cleaner for 60 minutes for each chemical, then pre-bake these components at 350°C for 72 hours in a high temperature oven. Pre-baking in the air can create oxidation layers on the stainless steel surface and further reduce the outgassing diffusing from the interior of the materials. After assembling all vacuum components together, we do a vacuum bakeout by wrapping the chamber with heating tapes, and bake the chamber to 200°C along with a turbomolecular pump (TMP) roughing the initial pressure. When the pressure drops below $\approx 10^{-8}$ Torr which reaches the limit of the turbomolecular pump, we close the roughing valve, turn on the titanium ion pumps and activate titanium sublimation pumps to take over the pumping. Once the vacuum pressure reaches the minimum plateau again, we slowly decrease the baking temperature to room temperature. The final pressure is $\approx 10^{-12}$ Torr at the main chamber and $\approx 10^{-10}$ Torr at the oven side.

2.4 Computer control

An ultracold atomic physics experiment requires precise timing and synchronization of every controlling and sensing signal. The computer control system is the conductor to orchestrate different instruments and drivers such that designated physical parameters are met at an exact timing. Many schemes have been used for the purpose of synchronized analog and digital voltage output/input, some of which have been developed as commercial products targeting quantum teleportation and quantum computing markets. These schemes can be roughly categorized to

1. Variable time base: a central commander sends out hardware triggers (usually digital) to synchronize downstream devices [144]–[146].

2. Constant time base: a central clock sends out constant hardware triggers to synchronize downstream devices [147].

3. Real-time system: a specialized real-time operating system (RTOS) integrates with other devices to operate the procedures simultaneously [148].

4. Others: schemes are standalone and do not belong to any categories above.

Our control system is of the last kind. It is based on the hardware developed at the University of Texas at Austin and University of Amsterdam [149]. The design idea of this control system is aiming to be inexpensive and easy to construct. The system is based on a parallel bus which distributes data from a central computer to analog and digital output boards. The bus takes digital pulses from a digital I/O board (National Instruments PCIe-6536B) installed on a PCI-e slot in a desktop computer, in which it has 32 digital channels with maximum 25 MHz clock. Digital signals are sent from the National Instruments I/O board through a 50-pin SCSI cable with an IDC header to the output hardware. The clock for the National Instruments I/O board can be set to $\leq$ 20 MHz, i.e. the timing resolution for digital or analog outputs can be as fast as 50 ns. 32 digital lines in the bus include 16-bit data bus, 8-bit address bus, 1 strobe line, and 1 trigger line. The remaining 6 digital lines can be utilized in the future for auxiliary I/O or high speed devices. The data bus encodes the 16-bit analog voltage levels to digital-to-analog converter (DAC), or 16 channels of digital levels. For example, in an analog output board, $2^0 \equiv 0$ encodes the lowest voltage -10 V of a 16-bit DAC from ± 10 V range, and $2^{16} - 1 \equiv 65535$ encodes the highest analog voltage $+10$ V. On the other hand, 2^0 encodes all logic **0** (low) of 16-channel in a digital output board, and 2^{16} encodes all logic **1** (high). The address bus indicates which analog or digital board in the system should receive the data at a time. Each analog or digital board has logic comparators to determine if the incoming data should be passed downstream by comparing the address bus signal with its own local address set manually. If the encoded address signal matches the local address, the strobe passes the comparator then enable the latches to accept and hold the incoming 16 bits data for either one analog or 16 digital channels. Finally, the trigger line sends out parallel pulses to every board and commands everyone to update the output simultaneously (Fig. 2.8).

Our control software is written in Python, and wrapped in LabVIEW (National Instruments) for a better graphical user interface (GUI) and some hardware drivers. Users define

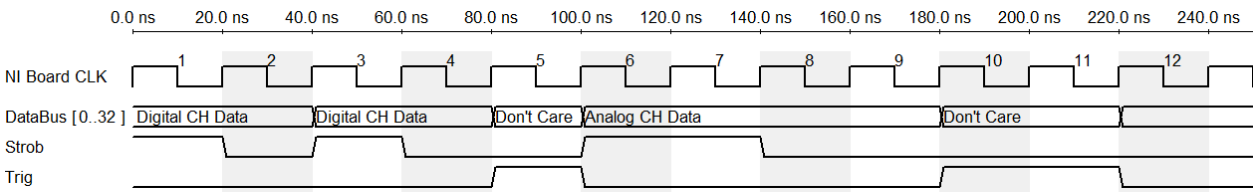

Figure 2.8. Example of a timing sequence of the bus for latching data and triggering outputs. Clock = 50 MHz.

what signals should be sent out at specific times, including analog voltage, digital logic, radio-frequency, etc.. The Python core takes users' input and calculates the exact timing when and which control board needs to be updated, then compiles the timing table as well as resolves any conflicts. The compiled table of timing sequences is uploaded to the flash memory of the National Instruments digital I/O board via NI IMAQdx, which initiates the procedure on its own internal clock instead of the CPU clock of the desktop computer. We have optimized the Python core codes so that the computation usually takes less than 500 ms for a $\approx$ 10-second experimental procedure with 1 μs temporal resolution – much shorter than the runtime using LabVIEW for the same task. The other part of the control software includes CCD camera control and readout, DMD control, data analysis, etc.. Drivers of other devices such as direct digital synthesizer (DDS), arbitrary waveform generator (AWG), microwave synthesizer, are also integrated into our control software. Typically our control system runs at 1 MHz resolution, i.e. 1 μs temporal resolution, and can be increased up to 20 MHz, primarily limited by the DAC. Our control system is comparably less pricey than commercial solutions. The digital and analog output channels have built-in 50 Ω buffers that can drive common radio-frequency components such as RF switches. On the contrary, commercial products often lack 50 Ω output buffers and still require extra effort to build. Our control system connects with the desktop computer by a 50-pin SCSI ribbon cable, therefore it is easier to be placed in different locations apart. We also note that the design of the analog output board includes several advanced features, e.g. ground loop isolation, precision voltage reference, electromagnetic interference (EMI) shielding.

3. EXPERIMENTAL PROCEDURE

In this chapter I describe our experimental procedures and basic laser cooling principals [150]–[153]. We cooperate several steps precisely in order to reach ultracold nano-Kelvin temperature for quantum physics experiments. The first cesium Bose-Einstein condensate in our lab as well as in Purdue University was achieved in January 2019, followed by the realization of homogeneous two-dimensional quantum gases within a few days. These experimental procedures stand on the shoulders of numerous theoretical and experimental work in history, accounting for atomic physics from classical kinetics to quantum mechanics. Extra attention and patience are required to operate the system.

3.1 Production of Bose-Einstein condensate

3.1.1 Laser cooling

Zeeman slower

The laser cooling process begins with a collimated atomic beam of cesium vapor coming from a hot oven. This atomic beam is collinear with a Zeeman slower, in which a selected velocity group of atoms can be slowed down in longitudinal direction by a counter-propagating laser beam. Ideally the frequency of Zeeman slower laser is always resonant to the atomic transition by Zeeman shift compensating for the Doppler shift [154] via a spatially varying magnetic field. During the Zeeman slowing, a moving atom is decelerated continuously by the resonant scattering

$$a(z) = -\frac{\hbar k \Gamma}{2m} \frac{s}{1 + s + \frac{4\delta(z)^2}{\Gamma^2}} \tag{3.1}$$

where $\hbar$ is the reduced Plank constant, $k = \frac{2\pi}{\lambda}$ is the wavenumber and $\lambda = 852$ nm is the laser wavelength, $\Gamma = 2\pi \times 5.2$ MHz is the transition linewidth, m is the cesium atomic mass, $s = \frac{I}{I_{sat}}$ is the saturation parameter which defines the efficiency of the Zeeman slower, $\delta(z)$ is the detuning at the position z of slower. The maximum deceleration is at $s \to \infty$, and at $\delta = 0$ when we have $\eta_s = \frac{s}{1+s}$, where η_s is the safety factor accounting for the ratio of the real

photon scattering rate and the theoretical maximum value $\frac{\Gamma}{2}$, and it has been parameterized in the design of the Zeeman slower. The detuning is

$$\delta(z) = kv(z) + \Delta - \frac{\mu'}{\hbar}B(z) \tag{3.2}$$

where $\mu' = \mu_B(g_e m_e - g_g m_g)$, and $\mu' = \mu_B$ in our case. Most people use the 'ideal' field profile, assuming constant deceleration (e.g adapted from Bell et al. [155]):

$$B_{\text{ideal}}(z) = \frac{\hbar k}{\mu'}\sqrt{v_0^2 + 2\eta a_m z} + B_a \tag{3.3}$$

where η is the cooling efficiency, v_0 is the maximum capture velocity chosen (or fixed by a given slower length and η), $a_m = -\frac{\hbar k\Gamma}{2m}$ is the maximum deceleration, setting $s = \infty$, and B_a is a bias field, or an equivalent laser detuning from the resonance as $B_a = \frac{\hbar}{\mu'}\Delta$. In this case the magnetic field gradient is

$$\frac{\partial B_{\text{ideal}}}{\partial z} = \frac{\hbar k}{\mu'}\frac{\eta a_m}{\sqrt{v_0^2 - 2\eta a z}} \tag{3.4}$$

which is a negative number because $a_m < 0$. A tapered-like magnetic field is designed to match the Doppler shift resulting from the moving atoms with a continuous deceleration. Atoms with the initial velocity $v \leq v_0$ entering the Zeeman slower exit with the final velocity $v_f = \sqrt{v_0^2 - 2a_z L}$, where L is the length of the Zeeman slower and $a_z \leq a_m$ is the deceleration.

Our Zeeman slower is designed with the safety factor $\eta_s = 0.5$, corresponding to slow atoms with initial velocities $v \leq v_0 = 127.6$ m/s down to $v_f = 36$ m/s (Fig. 3.1), within the capture velocity of the magneto-optical trap (MOT). A typical MOT maximum capture velocity v_c is the velocity of an atom stopped in a distance equal to the radius of the trap, by a force that is half of the maximum scattering force $v_c = \sqrt{2ar}$, where r is the trap radius, and a is the deceleration as $a = \frac{\hbar k\Gamma}{4m}$. Choosing a maximum trap radius of $r = 25$ mm and substituting the ^{133}Cs D_2 line's values into these equations: $m = 133$ amu $= 2.2 \times 10^{-25}$ kg, $\Gamma = 32.89 \times 10^6\ s^{-1}$, $k = 7.37 \times 10^6\ m^{-1}$, we get $a = 2.9 \times 10^4\ m/s^2$, $v_c = 38$ m/s [156].

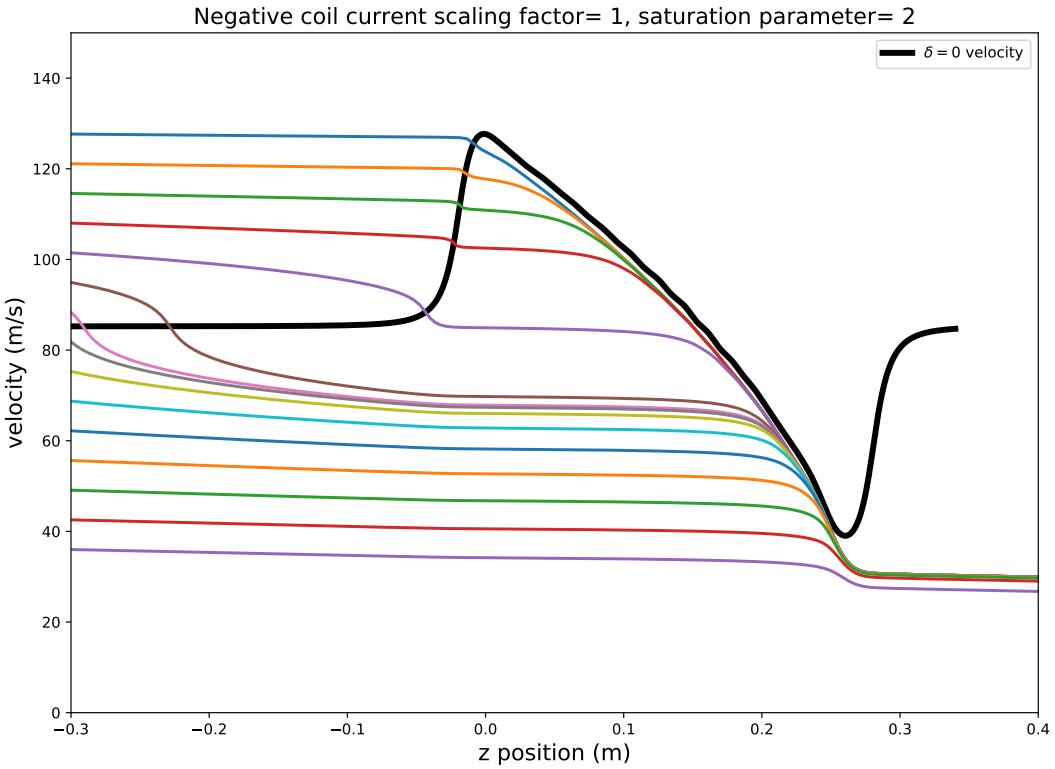

Figure 3.1. Simulation of atoms decelerated by the Zeeman slower.

The tapered coils are designed to run 1 A currents to generate the required profile of the magnetic field. The effective magnetic field of the Zeeman slower coil has a zero crossing in the middle, so the tapered ends of the positive field and the negative field are facing each other. We wind the Zeeman slower coils onto the tube using round AWG 16 magnetic wires before the Zeeman slower tube is assembled into the vacuum chamber, and apply Kapton tapes on each turn to secure the wires. A bias coil of two layers is firstly wound on the slower tube, designed to provide a uniform magnetic field, followed by two tapered coils with maximum ten layers wound on top of the bias coil for the positive and the negative magnetic fields. A cesium oven running at 60 °C generates a mean velocity $\bar{v} = 230$ m/s atomic beam end up with 13.6 % of the total atoms are expected to be slowed and trapped by the MOT, comparing to less than 0.5 % of the initial atom number being trapped without the Zeeman slower.

The final Zeeman slower parameters are optimized by maximizing the atom number captured by the MOT in 2 seconds, while we simultaneously adjust the MOT parameters to optimize the overall trapped atom number. The parameters used for designing the slower and for the actual operation are summarized in the Appendix B.

Table 3.1. D_2 line transitions for laser cooling and imaging

Experiment stage	Main	Detuning	Repump	Detuning
Zeeman slowing	$F = 4 \rightarrow F' = 5$	-140 MHz	$F = 3 \rightarrow F' = 4$	-100 MHz
MOT	$F = 4 \rightarrow F' = 5$	-40 MHz	$F = 3 \rightarrow F' = 4$	0
CMOT	$F = 4 \rightarrow F' = 5$	-50 MHz	$F = 3 \rightarrow F' = 4$	0
PGC	$F = 4 \rightarrow F' = 5$	-200 MHz	$F = 3 \rightarrow F' = 4$	0
dRSC (optical pumping)	$F = 3 \rightarrow F' = 2$	< 1 MHz	$F = 4 \rightarrow F' = 4$	< 1 MHz
dRSC (optical lattice)	$F = 4 \rightarrow F' = 5$	-20 GHz		
(Since Sep 2021)	$F = 4 \rightarrow F' = 4$	< 1 MHz		
Imaging	$F = 4 \rightarrow F' = 5$	0	$F = 3 \rightarrow F' = 4$	0

Magneto-optical trap

After slowing down the axial velocities, cesium atoms are captured, trapped and further cooled in the magneto-optical trap (MOT) [157]. A MOT consists of three pairs of orthogonal counter-propagating laser beams crossing at the chamber center (Fig. 3.2), and a magnetic quadrupole field whose center overlaps the laser beams. The laser beams have two frequencies of 40 MHz red-detuned from $|F = 4\rangle \rightarrow |F' = 5\rangle$ transition for cooling and trapping, and $|F = 3\rangle \rightarrow |F' = 4\rangle$ transition for repumping. The polarization of each MOT beam is σ^- relative to the local magnetic field. The σ^- transition incorporates with the magnetic field gradient from quadrupole coil provides both restoring force due the preferential scattering and damping force due to the Doppler cooling. The MOT parameters are tweaked to improve the loading rate of the atom number in the trap. The quadrupole gradient field is set at B' = 15 G/cm. Typically we collect $\approx 1 \times 10^8$ atoms in 2 seconds while the oven temperature is around 60°C.

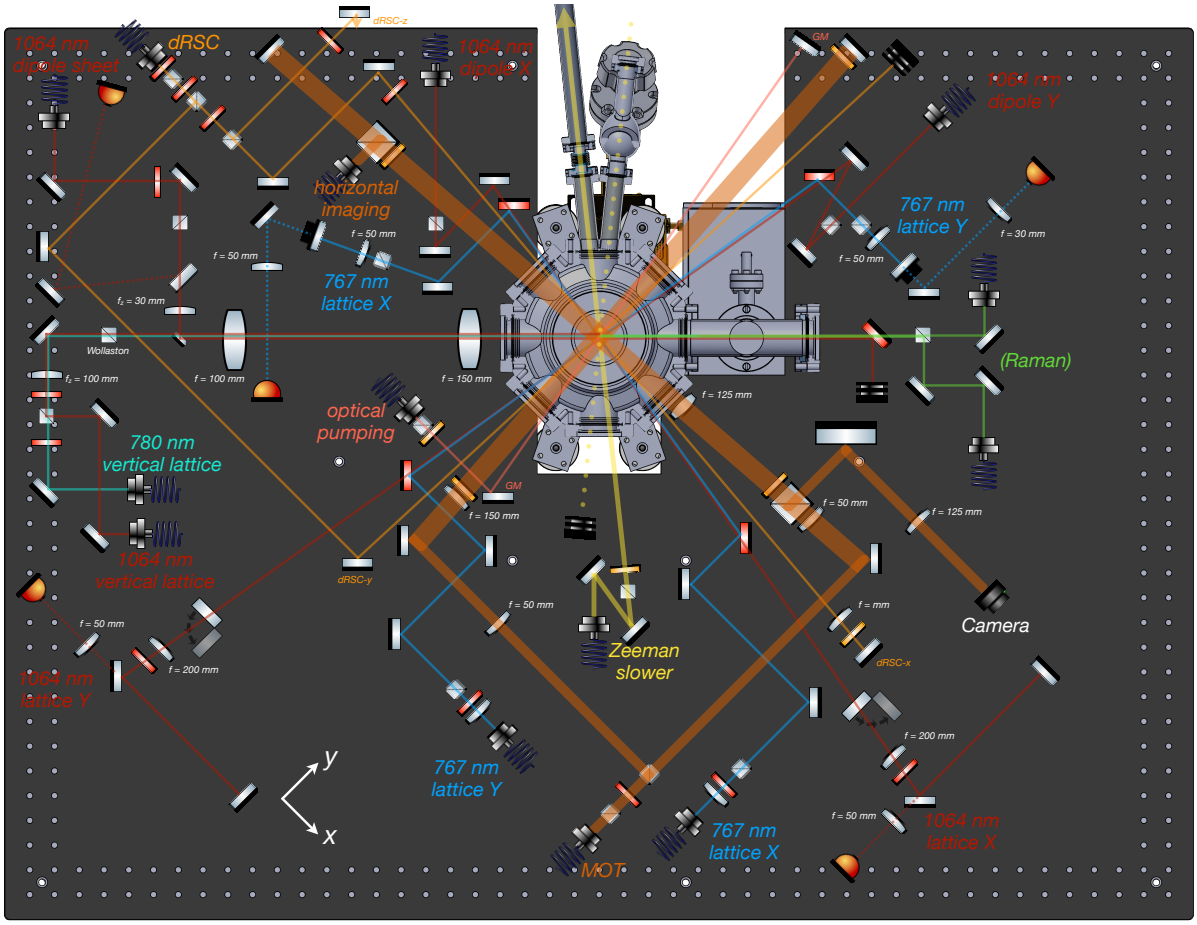

Figure 3.2. Top view of the optical layout on the middle optical breadboard. Symbols of components are annotated in Fig. 3.6.

Compressed MOT and optical molasses

After a sufficient number of atoms are collected inside the MOT, we suddenly increase the magnetic gradient and jump the cooling laser frequency to further 10 MHz red-detuned, meanwhile decrease the MOT laser power for 15 ms. This compressed MOT procedure (cMOT) increases the density of the cold atomic cloud. After cMOT, we simultaneously remove the quadrupole magnetic field, further red-detune the laser frequencies to ≈ 200 MHz from $|F = 4\rangle \rightarrow |F' = 5\rangle$ transition and decrease the intensities of the laser beams for the optical molasses to take place, which is also referred to as polarization gradient cooling (PGC)

or Sisyphus cooling [158], [159]. During the polarization gradient cooling, sub-Doppler effect can cool down the temperature of atoms to < 10 μK below the Doppler limit.

The setup of our MOT optics is depicted in Fig. 3.2. $x-$ and $y-$ MOT beams are derived from a fiber coupled from the output of the tapered amplifier (TA) after a 100 MHz up-shift AOM, and $z-$ MOT beam is from the other fiber coupled from the same AOM output. The optical power of $x-$ and $y-$ MOT beams are 40 mW, whereas the $z-$ MOT beam is 80 mW. The optimized optical intensity ratio of MOT x:y:z $\approx$ 1:1:2 matches the ratio of magnetic field gradient along each direction. $x-$ and $y-$ MOT beams are split from the fiber output, enlarged $\approx 3\times$ by pairs of singlet lenses forming ≈ 30 mm diameter beam sizes before entering the main chamber. These beams are retro-reflected by mirrors on the other sides of the chamber. The $z-$ MOT beam is formed by a $f = 150$ mm singlet lens, then combined with the vertical imaging beam via a polarization beam splitter (PBS). The $z-$ MOT beam passes through the bottom and top recessed viewports and a microscope objective, then retro-reflected by a wire-grid polarizer (Meadowlark VersaLight). Before September 2021, a custom-made thin broadband quarter waveplate is placed in front of the wire-grid polarizer and its angle is adjusted such that the $z-$ MOT beam is reflected by the wire-grid polarizer and the vertical imaging beam passes through.

Degenerate Raman sideband cooling

Following MOT and PGC, we further cool down atoms by three-dimensional degenerate Raman sideband cooling (dRSC) [160]–[162]. Atoms in the optical molasses are optically pumped to the $|F = 3\rangle$ hyperfine ground state after the removal of $F = 3$ in PGC beams by shutting off the $F = 3$ seeding laser to the tapered amplifier, followed by loading atoms into a three-dimensional optical lattice potential. A background magnetic field is switched on so that the magnetic Zeeman splitting $\Delta E_z = 1/4\mu_B B$ between adjacent magnetic sublevels matches the vibrational energy splitting $\hbar\omega$, where ω is the vibrational angular frequency of atoms in the optical lattices. The dRSC connects atoms between the degenerate Zeeman levels of different quantum states $|m_F, \nu\rangle$ and $|m_F \pm 1, \nu \pm 1\rangle$ via two-photon Raman coupling, where ν is the vibrational quantum number in the three-dimensional optical lattices, and m_F

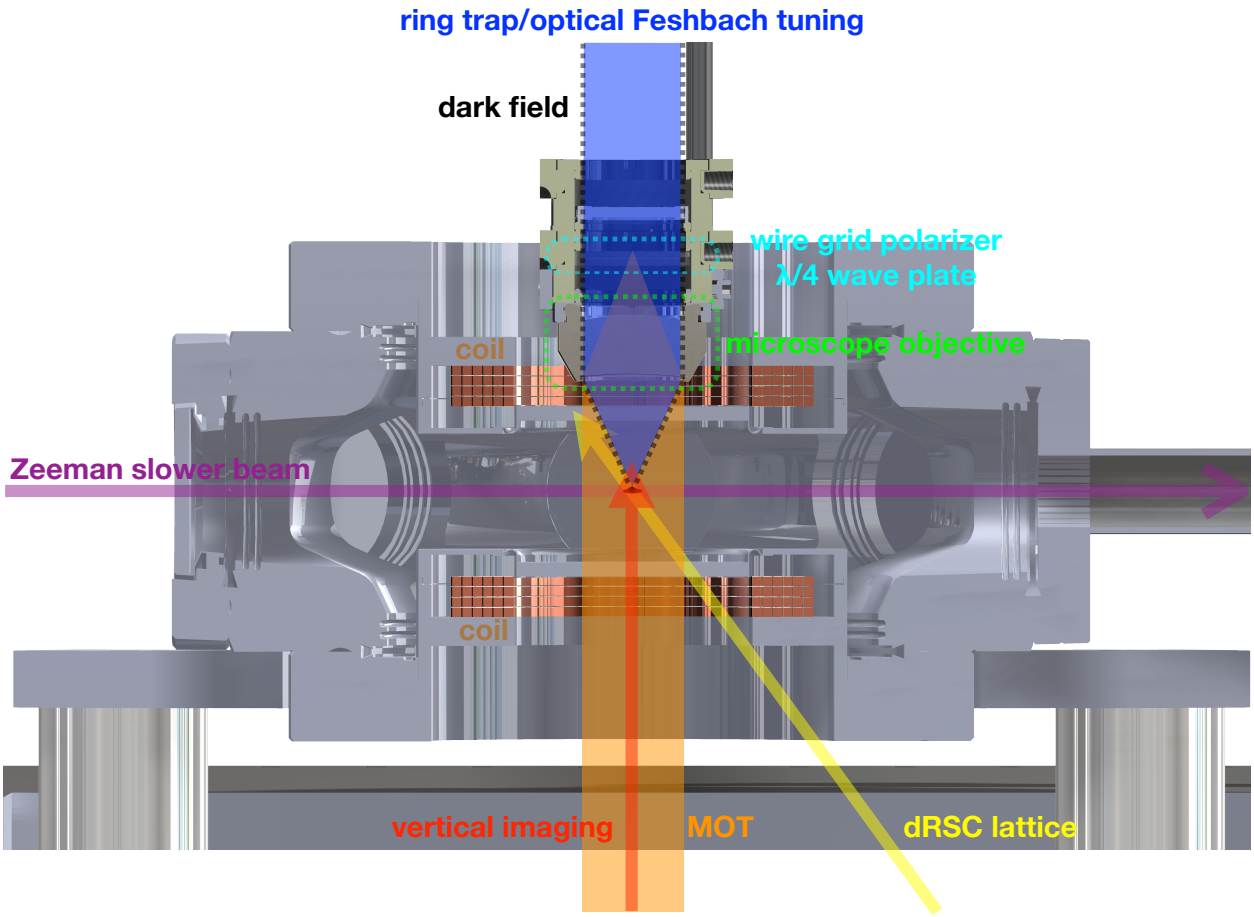

Figure 3.3. CAD drawing of the side cross section.

is the total spin quantum number along the principle axis, i.e. the background magnetic field vector. An optical pumping beam is applied with σ^+ polarization with respect to the principle axis to drive atoms from $|F = 3, m_F, \nu\rangle$ to $|F' = 2, m_F + 1, \nu\rangle$, followed by the spontaneous emission from excited state $|F' = 2, m_F+1, \nu\rangle$ to $|F = 3, \nu\rangle$ hyperfine ground state manifold, consequently the entropy is removed. If the optical pumping takes place in the Lamb-Dicke regime where the vibrational quantum number remains unchanged, the optical pumping eventually pumps all atoms to the $|F = 3, m_F = 3, \nu = 0, 1\rangle$ and $|F = 3, m_F = 2, \nu = 0\rangle$ states. On the other hand, atoms would populate in the $|F = 3, m_F = 2, \nu = 0\rangle$ state due to the continuous degenerate Raman coupling, so a π-component is required in the optical pumping beam to further remove these atoms. As a result, all atoms are driven to the lowest

vibrational ground state $|F = 3, m_F = 3, \nu = 0\rangle$ and stay there as it is the only dark state (Fig. 3.4).

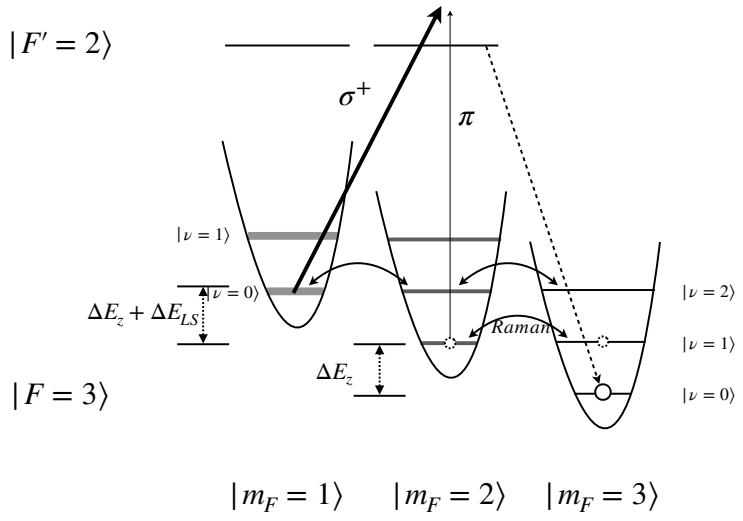

Figure 3.4. Diagram of the degenerate Raman sideband cooling. F: total atomic angular momentum, ΔE_z: Zeeman shift, ΔE_{LS}: light shift caused by the σ^+ light, $|\nu\rangle$: vibrational state. [161]

Experimentally we set up a retro-reflected counter-propagating laser beam that intersects with the other two orthogonal beams to form three-dimensional optical lattices (Fig. 3.2). The retro-reflected beam is defined as $\pm x'$ and the polarization of its retro-reflection is rotated $\approx 10°$ with respect to the incident polarization by a quarter waveplate. All optical lattice beams are derived from the same fiber coupled from the dRSC laser, and their polarizations (i.e. electric field vectors) all lie on a two-dimensional plane, resulting in a non-vanishing fictitious magnetic field for the two-photon Raman coupling. Before September 2021, the total optical power is 80 mW with frequency red-detuned 20 GHz from $|F = 4\rangle \rightarrow |F' = 5\rangle$ transition to reduce off-resonant scattering. The degenerate two-photon Raman coupling is carried out by such the same optical lattice beams via the vector light shift from their crossed electric fields, and the fictitious field from the tensor light shift is pointing to the direction

of the $\pm x'$ beams. The dRSC optical pumping beam is derived directly from the $F = 3$ repumper laser, and its polarization is tuned to σ^+ by a zeroth-order quarter waveplate, then retro-reflected along the same path by a gold mirror on the other side of the chamber to minimize recoil heating.

In the experimental procedures, dRSC is applied immediately after the PGC. The $F = 3$ repumper seed to the tapered amplifier in the MOT beam is first extinguished for 1 ms for the $F = 4$ component to polarize all atoms to the $|F = 3\rangle$ hyperfine ground state. Then the dRSC optical lattices pulse on to freeze and isolate all atoms to lattice sites locally. Meanwhile, the optical pumping beam whose frequency jumping to $|F = 3\rangle \rightarrow |F' = 2\rangle$ transition is applied to the atoms, and the frequency of the original MOT beams jumps to $|F = 4\rangle \rightarrow |F' = 4\rangle$ transition while its intensity is greatly reduced simultaneously, repumping atoms in the $|F = 4\rangle$ state to the $|F = 3\rangle$ state, then back to the cooling cycles again. The bias coils generate a background magnetic field along the principle axis, i.e. the direction of the optical pumping beam, and the Zeeman splitting for degenerate two-photon Raman coupling is created by the exact magnetic field tuned carefully. After a sufficient cooling time ≈ 3 ms, the optical pumping beam and the repumping beam are extinguished first, followed by ramping off the three-dimensional optical lattices in 100 μs, hence local ground state atoms are released into free space or additional optical dipole trap adiabatically.

In September 2021, we derive the dRSC laser from the tapered amplifier (TA) tuned to $|F = 4\rangle \rightarrow |F' = 4\rangle$ for dRSC optical lattices, two-photon Raman coupling, and repumping during dRSC together. Since the laser detuning is closer (≈ 9.5 GHz red-detuned from optical pumping $|F = 3\rangle \rightarrow |F' = 2\rangle$), both the dRSC optical lattice trap frequency and the Raman coupling rate increase, as a result we adjust the dRSC procedure such as laser intensities and durations correspondingly. With the new configuration, each dRSC cycle is ≈ 1 ms followed by ≈ 2 ms ramp off of the lattices. Although $|F = 4\rangle \rightarrow |F' = 3\rangle$ may have slightly larger detuning thus reducing the heating from off-resonant scattering, we find that the overall cooling performance is not better. Similar schemes have also been reported in literature [163]. By simplifying the laser system and locking the frequency of dRSC laser, we are able to improve the stability and reliability of laser cooling.

We optimize the dRSC parameters by minimizing the temperature and maximizing the number of atoms after dRSC, both in free space and after the optical dipole trap loading. More than 80% of atoms in the optical molasses are spin-polarized into $|F = 3, m_F = 3\rangle$ and cooled to very low temperature, of which we are unable to fit the TOF expansion in free space. We apply 2 – 3 dRSC cycles while the optical dipole trap is turned on and the free space temperature of atoms released from the optical dipole trap is 1.5 μK, the final peak phase-space density is ≈ 0.01 in the optical dipole trap. The dRSC is very efficient in aid of laser cooling, especially for elements lacking other sub-Doppler cooling mechanisms, and has been demonstrated to cool rubidium atoms directly to quantum degeneracy [164]–[166].

3.1.2 Evaporative cooling

Unlike some alkali metal elements such as rubidium that can be applied radio-frequency-induced evaporative cooling, the $|F = 3, m_F = 3\rangle$ ground state of cesium is not magnetically trappable. In order to perform the evaporative cooling to achieve Bose-Einstein condensate, we need to trap atoms in an optical dipole trap which utilizes the electric dipole force to attract the atoms in the region of high laser intensity. Normally, dipole traps operate at sufficiently large frequency detuning from any transition where the scattering rate is reduced while maintaining a reasonable trap depth at the focus of the laser beams.

The light shift of ground state atoms is given by the contribution of the D_1 and D_2 lines, whose line strengths have weights $\frac{1}{3}$ and $\frac{2}{3}$, respectively,

$$V(\mathbf{r}) = \frac{3\pi c^2}{2}\left(\frac{1}{3}\frac{\Gamma_1}{\omega_1^3\Delta_1} + \frac{2}{3}\frac{\Gamma_2}{\omega_2^3\Delta_2}\right) I(\mathbf{r}) = \alpha I(\mathbf{r}) \tag{3.5}$$

where c is the speed of light, $I(\mathbf{r})$ is the optical intensity of the laser beam at $\mathbf{r}$, $\Gamma_1 = 2\pi\times$ 4.575 MHz and $\Gamma_2 = 2\pi\times$ 5.234 MHz are the natural line widths of the D_1 and D_2 lines, respectively, $\omega_1 = 2\pi\times$ 335.1 THz and $\omega_2 = 2\pi\times$ 351.7 THz are the transition frequencies of D_1 and D_2 lines, respectively, $\Delta_1 = -2\pi\times$ 53.34 THz and $\Delta_2 = -2\pi\times$ 69.94 THz are the laser detuning of the 1064 nm dipole laser from D_1 and D_2 lines, respectively, giving $\alpha = -k_B\times$ 2.59 nK$\cdot$ cm^2/W. Therefore, the light shift induced by a red-detuned laser beam

form an attractive potential that confines the atoms in the intensity maximum. The photon scattering rate for a far-detuned laser is

$$\Gamma_{\rm sc}(\mathbf{r}) = \frac{\pi c^2 \Gamma^2}{2\hbar\omega_0^3}\left(\frac{2}{\Delta_2^2} + \frac{1}{\Delta_1^2}\right) I(\mathbf{r}) \approx \frac{\Gamma}{\Delta}\frac{V(\mathbf{r})}{\hbar} \tag{3.6}$$

where Γ is the linewidth, ω_0 is the transition frequency, and $\Delta = \omega - \omega_0$ is the laser frequency detuning. In our experiment, the dipole trap depth is $U_0 \approx k_B \times 3.4\ \mu$K, and the photon scattering rate is $\Gamma_{\rm sc} < 0.03$ Hz, which has negligible heating to the trapped atoms within the experiment time < 10 seconds.

We use two orthogonal ($x-$ and $y-$) laser beams and a thin sheet beam to form an optical dipole trap (Fig. 3.2). All three beams are crossing at the center of the chamber. Each $x-$ and $y-$ dipole beams typically has ≈ 3 W and beam diameter of $\omega_x \approx \omega_y \approx 730\ \mu$m. These two beams provide a horizontal trap frequency of $2\pi\times$ 12.5 Hz and a trap depth of $V_0 = k_B \times 3.4\ \mu$K, and form the major trapping potential to capture the laser-cooled atoms from dRSC. The sheet dipole beam is an elliptical beam (aspect ratio H25:V1) elongated horizontally and intersects the crossed dipole beams at the center of the chamber with a 45° angle (Fig. 3.2). The sheet dipole beam has vertical diameter of 60 μm and optical power $\approx$ 800 mW, forming a strong dipole trapping force to hold the atoms against the gravity. The sheet dipole beam also provides a higher trap frequency of $2\pi\times$ 73 Hz along the $z-$ direction, similar to the idea of 'dimple trap' [167] that helps the thermalization during the evaporative cooling process.

In the experiment, all three dipole beams are derived from a Nd:YAG laser (InnoLight, Mephisto MOPA) with single mode, single frequency and total output optical power 16 W. The laser is split into four parts, corresponding to $x-$, $y-$, sheet dipole beams and an additional beam for other use[1]. Each beam is frequency offset by an AOM (Crystal Technology/Gooch & Housego 3110-197) to avoid interference between each other. The frequency shifts are -110 MHz for $x-$beam, $+110$ MHz for $y-$beam, and -220 MHz for sheet beam (with 110 MHz double-pass). After the AOMs, laser beams are fiber coupled and sent to the main chamber. We chose optical fibers with a short length of 2 meters in order to reduce

[1]↑Currently it is used for vertical attractive addressing beam.

the stimulated Brillouin scattering (SBS), and make sure the fibers deliver the designate power continuously without degradation of the coupling efficiency. At each fiber output, zeroth-order half waveplate and high extinction ratio (> 1000:1) PBSs are placed to clean up the polarization fluctuation of each beam, and intensity feedback is set up for the sheet dipole beam to precisely control the final trap depth of the evaporative cooling.

We keep the three dipole beams turned on from the beginning of the experimental cycle, such that the thermal drift of the AOM and the change of thermal lensing effect of all optics are minimized. Since light shift of far-detuned dipole beams is small compared to the strong near-resonance radiation pressure from the MOT and the PGC, the performance of such cooling has very little influence and can be compensated by small laser detuning. After the PGC, we apply 2 – 3 cycles of dRSC to remove the kinetic energy of the atoms. Right after the last cycle of dRSC, we pulse on a magnetic gradient and a strong magnetic bias by only injecting the current to the top coil. The magnetic gradient provides an upward force to levitate the atoms against the gravity, and the strong magnetic bias forms a weak trapping force on the horizontal plane due to non-ideal Helmholtz configuration of the coil pair (Fig. C.3). We typically have 5×10^6 in the full-power dipole trap with magnetic levitation after 500 ms of self-evaporation.

The evaporative cooling method closely follows Ref. [168], yet the details of experimental parameters, procedures, and results are different to some extent. We first gradually reduce the magnetic gradient to tilt the overall trapping potential in 4 seconds, while quickly ramp down the magnetic bias to $B = 26$ G in 2 seconds, which corresponds to cesium s-wave scattering length 400 a_0, where a_0 is the Bohr radius. Then we keep reducing the magnetic gradient to zero and simultaneously ramping the magnetic bias to 21.2 G, corresponding to a scattering length of 220 a_0. The whole cooling process is aiming to lower down the trap depth of the overall trapping potential so the atoms with higher energy can escape, meanwhile keep sufficient trap frequency and proper scattering length for maintaining the collision rate for the remaining trapped atoms to thermalize. Finally, we typically have Bose-Einstein condensate of 5×10^4 atoms in an optical dipole trap, and the background magnetic field stays at 21.2 G to minimize the three-body recombination loss [169].

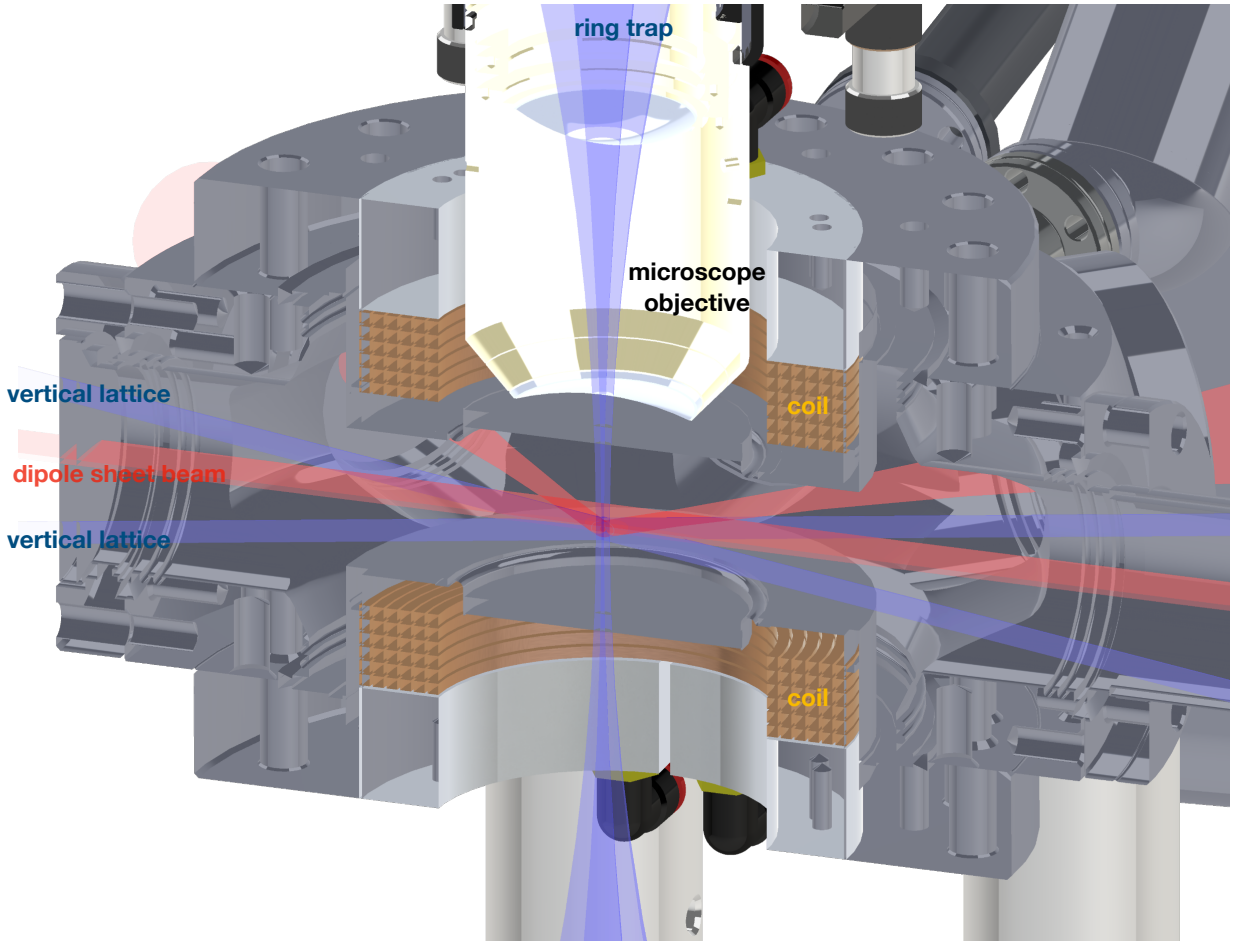

Figure 3.5. CAD drawing of the side cross section. Blue: 780 nm blue-detuned repulsive beam, Red: 1064 nm red-detuned attractive dipole beam.

3.2 Production of two-dimensional quantum gas

Our experiment usually begins with a nearly uniform 2D Bose gas confined in a quasi-2D box potential formed by all repulsive optical dipole beams. The vertical box confinement is provided by a single node of a repulsive standing-wave potential (3 μm periodicity) along the vertical (z-)direction. The node defines the horizontal 2D plane. The standing-wave potential is formed by the interference of two 780 nm vertical confinement beams crossing at the horizontal plane with 22° separation angle (Fig. 3.5). The measured vertical trap frequency in the node is $\omega_z/2\pi = 2.25 \pm 0.04$ kHz $\gg (k_B T, |\mu|)/\hbar$, thus freezing all atoms in the harmonic ground state as well as providing the harmonic oscillator length ≈ 183 nm along

the vertical (z-)direction. Here k_B is the Boltzmann constant, $T \lesssim 8$ nK is the temperature of the 2D gas and μ is the chemical potential. In our early setup, the horizontal boundary of the box is formed by a tightly focused 780 nm optical beam that scans the box boundary at a 15 kHz repetition rate to form a time-averaged, repulsive wall potential. The beam is controlled by a pair of acousto-optic deflector (AOD) and projected through a microscope objective. When the wall potential is removed, the residual global trap frequency in the horizontal plane, due to a weak magnetic trap from non-ideal Helmholtz coil configuration (Fig. C.3), is experimentally determined to be $\omega_r/2\pi < 2.25$ Hz through induced superfluid dipole oscillations.

In our later revised setup, we replaced the AOD with a digital micromirror device (DMD) to form the horizontal confinement of the box trap (Fig. 3.6). A 780 nm blue-detuned repulsive beam is expanded to ≈ 7 mm waist diameter via an air-spaced doublet collimator (Thorlabs F810APC-780), then reflected by the DMD (ViALUX DLP7000), and projected onto the atoms through a 2" doublet lens $f = 750$ mm and the microscope objective. This high-speed (22,727 Hz) DMD is capable of dynamically changing the shape of the trap, thus allowing us to compress or decompress, or even rotate the trapped gases. The demagnification of the relay optics is $\approx 25\times$ corresponding to ≈ 0.5 μm/pixel, which is smaller than the resolutions 1.3 μm and 0.8 μm of the microscope objectives (N.A. = 0.37 & 0.6, respectively. Numerical aperture N.A. $= n \sin\theta$, where the refractive index of the medium $n \approx 1$ and θ is the maximal one-half angular aperture).

To load a quantum gas into the 2D box potential, we first prepare $N \approx 5 \times 10^4$ nearly pure Bose-condensed cesium atoms in the $|F = 3, m_F = 3\rangle$ hyperfine ground state. The three-dimensional (3D) BEC is initially trapped in an oblate dipole trap formed by two crossed dipole beams and a horizontal sheet dipole beam. Near the end of the evaporative cooling as aforementioned description, the magnetic field is jumped to ≈ 18.8 G to prepare the final BEC at a smaller scattering length at $a_s \approx 100\, a_0$, so that the size of the condensate is smaller for box loading. We then ramp on the box potential in 200 ms to compress the 3D BEC into a thin sheet of 2D superfluid, followed by a 200 ms ramp to turn off all attractive 1064 nm dipole beams. The vertical alignment between the 3D BEC and the box potential has been carefully adjusted, and the single-node loading in the standing-wave potential is

confirmed by nulling the matter-wave interference pattern along the vertical (z-)axis during time-of-flight (TOF), which is sensitive to small number of atoms present in the adjacent nodes. The sample temperature is measured to be $T < 8$ nK after being released back to the 3D oblate trap using a reversed process.

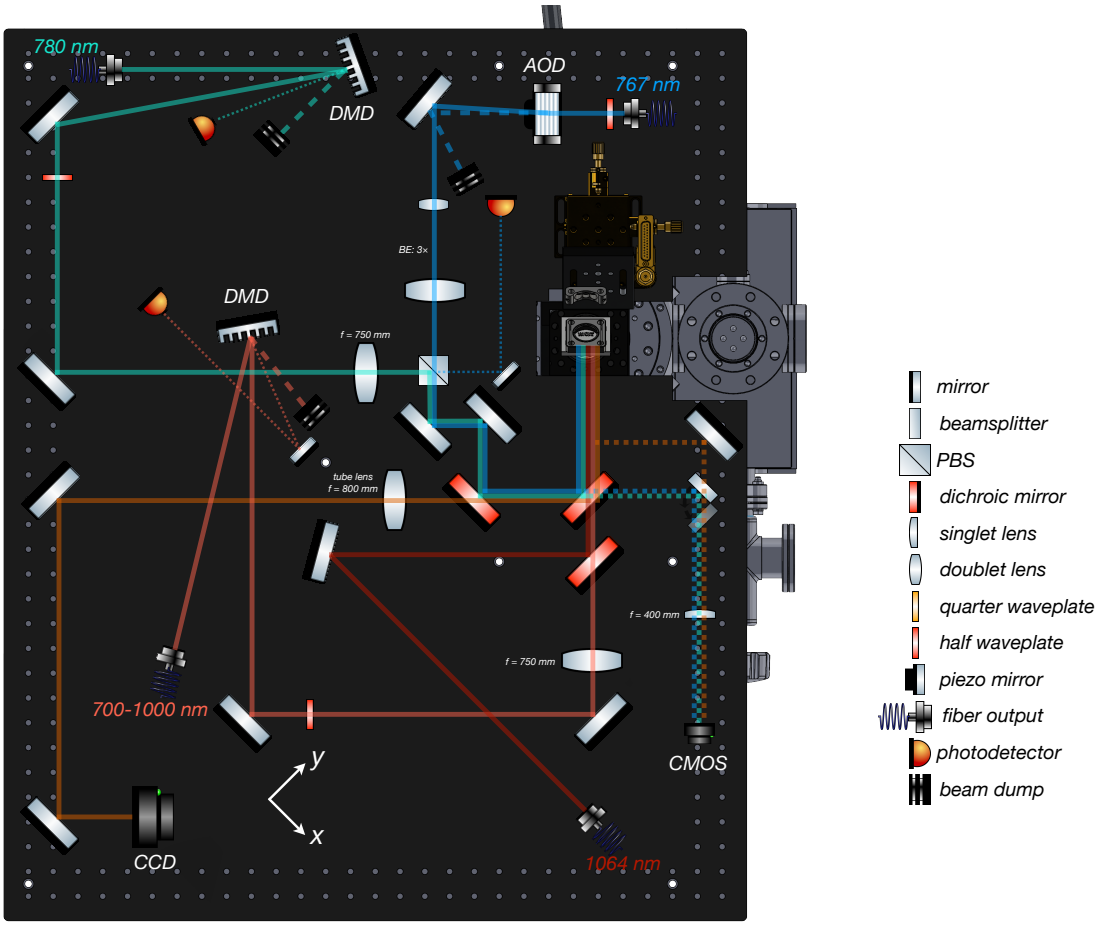

Figure 3.6. Top view of the optical layout on the top optical breadboard. AOD: acousto-optic deflector, DMD: digital micromirror device, CCD: charge-coupled device camera, CMOD: complementary metal-oxide-semiconductor camera, BE: beam expander.

3.3 Spatiotemporal optical control

3.3.1 Spatial control

In order to locally control ultracold atoms, a custom-made high-resolution microscope objective (N.A. = 0.6, Special Optics #54-32-27) is used to project engineered optical fields onto the atoms, inducing spatial-dependent optical Feshbach tuning of atomic interactions. The same beam is also used to add local potential offsets to the atoms and fine tune local chemical potentials to prevent mass transport or induce one. Subsequently, *in situ* absorption imaging is performed by sending a resonant laser beam vertically through the atomic sample. The shadow cast by the sample is imaged through the same microscope objective and recorded on a back-illuminated deep depletion CCD camera (Princeton Instruments PIXIS). The characterisation of imaging aberration is detailed in Appendix G.1.

3.3.2 Temporal control

The pattern of dynamic optical addressing beam is created using laser reflected from a DMD (ViALUX DLPV650LNIR). Each micro-mirror on a DMD has a linear size ≈ 10.8 μm, and can flip to two distinct angles $\pm 12°$, controlling the local intensity of the projected optical Feshbach tuning beam or a vertical addressing beam at a binary level (Fig. 3.7). The high-speed DMD (10,752 Hz) enables us to resolve cesium many-body dynamics to $\leq$ 100 μs time scale. The DMD is controlled by a LabVIEW program integrated with our computer control via ALP API (application programming interface). The computer control initializes the DMD to 'slave mode' and uploads a series of 2-bit depth frames to the control board of the DMD, followed by commanding 'run' the sequence. Each frame displays for a fixed 'illumination time' (or 'picture time') set by the program, then waits for external hardware triggers to advance on the next frame, while all micro-mirrors remain static in between. When specific micro-mirrors are updated, however, these micro-mirrors are reset before changing the status, i.e. micro-mirrors are released to 'reset' (0°) before flipping to $+12°$ (**1**) or $-12°$ (**0**). This unavoidable reset transient can take tens of microseconds, and could be a potential problem in the future experiments involving fast kinetics.

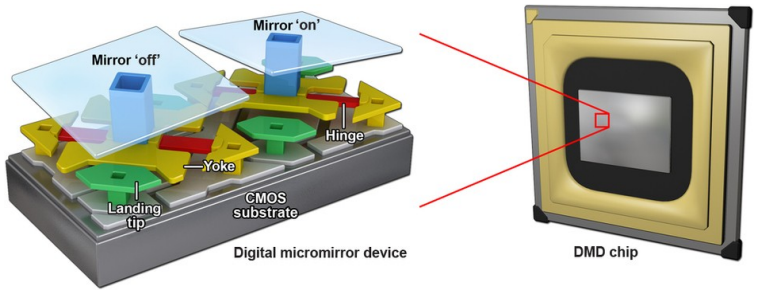

Figure 3.7. Left: An illustration of a pair of micromirrors, with one deflected in the 'off' direction and the other in the 'on' direction. Micro-mirror size $\approx 10\ \mu m \times 10\ \mu m$. Right: A 'zoomed-out' illustration of an entire DMD. Reprinted by permission from [170]. Copyright 2021 Springer Nature.

3.4 Optical lattices

In addition to the vertical lattices for two-dimensional box trap described in Section 3.2, we have also implemented horizontal optical lattices with both blue- and red-detuned lasers (Fig. 3.6). The blue-detuned 767 nm lattice beams are derived from a tapered amplified (Moglabs MSA003) seeded by a cateye laser (Moglabs CEL), followed by 80 MHz AOM (IntraAction ATM-801A2) for intensity control then coupled into optical fibers, where lattice beams have different (up and down) frequency shifts from the AOMs. Each lattice beam has $\approx$ 400 mW output after the cleanup PBS, corresponding to $\approx 30E_R$ with Gaussian beam diameter $\approx 500\ \mu$m at the center of the main chamber, where $E_R = \frac{\hbar^2 k^2}{2m}$ is the recoil energy, $\hbar$ is the reduced Planck constant, k is the wavenumber, and m is the mass of cesium atom. The horizontal 767 nm laser beams are combined with and separated from 1064 nm dipole beams via long-pass dichroic mirrors (Thorlabs DMLP900), where respective PBSs are installed before the combination and after the separation to clean the polarization. After separating the dichroic mirror, each 767 nm lattice beam is focused by a $f = 50$ mm convex lens to a back-side polished mirror (Thorlabs BB1-E03P) mounted on a kinematic mirror mounts with piezoelectric adjusters (Thorlabs POLARIS-K1S3P). These piezo actulators allows us to modulate the optical lattices in three dimensions. The retro-reflected beam from the mirror is again collimated by the same lens and cleaned by the PBS, then combined with 1064 nm beam and sent to the chamber. On the other hand, a weak transmission of 767 nm from the

back side of the polished mirror is collected by a $f = 30$ mm convex lens and projected onto a amplified photodector (Thorlabs PDA36A2) for intensity feedback. A 767 nm laser-line interference filter (Edmund Optics #65-116) is placed in front of each photodetector to block unwanted signals.

The red-detuned 1064 nm optical lattices are implemented by retro-reflecting the optical dipole trap beams. Each dipole beam is combined with and separated from the 767 nm blue-detuned lattice beam as described previously, and focused by a $f = 200$ mm convex lens to a Nd:YAG laser line mirror (Thorlabs NB1-K14) then retro-reflected. Between the lens and the retro-reflection mirror, there is a back-side polished mirror (Thorlabs BB1-E03P) on a precision kinematic mirror mount (Thorlabs POLARIS-K1) for the flexibility of adjustment. The weak transmission of the second pass from the polished mirror is collected by a $f = 50$ mm convex lens and projected onto a biased photodetector (Thorlabs DET36A2) for intensity feedback. Similarly, there is a 1064 nm laser-line interference filter (Newport 10LF04-1064) placed in front of each photodetector. To prevent the evaporative cooling from being altered by the optical lattices, we use optical beam shutters (Thorlabs SH05)[2] to block the retro-reflection of 1064 nm beams until the need of red-detuned optical lattices. The optical shutters are attached to heat sinks to dissipate the heat from dipole trap beams. The typical shutter open/close mechanical time is $3 - 4$ ms, which is sufficiently short so that we are able to ramp off the dipole trap laser power during the box trap loading, followed by opening the shutter and ramping the 1064 nm power back on for optical lattices.

Both blue- and red-detuned optical lattice beams are aligned to the *in situ* position of BEC in the optical dipole trap. The first pass of the 767 nm blue-detuned beam is optimized by pushing atoms in the 2D trap via repulsive force at both horizontal and vertical directions. That way we can clearly determine the intensity maximum of the repulsive beam from the minimum of the atomic density. The first pass of the 1064 nm re-detuned beam is naturally at the *in situ* position of BEC. Both second paths of blue- and red-detuned beams are optimized by reverse coupling to the optical fibers. We monitor the optical power of retro-reflection of each lattice beam at the fiber input side, and optimize the retro-reflection mirror so that the retro beam reversely propagates through the same optical path as the first pass. These

[2]↑At the time of writing this dissertation, the 1064 nm retro-reflection is completed but not enabled.

optimizations have been done with the operating optical power of optical lattices, to make sure the spatial mode-matching conditions are consistent with our experimental procedures.

The signals from photodetectors are sent to home-built high-speed PI (proportional-integral) servos for intensity feedback. The servo output controls the RF power to the AOM by a voltage variable attenuator (Mini-Circuits ZX73-2500-S+), followed by a RF digital switch (Mini-Circuits ZYSWA-2-50DR+) which provides fast RF switching and additional high RF isolation. Therefore, ramping the optical power of the lattice beams becomes straightforward. After ultracold atoms are compressed and loaded into a two-dimensional confinement, we slowly ramp up blue- and/or red-detuned optical lattice beams. At the time of writing this section, we don't have optical beam shutters for blue-detuned 767 nm optical lattice beams, so we usually shift the RF away from the operating frequency 80 MHz to $\approx$ 100 MHz, and essentially change the beam pointing after AOMs so that the laser beams are block by irises while they are not being used. The offset frequency is within the range of AOM response frequency, thus the AOMs keep warmed by the resonant RF oscillation and maintain thermal equilibrium. The optical lattice depth is calibrated by modulating the optical intensity via sinusoidally modulating the output voltage of the intensity servo, followed by monitoring the atom loss in the optical lattices. The spectrum of the parametric heating shows the ground state atoms are excited to the second excited band in the optical lattices and leave the trap when the modulating frequency is resonant. We also observe the suppression of atom loss when the modulating frequency is near the band gap of the optical lattices.

4. UNIVERSAL QUENCH DYNAMICS AND TOWNES SOLITON FORMATION

This chapter is adapted from *Physical Review Letters* Volume **125**, Issue 25, Page 250401, published on 15 December 2020. In this chapter, we experimentally study universal nonequilibrium dynamics of two-dimensional atomic Bose gases quenched from repulsive to attractive interactions. We observe the manifestation of modulational instability that, instead of causing collapse, fragments a large two-dimensional superfluid into multiple wave packets universally around a threshold atom number necessary for the formation of Townes solitons. We confirm that the density distributions of quench-induced solitary waves are in excellent agreement with the stationary Townes profiles. Furthermore, our density measurements in space and time domain reveal detailed information about this dynamical process, from the hyperbolic growth of density waves, the formation of solitons, to the subsequent collision and collapse dynamics, demonstrating multiple universal behaviors in an attractive many-body system in association with the formation of a quasi-stationary state.

4.1 Introduction

Predicting the evolution of multidimensional nonlinear systems under attractive interactions is a challenging task, owing to the instability to collapse [171]–[173]. Bright solitons are remarkable stationary states, established when the self-focusing effect responsible for collapse is exactly compensated by wave dispersion [174], [175]. In uniform two-dimensional (2D) systems with standard cubic interactions, such as Kerr medium [173], [176] or matter-waves formed by weakly interacting 2D Bose gases [84], [177], however, such intricate balance cannot be fulfilled except when a wave packet possesses a critical norm (or total atom number) known as the Townes threshold and a specific waveform known as the Townes profile [176], [178], [179] – only at which bright solitons can form. A Townes soliton is predicted to be unstable as long as the norm deviates from the Townes threshold [173], [178]. Despite extensive interests in multidimensional bright solitons [178]–[182], including recent advancements

on 2D spatial solitons in various nonlinear optics settings [173], [180], [183], an experimental realization and characterization of Townes solitons has remained elusive.

In soliton formation dynamics, modulational instability (MI) is a ubiquitous mechanism that causes the amplification of initial wave disturbances and fragmentation into solitary waves [171], [184]–[186]. In one-dimensional (1D) systems, MI is responsible for the formation of stable soliton trains, for example, in nonlinear fiber optics [187]–[189], in 1D Bose gases [185], [186], [190], [191], or in Bose-Einstein condensates in optical lattices [192]–[194]. In higher spatial-dimensions, transverse MI and wave fragmentation were studied in various types of bulk nonlinear optical media [183], [195], [196]. However, detailed dynamics of multidimensional MI and its possible connection to the universal formation of a quasi-stationary state, the unstable Townes solitons, have not been clearly demonstrated.

Using ultracold 2D Bose gases, we show that universal MI dynamics supports the critical formation of Townes solitons. Starting with a 2D superfluid of an initial density n_i and quenched to an attractive interaction $g_f < 0$, we show that MI causes collective modes with wavenumber around $k_\mathrm{MI} = \pi/\xi$ associated with the interaction length $\xi = \pi/\sqrt{2n_\mathrm{i}|g_f|}$ to grow predominantly [197]–[199], fragmenting the superfluid as illustrated in Fig. 4.1(a). Intriguingly, the characteristic atom number in each wave packet $\sim n_\mathrm{i}\xi^2 = \pi^2/2|g_f|$ well approaches the Townes threshold $N_\mathrm{th} = 5.85/|g_f|$ [179], thus opening up a pathway for Townes soliton formation. This relation should apply universally for any n_i and g_f provided no other length scales set in. We note that, due to the scaling symmetry in 2D, a Townes soliton forms under a scale-invariant profile [176] and MI can set the physical length scale ξ that depends only on the product of n_i and $|g_f|$.

We report the observation of universal dynamics and Townes soliton formation in quenched 2D Bose gases. We observe MI that breaks up an otherwise large 2D sample into fragments universally around the Townes threshold. We clearly identify solitary waves whose density distributions agree well with the Townes profiles – the stationary state solution of the 2D nonlinear Schrödinger equation (NLSE) [176], [179]. Our measurement further reveals universal solitary wave dynamics governed by the MI time scale and a universal scaling behavior in the density power spectra, allowing us to clearly identify a distinct time period for unsta-

ble growth of density waves (while conserving total atom number), followed by a short era of wave collapse and soliton formation.

4.2 Methods

We begin the experiment with a uniform 2D Bose gas deeply in the superfluid regime (1.2), which is formed by $N \approx 1.5 \times 10^4$ cesium atoms trapped inside a quasi-2D box potential. The atomic surface density is $n_{\rm i} \approx 5/\mu{\rm m}^2$ and the surface area is controlled by a wall-like potential that is removed following the interaction quench. The tight vertical (z-) confinement of the box freezes all atoms in the harmonic ground state along z-axis. The trap vibrational level spacing ($\omega_z = 2\pi \times 1750$ Hz) is more than two orders of magnitude larger than the attractive interaction energy studied, ensuring that the observed wave dynamics is effectively 2D [201]. The interaction strength $g = \sqrt{8\pi}a/l_z$ is controlled by the tunable s-wave scattering length a via a magnetic Feshbach resonance [59], and $l_z = 208$ nm is the vertical harmonic oscillator length; $g = g_{\rm i} = 0.115$ is the initial interaction strength.

We perform interaction quench (in 1 ms) to various $g = g_f$ in samples with a large surface area $A \approx (60\ \mu{\rm m})^2$. Following a variable hold time τ, we perform single-shot absorption imaging to record the sample density distribution as shown in Fig. 4.1(b). Around 30 samples are imaged for ensemble analyses. In a short hold time, we observe density blobs randomly clumping up throughout a sample. The sizes of the blobs are smaller with larger $|g_f|$. At longer hold time, $\tau \geq 30$ ms, the number of observed blobs reduces, becoming more isolated, although the mean size and atom number of surviving blobs remain nearly unchanged for $\tau \leq 200$ ms. The same quench protocol applied to samples in a three-dimensional trap ($\omega_z \approx 2\pi \times 100$ Hz with a weak radial trap frequency $\omega_r \approx 2\pi \times 13$ Hz) results in no observed density blobs.

4.3 Results

We characterize these isolated blobs (solitary waves) and compare their atom number with the Townes threshold. We approximate their density profiles by 2D Gaussians [179] and fit the mean size σ and atom number $\bar{N}_a$. Within the interaction range studied, $-0.004 \geq$

$g_f \geq -0.034$, in Fig. 4.1(c) we find that all rescaled atom numbers $\bar{N}_a|g_f|$ fall around $N_{\rm th}|g_f| = 5.85$, giving a mean $\overline{\bar{N}_a|g_f|} = 6(1)$. Interestingly, the standard deviation of the atom number δN_a scales with g_f accordingly, giving a mean fluctuation $\overline{\delta N_a|g_f|}$ =3.2(5)$\sim$ $0.5\overline{\bar{N}_a|g_f|}$. We believe that the number variation around the threshold results from the energy-time uncertainty relation, as we later show that these blobs form in a time scale $\sim \gamma^{-1}$, where $\hbar\gamma = \hbar^2 n_{\rm i}|g_f|/m$ is the interaction energy, m is the atomic mass, and $\hbar$ is the reduced Planck constant. Moreover, the size of these solitary waves also agrees with the prediction $\sigma \approx \xi$ in Fig. 4.1(d), indicating that MI provides the length scale for the formation of blobs. A size discrepancy at $\gamma \approx 2\pi \times 1.2$ Hz ($g_f = -0.004$) could likely be attributed to the influence of a very weak horizontal corrugation in the vertical confining potential.

To confirm that the quench-induced solitary waves indeed form Townes solitons, we compare their density distributions with the scale-invariant, isotropic Townes profile $n(r) = \alpha^2|\phi(\alpha r)|^2/(2|g_f|)$, where $\alpha = \sqrt{2n_0|g_f|/|\phi(0)|^2}$ is a scale factor. Given the peak density n_0, the characteristic size and density profile of a Townes soliton are uniquely determined. Here, the radial function $\phi(\tilde{r})$ is the stationary solution of the scale-invariant 2D NLSE [176], [179]. The stationary profile $\phi(\tilde{r})$ has been evaluated numerically [176], giving $|\phi(0)| \approx 2.207$, and the norm $\int |\phi(\tilde{r})|^2 d\tilde{\mathbf{r}} \approx 11.7$ sets the Townes threshold.

Since MI sets the length scale during the soliton formation process, $\alpha \sim \xi^{-1}$, the peak density of most solitons should be comparable to the initial sample density $n_0 \approx n_{\rm i}$. Figure 4.2 plots three isolated solitary waves of similar peak density that are randomly chosen from quenched samples ($g_f = -0.034$) at a long hold time $\tau = 100$ ms. Their individual density distributions, as well as the averaged radial density profile, indeed agree fairly well with the expected Townes profiles with no fitting parameters. More agreement with the Townes profiles is discussed in Chapter 5, where a single array of well-isolated solitons can form in an elongated sample following an interaction quench. Our observation confirms that Townes solitons can prevail from MI and explains why many randomly formed solitary waves, as observed in Fig. 4.1, are long-lived. We note that, in the absence of MI and fragmentation, a wave was observed to collapse only partially to a Townes profile [173].

We now turn to study the universal dynamics during the soliton formation process. We focus on the time evolution of density power spectrum [202] $S(k,\tau) = \langle|n(k,\tau)|^2\rangle/N$ in the

spatial frequency domain (momentum space), using Fourier transform of the sample density distribution. Here $k = |\mathbf{k}|$ is the momentum wavenumber of the azimuthally averaged spectrum, N is the total atom number, and $\langle . \rangle$ denotes ensemble averaging. In the power spectra (Fig. 4.3(a)), we clearly observe rapid growth of a nonzero momentum peak at short hold time (marked by an arrow), indicating the development of density waves at a dominant length scale throughout the sample. The nonzero momentum peak then dissipates at longer hold time until the power spectrum finally becomes monotonic and stationary, which signifies the collapse of density waves and fragmentation of the sample into solitons that later becomes uncorrelated in coordinate space.

The evidence of MI-induced wave amplification at different interaction strengths is best illustrated when we plot the relative growth spectra $\tilde{S}(k,\tau) = S(k,\tau)/S(k,\tau_0)$, normalized by the initial power spectrum at $\tau_0 = 2$ ms. This allows us to determine which mode has the largest growth rate. For different samples in Figs. 4.3(b) and (c), the momentum peak is clearly visible within $0.2/\mu\text{m} < k < 1/\mu\text{m}$ at short hold time. The growth patterns look similar for samples with different g_f, although the peak location, height, and the evolution time scale vary. We identify the peak wavenumber k_p and find consistency with the prediction from MI in Fig. 4.3(d).

Another remarkable prediction from MI is that, regardless of the dimensionality of the system, the power spectrum at k_p exhibits a universal time and amplitude scaling behavior with respect to the interaction time scale γ^{-1}. This is based on extending the Bogoliubov phonon picture to the regime under attractive interactions, which predicts that collective modes of opposite momenta are generated in pairs, as seeded from initial density perturbations, and subsequently form density waves along the associative directions while being amplified at a rate γ until significant depletion of the ground state atoms occurs (Appendix E).

In Fig. 4.3(e), we experimentally test the scaling relation in the peak growth spectra $\tilde{S}(k_p,\tau)$, covering the entire time period. We summarize the scaling relation as follows

$$\mathcal{S}(\tilde{\tau}) \approx \frac{\gamma}{\bar{\gamma}_\text{i}}[\tilde{S}(k_p,\tilde{\tau}) - 1], \tag{4.1}$$

where $\tilde{\tau} = \gamma\tau$ is the scaled time and $\mathcal{S}(\tilde{\tau})$ is the scaled spectrum. In the amplitude scaling, we normalize γ with the mean initial interaction energy unit $\bar{\gamma}_\mathrm{i} = 306\ \mathrm{s}^{-1}$ before the quench. We show that six power spectra, each with different γ, can collapse onto a single curve over a surprisingly long scaled time $\tilde{\tau} < 10$. The only exception is the spectrum at $g_f = -0.004$, where we have used $\gamma^* = 3.2\gamma$ to force its collapse within $\tilde{\tau} \leq 0.8$. This different behavior is likely due to a weak horizontal trap corrugation influencing the dynamics, as noted in Fig. 4.1(d).

From this universal spectrum, we identify two distinct regimes of dynamics, divided by a critical time $\tilde{\tau}_c \approx 0.8$ as shown in Fig. 4.3(e). We label the time period $\tilde{\tau} \leq \tilde{\tau}_c$ for MI with an amplified (hyperbolic) growth of density waves (Appendix E),

$$\tilde{S}(k_p, \tau) \approx 1 + \alpha \frac{\bar{\gamma}_\mathrm{i}}{\gamma} \sinh^2(\gamma\tau), \tag{4.2}$$

where $\alpha = 1.5(1)$ is determined from a fit to $\mathcal{S}(\tilde{\tau})$ for $\tilde{\tau} \leq 0.5$; $\alpha = 2$ is obtained from the theory calculation for $\tilde{\tau} \ll 1$, neglecting the depletion of ground state atoms, dissipation, or interaction between the collective modes. Beyond $\tilde{\tau} \geq \tilde{\tau}_c$ after $\mathcal{S}(\tilde{\tau})$ reaches order of unity, dynamics enters the second phase, decaying with a time constant $\Delta\tilde{\tau} \sim 0.8$ and transitioning to a slowly-evolving, quasi-stationary behavior.

Our data suggest the existence of a universal time and amplitude scaling behavior and a limit for the amplified density wave, followed by a universal dynamics for the wave collapse and soliton formation. For $g_f = -0.004$, however, $\tilde{S}(k_p, \tau)$ remains slowly-growing within $1 \leq \gamma^*\tau \leq 10$, suggesting less severe wave collapse.

Following the observed density wave collapse dynamics, a 2D sample fragments into many solitary wave packets of characteristic size $\sigma \sim \xi$. As seen in Fig. 4.1, due to close proximity of many wave packets (also with characteristic distances $\sim \xi$), collisions between them may induce collapses that lead to rapid atom number loss. Here, we show that MI time scale continues to dominate the collision dynamics and the total atom number loss in a quenched 2D Bose gas.

In a recent study of 1D soliton collisions [203], it is shown that merger occurs when solitons of similar phases collide, and two solitons of opposite phases appear to repel each

other. In 2D, the merger of two soliton-like wave packets should lead to a new atom number $N_a > N_{\rm th}$. This can induce collapse that quickly removes the merged soliton. For solitons or density blobs formed by MI with randomly seeded density waves in a large 2D sample, one expects no fixed phase relationship between neighbors. Merger can thus occur randomly throughout the sample and the total atom number loss may reveal the scaling of soliton binary collision losses.

In Fig. 4.4, we examine the total atom number loss for large samples quenched to different g_f (Fig. 4.1). We observe onset of loss in each sample at a time τ corresponding roughly to the critical time $\tilde{\tau}_c$, a behavior similarly observed for MI in 1D [185]. Beyond the critical time, we confirm that the loss curves can be well-captured by a simple two-body loss model, $\dot{N}/N = -\Gamma_{\rm 2body} N/A$. We attribute this behavior to the dominance of binary collisions between solitons or density blobs that trigger collapse and atom number loss; without triggered collapse, the usual three-body recombination loss should be negligible [169]. In Fig. 4.4(b), we find a linear dependence on $|g_f|$ in the measured loss coefficients $\Gamma_{\rm 2body}$. This in fact suggests a constant binary loss coefficient Γ_s for colliding wave packets, where $\Gamma_s = \Gamma_{\rm 2body} \bar{N}_a$ (Appendix E) and $\bar{N}_a |g_f| \approx 6$ is the measured universal number for solitary waves formed by MI.

We suspect this universal loss behavior results from MI scaling and 2D scale invariance, which suggests a constant binary loss coefficient,

$$\Gamma_s = \eta \frac{\hbar \pi}{m}, \tag{4.3}$$

independent of the interaction parameters $(n_{\rm i}, g_f)$. This is because the collision rate $\Gamma_s \sim \sigma \bar{v}$ and the dependences on length scales in the linear cross-section $\sigma \approx \xi$ and relative velocity $\bar{v} \approx \sqrt{2}\hbar\pi/m\xi$ cancel each other; the constant $\eta \approx \sqrt{2}$ is estimated for $\sim$50% probability of merger per collision or, equivalently, on average one soliton or density-blob loss per collision event. If Eq. (4.3) holds, we expect a collision lifetime $1/n_s\Gamma_s \sim \gamma^{-1}$, where $n_s = n_{\rm i}/\bar{N}_a$ is the initial soliton/blob density (Appendix E). This suggests that wave collapse and binary collision likely take place at the same rate during the second phase of the density evolution.

To unambiguously confirm the universality of collision dynamics, in Fig. 4.4(c) we deduce Γ_s independently using experimentally determined values ($\Gamma_{2\text{body}}$, $\bar{N}_a$) at each g_f. Our results conform very well with the prediction by Eq. (4.3), giving a mean $\eta \approx 1.5$. We emphasize here that the loss coefficients universally depend only on the physical constants $\hbar/m$ is a remarkable manifestation of MI and scale-invariant symmetry in 2D. The observations in Figs. 4.3 and 4.4 together confirm that interaction quench dynamics leads to Townes soliton formation at $\tau \gtrsim \gamma^{-1}$, followed by collision (that induces collapse) also at the same time scale γ^{-1} universally governed by MI.

4.4 Conclusion

In summary, we study the universal nonequilibrium dynamics in degenerate 2D Bose gases quenched from repulsive to attractive interactions, and observe the dynamical formation of Townes solitons from MI. Townes solitons are observed to be collisionally unstable. However, further stabilization and manipulation may be possible [180], [204]–[206]. We note that the initial shape and finite sample size can be further manipulated to invoke strong boundary effects in quench-induced MI (Chapter 5). Using slow interaction ramps may also induce MI dynamics deviating from the reported universal behavior. Soliton formation may be disrupted, leading to, for example, only partial collapse to the Townes profiles [173]. Lastly, we comment that controlled formation of 2D solitons via pair-production processes in MI may find future applications in matter-wave interferometry [207], [208], or even in the generation and distribution of many-body entanglement [209]–[212].

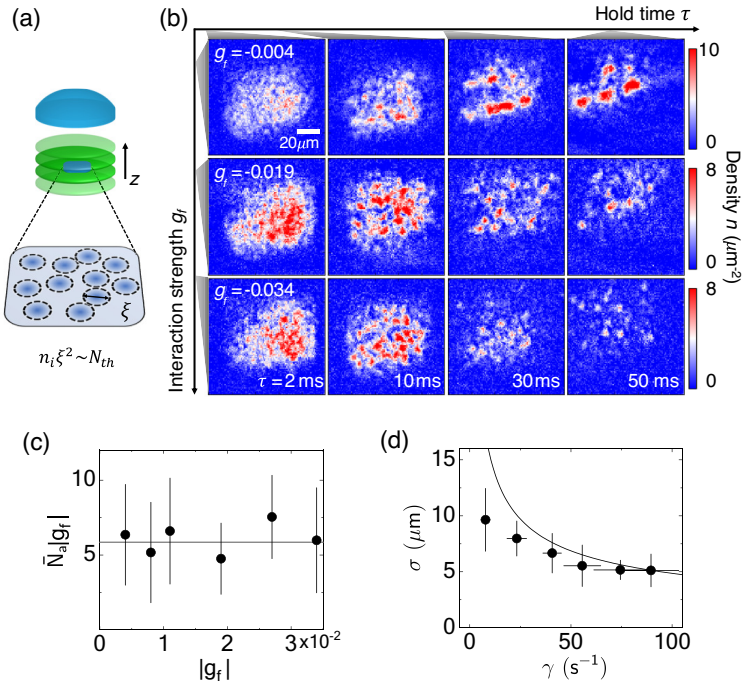

Figure 4.1. Universal solitary wave formation in quenched 2D Bose gases. (a) Interaction quench-induced MI fragments a 2D gas (blue shaded square) into wave packets of a characteristic size ξ (dashed circles) that contains atom number $\sim n_{\rm i}\xi^2$ approaching the Townes threshold $N_{\rm th}$. The 2D gas is confined in a single node of a repulsive standing-wave potential (green shaded ovals), evolves for a hold time τ, and is imaged via a microscope objective (blue hemisphere) (Chapter 3). (b) Single-shot images of samples quenched to the indicated interaction g_f (in each row) and held for the labeled time τ (in each column). Solitary waves (isolated density blobs) become visible at $\tau \geq 30$ ms. (c) Scaled mean atom number in a solitary wave $\bar{N}_a|g_f|$. Solid line marks the universal threshold $N_{\rm th}|g_f| = 5.85$. (d) Mean size σ versus interaction frequency γ. Solid line is the interaction length ξ. All data points in (c-d) are evaluated at $\tau = 42 \sim 50$ ms except for those of $g_f = -0.004$ which are evaluated at $\tau = 150 \sim 200$ ms. Error bars are standard errors. Uncertainties in g_f are smaller than the size of symbols. Reprinted figure with permission from [200], Copyright 2021 by APS.

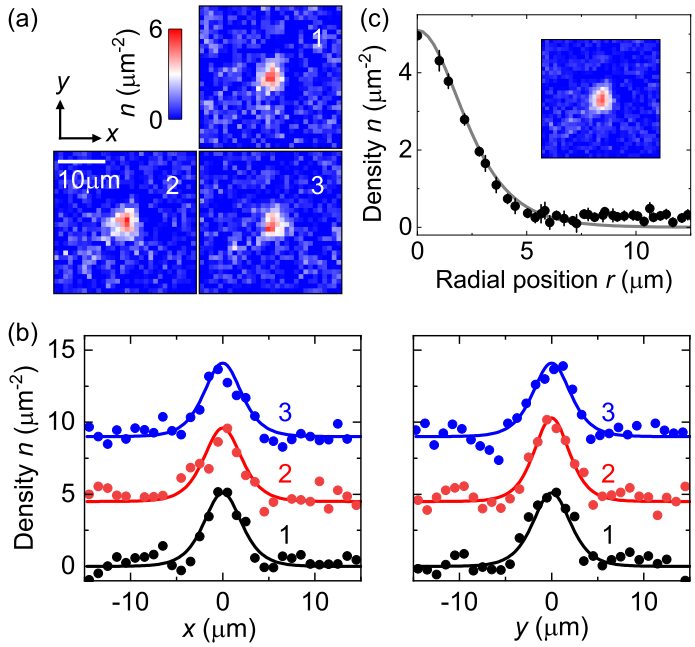

Figure 4.2. Townes solitons and the Townes profiles. (a) Sample images of single solitary waves ($g_f = -0.034$) recorded at $\tau = 100$ ms. (b) Density line cuts (solid circles) through the center of images as numerically labeled in (a). Each data is offset by $4.5/\mu\text{m}^2$ for viewing. Solid lines are the Townes profiles of peak densities $n_0 = 5.1/\mu\text{m}^2$ (for #1,#3) and $5.8/\mu\text{m}^2$ (for #2), respectively. (c) Azimuthally-averaged radial profile (solid circles) from the mean density image of (a) (inset: 30×30 μm^2), in close comparison with theory (solid curve) calculated using $n_0 = 5.1/\mu\text{m}^2$. Nearby dispersed blobs contribute to a small background at $r \gtrsim 7\mu$m. Reprinted figure with permission from [200], Copyright 2021 by APS.

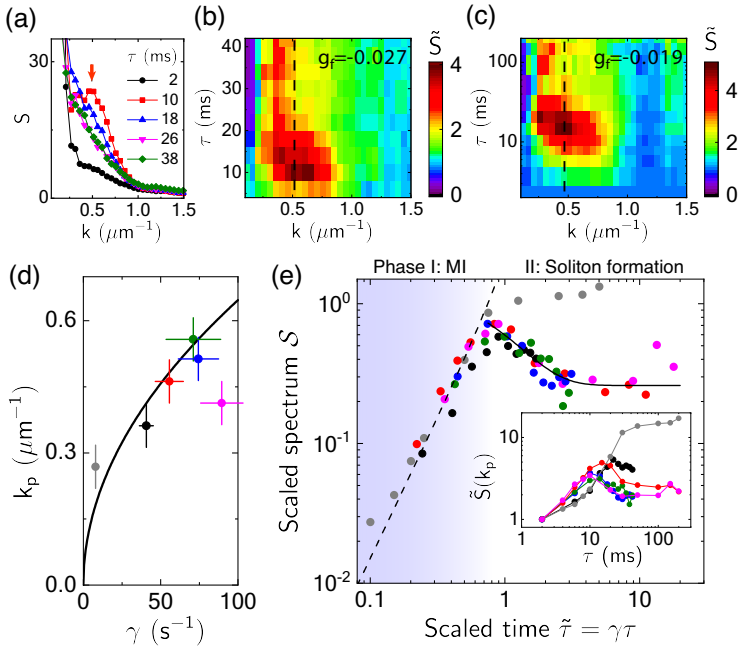

Figure 4.3. Dynamics and universal scaling in the density power spectra. (a) Sample spectra $S(k,\tau)$ at $g_f = -0.027$ and the indicated hold time τ. (b) Corresponding growth spectra $\tilde{S}(k,\tau) = S(k,\tau)/S(k,\tau_0)$ with $\tau_0 = 2$ ms. (c) Sample growth spectra $\tilde{S}$ at $g_f = -0.019$ and hold time up to 200 ms. Vertical dashed lines in (b-c) mark the peak wavenumber k_p. (d) k_p versus interaction energy $\hbar\gamma$ (filled circles) measured at $g_f = -0.004$ (gray), -0.011 (black), -0.019 (red), -0.027 (blue), and -0.034 (magenta and olive), respectively. Corresponding $\tilde{S}(k_p,\tau)$ are shown in the inset of (e). Solid line is the prediction $k_{\rm MI} = \sqrt{2\gamma m/\hbar}$. Error bars include systematic and statistical errors. (e) Scaled spectra $\mathcal{S}$ plotted using Eq. (4.1), which collapse approximately onto a single curve except for the one at $g_f = -0.004$. Dashed line (Solid line) is a hyperbolic (exponential) fit to Phase I, $\tilde{\tau} < 0.8$ (II, $\tilde{\tau} > 0.8$), of the collapsed spectra; see text. Reprinted figure with permission from [200], Copyright 2021 by APS.

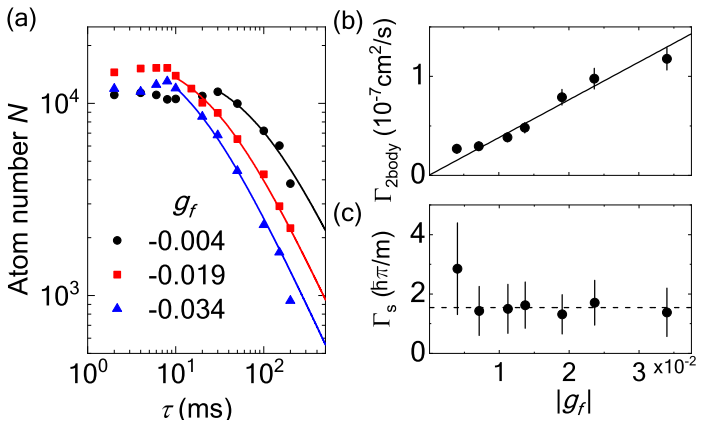

Figure 4.4. Universal soliton collision dynamics in 2D. (a) Sample loss curves in total atom number N measured at the indicated interaction g_f. Solid lines are two-body loss fits after atom loss initiates. (b) Fitted rate coefficients. Solid line is a linear fit, giving a slope $\Gamma_{2\text{body}}/|g_f| = 3.8(2) \times 10^{-6}\text{cm}^2/\text{s}$. (c) 2D soliton binary loss coefficients Γ_s determined from the rate coefficients in (b) and $\bar{N}_a$ as in Fig. 4.1(c), and compared with the universal prediction Eq. (4.3), giving a mean $\eta = 1.5(1)$ (dashed line) and agreeing with $\eta = 1.5(3)$ alternatively determined from the fitted slope in (b) and mean $\overline{\bar{N}_a|g_f|} = 6(1)$. Error bars are standard errors. Uncertainties in g_f are smaller than the size of symbols. Reprinted figure with permission from [200], Copyright 2021 by APS.

5. SCALE INVARIANT TOWNES SOLITONS

This chapter is adapted from *Physical Review Letters* Volume **127**, Issue 2, Page 023604, published on 9 July 2021. In this chapter, we report near-deterministic generation of two-dimensional (2D) matter-wave Townes solitons, and a precision test on scale invariance in attractive 2D Bose gases. We induce a shape-controlled modulational instability in an elongated 2D matter-wave to create an array of isolated solitary waves of various sizes and peak densities. We confirm scale invariance by observing the collapse of solitary-wave density profiles onto a single curve in a dimensionless coordinate rescaled according to their peak densities, and observe that the scale-invariant profiles measured at different coupling constants g can further collapse onto the universal profile of Townes solitons. The reported scaling behavior is tested with a nearly 60-fold difference in soliton interaction energies, and allows us to discuss the impact of a non-negligible magnetic dipole-dipole interaction (MDDI) on 2D scale invariance. We confirm that the effect of MDDI in our alkali cesium quasi-2D samples effectively conforms to the same scaling law governed by a contact interaction well within our experiment uncertainty.

5.1 Introduction

A scale-invariant system possesses self-similar features that can occur at all scales, where system observables exhibit general scaling behaviors. Weakly interacting two-dimensional (2D) Bose gases offer unique opportunities to explore scale invariance (SI) in a many-body system, because the effective contact interaction potential and single-particle dispersion both have the same scale dependence [75], [213]. The ability to tune the contact interaction strength g via a magnetic Feshbach resonance [59] further allows for explorations of SI over a wide parameter range, both in equilibrium and from out-of-equilibrium dynamics. At repulsive interactions ($g > 0$), SI has been observed in density observables associated with the equations of states, in normal and superfluid phases, and across the Berezinskii-Kosterlitz-Thouless superfluid phase transition, offering a rich understanding of scale-invariant 2D many-body phases [81], [82], [101], [214]–[216]. However, 2D Bose gases with attractive interactions ($g < 0$) have rarely been studied primarily due to an instability to collapse

under typical experiment trap conditions [172], [217]. When and how SI manifests in the unstable attractive regime has remained relatively unexplored.

One intriguing example occurs deep in quantum degeneracy, when attractive 2D Bose gases form matter-waves that may sustain a scale-invariant, quasi-stationary state – a prediction originally made for self-focusing optical beams called the Townes soliton [176]. Under SI, a Townes soliton may form at any length scale λ, but only under an isotropic wave function $\psi(\mathbf{r}) = \phi(r/\lambda)/\lambda$, where $\phi(\tilde{r})$ is a dimensionless Townes profile (Appendix F). The atom number in a Townes soliton is necessarily fixed at $N_{\rm ts} = \int |\phi(\tilde{r})|^2 d\tilde{\mathbf{r}} \approx 5.85/|g|$. At this atom number the matter-wave dispersion intricately balances against the mean field attraction. The main challenge for realizing scale-invariant 2D solitons is that they are unstable [178], [201], and have not been realized in equilibrium. In nonlinear optics, a Townes profile has been partially observed in a collapsed optical wave [173].

To date, an experimental demonstration of SI in 2D matter-wave solitons has remained elusive. Recently in Ref. [200], it is observed that an interaction quench in a homogeneous 2D superfluid to $g < 0$ can induce a modulational instability (MI) [185], which fragments a large sample into many density blobs with atom numbers universally around $N_{\rm ts}$. Townes solitons of similar peak densities (and sizes) are observed to form randomly from the blobs. However, dispersion, collisions and collapse of many blobs generate remnants throughout a large sample, making confirmation of SI in solitons a nontrivial task. Besides soliton formation in quench dynamics, an optical technique [219] has been developed very recently to deterministically imprint a Townes soliton in a two-component planar Bose gas [220].

We report a simple recipe to create isolated 2D solitons with peak densities differing by 20-fold, thus enabling unambiguous experimental tests on SI. Our method induces controlled MI in an elongated 2D superfluid that fragments into an array of solitary waves nearly free from background remnants. Using these samples, we confirm SI by observing their density profiles collapse onto a single curve in a dimensionless coordinate $\tilde{r} = \sqrt{n_p} r$, where n_p is the peak density that sets the length scale $\lambda = 1/\sqrt{n_p}$. We further confirm that the scale-invariant density profiles measured at different coupling constants g can collapse onto a universal curve, which agrees remarkably well with the Townes profile. Furthermore, we

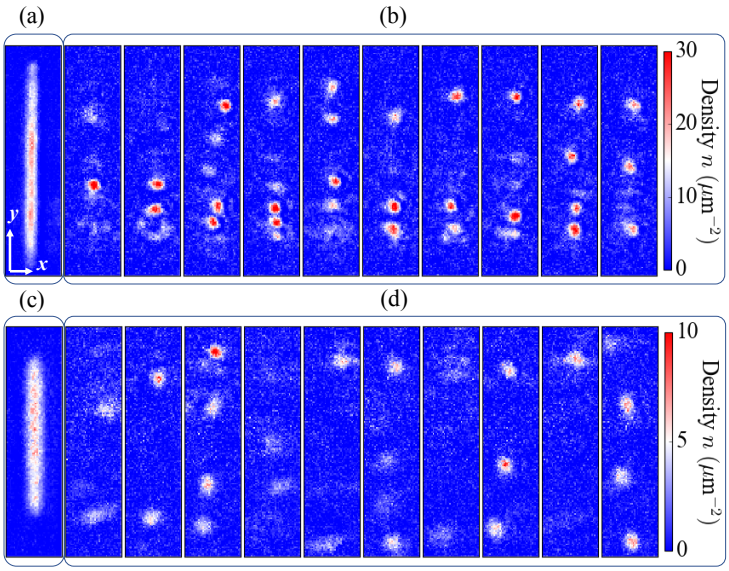

Figure 5.1. Formation of 2D matter-wave soliton trains. (a) An elongated 2D Bose gas of peak density $n_{\rm i} \approx 20/\mu{\rm m}^2$ is held at an initial coupling constant $g_{\rm i} \approx 0.129$ and quenched to a new coupling constant $g \approx -0.0215$, with simultaneous removal of the horizontal confinement in the x-y plane. Arrays of solitary waves are observed in shot-to-shot images in (b), taken after a 50 ms wait time. A different sample in (c) is prepared at a much lower initial peak density $n_{\rm i} \approx 6/\mu{\rm m}^2$ and quenched to $g \approx -0.0075$, similarly generating solitary waves as observed in (d). Image size in (a,b): $19{\times}77$ $\mu{\rm m}^2$. Image size in (c,d): $40{\times}160$ $\mu{\rm m}^2$. Reprinted figure with permission from [218], Copyright 2021 by APS.

discuss the effect of a non-local MDDI in our quasi-2D geometry, which conforms to the same scaling law governed by a contact interaction well within our experiment uncertainty.

5.2 Methods

Our experiment begins with a 2D superfluid formed by a variable number of cesium atoms ($N \approx 6 \times 10^3 \sim 1.5 \times 10^4$) polarized in the $|F = 3, m_F = 3\rangle$ hyperfine ground state and with a low temperature $T \lesssim 8$ nK. The superfluid is trapped inside a quasi-2D box potential formed by all repulsive optical dipole beams with an adjustable horizontal box confinement. The tight vertical (z-) confinement freezes all atoms in the harmonic ground state along the imaging axis, giving a trap vibrational frequency $\omega_z = 2\pi \times 2.25(1)$ kHz and a harmonic

oscillator length $l_z \approx 184$ nm. The 2D coupling constant $g = \sqrt{8\pi}a/l_z$ is controlled by a tunable s-wave scattering length a, initially prepared at $g = g_\mathrm{i} \approx 0.129$ and later quenched to a negative value $g < 0$ via a magnetic Feshbach resonance [59]. The coupling constant is calibrated with an uncertainty $\delta g \approx \pm 0.0005$ (Appendix F). Following the interaction quench and simultaneous removal of the horizontal box confinement, the 2D gas is allowed to evolve freely in the horizontal plane for a hold time of ~ 50 ms, which is sufficiently long to allow samples to fully fragment but short enough so that there is not a significant atom loss that could make a soliton unstable. Absorption imaging is then performed to record the density distribution; see Fig. 5.1 for sample images. The image resolution is experimentally determined to be ~ 1.5 μm ($1/\mathrm{e}^2$ Gaussian width) [200], [221].

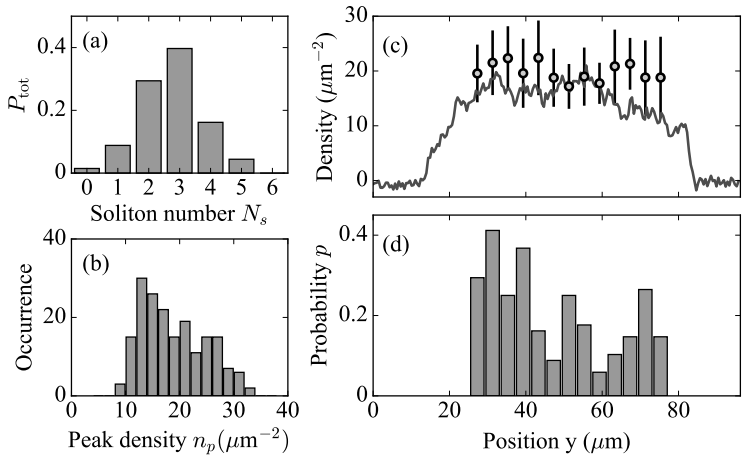

Figure 5.2. Soliton formation statistics. (a) Probability P_{tot} of finding N_s solitons after the quench, evaluated using 68 samples as shown in Fig. 5.1(b). (b) Occurrence of solitons with peak density n_p (Bin size: $2/\mu\mathrm{m}^2$). (c) Average peak density $\bar{n}_p$ versus position along the long (y-)axis (filled circles). Error bars represent standard deviation. Solid curve shows the density n_i of the initial sample through the long axis. (d) Probability for observing a soliton at position y in a quenched sample (Bin size: 4 μm). Reprinted figure with permission from [218], Copyright 2021 by APS.

To form a single array of isolated 2D solitons, we reduce the initial width of a superfluid so that MI can only manifest along its long axis (y-axis). As shown in Fig. 5.1(a), the sample has an initial peak density $n_\mathrm{i} \approx 18/\mu\mathrm{m}^2$, with a length $L \approx 65$ μm and a root-mean-square width $w \approx 3$ μm $\lesssim \xi$, where $\xi = \pi/\sqrt{2n_\mathrm{i}|g|} \approx 3.6$ μm is the half-wavelength of the most

unstable mode in MI [200] when we quench to $g \approx -0.0215$. Following the interaction quench, arrays of isotropic solitary waves are observed to form near-deterministically in every sample [Fig. 5.1(b)]. These well-separated solitary waves allow us to perform counting statistics (Fig. 5.2) and measure their density profiles. We confirm these solitary waves are Townes solitons by performing associated scaling tests (Figs. 5.3 and 5.4). In another set of examples as shown in Fig. 5.1(c-d), we prepare superfluids with much lower initial peak densities $n_{\mathrm{i}} \approx 5/\mu\mathrm{m}^2$, and quench the coupling constant to a less attractive value $g \approx -0.0075$. Arrays of solitons more than twice the size of those found in Fig. 5.1(b) can be identified in (d).

In all examples shown in Fig. 5.1, many solitons appear to be missing randomly from the observed arrays. This may be caused by imperfect soliton formation from MI, and the missing ones may have either dispersed or collapsed. In addition, collisions between neighboring solitons can trigger collapse and induce rapid loss [200], [203]. In Fig. 5.2, we analyze soliton formation statistics from our quench recipe, using images as shown in Fig. 5.1(b). In more than 98 % of the samples analyzed, we find $N_s \geq 1$ total number of solitons [Fig. 5.2(a)]. Thanks to a nearly remnant-free background, we collect solitons of peak densities over a finite range from $n_p \sim 8/\mu\mathrm{m}^2$ to $\sim 30/\mu\mathrm{m}^2$ [Fig. 5.2(b)]. This allows us to study their density scaling behavior. On the other hand, the average peak density $\bar{n}_p \approx 20/\mu\mathrm{m}^2$ [Fig. 5.2(c)] is comparable to the initial density $n_{\mathrm{i}} \approx 18/\mu\mathrm{m}^2$, and is approximately uniform along the sample. It is more likely to find solitons near the edge, as shown in the probability distribution $p(y)$ in Fig. 5.2(d), potentially due to a boundary effect that reduces soliton collision loss. We observe that low density samples as shown in Fig. 5.1(d) generate solitons with peak density $2/\mu\mathrm{m}^2 \lesssim n_p \lesssim 13/\mu\mathrm{m}^2$.

We collect solitons of different sizes from our quenched samples to perform the scaling tests. In Fig. 5.3, we show sample soliton images, sorted with n_p monotonically increasing from $7/\mu\mathrm{m}^2$ to $30/\mu\mathrm{m}^2$ for $g \approx -0.0215$ [in (a)] and from $1.5/\mu\mathrm{m}^2$ to $9/\mu\mathrm{m}^2$ for $g \approx -0.0075$ [in (b)]. The soliton size appears to monotonically decrease with respect to the increasing peak density, as shown in the radial density profiles $n(r)$ in Fig. 5.3 insets.

5.3 Results

We test the SI hypothesis by rescaling the density profiles $n(r)$ in a dimensionless form and search for a universal behavior. In Fig. 5.3, we plot the rescaled density $\tilde{n} = n/n_p$ as a function of the dimensionless radial position $\tilde{r} = \sqrt{n_p}r$. Indeed, despite a large variation in soliton size, we observe that all profiles measured at a fixed g collapse onto a single curve. No significant deviation from the collapse behavior is observed at any $\tilde{r}$.

To quantify the goodness of the profile collapse and confirm SI, we evaluate the reduced chi-square $\chi^2_\nu = \sum_{\mathrm{i}} \left[\tilde{n}_{\mathrm{i}} - \langle\tilde{n}\rangle_{\mathrm{i}}\right]^2 / \nu\sigma^2_{\mathrm{i}}$ from ~ 20 rescaled profiles, where $\langle\tilde{n}\rangle$ is the mean profile, σ_{i} is data uncertainty, and the index i labels data points collected within a test radius, giving in total $\nu \approx 190$ degrees of freedom. At $g \approx -0.0215$ as in Fig. 5.3(a), we find $\chi^2_\nu \approx 1.5$ for $\tilde{r} \lesssim 25$; for the profiles at $g \approx -0.0075$ as in Fig. 5.3(b), we obtain $\chi^2_\nu \approx 1.4$ for $\tilde{r} \lesssim 35$. The chi-square test $\chi^2_\nu \sim O(1)$ suggests a universal collapse and supports the SI hypothesis from these randomly collected solitons. Nevertheless, $\chi^2_\nu \gtrsim 1$ indicates that the standard deviation of collapsed profiles slightly exceeds the estimated measurement uncertainty. Since the statistical deviations from the mean profile show no clear dependence on soliton size or peak density [see also Fig. 5.4(b)], the chi-square test suggests not all quench-induced solitary waves possess perfect scale-invariant profiles.

We now show that the scale-invariant density distributions measured at different attractive interactions can be further rescaled to display a universal waveform – the Townes profile. Here, the coupling constant can be absorbed into the length scale factor λ such that, when plotted in the rescaled coordinate $R = \sqrt{|g|}\tilde{r}$, the density displays a universal profile $\tilde{n} = |\phi(R)|^2$. The radial wave function $\phi(R)$ is the stationary solution of a dimensionless 2D Gross-Pitaevskii equation (GPE),

$$\tilde{H}\phi = -\frac{1}{2}\left(\frac{d^2\phi}{dR^2} + \frac{1}{R}\frac{d\phi}{dR}\right) - |\phi|^2\phi = \tilde{\mu}\phi\,, \tag{5.1}$$

where the scaled chemical potential $\tilde{\mu} = -0.205$ is obtained while solving $\phi(R)$ (Appendix F).

In Fig. 5.4, we plot the measured scale-invariant mean density profiles $\langle\tilde{n}\rangle$ as a function of the rescaled radial position $R = \sqrt{|g|}\tilde{r}$. We find that four initially very different mean profiles

(inset) measured at $|g| \approx (0.0075, 0.0170, 0.0215, 0.034)$, respectively, can collapse onto a universal curve in the rescaled coordinate, which agrees very well with the GPE solution $|\phi(R)|^2$; only a small deviation $\Delta\tilde{n} \lesssim 0.015$ becomes visible at $R \gtrsim 3$, where $|\phi(R)|^2 \lesssim 0.02$. This could result from a very low fraction of collision remnants in the horizontal plane or from barely overlapping tails of adjacent solitons, which has little influence on the universal scaling tests near the core region $R \lesssim 3$. Integrating the scaled density to $R = 4$, we have estimated $\int \langle\tilde{n}\rangle d\mathbf{R} \approx 6.0 \pm 0.8 \sim N_{\rm ts}|g|$, agreeing reasonably with theory [Fig. 5.4(b)].

The observed universal scaling behavior is a remarkable manifestation of SI in 2D Bose gases effectively described by a mean field interaction Eq. (5.1). This universal behavior is also evidenced in Fig. 5.4 (b), where we plot the scaled atom number $N|g|$ of individual solitons as shown in Fig. 5.3. Almost all of them collapse to the universal number $N_{\rm ts}|g|$ to within the experiment uncertainty. The scaling behavior is tested with solitons of a nearly 60-fold difference in their peak interaction energies $\hbar\gamma = \hbar^2 n_p|g|/m$, where $\hbar$ is the reduced Planck constant, m is the atomic mass, and $\gamma \approx 2\pi \times (0.85 - 49)$ Hz.

It is however worth noting that a non-negligible MDDI potential is present in our alkali cesium samples [222]–[224]. Since a MDDI potential scales with the inter-atomic spacing as $1/r^3$, it could impact SI in a 2D Bose gas. For the effective 2D MDDI strength [201],

$$g_{\rm dd} = \frac{m}{\hbar^2}\frac{\mu_0\mu^2}{3\sqrt{2\pi}l_z}\,, \tag{5.2}$$

we find that $g_{\rm dd} \approx 0.00087$ is stronger than -10% of the smallest coupling constant $g \approx -0.0075$ explored, where μ_0 is the vacuum permeability, $\mu \approx 0.75\mu_B$ cesium magnetic dipole moment, and μ_B the Bohr magneton. It is thus necessary to examine the effect of MDDI in a GPE. The MDDI in our matter-wave solitons is in a highly oblate configuration, with spin polarized along the tightly confined z-axis. Integrating out wave function along this axis (assumed Gaussian), the rescaled MDDI Hamiltonian can be conveniently expressed as the following inverse Fourier transform [201], [225], [226]:

$$\tilde{H}_{\rm dd} = \frac{g_{\rm dd}}{|g_c|}\int \frac{d\mathbf{k}}{(2\pi)^2} e^{ikR\cos\theta_k} h_{\rm dd}\left(\sqrt{\frac{n_p|g_c|}{2}}kl_z\right)\tilde{n}(\mathbf{k})\,, \tag{5.3}$$

where we define g_c as the bare contact coupling constant, $\tilde{n}(\mathbf{k})$ is the Fourier transform of the rescaled density profile $\tilde{n}(\mathbf{R}) = |\phi(R)|^2$, and $h_{\rm dd}$ is the MDDI function that can potentially break SI (Appendix F). However, in the limit $\sqrt{n_p|g|}l_z \ll 1$, $h_{\rm dd} \approx 2$ is approximately constant within a finite k-range until $\tilde{n}(\mathbf{k})$ vanishes. Equation (5.3) thus transforms back to an effective contact interaction Hamiltonian:

$$\tilde{H}_{\rm dd} \approx 2\frac{g_{\rm dd}}{|g_c|}|\phi(R)|^2 \,. \tag{5.4}$$

This argument generally applies to weakly interacting 2D gases whose lateral size $w \gg l_z$ [200], [226]. As such, the full Hamiltonian in a modified GPE, $\tilde{H} + \tilde{H}_{\rm dd}$, can be effectively recast into $\tilde{H}$ in Eq. (5.1) by rescaling the coordinate R using $g = g_{\rm c} + 2g_{\rm dd}$.

We numerically confirm SI with the MDDI in our quasi-2D samples that have a small but finite $l_z \approx 184$ nm, giving $0.02 \lesssim \sqrt{n_g|g|}l_z \lesssim 0.15$ [1]. As shown in Fig. 5.4, sample numerical solutions at $g_c = -0.009$ collapse well to the universal Townes profile if we rescale the radial coordinate R using $g = g_{\rm c} + 2g_{\rm dd} \approx -0.0073$, which includes the MDDI shift.

The good agreement between our measurement results and the properly rescaled numerical solutions suggests our coupling constant g, which is evaluated using a calibrated scattering length, is already shifted by the MDDI [200], [224], [227]. This is likely the case, as our calibration procedure performed in a quasi-2D trap cannot discern the effect of MDDI from that of a two-body contact interaction (Appendix F). We conclude that the scaling tests performed in Figs. 5.3 and 5.4 confirm SI with the inclusion of a weak MDDI contribution in our quasi-2D geometry.

5.4 Conclusion

In summary, we demonstrate a near-deterministic method to form 2D matter-wave solitons and test the scaling symmetry in attractive 2D Bose gases previously inaccessible to other experiments. We show that SI manifests robustly through an unstable many-body state, formed remarkably from out-of-equilibrium quench dynamics [200]. In particular, our

[1] ↑More precisely, one should call this quasi-SI in quasi-2D samples with finite l_z, as there exists small differences in the rescaled profiles well below typical experiment uncertainty.

observation confirms that the Townes profile not only manifests in a self-similar nonlinear wave collapse, as partially observed in Ref. [173], it is also a prevalent SI profile in solitary waves formed from a modulational instability. The observed universal scaling behavior is under the influence of a non-negligible MDDI potential, which nevertheless imposes no influence on SI in a quasi-2D geometry. A recent study also reveals the insensitivity in the size and shape of a 2D superfluid to the MDDI [228]. Our recipe for instability-induced soliton formation may be further explored in a SI-breaking scenario, for example, through crossover to an MDDI-dominating regime [201], [223], either by tuning to a much smaller contact coupling g_c [227] or with a dipolar quantum gas [229]–[232]. Furthermore, our scaling analysis may be extended to test the dynamics of stronger attractive 2D Bose gases, where quantum correlations may begin to play an important role, such as those discussed in quantum droplets [233]–[238].

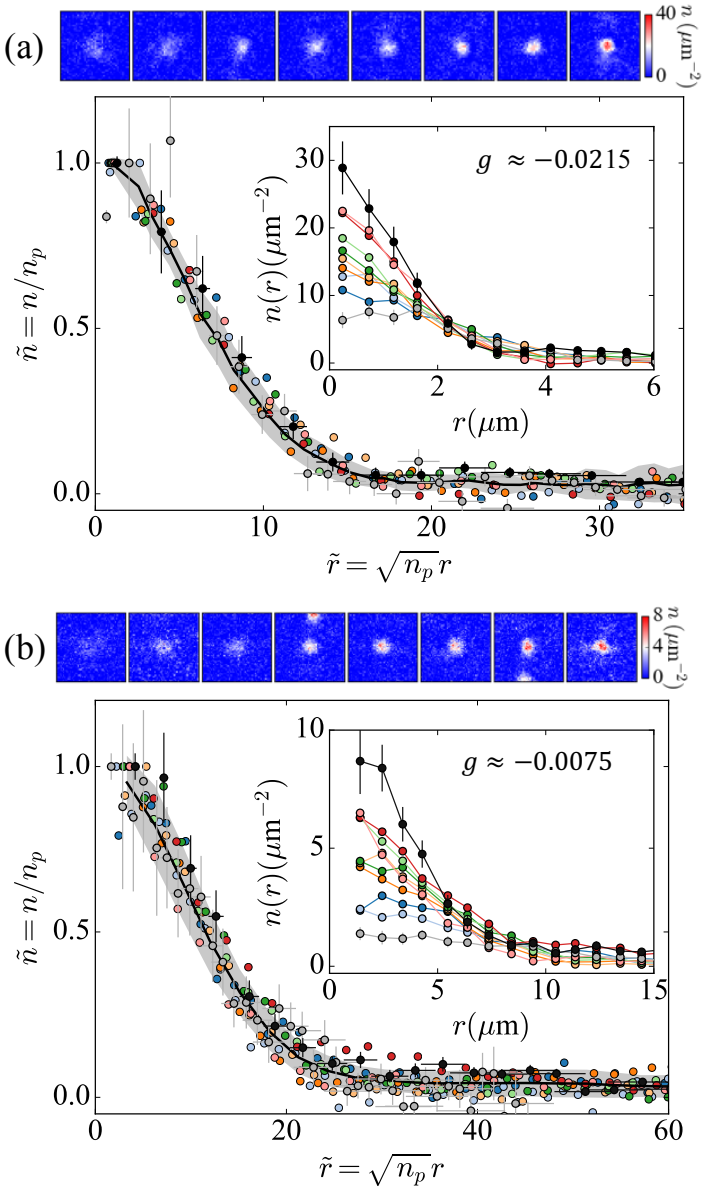

Figure 5.3. Testing scale invariance. (a) Images in the top panel, from left to right, show solitons of low to high peak densities, selected from samples as shown in Fig. 5.1(b). Image size: $19 \times 19\mu\text{m}^2$. Their radial density profiles $n(r)$ (filled circles, inset) approximately collapse onto a single curve in the rescaled coordinate $\tilde{r} = \sqrt{n_p}r$ and $\tilde{n} = n/n_p$. Error bars include statistical and systematic errors. Shaded band shows the standard deviation of 20 rescaled radial profiles around their mean $\langle\tilde{n}\rangle$ (solid curve). (b) similarly shows soliton images and profiles observed in Fig. 5.1(d). Image size: $60 \times 60\mu\text{m}^2$. Reprinted figure with permission from [218], Copyright 2021 by APS.

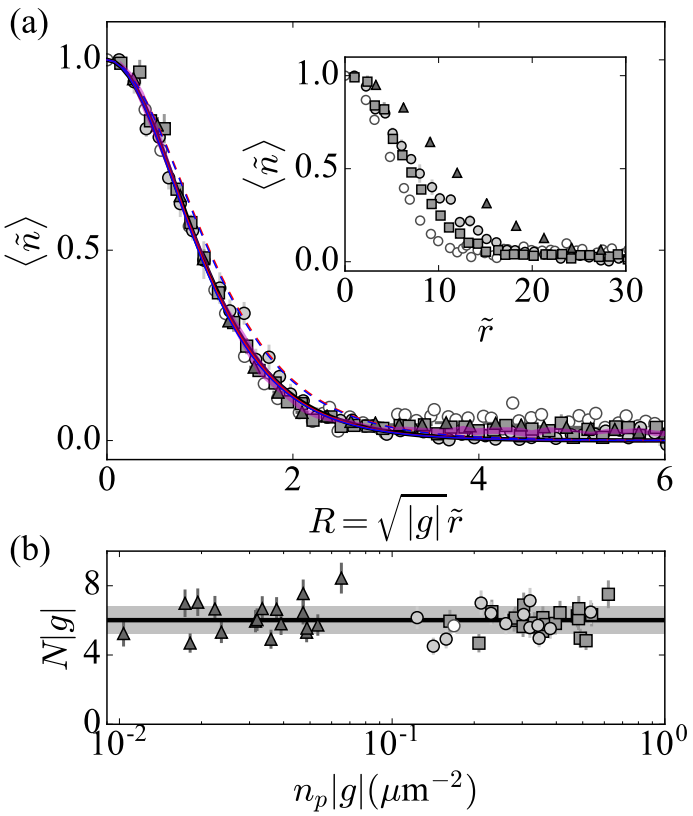

Figure 5.4. Universal soliton density profile. (a) Filled symbols show different scale-invariant mean profiles $\langle\tilde{n}\rangle$ (inset), measured at interaction strengths $g \approx -0.0075$ (triangle), -0.0170 (circle), and -0.0215 (square), respectively. Open circles display a scaled density profile reported in Ref. [200], for $g \approx -0.034$ and with a fixed $n_p \approx 5/\mu\mathrm{m}^2$. These profiles collapse onto a single curve in the rescaled radial coordinate $R = \sqrt{|g|}\tilde{r}$, and the magenta band marks their mean with standard error. Collapsed solid curves are the universal Townes profile (black) and the solutions of full GPE with the MDDI term Eq. (5.3), calculated using $g_c = -0.009$, $n_p = 1/\mu\mathrm{m}^2$ (red) and $10/\mu\mathrm{m}^2$ (blue), respectively, and rescaled using $g = g_c + 2g_{\mathrm{dd}}$. For comparison, dashed curves show the same solutions rescaled using $g = g_c$. (b) Universal atom number $N|g| = \int \tilde{n} d\mathbf{R}$ using soliton profiles as in Fig. 5.3 and integrated up to $R = 4$. Solid line and gray band indicate the mean and standard deviation. Reprinted figure with permission from [218], Copyright 2021 by APS.

6. QUASIPARTICLE PAIR-PRODUCTION AND QUANTUM ENTANGLEMENT

This chapter is adapted from *Physical Review Letter* Volume **127**, Issue 6, Page 060404, by Cheng-An Chen, Sergei Khlebnikov, and Chen-Lung Hung, published on 6 August 2021.
In this chapter, we report observation of quasiparticle pair-production by a modulational instability in an atomic superfluid and present a measurement technique that enables direct characterization of quasiparticle quantum entanglement. By quenching the atomic interaction to attractive and then back to weakly repulsive, we produce correlated quasiparticles and monitor their evolution in a superfluid through evaluating the *in situ* density noise power spectrum, which essentially measures a 'homodyne' interference between ground state atoms and quasiparticles of opposite momenta. We observe large amplitude growth in the power spectrum and subsequent coherent oscillations in a wide spatial frequency band within our resolution limit, demonstrating coherent quasiparticle generation and evolution. The spectrum is observed to oscillate below a quantum limit set by the Peres-Horodecki separability criterion of continuous-variable states, thereby confirming quantum entanglement between interaction quench-induced quasiparticles.

6.1 Introduction

Coherent pair-production processes are enabling mechanisms for entanglement generation in continuous variable states [239], [240]. In many-body systems, quasiparticle pair-production presents an interesting case, as interaction creates entanglement shared among collectively excited interacting particles. Entanglement distribution through quasiparticle propagation is a direct manifestation of transport property in a quantum many-body system [241], [242]. Controlling quasiparticle pair-production and detecting entanglement evolution thus opens a door to probing quantum many-body dynamics, enabling fundamental studies such as information propagation [243], [244], entanglement entropy evolution [245], many-body thermalization [246], as well as Hawking radiation of quasiparticles and thermodynamics of an analogue black hole [247]–[249].

In atomic quantum gases, coherent quasiparticle pair-production can be stimulated through an interaction quench, which results in a rapid change of quasiparticle dispersion relation that can project collective excitations, from either existing thermal or quantum populations, into a superposition of correlated quasiparticle pairs [250]–[252]. This has led to a prior observation of Sakharov oscillations in a quenched atomic superfluid [251], [253]. However, direct verification of quasiparticle entanglement has remained an open question.

An intriguing case occurs when the atomic interaction is quenched to an attractive value. In that case, not only a larger change of quasiparticle dispersion is involved, there is also an unstable band, in which quasiparticle dispersion $\epsilon(k)$ is purely imaginary, $\epsilon^2(k) < 0$, where k is the momentum wavenumber. As a consequence, the early time dynamics is governed by a modulational instability (MI), which continuously stimulates production of quasiparticle pairs and the ground state becomes unstable with respect to an exponential growth of density waves. This growth leads eventually to wave fragmentation and soliton formation [190]. Although these consequences of MI have been observed [185], [186], [200], [254], [255], the early-time evolution itself has only been recently studied [200]. Nevertheless, it is precisely the early-time dynamics that promises MI-enhanced pair-production and quantum entanglement. We note there is a parallel scheme using a roton instability for enhanced quasiparticle entanglement generation in dipolar quantum gases [256].

We demonstrate MI-enhanced coherent quasiparticle pair-production in a homogeneous 2D quantum gas quenched to an attractive interaction, and report an in situ detection method that enables direct characterization of quasiparticle entanglement beyond an existing method [247], [257]. Specifically, we monitor coherent quasiparticle evolution after quenching the interaction back to a positive value (see Fig. 6.1 for protocol). Through *in situ* imaging, we analyze the dynamics of density observables by a method analogous to the well-established homodyne detection technique in quantum optics [258]–[260] and confirm non-classical correlations, that is, quantum entanglement in quasiparticle pairs.

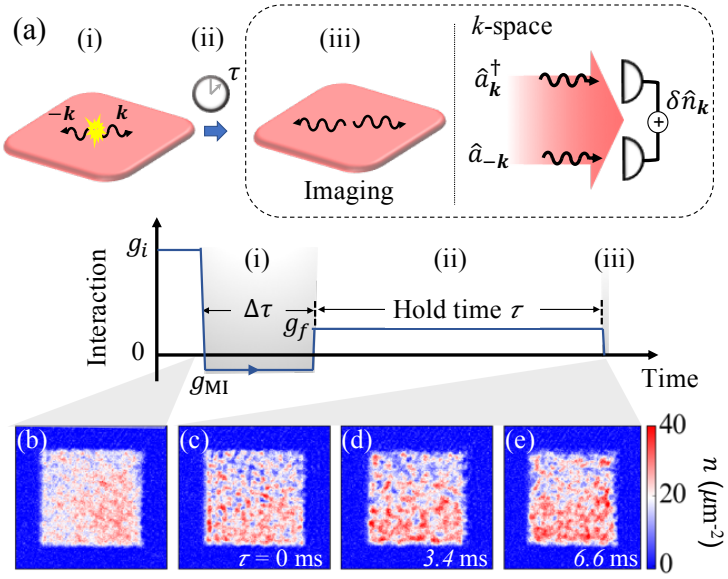

Figure 6.1. Experiment scheme for quasiparticle pair-production and detection. (a) A homogeneous 2D superfluid (red square) undergoes an interaction quench protocol from (i) $g = g_{\rm i} > 0$ to $g_{\rm MI} < 0$ for broadband generation of quasiparticle pairs of opposite momenta (illustrated by black curvy arrows) for a time duration $\Delta\tau$; (ii) A second interaction quench to $g = g_f > 0$ allows quasiparticles to evolve as phonons for a variable hold time τ; (iii) *In situ* density noise in spatial frequency domain, $\delta n_{\mathbf{k}}$, is essentially a 'homodyne' measurement of excitations in opposite momentum states interfering with ground state atoms. (b-e) Single-shot density images taken prior to (b) or after the interaction quench (c-e) and held for the indicated time τ. Image size: 77×77 μm^2. Reprinted figure with permission from [261], Copyright 2021 by APS.

6.2 Methods

Our analyses are based on the time evolution of *in situ* density noise, which is a manifestation of interference between quasiparticle excitations and the ground state atoms that serve as a coherent local oscillator [262]. In Fourier space, the density noise operator can be written as $\delta\hat{n}_{\mathbf{k}} \approx \sqrt{N}(\hat{a}_{\mathbf{k}}^\dagger + \hat{a}_{-\mathbf{k}})$, where $N \gg 1$ is the total atom number nearly all accounted for by the ground state atoms, and $\hat{a}_{\pm\mathbf{k}}^{(\dagger)}$ are the annihilation (creation) operators for $\pm\mathbf{k}$ single-particle momentum eigenstates. They are related to quasiparticle operators $\hat{\alpha}_{\pm\mathbf{k}}^\dagger$ by the Bogoliubov transformation. We study the density noise power spectrum $S(\mathbf{k}) = \langle|\delta n_{\mathbf{k}}|^2\rangle/N$, where $\langle\cdots\rangle$ denotes ensemble averaging. Within our resolution limit ($|\mathbf{k}| \lesssim 2.6/\mu$m), the power spec-

trum conveniently measures the combined variance of two-mode ($\pm\mathbf{k}$) quasiparticle quadrature operators $\hat{x}_{\mathbf{k}} + \hat{x}_{-\mathbf{k}}$ and $\hat{p}_{\mathbf{k}} - \hat{p}_{-\mathbf{k}}$, where $\hat{x}_{\mathbf{k}} = (\hat{\alpha}^\dagger_{\mathbf{k}} + \hat{\alpha}_{\mathbf{k}})/\sqrt{2}$ and $\hat{p}_{\mathbf{k}} = \mathrm{i}(\hat{\alpha}^\dagger_{\mathbf{k}} - \hat{\alpha}_{\mathbf{k}})/\sqrt{2}$ (Appendix G). Since pair-production should be isotropic in our quantum gas samples, in the following we discuss azimuthally averaged spectrum $S(k)$, and use $\pm k$ to denote opposite momenta. In the superfluid ground state absent quasiparticle (phonon) excitations, the Bogoliubov theory predicts $S(k) = C_k$, where $C_k = \epsilon_k/\epsilon(k, g)$ is the ground-state squeezing parameter, ϵ_k the single-particle energy, $\epsilon(k, g) = \sqrt{\epsilon_k^2 + 2\frac{\hbar^2}{m}\bar{n}g\epsilon_k}$ the phonon dispersion relation, $\bar{n}$ the mean density, g the interaction at the time of the measurement, m the atomic mass, and $\hbar$ the reduced Planck constant.

In the presence of quasiparticles with non-classical correlation, the power spectrum would squeeze below the ground-state level, i.e., to $S(k) < C_k$. This intuitive bound can be formally derived following Refs. [263], [264], which considers a continuous-variable version of the Peres-Horodecki separability criterion for bipartite entanglement. Adapted to our case (Appendix G), the criterion states that the variance of two-mode quadratures must satisfy

$$S(k) = \frac{C_k}{2}\left[\langle(\hat{x}_k + \hat{x}_{-k})^2\rangle + \langle(\hat{p}_k - \hat{p}_{-k})^2\rangle\right] \geq C_k\,, \tag{6.1}$$

in the absence of quasiparticle entanglement. For non-interacting atoms ($g = 0$), $C_k = 1$, and the above inequality represents the limit of atomic shot-noise. For phonons in a superfluid ($g > 0$), the separability criterion requires a lower limit ($C_k < 1$).

In the final state of our quench protocol ($g > 0$), coherent quasiparticle pairs interfere and $S(k)$ should be time-dependent. In the special case of noninteracting phonons, that dependence has the form

$$S(k, \tau) = C_k\left[1 + \bar{N}_k + \Delta N_k \cos\phi_k(\tau)\right], \tag{6.2}$$

where $\bar{N}_k = \langle\hat{\alpha}^\dagger_k\hat{\alpha}_k\rangle + \langle\hat{\alpha}^\dagger_{-k}\hat{\alpha}_{-k}\rangle$ is the mean total phonon number in $\pm k$ modes, $\Delta N_k = 2|\langle\hat{\alpha}_k\hat{\alpha}_{-k}\rangle|$ is the pair correlation amplitude, and $\phi_k(\tau) = 2\epsilon(k, g)\tau/\hbar + \phi_k(0)$ is the argument of $\langle\hat{\alpha}_k\hat{\alpha}_{-k}\rangle$ that evolves at twice the phonon frequency. In this case, violation of the inequality Eq. (6.1) is equivalent to having $\Delta N_k > \bar{N}_k$ [265], [266]. The presence of maximal two-mode

squeezing $S(k)/C_k < 1$ occurs at $\phi_k \approx (2l+1)\pi$, alternating with maximal anti-squeezing $S(k)/C_k > 1$ at $\phi_k \approx 2l\pi$ (l is an integer). In practice, oscillations of $S(k)$ are inevitably damped. Nevertheless, $\pm k$ modes are entangled as long as ΔN_k remains larger than $\bar{N}_k$, or more generally $S(k)$ shows squeezing ($< C_k$) – a key signature that we demonstrate.

To carry out the experiment, we prepare uniform superfluid samples formed by $N \approx 4.9 \times 10^4$ nearly pure Bose-condensed cesium atoms loaded inside a quasi-2D box potential, which compresses all atoms in the harmonic ground state along the imaging (z-) direction [200] with $l_z = 184$ nm being the harmonic oscillator length. A time-of-flight measurement estimates the sample temperature $T \lesssim 8$ nK. Mean atomic surface density $\bar{n} \approx 21/\mu\text{m}^2$ is approximately uniform within a horizontal box size of $\approx 48 \times 48$ μm^2. The interaction strength of the quasi-2D gas $g = \sqrt{8\pi}a/l_z$ is controlled by the s-wave scattering length a via a magnetic Feshbach resonance [59], giving an initial interaction strength $g = g_\text{i} \approx 0.127$. An uncertainty in g ($\delta g \approx \pm 0.0006$) is primarily contributed by the uncertainty in the magnetic field at the scattering length zero-crossing [200].

6.3 Results

As illustrated in Fig. 6.1(a), an MI period is initiated by quenching the atomic interaction (within 0.8 ms) to a negative value $g_\text{MI} \approx -0.026$. The quench time scale is short compared to the initial phonon cycle $2\pi\hbar/\epsilon(k, g_\text{i}) \gtrsim 2.5$ ms for $k \lesssim 2.6/\mu$m, and the interaction quench is considered quasi-instantaneous. To terminate the MI after additional short hold time $\Delta\tau \approx$ 1–2 ms, we quench the atomic interaction back to a small positive value $g_f \approx 0.007$, allowing quasiparticles to evolve as phonons in a stable superfluid for another variable time τ before we perform *in situ* absorption imaging. We have also analyzed quenches without an MI period ($\Delta\tau = 0$). Figures 6.1(b-e) show sample images measured before and after we initiate the quench protocol. We evaluate $\delta n_\mathbf{k}$ for each sample through Fourier analysis [221] and obtain their density noise power spectra. Typically around 50 experiment repetitions are analyzed for each hold time τ. Each power spectrum has been carefully calibrated with respect to the atomic shot-noise measured from high temperature normal gases (Appendix G) [221].

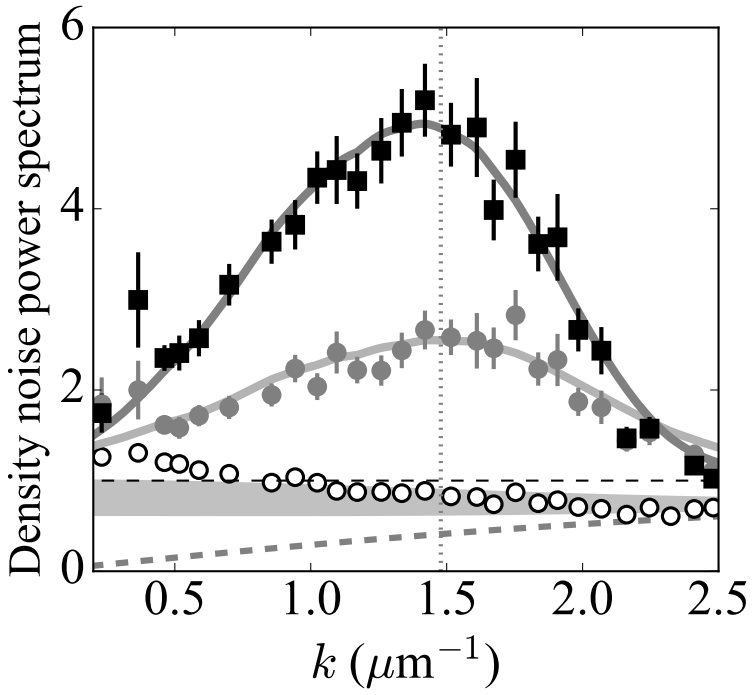

Figure 6.2. Growth of density noise during the MI period. Density noise power spectra measured before, $S_0(k)$ (open circles), and right after the MI period, $S(k,0)$, with $\Delta\tau \approx 1$ ms (gray circles) and 2 ms (black squares), respectively. Horizontal dashed line marks the atomic shot-noise level. Gray band represents calculated initial phonon spectrum assuming equilibrium temperature $T = 8 \pm 2$ nK. Dashed curve shows the squeezing parameter C_k at $g = g_\mathrm{i} \approx 0.127$. Solid curves are theory fits to data; (Appendix G). Vertical dotted line marks the wavenumber k_c, below (above) which quasiparticles are expected to be unstable (stable) at $g = g_\mathrm{MI} \approx -0.026$. Reprinted figure with permission from [261], Copyright 2021 by APS.

We expect amplified density fluctuations following the MI period due to sudden change of quasiparticle energy dispersion and pair-production [200], [250], [251]. To quantify the growth of density fluctuations, in Fig. 6.2 we compare the density noise power spectra measured before and immediately after the MI period, that is, for hold time $\tau = 0$. Before MI, the initial spectrum $S_0(k)$ is mostly below the atomic shot-noise due to low temperature $T \lesssim 8$ nK and small initial squeezing parameter $C_k < 1$. Excessive noise in $k \lesssim 0.75/\mu$m may be due to technical heating in the box potential. After the MI time period $\Delta\tau$, we indeed find a significant increase in the density noise, $S(k,0) > 1$. The growth occurs both

in the instability band $k \lesssim k_c = 2\sqrt{\bar{n}|g_{\rm MI}|} \approx 1.5/\mu$m, where the dispersion $\epsilon(k, g_{\rm MI})$ is purely imaginary, and in the stable regime $k \gtrsim k_c$ as well. Within these short MI periods, we observe the largest growth near $k \approx k_c$, where $\epsilon(k, g_{\rm MI}) \approx 0$. We comment that for a much longer MI period, density waves in the instability band eventually dominate the noise power spectrum due to continuously stimulated quasiparticle pairs, as observed in [200].

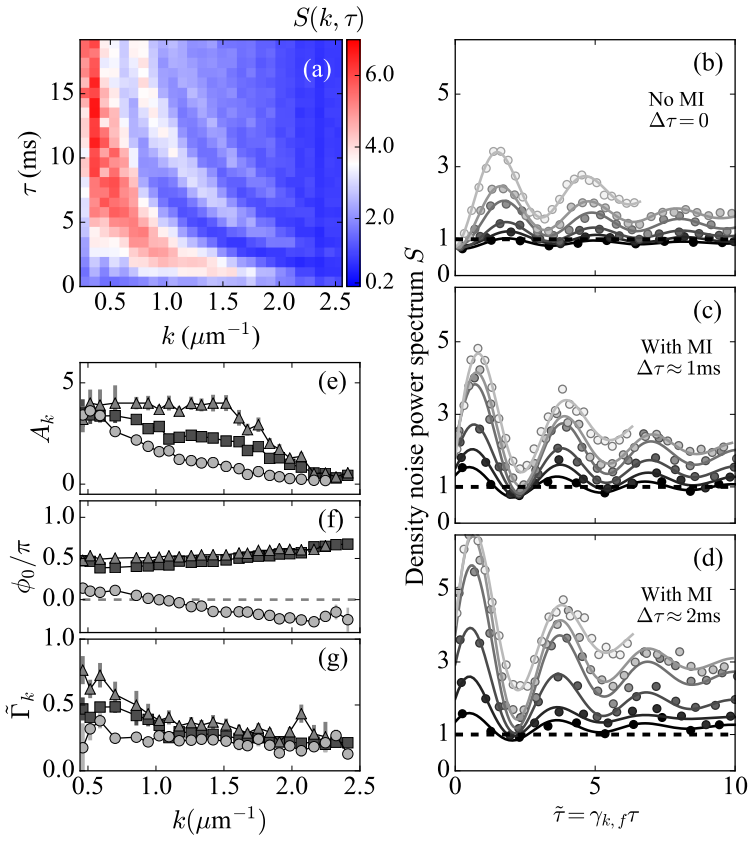

Figure 6.3. Coherent oscillations in the density noise power spectrum. (a) Full evolution of the power spectrum $S(k, \tau)$ with $\Delta\tau \approx 1$ ms, showing coherent oscillations in time and k-space. (b-d) Synchronized oscillations of $S(k, \tilde{\tau})$ plotted in the rescaled time unit $\tilde{\tau} = \gamma_{k,f}\tau$ for various $k \approx (1, 1.3, 1.6, 1.8, 2.1, 2.2)/\mu$m (Gray circles from bright to dark). Horizontal dashed lines mark the atomic shot-noise limit. Solid lines are sinusoidal fits. Fitted amplitude A_k, phase offset ϕ_0, and decay rate $\tilde{\Gamma}_k$ from samples with $\Delta\tau \approx 0$ ms (filled circles), 1 ms (filled squares), and 2 ms (filled triangles) are plotted in (e-g), respectively. Reprinted figure with permission from [261], Copyright 2021 by APS.

Our measured spectra can be well-captured by a model that considers coherent evolution from quasiparticle pair-production within the Bogoliubov theory and their damping as well as decoherence due to coupling to single-particle Markovian quantum noise. We refer to the coherent signal in the absence of damping as: $S_{\rm coh}(k) = S_0(k)[1 + \frac{\epsilon(k,g_{\rm i})^2 - \epsilon(k,g_{\rm MI})^2}{\epsilon(k,g_{\rm MI})^2} \sin^2 \frac{\epsilon(k,g_{\rm MI})\Delta\tau}{\hbar}]$, which describes the hyperbolic growth of density fluctuations in the instability band ($k \lesssim k_c$) [200] and sinusoidal Sakharov oscillations for stable modes ($k \gtrsim k_c$) [251]. On the other hand, quantum noise causes damping (reduction) of the coherent signal and the appearance of an additive incoherent background $S_{\rm inc}(k)$. The total power spectrum at the end of the MI period is $S(k,0) = \mathrm{e}^{-\Gamma_k \Delta\tau} S_{\rm coh}(k) + S_{\rm inc}(k)$, where $S_{\rm inc}(k) = \frac{1}{2}\{\eta_- \frac{\Gamma_k^2}{\Gamma_k^2 + 4\epsilon(k,g_{\rm MI})^2/\hbar^2}[1 - \mathrm{e}^{-\Gamma_k\Delta\tau}(\cos\frac{2\epsilon(k,g_{\rm MI})\Delta\tau}{\hbar} - \frac{2\epsilon(k,g_{\rm MI})}{\hbar\Gamma_k}\sin\frac{2\epsilon(k,g_{\rm MI})\Delta\tau}{\hbar})] + \eta_+(1 - \mathrm{e}^{-\Gamma_k\Delta\tau})\}$, with $\eta_\pm = 1 \pm \epsilon_k^2/\epsilon(k,g_{\rm MI})^2$. The coherent and incoherent contributions are coupled by a k-dependent damping rate Γ_k. Our theory fits (solid curves in Fig. 6.2) suggest $\Gamma_k \sim 0.5\epsilon_k/\hbar$ (Appendix G), which is of the same order of magnitude as the decay rate extracted from the subsequent time-evolution measurements at $g = g_f$ (Fig. 6.3).

To demonstrate phase coherence and pair-correlation in quasiparticles, we plot the complete time and momentum dependence of the density noise power spectrum $S(k,\tau)$, as shown in Fig. 6.3(a). Here, oscillatory behavior is clearly visible over the entire spectrum. The oscillations are a manifestation of the interference between coherent quasiparticles of opposite momenta $\pm k$, as suggested by Eq. (6.2), with the relative phase winding up in time as $\phi_k(\tau) = 2\gamma_{k,f}\tau + \phi_0$, where $\gamma_{k,f} = \epsilon(k,g_f)/\hbar$ is the expected Bogoliubov phonon frequency and ϕ_0 is an initial phase difference. In Fig. 6.3(b-d), we plot $S(k,\tilde{\tau})$ in the rescaled time $\tilde{\tau} = \gamma_{k,f}\tau$ and confirm that all spectra oscillate synchronously with a time period $\approx \boldsymbol{\pi}$, thus validating the phonon interference picture. For comparison, we also plot the evolution of samples with a direct interaction quench from $g_{\rm i}$ to g_f without an MI period ($\Delta\tau = 0$). Oscillations in $S(k,\tilde{\tau})$ can also be observed, albeit with smaller amplitudes and phase offsets $\phi_0 \approx 0$, as these oscillations result solely from the interference of in-phase quasiparticle projections from suddenly decreasing the Bogoliubov energy [251]. In either case, with or without MI, we observe that phase coherence is lost in a few cycles and the density noise spectra reach new steady-state values.

To quantify phase coherence and dissipation at final $g = g_f$, we perform simple sinusoidal fits $S(k,\tilde{\tau}) = S_f - S_o e^{-\tilde{\Gamma}_k \tilde{\tau}} - A_k e^{-\tilde{\Gamma}_k \tilde{\tau}} \cos(2\tilde{\tau} + \phi_0)$ to the data to extract $(A_k,\ \phi_0,\ \tilde{\Gamma}_k)$, as shown in Fig. 6.3(e-g) (the steady-state values S_f and S_o are not shown). The larger oscillation amplitudes A_k found in samples with $\Delta\tau \approx 1$ ms and 2 ms show that MI-induced quasiparticles are highly phase coherent. This can also be seen in the non-zero phase offset $\phi_0 \gtrsim \pi/2$ at $k \gtrsim 0.5/\mu$m in Fig. 6.3(f), which is coherently accumulated during the MI period. Furthermore, in Fig. 6.3(g), we observe a nearly constant decay rate $\tilde{\Gamma}_k \approx 0.31(8)$ at $k \gtrsim 0.8\ /\mu$m for these MI-induced oscillations. This is close to the decay rate $\tilde{\Gamma}_k \approx 0.22(4)$ in samples without an MI period ($\Delta\tau = 0$), suggesting that the short MI dynamics does not heat up the sample significantly to increase the phonon dissipation rate.

We now focus on identifying a key signature of non-classical correlations. To search for entanglement in the final phonon basis, we evaluate the squeezing parameter $C_k = \epsilon_k/\epsilon(k, g_f)$ at $g = g_f$ and plot the rescaled phonon spectra $\tilde{S}(k,\tilde{\tau}) = S(k,\tilde{\tau})/C_k$, as shown in Figs. 6.4(a-c) [1]. In this basis, the phonon spectra at momenta $k \gtrsim 1.5/\mu$m can be observed to oscillate above and below the rescaled quantum limit $\tilde{S} = 1$, showing signatures of two-mode squeezing and anti-squeezing as time evolves. The first minimum $\tilde{S}_{\text{min}}$ identified at various momenta k is plotted in Fig. 6.4(d), in which we find that $\tilde{S}_{\text{min}}$ violates the inequality Eq. (6.1) in a wider range for the MI sample with $\Delta\tau \approx 1$ ms than it does for the samples without MI or with longer $\Delta\tau$. The strongest violation is in the range of $2.1/\mu\text{m} \lesssim k \lesssim 2.2/\mu$m and has average $\tilde{S}_{\text{min}} \approx 0.77(7) < 1$, compared to $\tilde{S}_{\text{min}} \approx 0.84(8)$ without MI and $\tilde{S}_{\text{min}} \approx 0.91(5)$ for $\Delta\tau \approx 2$ ms. Lastly, we comment that the initial violation of inequality for samples without MI at $\tilde{\tau} \approx 0$ is also clear. However, fewer modes show squeezing when the phonon spectra return back to the first minima $\tilde{S}_{\text{min}}$.

[1]↑We note a ±20 % variation of mean density across the analysis region ($38 \times 38\ \mu\text{m}^2$). As a result, the squeezing parameter C_k has at most a small ±4% variation relative to the mean within the reported momentum range as shown in Fig. 6.4.

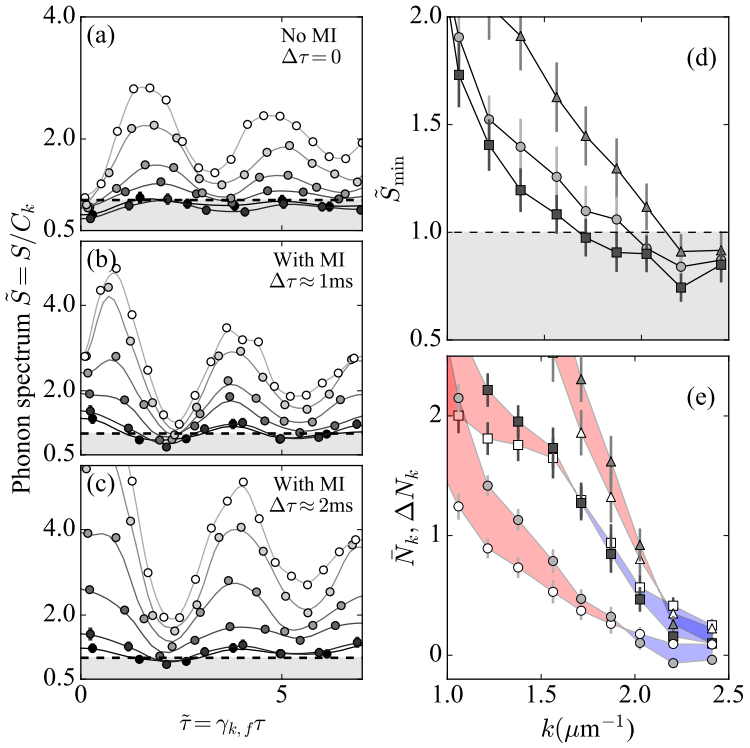

Figure 6.4. Testing two-mode squeezing and quantum entanglement in the phonon basis. (a-c) Rescaled phonon spectrum $\tilde{S}(k, \tilde{\tau})$ for $k \approx (1.3, 1.6, 1.8, 2.1, 2.2, 2.4)/\mu$m (filled circles from bright to dark), evaluated using data as shown in Figs. 6.3(b-d). Solid curves are guides to the eye. (d) First minima $\tilde{S}_{\min}$ in the phonon spectra of various wavenumber k, at $\Delta\tau \approx 0$ ms (filled circles), 1 ms (squares), and 2 ms (triangles), respectively. In (a-d), horizontal dashed lines mark the quantum limit, below which Eq. (6.1) is violated. Error bars include systematic and statistical errors. (e) Mean phonon population $\bar{N}_k$ (filled symbols) and pair-correlation amplitude ΔN_k (open symbols) extracted using the first minima and maxima identified in (a, circles), (b, squares), and (c, triangles), respectively. Blue (red) shaded areas mark the region where $\Delta N_k > \bar{N}_k$ ($\Delta N_k < \bar{N}_k$). Error bars represent statistical errors. Reprinted figure with permission from [261], Copyright 2021 by APS.

To further interpret our result, we extract the mean phonon number $\bar{N}_k$ and the pair-correlation amplitude ΔN_k by using the first maximum $\tilde{S}_{\max}$ and minimum $\tilde{S}_{\min}$ identified in $\tilde{S}(k, \tilde{\tau})$ at each k in Figs. 6.4(a-c),

$$\begin{aligned} \bar{N}_k &\approx \frac{\tilde{S}_{\max} + \tilde{S}_{\min}}{2} - 1 \\ \Delta N_k &\approx \frac{\tilde{S}_{\max} - \tilde{S}_{\min}}{2}. \end{aligned} \tag{6.3}$$

As shown in Fig. 6.4(e), both $\bar{N}_k$ and ΔN_k have comparably increased due to pair-production in MI samples of $\Delta\tau \neq 0$. Quantum entanglement appears to better prevail for $\Delta\tau \approx 1$ ms and at $k \gtrsim 1.5/\mu$m, where $\Delta N_k \gtrsim \bar{N}_k$. This may be understood as any excessive incoherent population $\bar{N}_k - \Delta N_k > 0$ in our samples can be due partially to quasiparticle dissipation during the quench and partially to incoherent (thermal) phonons present in the initial state. The latter are better suppressed at $k > 1.5/\mu$m as $\epsilon(k, g_{\rm i}) > k_B T \approx \hbar \times 1$ kHz.

6.4 Conclusion

In summary, we observe pair-correlation signal and non-classical correlation in atomic quantum gases quenched to an attractive interaction, with two-mode squeezing $\tilde{S}_{\rm min} \approx 0.8 < 1$ below the quantum limit. Further reduction of initial incoherent phonon populations or of decoherence during pair-production processes may increase the non-classical signal in future experiments. Reaching $\tilde{S} < 0.5$ could open up applications requiring Einstein–Podolsky–Rosen entangled quasiparticle pairs [209]–[211], [267], [268]. Our method may be extended to analyze entanglement distribution between non-causal regions before the interaction quench. Furthermore, in analogy to the discussion in Ref. [269], extending our analyses of two-mode quadrature variance to skewness [270] and other higher-order correlation terms may provide necessary observables for probing entanglement entropy and transport in a quantum gas.

7. A COMPACT AND VERSATILE QUANTUM GAS MACHINE

In this chapter we report an important system upgrade made in 2021. We replace our first generation N.A.[1] = 0.37 microscope objective with the new N.A. = 0.6 microscope objective. Meanwhile we upgrade the main coils to a more compact design which can be placed closer to the atoms and attached to cooling plates. In addition, we implement the horizontal (x- and y-axis) optical lattices with two different wavelengths: 767 nm for repulsive potentials and 1064 nm for attractive potentials. We have also re-optimized a few parameters such as beam alignment of dipole traps and optical aberrations of imaging.

7.1 Introduction

Quantum gas experiments such as Bose-Einstein condensate and degenerate Fermi gas have been among the most important platforms in modern physics. In recent years, different species have been laser-cooled to their ground states or nearly ground states, in which quantum effects surpass classical ones and open up all kinds of possibilities to explore few-body and many-body quantum physics. The advance of quantum gas experiments [91] from high-resolution quantum gas microscope [56] to ultracold atoms in the International Space Station (ISS) [271], enabling us to engineer a wide range of Hamiltonian as well as showing the great potential in the field of quantum computing and quantum information.

Since the first experimental demonstration of Bose-Einstein condensate in dilute gases [272], [273], Bose gases have been of great interest due to their peculiar properties. An ultracold Bose gas can be microscopically occupied by atoms or molecules all in the same ground state, making it an ideal platform for studying many-body Hamiltonian. In addition to samples with a big group of particles, atoms or molecules can also be trapped in arranged distance and geometry thanks to optical lattices and optical tweezers. These atoms or molecules resemble the ordered structures in solid state crystals, yet with higher

[1]↑Numerical aperture $N.A. \equiv n \sin\theta$, where the refractive index of the medium $n \approx 1$ and θ is the one-half angular aperture.

degrees of freedom of control and much more tunability than conventional condensed matter experiments.

To prepare samples in quantum degeneracy, however, requires a series of precise operations and detections. In contrast to experiments like optical tweezer arrays, where the trapping frequency is oftentimes high enough such that atoms are in the vibrational ground state or low energy states, ultracold Bose gases in 1D/2D/3D are more strict with the temperature, or essentially the de Broglie thermal wavelength of every particle. This poses the limitations for the sizes of the apparatuses and the time spent in each experimental realization. For instance, a quantum gas microscope machine usually consists of a Zeeman slower for precooling, a chamber for magneto-optical trap (MOT) followed by sub-Doppler cooling, and a "science" chamber for evaporative cooling and high-resolution optical control and imaging. The physical separation of "MOT" and "science" chamber hinders the vacuum chamber from being compact, and also prolongs each experimental cycle because of the time for transporting samples from one chamber to the other, in company with unavoidable particle loss and/or heating due to this transportation.

In this chapter, we demonstrate a state-of-the-art yet very compact quantum gas machine. We show that, without compromising any optical access and resolution, ultracold quantum gases can be prepared, controlled, and detected with sub-micrometer spatial resolution and sub-millisecond temporal resolution. We also show that this machine is not only capable of producing samples of one species, but also has high flexibility to be extended for the second or more other species. This novel design of apparatus has proven its scientific significance for studying frontier quantum physics by its predecessor [200], [218], [261], and it is ready to study many cutting edge physics problems from cosmology to quantum simulation.

7.2 Methods

Our apparatus is designed aiming for that, it only occupies a comparable small part of a conventional optical table, but is very efficient in terms of the quality, the speed, and the precision of the sample preparation. The sample preparation begins from a cesium ampule which is installed in a 1.33" CF nipple, with silver-plated copper gaskets to protect the

sealing from the attack of this active alkali metal. The cesium ampule is heated to 60°C via heating wires outside the nipple, and the cesium vapor is going through a necessary all-metal angle valve. This all-metal angle valve gives us the flexibility to replace the cesium source when we run it out, or with other elements in the future. The all-metal valve is also heated to ≈ 60°C, which effectively determines the velocities of atoms during the Zeeman slowing in the next stage. The heated part of the all-metal valve is in line with two 2 mm diameter skimmers and a Zeeman slower tube. These two skimmers are heated to 10°C above the cesium source by heating bands, ensuring that no clogging of cesium would occur in the apertures. These skimmers also provide differential pumping and atomic beam collimating, where an in-vacuum copper tube is installed following the first skimmer to further reduce the solid angle of the atomic beam [274], [275]. The nipple between two skimmers is cooled to < 0°C via a Peltier thermoelectric cooler backed by water cooling; this section can capture cesium atoms blocked by the second skimmer. A 25 L/s ion pump is installed between the second skimmer and the Zeeman slower. Thanks to the very low vacuum conductance provided by skimmers and the removal of unwanted atoms by cold capture, the vacuum pressure with this ion pump is only $\approx 1 \times 10^{-9}$ Torr.

The length of the Zeeman slower is designed to be 40 cm, which greatly reduces the longitudinal size of the apparatus. The Zeeman slower tube is merged with a multi-port vacuum flange. This flange combines the Zeeman slower of cesium atom and the other port (sealed by an in-line all-metal valve and a vacuum viewport at the moment) reserved for other species in the future, where both entrances are aligned to the center of the main chamber. The main vacuum chamber includes a pre-backed electropolished stainless steel octagon, seven 2.75" CF side viewports, top and bottom recessed viewports. The top and bottom viewports are designed so that the distance between the center of the chamber and the air-side surface of the glass is ≈ 20 mm, compatible with 1" horizontal MOT beams and the working distance of the high-resolution microscope objective (described in the following section). The main chamber is pumped by a 75 L/s ion pump and two titanium sublimation pumps (TSP), giving an overall pumping rate > 100 L/s. We are able to reach ultra-high vacuum (UHV) $\approx 1 \times 10^{12}$ Torr in the main chamber after careful preparation and baking. Following the longitudinal cooling of the Zeeman slower, atoms are trapped in a

MOT and further cooled by polarization gradient cooling (PGC) and degenerate Raman sideband cooling (dRSC) [161]. Finally, we load atoms in a red-detuned far-off-resonance optical dipole trap (FORT) and carry out evaporative cooling till the atoms reach quantum degeneracy [168], i.e. Bose-Einstein condensate.

The essence of our apparatus is the single chamber design. Most quantum gas microscope apparatuses use a separated "science" chamber for high-resolution control and probing, such that the optical access of the microscope objective or other optical manipulations is free from the optical obstruction of MOT optics or laser beams. Nevertheless, the means for sample transportation is either magnetic via a series of bulky coils [276], or optical via conveyor beams [277]. On the contrary, we integrate the MOT optics into the high-resolution microscope objective and eliminate the need for the "science" chamber. The benefit is huge – since all laser cooling optics are together, we do not have extra setup for optical pumping and others. MOT beams can be readily used for fluorescence imaging, and other laser cooling methods continue to assist as needed, such as degenerate Raman sideband cooling. Furthermore, the stability, the repeatability, and the efficiency of sample preparation are greatly improved with a unified chamber. Last but not least, spatial overlap of laser cooling and high-resolution control/probe is the key for experiments of multi-species quantum gases.

To carry out our idea, we cooperate with commercial companies to customize a couple of optical components (Fig. 7.1). The high-resolution microscope objective (Special Optics #53-32-27, N.A. $= 0.6$) is carefully designed so that the position of its back focal point has a holder for a designated optics. Besides, a wire-grid linear polarizer film is attached to a customized achromatic quarter waveplate (Meadowlark Optics) by optical adhesive. The anti-reflection (AR) coating and working wavelengths of both optics cover all wavelengths we would use, and the angle between polarizations of the wire-grid polarizer and the quarter waveplate is carefully aligned via precision interferometer before the attaching. The diameter and the thickness of this compound optics is designed to cooperate with the microscope objective, thus the wire-grid polarizer layer is $\approx \pm 2$ mm from the back focal point. When a collimated beam, e.g. vertical MOT beam, propagates into the microscope objective from the front side, it will focus approximately onto the wire-grid polarizer. Therefore, a circular polarized MOT beam will first be phase-retarded by the achromatic quarter waveplate and becomes

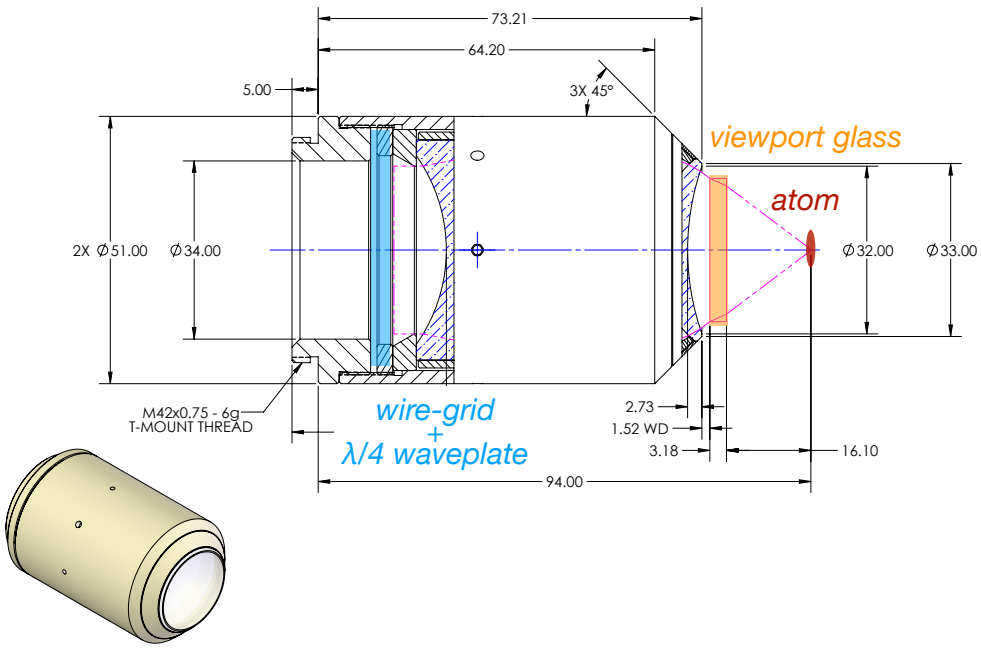

Figure 7.1. CAD drawing of the microscope objective shows the integrated optics.

linear polarized. It is then retro-reflected by the wire-grid polarizer, phase-retarded again, and collimated by the same microscope objective. The retro-reflected MOT beam will not have the same beam size due to the cutoff inside the microscope objective while propagating through many optical components, however it is well-designed by us so that, the $\approx \pm 2$ mm tunable range of the holder is enough to change the collimation of the retro-reflection to balance the radiation pressure force of MOT.

To achieve high-resolution quantum control and imaging, the microscope objective is the leading role. Our microscope objective is designed to compensate for the thickness of the vacuum viewport (≈ 3.18 mm) and be diffraction limit across wavelength 760 – 890 nm. It has full width half maximum (FWHM) of Huygens point spread function $\lesssim 0.8$ μm at 852 nm (Fig. 7.2), and still remains a compact size with its diameter = 51 mm. As a result, we are able to install the magnetic coil by the microscope objective within the recessed part of the viewport. The frame of the microscope objective is made of plastic Ulem (Polyetherimide) to avoid the eddy current, and has good mechanical strength and thermal stability. The exit pupil diameter of the microscope objective is 32 mm, compatible with standard 2" mirrors

for 90° turning. An achromatic tube lens (i.e. eyepiece) is also custom-made to match the dispersion of the microscope objective, giving a $\approx 30\times$ magnification of this paired optics.

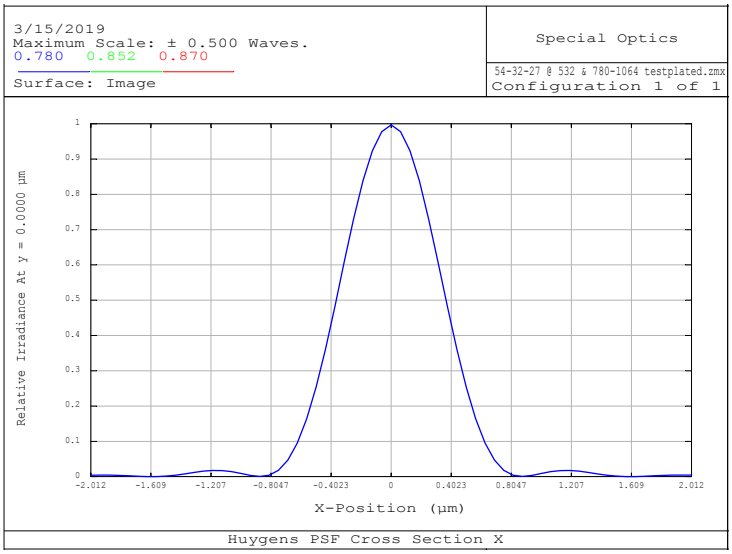

Figure 7.2. Huygens point spread function (PSF) of the microscope objective simulated by ray tracing shows the optical resolution $R \leq 0.8\mu m$.

Even though the recessed viewport has reduced significant distance from the center of the main chamber to the microscope objective, the 1" diameter horizontal MOT beams bring out the required minimum working distance for the microscope objective spatially. In order to maximize the high resolution while remaining compact, our microscope objective is designed to be placed very close to the vacuum viewport. As a result, the gap between the viewport glass to the front of the microscope objective is merely 1.5 mm, and the installation becomes a potential issue. We develop a precise method to circumvent the possible dangerous collision while pushing the microscope objective forward. We first carefully make the coil and the coil holder so that we have detailed dimensions of all mechanical ports, then we attach a photoresistor and a LED on the opposite sides of the interior rim as wellas near the bottom of the coil. We meticulously align the photoresistor and the LED with the viewport glass, then turn on the LED. We can measure the resistance of the photoresistor lit by the LED. The photoresistor is very sensitive to the light, and the luminous flux of LED can be well controlled by the current, therefore we have readings of photoresistance when a

dummy object is approaching the viewport and partly shading the light form the LED. These readings exactly gauge the gap between the viewport glass and the microscope objective (or any opaque objective of the same dimension and shape), hence help us to maneuver the microscope objective during the installation.

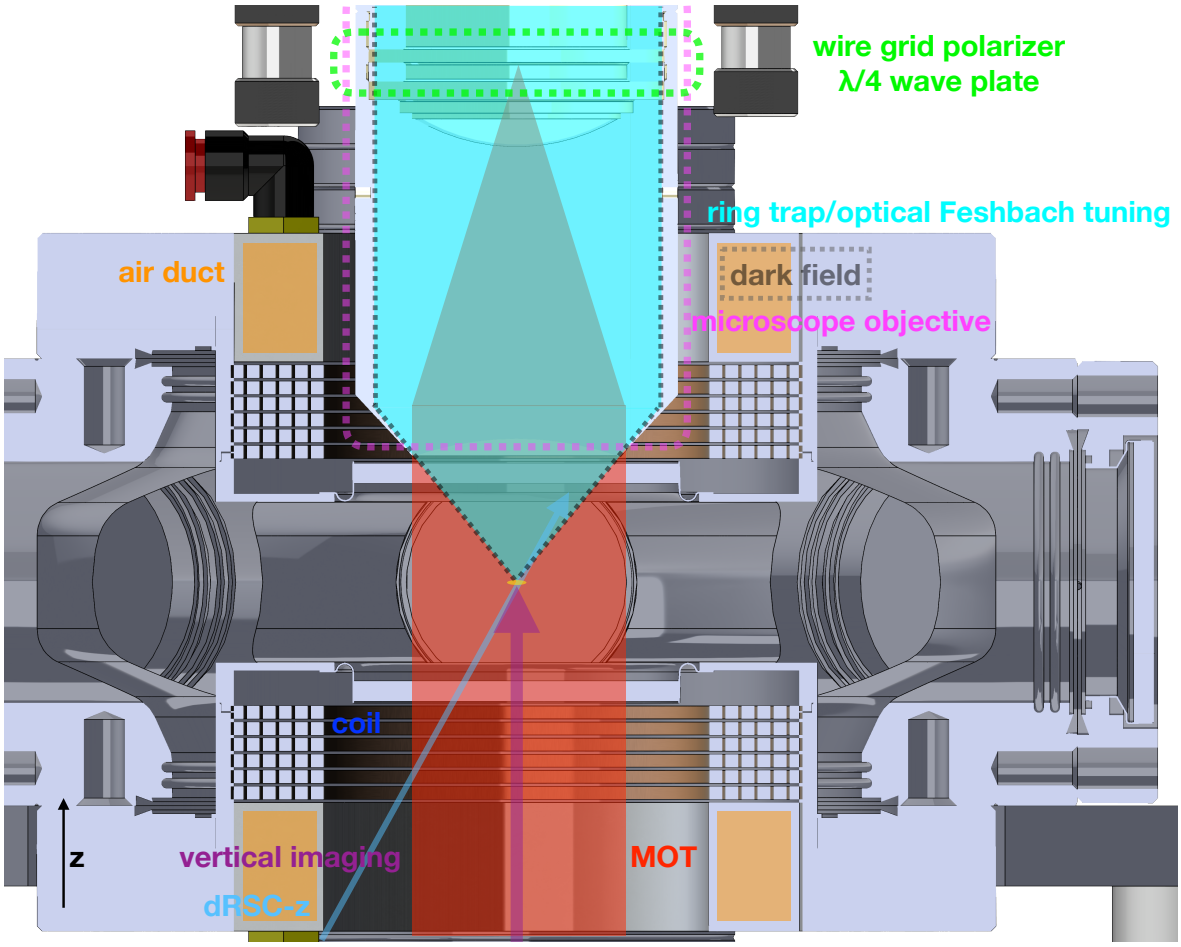

Figure 7.3. The cross-section diagram of the microscope objective, along with the magnetic coil, the air cooling duct, and the main chamber. Different lasers are indicated in different colors.

The heat generated by the magnetic coil often induces tiny air flow around the microscope objective and thermal expansion of every element nearby. To mitigate this problem, liquid cooling methods have been widely used to dissipate the heat. Common liquid cooling involves using either hollow magnetic wires or stacked "Bitter-type" coil [278], [279], whereas the former requires a booster pump to increase the liquid pressure $\gtrsim$ 100 PSI to overcome the

flow friction in the narrow tubing, and the later requires complicated and elaborate work to manufacture the coils. Besides, the vibrations from the circulation of the cooling liquid and the potential leakage due to the aging of the pipeline have been troublesome issues at all times.

In place of liquid cooling, we propose and implement air cooling to stabilize the coil temperature (Fig. 7.3). Cold air is pumped from the air-conditioner in the laboratory to the standard 1/4" air pipes with flow rate 10 L/s. The air pipes connect the duct for heat exchanging, where the magnetic coil is attached via thermal conductive epoxy adhesive. Since the recoil of air flow is extremely small, there is nearly no vibration caused by the air flow even if we increase the flow rate > 10 L/s. Moreover, air cooling is risk-free and worry-free – the disturbance from the leak air is negligible, if there is any, and harmless to optics compared to liquid. In Table 7.1 we list the head-to-head comparison between air and water cooling methods given the same tunnel and material of a cold plate, and show that with reasonable parameters used in most laboratories, the estimated cooling performance of both are within a similar order, hence air cooling is considered as a prominent alternative to liquid methods.

Table 7.1. Heat transfer $\frac{dQ}{dt} = hA\Delta T$, where A is the surface area, ΔT is the temperature difference, $h = \frac{q}{\Delta T}$ is the heat transfer coefficient, $q = -k\nabla T$ is the heat flux, k is the thermal conductivity, and ∇T is the temperature gradient. Flow rates are experimentally measured in conventional labs.

	Air	Water
Thermal conductivity k $(\frac{W}{mK})$	0.026	0.6
Viscosity $(Pa \cdot s)$	$\sim 20\mu$	$\sim 10m$
Flow rate (LPM)	≥ 10	≤ 1
Heat transfer coefficient h $(\frac{W}{m^2K})$	0.043	0.1

7.3 Other upgrades

In addition to the novel designs of the microscope objective and cooling system, our quantum gas machine is capable of high-speed optical control thanks to the digital micromirror device (DMD) and the acousto-optic deflector (AOM). We combine several laser

beams and project them to the atomic samples through the microscope objective. A blue-detuned 780 nm laser controlled by a high-speed DMD (ViALUX DLP7000) is used for horizontal "box" confinement, enabling us to dynamically change the trap geometry. Another blue-detuned 767 nm laser deflected by an AOD is used for stirring and modulating the local atomic density. An arbitrary waveform generator (AWG) is responsible for the radio-frequency (RF) source for the AOD, which allows us to send multi-tone RF and generate multiple deflected beams simultaneously. A tunable 700 – 1030 nm single-frequency Ti:Sapphire laser (Coherent MBR110) controlled by the second DMD (ViALUX DLPV650LNIR) can be conveniently used for multiple purposes from optical Feshbach tuning to photoassociation. The setup of DMDs can be handily converted between image plane and Fourier plane, giving us the flexibility to control them for either optical intensities or phases. A 1064 nm laser derived from a Nd:YAG laser (InnoLight Mephisto MOPA) and a 532 nm laser derived from the other Nd:YAG laser (Lighthouse Photonics Sprout-G) are optionally used for attractive and repulsive potentials, respectively. These laser beams are combined by different dichroic mirrors and sent to the back of the microscope objective. On the other hand, a 852 nm resonant imaging beam illuminates the atomic samples and produces absorption images on a CCD camera (Princeton Instruments PIXIS).

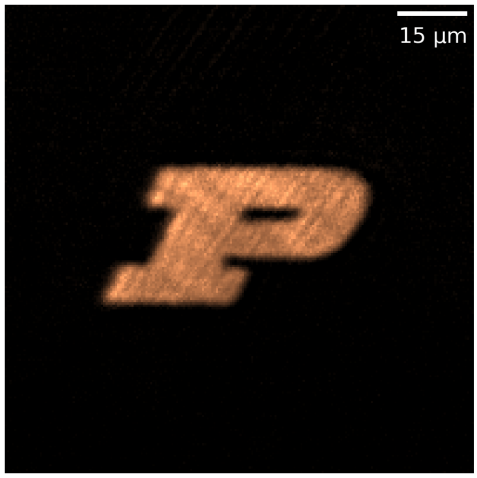

Figure 7.4. A sample of the absorption image shows the *Motion P* logo of *Purdue University*, created by trapping ≈ 50,000 ultracold cesium atoms into a homogeneous and tunable 2D box potential. Average of 5 images.

Our quantum gas machine is versatile for many kinds of outstanding research. The machine is equipped with two-color three-dimensional optical lattices for both attractive and repulsive potentials, and the horizontal lattice constants are 532 nm and 383.5 nm. The incommensurate lattice constants enable us to study eigenstate thermalization hypothesis (ETH) [38], [280], many-body localization [281], [282], quantum transport [283], etc.. In particular, the repulsive optical lattices formed by 767 nm can be spatially shifted by the piezoelectric actuators on the mirror mounts of retro-reflection, this opens up the possibility to modulate the phase of optical lattices thus probing the energy band gap structures of Floquet-Bloch bands [284], [285]. The vertical lattice constants are 3 μm and 4 μm, allowing us to load atoms into one or two 2D layers vertically for 2D gas experiments or atomic mirror experiments [286], [287], respectively. Along with optical intensity feedback, our optical lattice setup is able to explore a broad range of physics such as the phase transition of Mott-insulator and superfluid, as well as quantum entanglement and nonequilibrium dynamics in low-dimensions.

7.4 Conclusion

In this chapter, we have shown that we have designed and built a compact yet multi-functional quantum gas machine suitable for searching and studying new physics. Our machine can produce Bose-Einstein condensate of $\approx 5\times10^4$ cesium atoms every 9 seconds, these ultracold samples (< 10 nK) can be loaded into 2 dimensional box trap potential (Fig. 7.4) or 1D/2D/3D optical lattices immediately without extra transportation needed. Our apparatus can be readily extended to accommodate multiple species, and different probing techniques as well, e.g. fluorescence imaging and phase-contrast imaging. Our design is also unique in a way that it requires less complicated and laborious work to build, but its performance is among the state-of-the-art quantum gas machines in the world. At the time of writing this chapter, there are still many parameters not fully optimized in our experimental procedure concerning the BEC production. We believe that upon careful adjustments, the overall efficiency will be similar to our previous generation of apparatus (with N.A. = 0.37 microscope objective), i.e. production of $\approx 1\times10^5$ Bose-Einstein condensate every 9 seconds. Examples

of the remaining interested parameters are magnetic fields at different laser cooling stages and fine tuning of the laser beam overlaps. In most of our research projects of 2D quantum gases as of now, the demand of more total atom number is not crucial. We also note that the oven source is operated at relatively low temperature (60°C) for cesium, and can replenish the atomic beam and boost the atom number in MOT by increasing the oven temperature to 70°C. In the future, our tasks will be of two primary directions. In the 2D superfluid regime without horizontal optical lattices, we will explore Townes solitons and vortices in 2D gases, interaction quench dynamics, quasiparticle transport and thermodynamics in an acoustic black hole. The dynamic control of trap shape and stir beam could help us to adjust the conditions for formation and evolution of solitons and vortices. On the other hand, with the optical lattices we will study quantum transport and quantum criticality near the superfluid-Mott insulator phase transition, and engineer spatial interaction tuning to investigate more nonequilibrium dynamics.

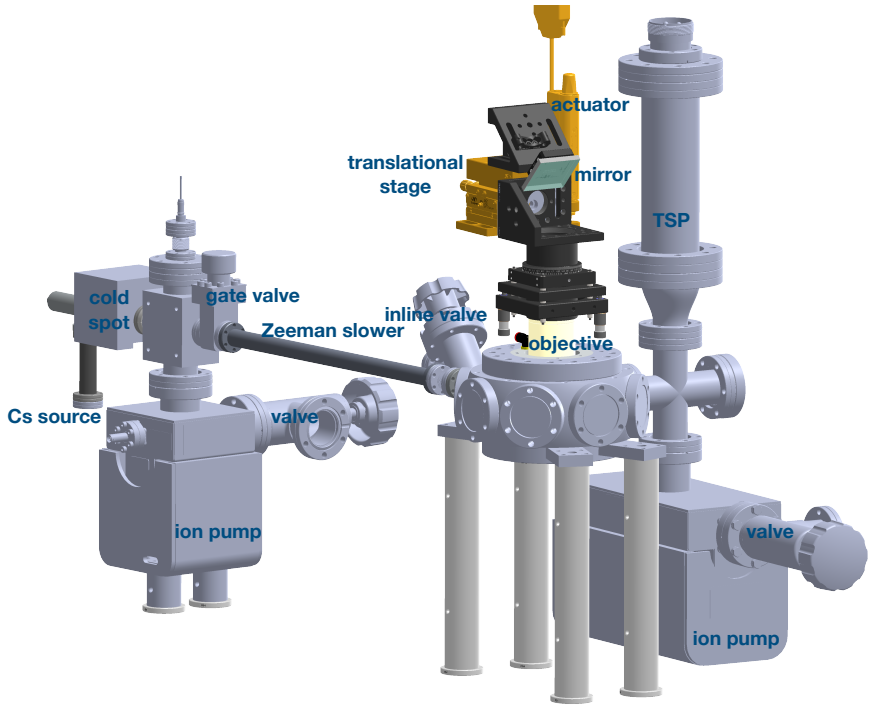

Figure 7.5. CAD drawing of the full chamber. The main coils are recessed in the top and bottom viewports. TSP: titanium sublimation pump.

8. SUMMARY

8.1 Review of past work

We are interested in nonequilibrium transport occurring through a simple interface connecting two separate regions of interaction quenches or in a superfluid under spatially periodic modulation of interaction parameters, as transport often occurs via the evolution of quasiparticles in many-body quantum systems [288]. Quasiparticle transport can account for the propagation of correlation, entropy transport and entanglement distribution within a quantum system. Exploring quasiparticle transport in a quantum gas may provide valuable new insights to quantum material research. With the ability to engineer the Hamiltonian, our state-of-the-art quantum gas machine opens up the possibility of exploring nonequilibrium dynamics in an ultracold atomic system.

Our remarkable results from this novel and versatile machine includes the first experimental realization of 2D matter-wave Townes solitons [200]. The Townes solitons are of unique many-body states, allowing us to readily study quantum coherence such as matter-wave interferometry. We have shown the universality and the scale invariance of Townes solitons, which paves a new way to study out-of-equilibrium quench dynamics [218]. In particular, our quench protocol is valuable and practical for various applications, and can be quickly adopted by numerous quantum gas groups. We have also linked the quasiparticle theory to the attractive interaction, and presented a comprehensive picture of the hyperbolic amplification seeded by quantum and thermal fluctuations. The amplification of quantum fluctuations is especially interesting since it may enable us to generate and detect quantum entanglement via interaction quench.

We have observed the quasiparticle entanglement by employing both our quench protocol and the static structure factor [261]. The static structure factor has been known for decades and extensively used in condensed matter physics, but little is known about its connection with 'homodyne' interferometry and quantum phonons. These critical discoveries provide us with accessible tools to measure entanglement entropy in a many-body system [289], in contrast to probing atom occupation in each lattice site with the quantum gas microscope [290]. In addition, entanglement entropy in superfluids or optical lattices has been found

important to black hole physics and high-energy physics. Such future applications will be depicted in Section 8.2.

At the time of writing this dissertation, we have set up all planned setup. The quantum gas machine has been up and running stably, and continues producing high quality data. We are working toward the superfluid-Mott insulator phase transition in the optical lattices, as well as other dynamics where the ultracold gas is driven out of equilibrium. We are able to address quantum gases by lasers with a broad range of wavelengths and high spatial-temporal resolution, which allows us to control the quantum dynamics via attractive and repulsive potentials, near or close detuning, in spacetime. We are also interested in other outstanding physics topics such as super/subradiance of collective excitations [286], [287], matter-wave solitons, quantum entanglement entropy, vortices in superfluid.

8.2 Outlook and future work

8.2.1 Optical Feshbach tuning

On the purpose of realizing optical Feshbach tuning, a practicable means has been reported with a combination of the Stark light shift and a narrow magnetic Feshbach resonance [124]. We can prepare laser-cooled atoms loaded into a crossed dipole trap, where the atoms will be further cooled by evaporative cooling. After cooling at magnetic field $B = 24$ G for a moment, the magnetic field will jump to near a Feshbach resonance located at 47.8 G, where the evaporative cooling continues at $B = 48$ – 48.1 G, corresponding to s-wave scattering length $a_s = 300 - 400\ a_0$ and facilitate the thermalization to finish the final stage of the evaporative cooling. Once reaching Bose-Einstein condensate, the quantum gas will be loaded into a 2D box trap and illuminated with a designated spatial intensity pattern of a circularly polarized (σ^-) optical Feshbach light at wavelength around 890 nm. This is a 'magic' wavelength, chosen in between cesium D_1 (894 nm) and D_2 lines (852 nm), where the scalar and vector light shifts nearly cancel each other for the ground state atoms $|F = 3, m_F = 3\rangle$, in which we prepare our cesium quantum gases. Optical Feshbach illumination thus imposes either zero or a small chosen total light shift on the ground state atoms. In addition, a non-zero total light shift is felt by the molecular state near the scattering threshold respon-

sible for the magnetic Feshbach resonance at $B = 47.8$ G, thereby inducing the prescribed optical Feshbach tuning and can modify the atomic scattering length instantaneously upon illumination. More discussion about the figure of merit can be found in Appendix D.

8.2.2 Phononic crystal

The ability of aforementioned spatial interaction control will enable us to engineer 'phononic band gap crystals' in a homogeneous superfluid. The produced 2D superfluid can be viewed as a medium governing the speed of sound and serves as a particle reservoir. In superfluid, the speed of sound $c = \sqrt{\frac{ng}{m}}$, where n is the surface density, g is the interaction parameter, and m is the mass of atom. The two-dimensional interaction parameter is a function of s-wave scattering length $g_{2D} = \frac{\sqrt{8\pi}\hbar^2 a_s}{m l_z}$, here a_s is the s-wave scattering length and l_z is the oscillator length in the tight confining direction of quasi-2D regime.

By means of changing interaction spatially, we can vary the sound speed in the superfluid. As a result, the reflection of acoustic waves is analogue to light reflected off an interface, and the region with lower sound speed can serve as a phononic waveguide that confines and guides phonon transport [291]–[293]. A periodic modulation of sound speed in a phononic waveguide can create a phononic crystal, similar to the periodic structure of waveguide of a photonic crystal [294]. Since the phononic crystal is formed by a superfluid at a finite temperature, quantum and thermal phonon fluctuations also populate phonon modes in the phononic crystal, and it is expected that density fluctuations should be suppressed in the band gap region. As we change the interaction parameter and periodicity dynamically, a energy band gap will be opened and fluctuations at the corresponding length scale should either disperse into ambient non-modulated superfluid region or may cease to transport due to zero available density of states, thus the phonon and entropy transport will be studied in such a closed quantum system [288].

8.2.3 Acoustic black hole

The possibility of generating a 'horizon' in generic hydrodynamic systems was first pointed out by Unruh in 1981 as an analogue of black hole event horizon [295], [296]. Take su-

perfluid hydrodynamics for example, when a superfluid is subject to a spatially non-uniform flow speed v_s (or a non-uniform speed of sound c), its flow equation is analogous to the equation of a scalar field in a curved space-time [297]. An 'acoustic horizon' can form when the flow speed crosses over from being subsonic ($|v_s| < c$) to supersonic ($|v_s| > c$) and any sound waves that traverses the horizon ($|v_s| = c$) into the supersonic region cannot escape, thus establishing an acoustic analogue of a black hole horizon [67].

Similarly to Hawking radiation [298], [299], 'acoustic Hawking radiation' happens near an event horizon where an effective large space-time curvature can distort the physical quantum vacuum and scatter virtual phonons from the boundary of the black hole into pairs of radiation modes: those with positive energies can radiate out of the horizon, forming the Hawking radiation. Their negative frequency partners, on the other hand, remain trapped inside the black hole, reducing its energy. Preliminary observation of Hawking radiation was recently reported in an acoustic black hole formed by an one-dimensional Bose-Einstein condensate subject to a 'waterfall' potential [247], [300]. Measurements of Hawking radiation spectrum as well as the entanglement between Hawking phonon pairs can be performed using *in situ* density fluctuation measurements [257].

A quantum critical gas may also possess an acoustic horizon when there is particle flow crossing from the superfluid to the critical region. This horizon can emit Hawking phonons that reflect the surface gravity in the vicinity of the critical region due to the vanishing superfluid order and also the sound speed. The experiment condition corresponds to those of inducing the quantum critical mass transport, where a chemical potential gradient induces global particle flow from the superfluid reservoir into the quantum critical region. While the global mass transport reflects the dc or ac response of a critical gas to the thermodynamic force $\nabla\mu$, we expect that (Hawking) phonon generation near the critical boundary to reflect dynamics of near-equilibrium quantum or, in general, thermal fluctuations subject to a spatial quench from superfluid hydrodynamics into quantum critical hydrodynamic behavior.

With the capability of controlling interaction spatially by laser operated at magic wavelength, we will be able to create an acoustic horizon and observe acoustic Hawking radiation without imposing any light shift, as a result, there is no inducing mass flow. Unlike previous acoustic black hole experiments whose phonon modes are vulnerable to the 'waterfall'

potential [301], the atomic density in our experiment will be homogeneous across the entire 2D quantum gas thanks to the repulsive box potential. Temperature can also be precisely controlled by the trap depth of the box, therefore correlations of quantum fluctuation can be probed unambiguously [302], [303].

REFERENCES

[1] E. Altman, K. R. Brown, G. Carleo, L. D. Carr, E. Demler, C. Chin, B. DeMarco, S. E. Economou, M. A. Eriksson, K.-M. C. Fu, *et al.*, "Quantum simulators: Architectures and opportunities," *PRX Quantum*, vol. 2, no. 1, p. 017 003, 2021.

[2] R. Somma, G. Ortiz, J. E. Gubernatis, E. Knill, and R. Laflamme, "Simulating physical phenomena by quantum networks," *Physical Review A*, vol. 65, no. 4, p. 042 323, 2002.

[3] S. Somaroo, C. Tseng, T. Havel, R. Laflamme, and D. G. Cory, "Quantum simulations on a quantum computer," *Physical Review Letters*, vol. 82, no. 26, p. 5381, 1999.

[4] R. Blatt and C. F. Roos, "Quantum simulations with trapped ions," *Nature Physics*, vol. 8, no. 4, pp. 277–284, 2012.

[5] I. Buluta and F. Nori, "Quantum simulators," *Science*, vol. 326, no. 5949, pp. 108–111, 2009.

[6] C. Tseng, S. Somaroo, Y. Sharf, E. Knill, R. Laflamme, T. F. Havel, and D. G. Cory, "Quantum simulation of a three-body-interaction hamiltonian on an nmr quantum computer," *Physical Review A*, vol. 61, no. 1, p. 012 302, 1999.

[7] K. Kim, M.-S. Chang, S. Korenblit, R. Islam, E. E. Edwards, J. K. Freericks, G.-D. Lin, L.-M. Duan, and C. Monroe, "Quantum simulation of frustrated ising spins with trapped ions," *Nature*, vol. 465, no. 7298, pp. 590–593, 2010.

[8] E. Edwards, S. Korenblit, K. Kim, R. Islam, M.-S. Chang, J. Freericks, G.-D. Lin, L.-M. Duan, and C. Monroe, "Quantum simulation and phase diagram of the transverse-field ising model with three atomic spins," *Physical Review B*, vol. 82, no. 6, p. 060 412, 2010.

[9] R. Gerritsma, B. Lanyon, G. Kirchmair, F. Zähringer, C. Hempel, J. Casanova, J. J. García-Ripoll, E. Solano, R. Blatt, and C. F. Roos, "Quantum simulation of the klein paradox with trapped ions," *Physical Review Letters*, vol. 106, no. 6, p. 060 503, 2011.

[10] J. T. Barreiro, M. Müller, P. Schindler, D. Nigg, T. Monz, M. Chwalla, M. Hennrich, C. F. Roos, P. Zoller, and R. Blatt, "An open-system quantum simulator with trapped ions," *Nature*, vol. 470, no. 7335, pp. 486–491, 2011.

[11] B. P. Lanyon, C. Hempel, D. Nigg, M. Müller, R. Gerritsma, F. Zähringer, P. Schindler, J. T. Barreiro, M. Rambach, G. Kirchmair, *et al.*, "Universal digital quantum simulation with trapped ions," *Science*, vol. 334, no. 6052, pp. 57–61, 2011.

[12] I. Bloch, J. Dalibard, and W. Zwerger, "Many-body physics with ultracold gases," *Reviews of Modern Physics*, vol. 80, no. 3, p. 885, 2008.

[13] P. Schindler, M. Müller, D. Nigg, J. T. Barreiro, E. A. Martinez, M. Hennrich, T. Monz, S. Diehl, P. Zoller, and R. Blatt, "Quantum simulation of dynamical maps with trapped ions," *Nature Physics*, vol. 9, no. 6, pp. 361–367, 2013.

[14] I. Bloch, "Ultracold quantum gases in optical lattices," *Nature Physics*, vol. 1, no. 1, pp. 23–30, 2005.

[15] M. Greiner and S. Fölling, "Optical lattices," *Nature*, vol. 453, no. 7196, pp. 736–738, 2008.

[16] A. D. Greentree, C. Tahan, J. H. Cole, and L. C. Hollenberg, "Quantum phase transitions of light," *Nature Physics*, vol. 2, no. 12, pp. 856–861, 2006.

[17] M. J. Hartmann, F. G. Brandao, and M. B. Plenio, "Strongly interacting polaritons in coupled arrays of cavities," *Nature Physics*, vol. 2, no. 12, pp. 849–855, 2006.

[18] D. G. Angelakis, M. F. Santos, and S. Bose, "Photon-blockade-induced mott transitions and x y spin models in coupled cavity arrays," *Physical Review A*, vol. 76, no. 3, p. 031 805, 2007.

[19] J. Chiaverini and W. Lybarger Jr, "Laserless trapped-ion quantum simulations without spontaneous scattering using microtrap arrays," *Physical Review A*, vol. 77, no. 2, p. 022 324, 2008.

[20] R. J. Clark, T. Lin, K. R. Brown, and I. L. Chuang, "A two-dimensional lattice ion trap for quantum simulation," *Journal of Applied Physics*, vol. 105, no. 1, p. 013 114, 2009.

[21] R. Schmied, J. H. Wesenberg, and D. Leibfried, "Optimal surface-electrode trap lattices for quantum simulation with trapped ions," *Physical Review Letters*, vol. 102, no. 23, p. 233 002, 2009.

[22] A. van Oudenaarden and J. Mooij, "One-dimensional mott insulator formed by quantum vortices in josephson junction arrays," *Physical Review Letters*, vol. 76, no. 26, p. 4947, 1996.

[23] T. Yamamoto, M. Watanabe, J. You, Y. A. Pashkin, O. Astafiev, Y. Nakamura, F. Nori, and J. S. Tsai, "Spectroscopy of superconducting charge qubits coupled by a josephson inductance," *Physical Review B*, vol. 77, no. 6, p. 064 505, 2008.

[24] E. Manousakis, "A quantum-dot array as model for copper-oxide superconductors: A dedicated quantum simulator for the many-fermion problem," *Journal of Low Temperature Physics*, vol. 126, no. 5-6, pp. 1501–1513, 2002.

[25] T. Byrnes, P. Recher, N. Y. Kim, S. Utsunomiya, and Y. Yamamoto, "Quantum simulator for the hubbard model with long-range coulomb interactions using surface acoustic waves," *Physical Review Letters*, vol. 99, no. 1, p. 016 405, 2007.

[26] T. Byrnes, N. Y. Kim, K. Kusudo, and Y. Yamamoto, "Quantum simulation of fermi-hubbard models in semiconductor quantum-dot arrays," *Physical Review B*, vol. 78, no. 7, p. 075 320, 2008.

[27] M. Saffman, T. G. Walker, and K. Mølmer, "Quantum information with rydberg atoms," *Reviews of Modern Physics*, vol. 82, no. 3, p. 2313, 2010.

[28] H. Weimer, M. Müller, I. Lesanovsky, P. Zoller, and H. P. Büchler, "A rydberg quantum simulator," *Nature Physics*, vol. 6, no. 5, pp. 382–388, 2010.

[29] P. Schauß, M. Cheneau, M. Endres, T. Fukuhara, S. Hild, A. Omran, T. Pohl, C. Gross, S. Kuhr, and I. Bloch, "Observation of spatially ordered structures in a two-dimensional rydberg gas," *Nature*, vol. 491, no. 7422, pp. 87–91, 2012.

[30] T. D. Ladd, F. Jelezko, R. Laflamme, Y. Nakamura, C. Monroe, and J. L. O'Brien, "Quantum computers," *Nature*, vol. 464, no. 7285, pp. 45–53, 2010.

[31] I. Buluta, S. Ashhab, and F. Nori, "Natural and artificial atoms for quantum computation," *Reports on Progress in Physics*, vol. 74, no. 10, p. 104 401, 2011.

[32] X. Liu, C. Guo, Y. Liu, Y. Yang, J. Song, J. Gao, Z. Wang, W. Wu, D. Peng, P. Zhao, *et al.*, "Redefining the quantum supremacy baseline with a new generation sunway supercomputer," *arXiv preprint arXiv:2111.01066*, 2021.

[33] F. Arute, K. Arya, R. Babbush, D. Bacon, J. C. Bardin, R. Barends, R. Biswas, S. Boixo, F. G. Brandao, D. A. Buell, *et al.*, "Quantum supremacy using a programmable superconducting processor," *Nature*, vol. 574, no. 7779, pp. 505–510, 2019.

[34] Y. Wu, W.-S. Bao, S. Cao, F. Chen, M.-C. Chen, X. Chen, T.-H. Chung, H. Deng, Y. Du, D. Fan, *et al.*, "Strong quantum computational advantage using a superconducting quantum processor," *Physical Review Letters*, vol. 127, no. 18, p. 180 501, 2021.

[35] I. M. Georgescu, S. Ashhab, and F. Nori, "Quantum simulation," *Reviews of Modern Physics*, vol. 86, no. 1, p. 153, 2014.

[36] S. Chu, "Cold atoms and quantum control," *Nature*, vol. 416, no. 6877, pp. 206–210, 2002.

[37] D. Jaksch and P. Zoller, "The cold atom hubbard toolbox," *Annals of Physics*, vol. 315, no. 1, pp. 52–79, 2005.

[38] C. Gross and I. Bloch, "Quantum simulations with ultracold atoms in optical lattices," *Science*, vol. 357, no. 6355, pp. 995–1001, 2017.

[39] M. Lewenstein, A. Sanpera, V. Ahufinger, B. Damski, A. Sen, and U. Sen, "Ultracold atomic gases in optical lattices: Mimicking condensed matter physics and beyond," *Advances in Physics*, vol. 56, no. 2, pp. 243–379, 2007.

[40] I. Bloch, J. Dalibard, and S. Nascimbene, "Quantum simulations with ultracold quantum gases," *Nature Physics*, vol. 8, no. 4, pp. 267–276, 2012.

[41] L.-M. Duan, E. Demler, and M. D. Lukin, "Controlling spin exchange interactions of ultracold atoms in optical lattices," *Physical Review Letters*, vol. 91, no. 9, p. 090 402, 2003.

[42] H. Bernien, S. Schwartz, A. Keesling, H. Levine, A. Omran, H. Pichler, S. Choi, A. S. Zibrov, M. Endres, M. Greiner, *et al.*, "Probing many-body dynamics on a 51-atom quantum simulator," *Nature*, vol. 551, no. 7682, pp. 579–584, 2017.

[43] A. Polkovnikov, K. Sengupta, A. Silva, and M. Vengalattore, "Colloquium: Nonequilibrium dynamics of closed interacting quantum systems," *Reviews of Modern Physics*, vol. 83, no. 3, p. 863, 2011.

[44] P. A. Lee, N. Nagaosa, and X.-G. Wen, "Doping a mott insulator: Physics of high-temperature superconductivity," *Reviews of Modern Physics*, vol. 78, no. 1, p. 17, 2006.

[45] K. Le Hur and T. M. Rice, "Superconductivity close to the mott state: From condensed-matter systems to superfluidity in optical lattices," *Annals of Physics*, vol. 324, no. 7, pp. 1452–1515, 2009.

[46] D. Jaksch, C. Bruder, J. I. Cirac, C. W. Gardiner, and P. Zoller, "Cold bosonic atoms in optical lattices," *Physical Review Letters*, vol. 81, no. 15, p. 3108, 1998.

[47] S. Sachdev, "Quantum phase transitions," *Handbook of Magnetism and Advanced Magnetic Materials*, 2007.

[48] D. Chang, J. Douglas, A. González-Tudela, C.-L. Hung, and H. Kimble, "Colloquium: Quantum matter built from nanoscopic lattices of atoms and photons," *Reviews of Modern Physics*, vol. 90, no. 3, p. 031 002, 2018.

[49] N. Goldman, J. C. Budich, and P. Zoller, "Topological quantum matter with ultracold gases in optical lattices," *Nature Physics*, vol. 12, no. 7, pp. 639–645, 2016.

[50] C. Honerkamp and W. Hofstetter, "Ultracold fermions and the su (n) hubbard model," *Physical Review Letters*, vol. 92, no. 17, p. 170 403, 2004.

[51] A. Rapp, G. Zaránd, C. Honerkamp, and W. Hofstetter, "Color superfluidity and "baryon" formation in ultracold fermions," *Physical Review Letters*, vol. 98, no. 16, p. 160 405, 2007.

[52] R. P. Feynman, "Simulating physics with computers," *International Journal of Theoretical Physics*, vol. 21, no. 6/7, 1982.

[53] R. P. Feynman, "Quantum mechanical computers," *Optics News*, vol. 11, no. 2, pp. 11–20, 1985.

[54] S. Lloyd, "Universal quantum simulators," *Science*, pp. 1073–1078, 1996.

[55] J. I. Cirac and P. Zoller, "Goals and opportunities in quantum simulation," *Nature Physics*, vol. 8, no. 4, pp. 264–266, 2012.

[56] W. S. Bakr, J. I. Gillen, A. Peng, S. Fölling, and M. Greiner, "A quantum gas microscope for detecting single atoms in a hubbard-regime optical lattice," *Nature*, vol. 462, no. 7269, pp. 74–77, 2009.

[57] H. Feshbach, "Unified theory of nuclear reactions," *Annals of Physics*, vol. 5, no. 4, pp. 357–390, 1958.

[58] U. Fano, "Effects of configuration interaction on intensities and phase shifts," *Physical Review*, vol. 124, no. 6, p. 1866, 1961.

[59] C. Chin, R. Grimm, P. Julienne, and E. Tiesinga, "Feshbach resonances in ultracold gases," *Reviews of Modern Physics*, vol. 82, no. 2, p. 1225, 2010.

[60] D. M. Bauer, M. Lettner, C. Vo, G. Rempe, and S. Dürr, "Control of a magnetic feshbach resonance with laser light," *Nature Physics*, vol. 5, no. 5, pp. 339–342, 2009.

[61] D. M. Bauer, M. Lettner, C. Vo, G. Rempe, and S. Dürr, "Combination of a magnetic feshbach resonance and an optical bound-to-bound transition," *Physical Review A*, vol. 79, no. 6, p. 062 713, 2009.

[62] R. Yamazaki, S. Taie, S. Sugawa, and Y. Takahashi, "Submicron spatial modulation of an interatomic interaction in a bose-einstein condensate," *Physical Review Letters*, vol. 105, no. 5, p. 050 405, 2010.

[63] H. Wu and J. E. Thomas, "Optical control of feshbach resonances in fermi gases using molecular dark states," *Physical Review Letters*, vol. 108, no. 1, p. 010 401, 2012.

[64] N. Arunkumar, A. Jagannathan, and J. Thomas, "Designer spatial control of interactions in ultracold gases," *Physical Review Letters*, vol. 122, no. 4, p. 040 405, 2019.

[65] N. Navon, S. Piatecki, K. Günter, B. Rem, T. C. Nguyen, F. Chevy, W. Krauth, and C. Salomon, "Dynamics and thermodynamics of the low-temperature strongly interacting bose gas," *Physical Review Letters*, vol. 107, no. 13, p. 135 301, 2011.

[66] P. Makotyn, C. E. Klauss, D. L. Goldberger, E. Cornell, and D. S. Jin, "Universal dynamics of a degenerate unitary bose gas," *Nature Physics*, vol. 10, no. 2, pp. 116–119, 2014.

[67] C. Barceló, S. Liberati, and M. Visser, "Analogue gravity," *Living Reviews in Relativity*, vol. 14, no. 1, p. 3, 2011.

[68] L. J. Garay, J. Anglin, J. I. Cirac, and P. Zoller, "Sonic black holes in dilute bose-einstein condensates," *Physical Review A*, vol. 63, no. 2, p. 023 611, 2001.

[69] M. Greiner, O. Mandel, T. Esslinger, T. W. Hänsch, and I. Bloch, "Quantum phase transition from a superfluid to a mott insulator in a gas of ultracold atoms," *Nature*, vol. 415, no. 6867, pp. 39–44, 2002.

[70] P. Coleman and A. J. Schofield, "Quantum criticality," *Nature*, vol. 433, no. 7023, pp. 226–229, 2005.

[71] S. Sachdev and B. Keimer, "Quantum criticality," *arXiv preprint arXiv:1102.4628*, 2011.

[72] D. Bishop and J. Reppy, "Study of the superfluid transition in two-dimensional he 4 films," *Physical Review Letters*, vol. 40, no. 26, p. 1727, 1978.

[73] A. Safonov, S. Vasilyev, I. Yasnikov, I. Lukashevich, and S. Jaakkola, "Observation of quasicondensate in two-dimensional atomic hydrogen," *Physical Review Letters*, vol. 81, no. 21, p. 4545, 1998.

[74] P. Minnhagen, "The two-dimensional coulomb gas, vortex unbinding, and superfluid-superconducting films," *Reviews of Modern Physics*, vol. 59, no. 4, p. 1001, 1987.

[75] A. Posazhennikova, "Colloquium: Weakly interacting, dilute bose gases in 2d," *Reviews of Modern Physics*, vol. 78, no. 4, p. 1111, 2006.

[76] D. Snoke, "Spontaneous bose coherence of excitons and polaritons," *Science*, vol. 298, no. 5597, pp. 1368–1372, 2002.

[77] L. Butov, "Condensation and pattern formation in cold exciton gases in coupled quantum wells," *Journal of Physics: Condensed Matter*, vol. 16, no. 50, R1577, 2004.

[78] J. Kasprzak, M. Richard, S. Kundermann, A. Baas, P. Jeambrun, J. Keeling, F. Marchetti, M. Szymańska, R. André, J. Staehli, *et al.*, "Bose–einstein condensation of exciton polaritons," *Nature*, vol. 443, no. 7110, pp. 409–414, 2006.

[79] A. Amo, J. Lefrère, S. Pigeon, C. Adrados, C. Ciuti, I. Carusotto, R. Houdré, E. Giacobino, and A. Bramati, "Superfluidity of polaritons in semiconductor microcavities," *Nature Physics*, vol. 5, no. 11, pp. 805–810, 2009.

[80] S. Tung, G. Lamporesi, D. Lobser, L. Xia, and E. A. Cornell, "Observation of the presuperfluid regime in a two-dimensional bose gas," *Physical Review Letters*, vol. 105, no. 23, p. 230 408, 2010.

[81] C.-L. Hung, X. Zhang, N. Gemelke, and C. Chin, "Observation of scale invariance and universality in two-dimensional bose gases," *Nature*, vol. 470, no. 7333, pp. 236–239, 2011.

[82] R. Desbuquois, L. Chomaz, T. Yefsah, J. Léonard, J. Beugnon, C. Weitenberg, and J. Dalibard, "Superfluid behaviour of a two-dimensional bose gas," *Nature Physics*, vol. 8, no. 9, pp. 645–648, 2012.

[83] I. B. Spielman, W. D. Phillips, and J. V. Porto, "Mott-insulator transition in a two-dimensional atomic bose gas," *Physical Review Letters*, vol. 98, no. 8, p. 080 404, 2007.

[84] L. Chomaz, L. Corman, T. Bienaimé, R. Desbuquois, C. Weitenberg, S. Nascimbene, J. Beugnon, and J. Dalibard, "Emergence of coherence via transverse condensation in a uniform quasi-two-dimensional bose gas," *Nature Communications*, vol. 6, p. 6162, 2015.

[85] X. Zhang, C.-L. Hung, S.-K. Tung, and C. Chin, "Observation of quantum criticality with ultracold atoms in optical lattices," *Science*, vol. 335, no. 6072, pp. 1070–1072, 2012.

[86] X. Zhang, C.-L. Hung, S.-K. Tung, N. Gemelke, and C. Chin, "Exploring quantum criticality based on ultracold atoms in optical lattices," *New Journal of Physics*, vol. 13, no. 4, p. 045 011, 2011.

[87] R. Ozeri, L. Khaykovich, and N. Davidson, "Long spin relaxation times in a single-beam blue-detuned optical trap," *Physical Review A*, vol. 59, no. 3, R1750, 1999.

[88] J. Ville, T. Bienaimé, R. Saint-Jalm, L. Corman, M. Aidelsburger, L. Chomaz, K. Kleinlein, D. Perconte, S. Nascimbène, J. Dalibard, *et al.*, "Loading and compression of a single two-dimensional bose gas in an optical accordion," *Physical Review A*, vol. 95, no. 1, p. 013 632, 2017.

[89] K. Hueck, N. Luick, L. Sobirey, J. Siegl, T. Lompe, and H. Moritz, "Two-dimensional homogeneous fermi gases," *Physical Review Letters*, vol. 120, no. 6, p. 060 402, 2018.

[90] W. Ketterle, D. S. Durfee, and D. Stamper-Kurn, "Making, probing and understanding bose-einstein condensates," *arXiv preprint cond-mat/9904034*, 1999.

[91] H. J. Lewandowski, D. Harber, D. L. Whitaker, and E. A. Cornell, "Simplified system for creating a bose–einstein condensate," *Journal of Low Temperature Physics*, vol. 132, no. 5-6, pp. 309–367, 2003.

[92] T.-L. Ho and Q. Zhou, "Obtaining the phase diagram and thermodynamic quantities of bulk systems from the densities of trapped gases," *Nature Physics*, vol. 6, no. 2, pp. 131–134, 2010.

[93] S. Nascimbène, N. Navon, K. Jiang, F. Chevy, and C. Salomon, "Exploring the thermodynamics of a universal fermi gas," *Nature*, vol. 463, no. 7284, pp. 1057–1060, 2010.

[94] N. Navon, S. Nascimbene, F. Chevy, and C. Salomon, "The equation of state of a low-temperature fermi gas with tunable interactions," *Science*, vol. 328, no. 5979, pp. 729–732, 2010.

[95] V. N. Popov, "On the theory of the superfluidity of two-and one-dimensional bose systems," *Teoreticheskaya i Matematicheskaya Fizika*, vol. 11, no. 3, pp. 354–365, 1972.

[96] D. S. Fisher and P. Hohenberg, "Dilute bose gas in two dimensions," *Physical Review B*, vol. 37, no. 10, p. 4936, 1988.

[97] N. Prokof'ev, O. Ruebenacker, and B. Svistunov, "Critical point of a weakly interacting two-dimensional bose gas," *Physical Review Letters*, vol. 87, no. 27, p. 270 402, 2001.

[98] N. Prokof'ev and B. Svistunov, "Two-dimensional weakly interacting bose gas in the fluctuation region," *Physical Review A*, vol. 66, no. 4, p. 043 608, 2002.

[99] Z. Hadzibabic, P. Krüger, M. Cheneau, S. P. Rath, and J. Dalibard, "The trapped two-dimensional bose gas: From bose–einstein condensation to berezinskii–kosterlitz–thouless physics," *New Journal of Physics*, vol. 10, no. 4, p. 045 006, 2008.

[100] S. P. Rath, T. Yefsah, K. J. Günter, M. Cheneau, R. Desbuquois, M. Holzmann, W. Krauth, and J. Dalibard, "Equilibrium state of a trapped two-dimensional bose gas," *Physical Review A*, vol. 82, no. 1, p. 013 609, 2010.

[101] T. Yefsah, R. Desbuquois, L. Chomaz, K. J. Günter, and J. Dalibard, "Exploring the thermodynamics of a two-dimensional Bose gas," *Physical Review Letters*, vol. 107, no. 13, p. 130 401, 2011.

[102] S. Bose, "Thermal equilibrium of the radiation ŕeld in the presence of matter," *Z. Phys*, vol. 26, no. 1, 1924.

[103] D. Petrov, M. Holzmann, and G. Shlyapnikov, "Bose-einstein condensation in quasi-2d trapped gases," *Physical Review Letters*, vol. 84, no. 12, p. 2551, 2000.

[104] V. Berezinsky, "Destruction of long-range order in one-dimensional and two-dimensional systems possessing a continuous symmetry group. ii. quantum systems.," *Zh. Eksp. Teor. Fiz.*, vol. 61, p. 610, 1972.

[105] J. M. Kosterlitz and D. J. Thouless, "Ordering, metastability and phase transitions in two-dimensional systems," *Journal of Physics C: Solid State Physics*, vol. 6, no. 7, p. 1181, 1973.

[106] C. J. Pethick and H. Smith, *Bose–Einstein condensation in dilute gases*. Cambridge university press, 2008.

[107] Z. Hadzibabic, P. Krüger, M. Cheneau, B. Battelier, and J. Dalibard, "Berezinskii–kosterlitz–thouless crossover in a trapped atomic gas," *Nature*, vol. 441, no. 7097, pp. 1118–1121, 2006.

[108] Z. Hadzibabic and J. Dalibard, "Two-dimensional bose fluids: An atomic physics perspective," *La Rivista del Nuovo Cimento*, vol. 34, no. 6, pp. 389–434, 2011.

[109] D. R. Nelson and J. Kosterlitz, "Universal jump in the superfluid density of two-dimensional superfluids," *Physical Review Letters*, vol. 39, no. 19, p. 1201, 1977.

[110] J. J. Sakurai and E. D. Commins, *Modern Quantum Mechanics (Revised Edition)*, 1995.

[111] P. S. Julienne and F. H. Mies, "Collisions of ultracold trapped atoms," *JOSA B*, vol. 6, no. 11, pp. 2257–2269, 1989.

[112] G. Gribakin and V. Flambaum, "Calculation of the scattering length in atomic collisions using the semiclassical approximation," *Physical Review A*, vol. 48, no. 1, p. 546, 1993.

[113] K. M. Jones, E. Tiesinga, P. D. Lett, and P. S. Julienne, "Ultracold photoassociation spectroscopy: Long-range molecules and atomic scattering," *Reviews of Modern Physics*, vol. 78, no. 2, p. 483, 2006.

[114] Y. Ding, "Radio-frequency-controlled cold collisions and universal properties of unitary bose gases," Ph.D. dissertation, Purdue University, 2017.

[115] D. Blume and C. H. Greene, "Fermi pseudopotential approximation: Two particles under external confinement," *Physical Review A*, vol. 65, no. 4, p. 043 613, 2002.

[116] C. Chin, V. Vuletić, A. J. Kerman, and S. Chu, "High resolution feshbach spectroscopy of cesium," *Physical Review Letters*, vol. 85, no. 13, p. 2717, 2000.

[117] C. Chin, V. Vuletić, A. J. Kerman, S. Chu, E. Tiesinga, P. J. Leo, and C. J. Williams, "Precision feshbach spectroscopy of ultracold cs 2," *Physical Review A*, vol. 70, no. 3, p. 032 701, 2004.

[118] M. Theis, G. Thalhammer, K. Winkler, M. Hellwig, G. Ruff, R. Grimm, and J. H. Denschlag, "Tuning the scattering length with an optically induced feshbach resonance," *Physical Review Letters*, vol. 93, no. 12, p. 123 001, 2004.

[119] F. Fatemi, K. Jones, and P. D. Lett, "Observation of optically induced feshbach resonances in collisions of cold atoms," *Physical Review Letters*, vol. 85, no. 21, p. 4462, 2000.

[120] P. Fedichev, Y. Kagan, G. Shlyapnikov, and J. Walraven, "Influence of nearly resonant light on the scattering length in low-temperature atomic gases," *Physical Review Letters*, vol. 77, no. 14, p. 2913, 1996.

[121] K. Enomoto, K. Kasa, M. Kitagawa, and Y. Takahashi, "Optical feshbach resonance using the intercombination transition," *Physical Review Letters*, vol. 101, no. 20, p. 203 201, 2008.

[122] O. Thomas, C. Lippe, T. Eichert, and H. Ott, "Experimental realization of a rydberg optical feshbach resonance in a quantum many-body system," *Nature Communications*, vol. 9, no. 1, pp. 1–6, 2018.

[123] A. Jagannathan, N. Arunkumar, J. Joseph, and J. Thomas, "Optical control of magnetic feshbach resonances by closed-channel electromagnetically induced transparency," *Physical Review Letters*, vol. 116, no. 7, p. 075 301, 2016.

[124] L. W. Clark, L.-C. Ha, C.-Y. Xu, and C. Chin, "Quantum dynamics with spatiotemporal control of interactions in a stable bose-einstein condensate," *Physical Review Letters*, vol. 115, no. 15, p. 155 301, 2015.

[125] N. Bogoliubov, "On the theory of superfluidity," *J. Phys*, vol. 11, no. 1, p. 23, 1947.

[126] R. Dodd, C. W. Clark, M. Edwards, and K. Burnett, "Characterizing the coherence of bose-einstein condensates and atom lasers," *Optics Express*, vol. 1, no. 10, pp. 284–292, 1997.

[127] S. Giorgini, L. Pitaevskii, and S. Stringari, "Anomalous fluctuations of the condensate in interacting bose gases," *Physical Review Letters*, vol. 80, no. 23, p. 5040, 1998.

[128] M. Naraschewski and R. Glauber, "Spatial coherence and density correlations of trapped bose gases," *Physical Review A*, vol. 59, no. 6, p. 4595, 1999.

[129] R. P. Feynman, "Atomic theory of the two-fluid model of liquid helium," *Physical Review*, vol. 94, no. 2, p. 262, 1954.

[130] L. Van Hove, "Correlations in space and time and born approximation scattering in systems of interacting particles," *Physical Review*, vol. 95, no. 1, p. 249, 1954.

[131] R. Feynman and M. Cohen, "Energy spectrum of the excitations in liquid helium," *Physical Review*, vol. 102, no. 5, p. 1189, 1956.

[132] J. Javanainen, "Spectrum of light scattered from a degenerate bose gas," *Physical Review Letters*, vol. 75, no. 10, p. 1927, 1995.

[133] F. Zambelli, L. Pitaevskii, D. Stamper-Kurn, and S. Stringari, "Dynamic structure factor and momentum distribution of a trapped bose gas," *Physical Review A*, vol. 61, no. 6, p. 063 608, 2000.

[134] R. Landig, F. Brennecke, R. Mottl, T. Donner, and T. Esslinger, "Measuring the dynamic structure factor of a quantum gas undergoing a structural phase transition," *Nature Communications*, vol. 6, no. 1, pp. 1–6, 2015.

[135] C. Bradley, J. Chen, and R. G. Hulet, "Instrumentation for the stable operation of laser diodes," *Review of Scientific Instruments*, vol. 61, no. 8, pp. 2097–2101, 1990.

[136] K. Libbrecht and J. L. Hall, "A low-noise high-speed diode laser current controller," *Review of Scientific Instruments*, vol. 64, no. 8, pp. 2133–2135, 1993.

[137] C. J. Erickson, M. Van Zijll, G. Doermann, and D. S. Durfee, "An ultrahigh stability, low-noise laser current driver with digital control," *Review of Scientific Instruments*, vol. 79, no. 7, p. 073 107, 2008.

[138] D. L. Troxel, C. J. Erickson, and D. S. Durfee, "Note: Updates to an ultra-low noise laser current driver," *Review of Scientific Instruments*, vol. 82, no. 9, p. 096 101, 2011.

[139] K. Libbrecht and A. Libbrecht, "A versatile thermoelectric temperature controller with 10 mk reproducibility and 100 mk absolute accuracy," *Review of Scientific Instruments*, vol. 80, no. 12, p. 126 107, 2009.

[140] D. A. Steck, *Cesium D line data*, 2003.

[141] D. McCarron, S. King, and S. Cornish, "Modulation transfer spectroscopy in atomic rubidium," *Measurement Science and Technology*, vol. 19, no. 10, p. 105 601, 2008.

[142] A. Kobyakov, M. Sauer, and D. Chowdhury, "Stimulated brillouin scattering in optical fibers," *Advances in Optics and Photonics*, vol. 2, no. 1, pp. 1–59, 2010.

[143] Circuit-fantasist, *Howland current source (an implementation)*, Feb. 2009. [Online]. Available: https://commons.wikimedia.org/wiki/File:Howland_current_source_1000.jpg.

[144] A. Keshet and W. Ketterle, "A distributed, graphical user interface based, computer control system for atomic physics experiments," *Review of Scientific Instruments*, vol. 84, no. 1, p. 015 105, 2013.

[145] P. T. Starkey, C. J. Billington, S. P. Johnstone, M. Jasperse, K. Helmerson, L. D. Turner, and R. P. Anderson, "A scripted control system for autonomous hardware-timed experiments," *Review of Scientific Instruments*, vol. 84, no. 8, p. 085 111, 2013.

[146] Z. Smith, C. Herold, jqi-sr-lab, J. Tiamsuphat, breschovsky, RbDisorderLab, and N. Pisenti, *Jqiamo/setlist*, version v2.0.1, Jul. 2019. DOI: 10.5281/zenodo.3344809. [Online]. Available: https://doi.org/10.5281/zenodo.3344809.

[147] S. F. Owen and D. S. Hall, "Fast line-based experiment timing system for labview," *Review of Scientific Instruments*, vol. 75, no. 1, pp. 259–265, 2004.

[148] S. Bourdeauducq, R. Jördens, P. Zotov, J. Britton, D. Slichter, D. Leibrandt, D. Allcock, A. Hankin, F. Kermarrec, Y. Sionneau, R. Srinivas, T. R. Tan, and J. Bohnet, *Artiq 1.0*, version 1.0, May 2016. DOI: 10.5281/zenodo.51303. [Online]. Available: https://doi.org/10.5281/zenodo.51303.

[149] *A laboratory control system for cold atom experiments*. [Online]. Available: http://strontiumbec.com/?http://www.strontiumbec.com/Control/Control.html.

[150] H. J. Metcalf and P. Van der Straten, "Laser cooling and trapping of neutral atoms," *The Optics Encyclopedia: Basic Foundations and Practical Applications*, 2007.

[151] D. J. Wineland and W. M. Itano, "Laser cooling of atoms," *Physical Review A*, vol. 20, no. 4, p. 1521, 1979.

[152] W. D. Phillips, "Nobel lecture: Laser cooling and trapping of neutral atoms," *Reviews of Modern Physics*, vol. 70, no. 3, p. 721, 1998.

[153] F. Schreck and K. v. Druten, "Laser cooling for quantum gases," *Nature Physics*, pp. 1–9, 2021.

[154] W. D. Phillips, J. V. Prodan, and H. J. Metcalf, "Laser cooling and electromagnetic trapping of neutral atoms," *JOSA B*, vol. 2, no. 11, pp. 1751–1767, 1985.

[155] S. Bell, M. Junker, M. Jasperse, L. Turner, Y.-J. Lin, I. Spielman, and R. E. Scholten, "A slow atom source using a collimated effusive oven and a single-layer variable pitch coil zeeman slower," *Review of Scientific Instruments*, vol. 81, no. 1, p. 013 105, 2010.

[156] C. Slowe, L. Vernac, and L. V. Hau, "High flux source of cold rubidium atoms," *Review of Scientific Instruments*, vol. 76, no. 10, p. 103 101, 2005.

[157] E. Raab, M. Prentiss, A. Cable, S. Chu, and D. E. Pritchard, "Trapping of neutral sodium atoms with radiation pressure," *Physical Review Letters*, vol. 59, no. 23, p. 2631, 1987.

[158] P. D. Lett, R. N. Watts, C. I. Westbrook, W. D. Phillips, P. L. Gould, and H. J. Metcalf, "Observation of atoms laser cooled below the doppler limit," *Physical Review Letters*, vol. 61, no. 2, p. 169, 1988.

[159] J. Dalibard and C. Cohen-Tannoudji, "Laser cooling below the doppler limit by polarization gradients: Simple theoretical models," *JOSA B*, vol. 6, no. 11, pp. 2023–2045, 1989.

[160] V. Vuletić, C. Chin, A. J. Kerman, and S. Chu, "Degenerate raman sideband cooling of trapped cesium atoms at very high atomic densities," *Physical Review Letters*, vol. 81, no. 26, p. 5768, 1998.

[161] A. J. Kerman, V. Vuletić, C. Chin, and S. Chu, "Beyond optical molasses: 3d raman sideband cooling of atomic cesium to high phase-space density," *Physical Review Letters*, vol. 84, no. 3, p. 439, 2000.

[162] D.-J. Han, S. Wolf, S. Oliver, C. McCormick, M. T. DePue, and D. S. Weiss, "3d raman sideband cooling of cesium atoms at high density," *Physical Review Letters*, vol. 85, no. 4, p. 724, 2000.

[163] G. Di Domenico, N. Castagna, G. Mileti, P. Thomann, A. Taichenachev, and V. Yudin, "Laser collimation of a continuous beam of cold atoms using zeeman-shift degenerate-raman-sideband cooling," *Physical Review A*, vol. 69, no. 6, p. 063 403, 2004.

[164] J. Hu, A. Urvoy, Z. Vendeiro, V. Crépel, W. Chen, and V. Vuletić, "Creation of a bose-condensed gas of 87rb by laser cooling," *Science*, vol. 358, no. 6366, pp. 1078–1080, 2017.

[165] A. Urvoy, Z. Vendeiro, J. Ramette, A. Adiyatullin, and V. Vuletić, "Direct laser cooling to bose-einstein condensation in a dipole trap," *Physical Review Letters*, vol. 122, no. 20, p. 203 202, 2019.

[166] P. Solano, Y. Duan, Y.-T. Chen, A. Rudelis, C. Chin, and V. Vuletić, "Strongly correlated quantum gas prepared by direct laser cooling," *Physical Review Letters*, vol. 123, no. 17, p. 173 401, 2019.

[167] S. Stellmer, B. Pasquiou, R. Grimm, and F. Schreck, "Laser cooling to quantum degeneracy," *Physical Review Letters*, vol. 110, no. 26, p. 263 003, 2013.

[168] C.-L. Hung, X. Zhang, N. Gemelke, and C. Chin, "Accelerating evaporative cooling of atoms into bose-einstein condensation in optical traps," *Physical Review A*, vol. 78, no. 1, p. 011 604, 2008.

[169] T. Kraemer, M. Mark, P. Waldburger, J. G. Danzl, C. Chin, B. Engeser, A. D. Lange, K. Pilch, A. Jaakkola, H.-C. Nägerl, *et al.*, "Evidence for efimov quantum states in an ultracold gas of caesium atoms," *Nature*, vol. 440, no. 7082, p. 315, 2006.

[170] J. Allen, "Application of patterned illumination using a dmd for optogenetic control of signaling," *Nature Methods*, vol. 14, no. 11, pp. 1114–1114, 2017.

[171] P. A. Robinson, "Nonlinear wave collapse and strong turbulence," *Reviews of Modern Physics*, vol. 69, pp. 507–574, 2 Apr. 1997.

[172] E. A. Donley, N. R. Claussen, S. L. Cornish, J. L. Roberts, E. A. Cornell, and C. E. Wieman, "Dynamics of collapsing and exploding bose–einstein condensates," *Nature*, vol. 412, no. 6844, p. 295, 2001.

[173] K. Moll, A. L. Gaeta, and G. Fibich, "Self-similar optical wave collapse: Observation of the townes profile," *Physical Review Letters*, vol. 90, no. 20, p. 203 902, 2003.

[174] N. J. Zabusky and M. D. Kruskal, "Interaction of solitons in a collisionless plasma and the recurrence of initial states," *Physical Review Letters*, vol. 15, no. 6, p. 240, 1965.

[175] A. Shabat and V. Zakharov, "Exact theory of two-dimensional self-focusing and one-dimensional self-modulation of waves in nonlinear media," *Soviet Physics JETP*, vol. 34, no. 1, p. 62, 1972.

[176] R. Y. Chiao, E. Garmire, and C. H. Townes, "Self-trapping of optical beams," *Physical Review Letters*, vol. 13, no. 15, p. 479, 1964.

[177] C.-L. Hung, X. Zhang, N. Gemelke, and C. Chin, "Observation of scale invariance and universality in two-dimensional bose gases," *Nature*, vol. 470, no. 7333, pp. 236–239, Feb. 2011.

[178] Y. V. Kartashov, B. A. Malomed, and L. Torner, "Solitons in nonlinear lattices," *Reviews of Modern Physics*, vol. 83, no. 1, p. 247, 2011.

[179] B. A. Malomed, "Multidimensional solitons: Well-established results and novel findings," *The European Physical Journal Special Topics*, vol. 225, no. 13-14, pp. 2507–2532, 2016.

[180] J. W. Fleischer, M. Segev, N. K. Efremidis, and D. N. Christodoulides, "Observation of two-dimensional discrete solitons in optically induced nonlinear photonic lattices," *Nature*, vol. 422, no. 6928, p. 147, 2003.

[181] S. L. Cornish, S. T. Thompson, and C. E. Wieman, "Formation of bright matter-wave solitons during the collapse of attractive bose-einstein condensates," *Physical Review Letters*, vol. 96, p. 170 401, 17 May 2006.

[182] Y. V. Kartashov, G. E. Astrakharchik, B. A. Malomed, and L. Torner, "Frontiers in multidimensional self-trapping of nonlinear fields and matter," *Nature Reviews Physics*, p. 1, 2019.

[183] Z. Chen, M. Segev, and D. N. Christodoulides, "Optical spatial solitons: Historical overview and recent advances," *Reports on Progress in Physics*, vol. 75, no. 8, p. 086 401, 2012.

[184] V. E. Zakharov and L. Ostrovsky, "Modulation instability: The beginning," *Physica D: Nonlinear Phenomena*, vol. 238, no. 5, pp. 540–548, 2009.

[185] J. H. Nguyen, D. Luo, and R. G. Hulet, "Formation of matter-wave soliton trains by modulational instability," *Science*, vol. 356, no. 6336, pp. 422–426, 2017.

[186] P. Everitt, M. Sooriyabandara, M. Guasoni, P. Wigley, C. Wei, G. McDonald, K. Hardman, P. Manju, J. Close, C. Kuhn, *et al.*, "Observation of a modulational instability in bose-einstein condensates," *Physical Review A*, vol. 96, no. 4, p. 041 601, 2017.

[187] K. Tai, A. Hasegawa, and A. Tomita, "Observation of modulational instability in optical fibers," *Physical Review Letters*, vol. 56, no. 2, p. 135, 1986.

[188] D. Solli, G. Herink, B. Jalali, and C. Ropers, "Fluctuations and correlations in modulation instability," *Nature Photonics*, vol. 6, no. 7, p. 463, 2012.

[189] J. M. Dudley, F. Dias, M. Erkintalo, and G. Genty, "Instabilities, breathers and rogue waves in optics," *Nature Photonics*, vol. 8, no. 10, p. 755, 2014.

[190] K. E. Strecker, G. B. Partridge, A. G. Truscott, and R. G. Hulet, "Formation and propagation of matter-wave soliton trains," *Nature*, vol. 417, no. 6885, p. 150, 2002.

[191] L. Khaykovich, F. Schreck, G. Ferrari, T. Bourdel, J. Cubizolles, L. D. Carr, Y. Castin, and C. Salomon, "Formation of a matter-wave bright soliton," *Science*, vol. 296, no. 5571, pp. 1290–1293, 2002.

[192] V. V. Konotop and M. Salerno, "Modulational instability in bose-einstein condensates in optical lattices," *Physical Review A*, vol. 65, p. 021 602, 2 Jan. 2002.

[193] I. Carusotto, D. Embriaco, and G. C. La Rocca, "Nonlinear atom optics and bright-gap-soliton generation in finite optical lattices," *Physical Review A*, vol. 65, no. 5, p. 053 611, 2002.

[194] O. Morsch and M. Oberthaler, "Dynamics of bose-einstein condensates in optical lattices," *Reviews of Modern Physics*, vol. 78, pp. 179–215, 1 Feb. 2006.

[195] A. V. Mamaev, M. Saffman, D. Z. Anderson, and A. A. Zozulya, "Propagation of light beams in anisotropic nonlinear media: From symmetry breaking to spatial turbulence," *Physical Review A*, vol. 54, pp. 870–879, 1 Jul. 1996.

[196] Y. S. Kivshar and D. E. Pelinovsky, "Self-focusing and transverse instabilities of solitary waves," *Physics Reports*, vol. 331, no. 4, pp. 117–195, 2000.

[197] L. Salasnich, A. Parola, and L. Reatto, "Modulational instability and complex dynamics of confined matter-wave solitons," *Physical Review Letters*, vol. 91, p. 080 405, 8 Aug. 2003.

[198] L. D. Carr and J. Brand, "Spontaneous soliton formation and modulational instability in bose-einstein condensates," *Physical Review Letters*, vol. 92, p. 040 401, 4 Jan. 2004.

[199] A. H. Guth, M. P. Hertzberg, and C. Prescod-Weinstein, "Do dark matter axions form a condensate with long-range correlation?" *Physical Review D*, vol. 92, no. 10, p. 103 513, 2015.

[200] C.-A. Chen and C.-L. Hung, "Observation of universal quench dynamics and townes soliton formation from modulational instability in two-dimensional bose gases," *Physical Review Letters*, vol. 125, p. 250 401, 25 Dec. 2020.

[201] P. Pedri and L. Santos, "Two-dimensional bright solitons in dipolar bose-einstein condensates," *Physical Review Letters*, vol. 95, no. 20, p. 200 404, 2005.

[202] C.-L. Hung, V. Gurarie, and C. Chin, "From cosmology to cold atoms: Observation of sakharov oscillations in a quenched atomic superfluid," *Science*, vol. 341, no. 6151, pp. 1213–1215, 2013.

[203] J. H. Nguyen, P. Dyke, D. Luo, B. A. Malomed, and R. G. Hulet, "Collisions of matter-wave solitons," *Nature Physics*, vol. 10, no. 12, p. 918, 2014.

[204] H. Saito and M. Ueda, "Dynamically stabilized bright solitons in a two-dimensional bose-einstein condensate," *Physical Review Letters*, vol. 90, p. 040 403, 4 Jan. 2003.

[205] N. K. Efremidis, J. Hudock, D. N. Christodoulides, J. W. Fleischer, O. Cohen, and M. Segev, "Two-dimensional optical lattice solitons," *Physical Review Letters*, vol. 91, p. 213 906, 21 Nov. 2003.

[206] B. B. Baizakov, B. A. Malomed, and M. Salerno, "Multidimensional solitons in a low-dimensional periodic potential," *Physical Review A*, vol. 70, p. 053 613, 5 Nov. 2004.

[207] A. D. Cronin, J. Schmiedmayer, and D. E. Pritchard, "Optics and interferometry with atoms and molecules," *Reviews of Modern Physics*, vol. 81, no. 3, p. 1051, 2009.

[208] B. Lücke, M. Scherer, J. Kruse, L. Pezzé, F. Deuretzbacher, P. Hyllus, J. Peise, W. Ertmer, J. Arlt, L. Santos, *et al.*, "Twin matter waves for interferometry beyond the classical limit," *Science*, vol. 334, no. 6057, pp. 773–776, 2011.

[209] K. Lange, J. Peise, B. Lücke, I. Kruse, G. Vitagliano, I. Apellaniz, M. Kleinmann, G. Tóth, and C. Klempt, "Entanglement between two spatially separated atomic modes," *Science*, vol. 360, no. 6387, pp. 416–418, 2018.

[210] P. Kunkel, M. Prüfer, H. Strobel, D. Linnemann, A. Frölian, T. Gasenzer, M. Gärttner, and M. K. Oberthaler, "Spatially distributed multipartite entanglement enables epr steering of atomic clouds," *Science*, vol. 360, no. 6387, pp. 413–416, 2018.

[211] M. Fadel, T. Zibold, B. Décamps, and P. Treutlein, "Spatial entanglement patterns and einstein-podolsky-rosen steering in bose-einstein condensates," *Science*, vol. 360, no. 6387, pp. 409–413, 2018.

[212] D. Shin, B. Henson, S. Hodgman, T. Wasak, J. Chwedeńczuk, and A. Truscott, "Bell correlations between spatially separated pairs of atoms," *Nature Communications*, vol. 10, no. 1, pp. 1–7, 2019.

[213] L. Pitaevskii and A. Rosch, "Breathing modes and hidden symmetry of trapped atoms in two dimensions," *Physical Review A*, vol. 55, no. 2, R853, 1997.

[214] A. Rançon and N. Dupuis, "Universal thermodynamics of a two-dimensional Bose gas," *Physical Review A*, vol. 85, no. 6, p. 063 607, 2012.

[215] L.-C. Ha, C.-L. Hung, X. Zhang, U. Eismann, S.-K. Tung, and C. Chin, "Strongly interacting two-dimensional bose gases," *Physical Review Letters*, vol. 110, no. 14, p. 145 302, 2013.

[216] R. Desbuquois, T. Yefsah, L. Chomaz, C. Weitenberg, L. Corman, S. Nascimbène, and J. Dalibard, "Determination of scale-invariant equations of state without fitting parameters: Application to the two-dimensional Bose gas across the Berezinskii-Kosterlitz-Thouless transition," *Physical Review Letters*, vol. 113, no. 2, p. 020 404, 2014.

[217] Y. Kagan, A. E. Muryshev, and G. V. Shlyapnikov, "Collapse and bose-einstein condensation in a trapped bose gas with negative scattering length," *Physical Review Letters*, vol. 81, pp. 933–937, 5 Aug. 1998.

[218] C.-A. Chen and C.-L. Hung, "Observation of scale invariance in two-dimensional matter-wave townes solitons," *Physical Review Letters*, vol. 127, p. 023 604, 2 Jul. 2021.

[219] Y. Zou, E. Le Cerf, B. Bakkali-Hassani, C. Maury, G. Chauveau, P. C. M. Castilho, R. Saint-Jalm, S. Nascimbene, J. Dalibard, and J. Beugnon, "Optical control of the density and spin spatial profiles of a planar Bose gas," *Journal of Physics B: Atomic, Molecular and Optical Physics*, 2021.

[220] B. Bakkali-Hassani, C. Maury, Y.-Q. Zou, É. Le Cerf, R. Saint-Jalm, P. C. M. Castilho, S. Nascimbene, J. Dalibard, and J. Beugnon, "Realization of a townes soliton in a two-component planar bose gas," *Physical Review Letters*, vol. 127, p. 023 603, 2 Jul. 2021.

[221] C.-L. Hung, X. Zhang, L.-C. Ha, S.-K. Tung, N. Gemelke, and C. Chin, "Extracting density–density correlations from in situ images of atomic quantum gases," *New Journal of Physics*, vol. 13, no. 7, p. 075 019, 2011.

[222] S. Giovanazzi, A. Görlitz, and T. Pfau, "Tuning the dipolar interaction in quantum gases," *Physical Review Letters*, vol. 89, no. 13, p. 130 401, 2002.

[223] T. Lahaye, C. Menotti, L. Santos, M. Lewenstein, and T. Pfau, "The physics of dipolar bosonic quantum gases," *Reports on Progress in Physics*, vol. 72, no. 12, p. 126 401, 2009.

[224] A. J. Olson, D. L. Whitenack, and Y. P. Chen, "Effects of magnetic dipole-dipole interactions in atomic Bose-Einstein condensates with tunable s-wave interactions," *Physical Review A*, vol. 88, no. 4, p. 043 609, 2013.

[225] U. R. Fischer, "Stability of quasi-two-dimensional Bose-Einstein condensates with dominant dipole-dipole interactions," *Physical Review A*, vol. 73, no. 3, p. 031 602, 2006.

[226] C. Mishra and R. Nath, "Dipolar condensates with tilted dipoles in a pancake-shaped confinement," *Physical Review A*, vol. 94, no. 3, p. 033 633, 2016.

[227] S. E. Pollack, D. Dries, M. Junker, Y. Chen, T. Corcovilos, and R. Hulet, "Extreme tunability of interactions in a Li 7 Bose-Einstein condensate," *Physical Review Letters*, vol. 102, no. 9, p. 090 402, 2009.

[228] Y.-Q. Zou, B. Bakkali-Hassani, C. Maury, É. Le Cerf, S. Nascimbene, J. Dalibard, and J. Beugnon, "Magnetic dipolar interaction between hyperfine clock states in a planar alkali Bose gas," *Physical Review Letters*, vol. 125, no. 23, p. 233 604, 2020.

[229] A. Griesmaier, J. Werner, S. Hensler, J. Stuhler, and T. Pfau, "Bose-Einstein condensation of chromium," *Physical Review Letters*, vol. 94, no. 16, p. 160 401, 2005.

[230] M. Lu, N. Q. Burdick, S. H. Youn, and B. L. Lev, "Strongly dipolar Bose-Einstein condensate of dysprosium," *Physical Review Letters*, vol. 107, no. 19, p. 190 401, 2011.

[231] K. Aikawa, A. Frisch, M. Mark, S. Baier, A. Rietzler, R. Grimm, and F. Ferlaino, "Bose-Einstein condensation of erbium," *Physical Review Letters*, vol. 108, no. 21, p. 210 401, 2012.

[232] D. Petter, G. Natale, R. van Bijnen, A. Patscheider, M. Mark, L. Chomaz, and F. Ferlaino, "Probing the roton excitation spectrum of a stable dipolar Bose gas," *Physical Review Letters*, vol. 122, no. 18, p. 183 401, 2019.

[233] D. Petrov, "Quantum mechanical stabilization of a collapsing Bose-Bose mixture," *Physical Review Letters*, vol. 115, no. 15, p. 155 302, 2015.

[234] I. Ferrier-Barbut, H. Kadau, M. Schmitt, M. Wenzel, and T. Pfau, "Observation of quantum droplets in a strongly dipolar Bose gas," *Physical Review Letters*, vol. 116, no. 21, p. 215 301, 2016.

[235] L. Chomaz, S. Baier, D. Petter, M. Mark, F. Wächtler, L. Santos, and F. Ferlaino, "Quantum-fluctuation-driven crossover from a dilute Bose-Einstein condensate to a macrodroplet in a dipolar quantum fluid," *Physical Review X*, vol. 6, no. 4, p. 041 039, 2016.

[236] G. Semeghini, G. Ferioli, L. Masi, C. Mazzinghi, L. Wolswijk, F. Minardi, M. Modugno, G. Modugno, M. Inguscio, and M. Fattori, "Self-bound quantum droplets of atomic mixtures in free space," *Physical Review Letters*, vol. 120, no. 23, p. 235 301, 2018.

[237] C. Cabrera, L. Tanzi, J. Sanz, B. Naylor, P. Thomas, P. Cheiney, and L. Tarruell, "Quantum liquid droplets in a mixture of Bose-Einstein condensates," *Science*, vol. 359, no. 6373, pp. 301–304, 2018.

[238] P. Cheiney, C. Cabrera, J. Sanz, B. Naylor, L. Tanzi, and L. Tarruell, "Bright soliton to quantum droplet transition in a mixture of Bose-Einstein condensates," *Physical Review Letters*, vol. 120, no. 13, p. 135 301, 2018.

[239] T. E. Keller and M. H. Rubin, "Theory of two-photon entanglement for spontaneous parametric down-conversion driven by a narrow pump pulse," *Physical Review A*, vol. 56, no. 2, p. 1534, 1997.

[240] J.-W. Pan, Z.-B. Chen, C.-Y. Lu, H. Weinfurter, A. Zeilinger, and M. Żukowski, "Multiphoton entanglement and interferometry," *Reviews of Modern Physics*, vol. 84, no. 2, p. 777, 2012.

[241] J. Eisert, M. Friesdorf, and C. Gogolin, "Quantum many-body systems out of equilibrium," *Nature Physics*, vol. 11, no. 2, pp. 124–130, 2015.

[242] S. Finazzi and I. Carusotto, "Entangled phonons in atomic bose-einstein condensates," *Physical Review A*, vol. 90, no. 3, p. 033 607, 2014.

[243] P. Jurcevic, B. P. Lanyon, P. Hauke, C. Hempel, P. Zoller, R. Blatt, and C. F. Roos, "Quasiparticle engineering and entanglement propagation in a quantum many-body system," *Nature*, vol. 511, no. 7508, pp. 202–205, 2014.

[244] M. Cheneau, P. Barmettler, D. Poletti, M. Endres, P. Schauß, T. Fukuhara, C. Gross, I. Bloch, C. Kollath, and S. Kuhr, "Light-cone-like spreading of correlations in a quantum many-body system," *Nature*, vol. 481, no. 7382, pp. 484–487, 2012.

[245] P. Calabrese and J. Cardy, "Entanglement entropy and quantum field theory," *Journal of Statistical Mechanics: Theory and Experiment*, vol. 2004, no. 06, P06002, 2004.

[246] D. A. Abanin, E. Altman, I. Bloch, and M. Serbyn, "Colloquium: Many-body localization, thermalization, and entanglement," *Reviews of Modern Physics*, vol. 91, no. 2, p. 021 001, 2019.

[247] J. Steinhauer, "Observation of quantum hawking radiation and its entanglement in an analogue black hole," *Nature Physics*, vol. 12, no. 10, pp. 959–965, 2016.

[248] J. R. M. de Nova, K. Golubkov, V. I. Kolobov, and J. Steinhauer, "Observation of thermal hawking radiation and its temperature in an analogue black hole," *Nature*, vol. 569, no. 7758, pp. 688–691, 2019.

[249] J. Hu, L. Feng, Z. Zhang, and C. Chin, "Quantum simulation of unruh radiation," *Nature Physics*, vol. 15, no. 8, pp. 785–789, 2019.

[250] J.-C. Jaskula, G. B. Partridge, M. Bonneau, R. Lopes, J. Ruaudel, D. Boiron, and C. I. Westbrook, "Acoustic analog to the dynamical casimir effect in a bose-einstein condensate," *Physical Review Letters*, vol. 109, no. 22, p. 220 401, 2012.

[251] C.-L. Hung, V. Gurarie, and C. Chin, "From cosmology to cold atoms: Observation of sakharov oscillations in a quenched atomic superfluid," *Science*, vol. 341, no. 6151, pp. 1213–1215, 2013.

[252] M. Schemmer, A. Johnson, and I. Bouchoule, "Monitoring squeezed collective modes of a one-dimensional bose gas after an interaction quench using density-ripple analysis," *Physical Review A*, vol. 98, no. 4, p. 043 604, 2018.

[253] A. Rançon, C.-L. Hung, C. Chin, and K. Levin, "Quench dynamics in bose-einstein condensates in the presence of a bath: Theory and experiment," *Physical Review A*, vol. 88, no. 3, p. 031 601, 2013.

[254] T. Mežnaršič, T. Arh, J. Brence, J. Pišljar, K. Gosar, Ž. Gosar, E. Zupanič, P. Jeglič, *et al.*, "Cesium bright matter-wave solitons and soliton trains," *Physical Review A*, vol. 99, no. 3, p. 033 625, 2019.

[255] J. Sanz, A. Frölian, C. Chisholm, C. Cabrera, and L. Tarruell, "Interaction control and bright solitons in coherently-coupled bose-einstein condensates," *arXiv preprint arXiv:1912.06041*, 2019.

[256] Z. Tian, S.-Y. Chä, and U. R. Fischer, "Roton entanglement in quenched dipolar bose-einstein condensates," *Physical Review A*, vol. 97, no. 6, p. 063 611, 2018.

[257] J. Steinhauer, "Measuring the entanglement of analogue hawking radiation by the density-density correlation function," *Physical Review D*, vol. 92, no. 2, p. 024 043, 2015.

[258] A. Furusawa, J. L. Sørensen, S. L. Braunstein, C. A. Fuchs, H. J. Kimble, and E. S. Polzik, "Unconditional quantum teleportation," *Science*, vol. 282, no. 5389, pp. 706–709, 1998.

[259] S. L. Braunstein and H. J. Kimble, "Teleportation of continuous quantum variables," *Physical Review Letters*, vol. 80, no. 4, p. 869, 1998.

[260] A. I. Lvovsky and M. G. Raymer, "Continuous-variable optical quantum-state tomography," *Reviews of Modern Physics*, vol. 81, no. 1, p. 299, 2009.

[261] C.-A. Chen, S. Khlebnikov, and C.-L. Hung, "Observation of quasiparticle pair production and quantum entanglement in atomic quantum gases quenched to an attractive interaction," *Physical Review Letters*, vol. 127, p. 060 404, 6 Aug. 2021.

[262] A. J. Ferris, M. K. Olsen, E. G. Cavalcanti, and M. J. Davis, "Detection of continuous variable entanglement without coherent local oscillators," *Physical Review A*, vol. 78, no. 6, p. 060 104, 2008.

[263] L.-M. Duan, G. Giedke, J. I. Cirac, and P. Zoller, "Inseparability criterion for continuous variable systems," *Physical Review Letters*, vol. 84, no. 12, p. 2722, 2000.

[264] R. Simon, "Peres-horodecki separability criterion for continuous variable systems," *Physical Review Letters*, vol. 84, no. 12, p. 2726, 2000.

[265] S. Robertson, F. Michel, and R. Parentani, "Controlling and observing nonseparability of phonons created in time-dependent 1d atomic bose condensates," *Physical Review D*, vol. 95, no. 6, p. 065 020, 2017.

[266] S. Robertson, F. Michel, and R. Parentani, "Assessing degrees of entanglement of phonon states in atomic bose gases through the measurement of commuting observables," *Physical Review D*, vol. 96, no. 4, p. 045 012, 2017.

[267] M. Reid and P. Drummond, "Quantum correlations of phase in nondegenerate parametric oscillation," *Physical Review Letters*, vol. 60, no. 26, p. 2731, 1988.

[268] J. Peise, I. Kruse, K. Lange, B. Lücke, L. Pezzè, J. Arlt, W. Ertmer, K. Hammerer, L. Santos, A. Smerzi, *et al.*, "Satisfying the einstein–podolsky–rosen criterion with massive particles," *Nature Communications*, vol. 6, no. 1, pp. 1–8, 2015.

[269] I. Klich and L. Levitov, "Quantum noise as an entanglement meter," *Physical Review Letters*, vol. 102, no. 10, p. 100 502, 2009.

[270] J. Armijo, T. Jacqmin, K. Kheruntsyan, and I. Bouchoule, "Probing three-body correlations in a quantum gas using the measurement of the third moment of density fluctuations," *Physical Review Letters*, vol. 105, no. 23, p. 230 402, 2010.

[271] D. C. Aveline, J. R. Williams, E. R. Elliott, C. Dutenhoffer, J. R. Kellogg, J. M. Kohel, N. E. Lay, K. Oudrhiri, R. F. Shotwell, N. Yu, *et al.*, "Observation of bose–einstein condensates in an earth-orbiting research lab," *Nature*, vol. 582, no. 7811, pp. 193–197, 2020.

[272] M. H. Anderson, J. R. Ensher, M. R. Matthews, C. E. Wieman, and E. A. Cornell, "Observation of bose-einstein condensation in a dilute atomic vapor," *Science*, vol. 269, no. 5221, pp. 198–201, 1995.

[273] K. B. Davis, M.-O. Mewes, M. R. Andrews, N. J. van Druten, D. S. Durfee, D. Kurn, and W. Ketterle, "Bose-einstein condensation in a gas of sodium atoms," *Physical Review Letters*, vol. 75, no. 22, p. 3969, 1995.

[274] C. Lucas, "Measurements of the atomic beam formed by a focusing capillary array," *Journal of Physics E: Scientific Instruments*, vol. 6, no. 10, p. 991, 1973.

[275] R. Brinkmann and S. Trajmar, "Effective path length corrections in beam-beam scattering experiments," *Journal of Physics E: Scientific Instruments*, vol. 14, no. 2, p. 245, 1981.

[276] M. Greiner, "Ultracold quantum gases in three-dimensional optical lattice potentials," Ph.D. dissertation, lmu, 2003.

[277] T. Klostermann, C. R. Cabrera, H. von Raven, J. F. Wienand, C. Schweizer, I. Bloch, and M. Aidelsburger, "Fast long-distance transport of cold cesium atoms," *arXiv preprint arXiv:2109.03804*, 2021.

[278] J. L. Siegel, D. Barker, J. A. Fedchak, J. Scherschligt, and S. Eckel, "A bitter-type electromagnet for complex atomic trapping and manipulation," *Review of Scientific Instruments*, vol. 92, no. 3, p. 033 201, 2021.

[279] K. Roux, B. Cilenti, V. Helson, H. Konishi, and J.-P. Brantut, "Compact bulk-machined electromagnets for quantum gas experiments," *SciPost Physics*, vol. 6, no. ARTICLE, p. 048, 2019.

[280] L. D'Alessio, Y. Kafri, A. Polkovnikov, and M. Rigol, "From quantum chaos and eigenstate thermalization to statistical mechanics and thermodynamics," *Advances in Physics*, vol. 65, no. 3, pp. 239–362, 2016.

[281] M. Schreiber, S. S. Hodgman, P. Bordia, H. P. Lüschen, M. H. Fischer, R. Vosk, E. Altman, U. Schneider, and I. Bloch, "Observation of many-body localization of interacting fermions in a quasirandom optical lattice," *Science*, vol. 349, no. 6250, pp. 842–845, 2015.

[282] J.-y. Choi, S. Hild, J. Zeiher, P. Schauß, A. Rubio-Abadal, T. Yefsah, V. Khemani, D. A. Huse, I. Bloch, and C. Gross, "Exploring the many-body localization transition in two dimensions," *Science*, vol. 352, no. 6293, pp. 1547–1552, 2016.

[283] P. M. Preiss, R. Ma, M. E. Tai, A. Lukin, M. Rispoli, P. Zupancic, Y. Lahini, R. Islam, and M. Greiner, "Strongly correlated quantum walks in optical lattices," *Science*, vol. 347, no. 6227, pp. 1229–1233, 2015.

[284] K. Sandholzer, A.-S. Walter, J. Minguzzi, Z. Zhu, K. Viebahn, and T. Esslinger, "Controlling individual band gaps in a floquet-engineered lattice," *arXiv preprint arXiv:2110.08251*, 2021.

[285] F. Görg, K. Sandholzer, J. Minguzzi, R. Desbuquois, M. Messer, and T. Esslinger, "Realization of density-dependent peierls phases to engineer quantized gauge fields coupled to ultracold matter," *Nature Physics*, vol. 15, no. 11, pp. 1161–1167, 2019.

[286] J. Rui, D. Wei, A. Rubio-Abadal, S. Hollerith, J. Zeiher, D. M. Stamper-Kurn, C. Gross, and I. Bloch, "A subradiant optical mirror formed by a single structured atomic layer," *Nature*, vol. 583, no. 7816, pp. 369–374, 2020.

[287] G. Ferioli, A. Glicenstein, L. Henriet, I. Ferrier-Barbut, and A. Browaeys, "Storage and release of subradiant excitations in a dense atomic cloud," *Physical Review X*, vol. 11, no. 2, p. 021 031, 2021.

[288] C.-C. Chien, S. Peotta, and M. Di Ventra, "Quantum transport in ultracold atoms," *Nature Physics*, vol. 11, no. 12, pp. 998–1004, 2015.

[289] A. Del Maestro, H. Barghathi, and B. Rosenow, "Measuring post-quench entanglement entropy through density correlations," *arXiv preprint arXiv:2111.06755*, 2021.

[290] R. Islam, R. Ma, P. M. Preiss, M. E. Tai, A. Lukin, M. Rispoli, and M. Greiner, "Measuring entanglement entropy in a quantum many-body system," *Nature*, vol. 528, no. 7580, pp. 77–83, 2015.

[291] Y. Kagan, D. Kovrizhin, and L. Maksimov, "Anomalous tunneling of phonon excitations between two bose-einstein condensates," *Physical Review Letters*, vol. 90, no. 13, p. 130 402, 2003.

[292] I. Danshita, S. Kurihara, and S. Tsuchiya, "Bogoliubov excitations in a kronig-penney potential," *Physical Review A*, vol. 72, no. 5, p. 053 611, 2005.

[293] A. Recati, P. Fedichev, W. Zwerger, J. Von Delft, and P. Zoller, "Atomic quantum dots coupled to a reservoir of a superfluid bose-einstein condensate," *Physical Review Letters*, vol. 94, no. 4, p. 040 404, 2005.

[294] J. S. Douglas, T. Caneva, and D. E. Chang, "Photon molecules in atomic gases trapped near photonic crystal waveguides," *Physical Review X*, vol. 6, no. 3, p. 031 017, 2016.

[295] W. G. Unruh, "Experimental black-hole evaporation?" *Physical Review Letters*, vol. 46, no. 21, p. 1351, 1981.

[296] W. G. Unruh, "Sonic analogue of black holes and the effects of high frequencies on black hole evaporation," *Physical Review D*, vol. 51, no. 6, p. 2827, 1995.

[297] M. Visser, "Acoustic black holes: Horizons, ergospheres and hawking radiation," *Classical and Quantum Gravity*, vol. 15, no. 6, p. 1767, 1998.

[298] S. W. Hawking, "Particle creation by black holes," *Communications in Mathematical Physics*, vol. 43, no. 3, pp. 199–220, 1975.

[299] S. W. Hawking, "Black hole explosions?" *Nature*, vol. 248, no. 5443, pp. 30–31, 1974.

[300] J. Steinhauer, "Observation of self-amplifying hawking radiation in an analogue black-hole laser," *Nature Physics*, vol. 10, no. 11, p. 864, 2014.

[301] V. I. Kolobov, K. Golubkov, J. R. M. de Nova, and J. Steinhauer, "Observation of stationary spontaneous hawking radiation and the time evolution of an analogue black hole," *Nature Physics*, vol. 17, no. 3, pp. 362–367, 2021.

[302] Y.-H. Wang, T. Jacobson, M. Edwards, and C. Clark, "Induced density correlations in a sonic black hole condensate," *SciPost Physics*, vol. 3, no. 3, p. 022, 2017.

[303] Y.-H. Wang, T. Jacobson, M. Edwards, and C. W. Clark, "Mechanism of stimulated hawking radiation in a laboratory bose-einstein condensate," *Physical Review A*, vol. 96, no. 2, p. 023 616, 2017.

[304] F. Le Kien, P. Schneeweiss, and A. Rauschenbeutel, "Dynamical polarizability of atoms in arbitrary light fields: General theory and application to cesium," *The European Physical Journal D*, vol. 67, no. 5, pp. 1–16, 2013.

[305] L. Feng, L. W. Clark, A. Gaj, and C. Chin, "Coherent inflationary dynamics for bose–einstein condensates crossing a quantum critical point," *Nature Physics*, vol. 14, no. 3, p. 269, 2018.

[306] L. Pitaevskii and S. Stringari, *Bose-Einstein condensation and superfluidity*. Oxford University Press, 2016, vol. 164.

[307] H. Saito and M. Ueda, "Intermittent implosion and pattern formation of trapped bose-einstein condensates with an attractive interaction," *Physical Review Letters*, vol. 86, pp. 1406–1409, 8 Feb. 2001.

[308] H. Saito and M. Ueda, "Mean-field analysis of collapsing and exploding bose-einstein condensates," *Physical Review A*, vol. 65, no. 3, p. 033 624, 2002.

A. CESIUM FESHBACH RESONANCES

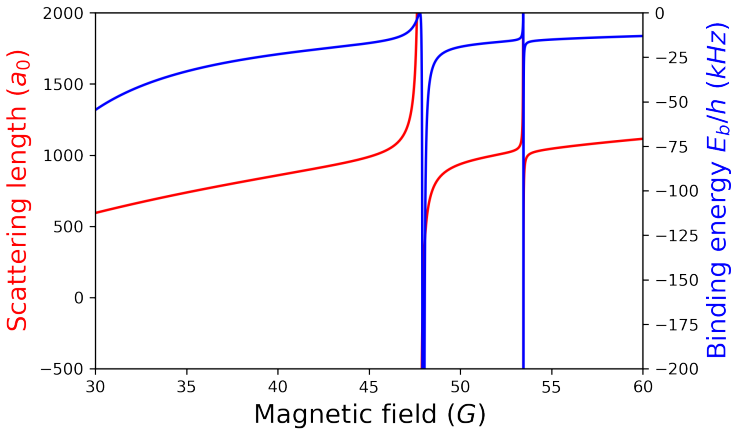

Figure A.1. Feshbach resonances near 48 G.

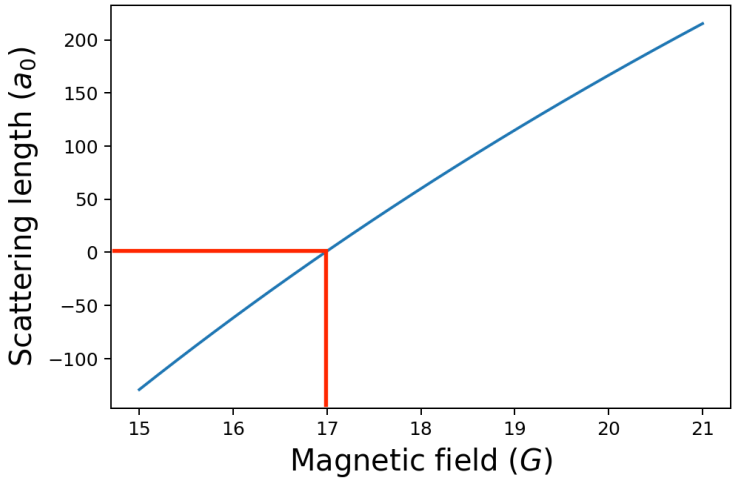

Figure A.2. Feshbach resonances near 17 G. Red solid line indicates the zero crossing.

B. ZEEMAN SLOWER DETAIL

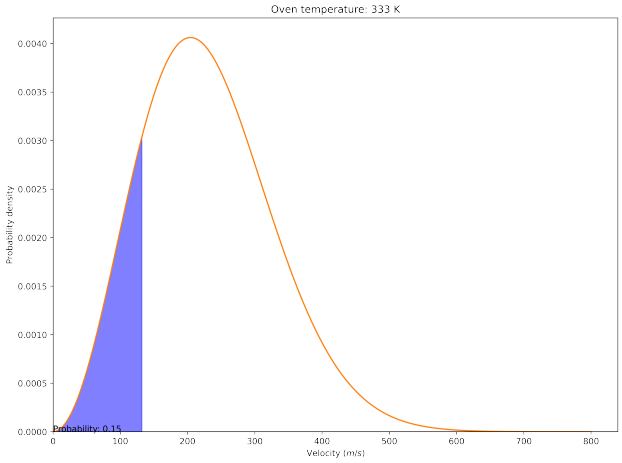

Figure B.1. Atomic velocity distribution. Blue shadow: capture range of the Zeeman slower.

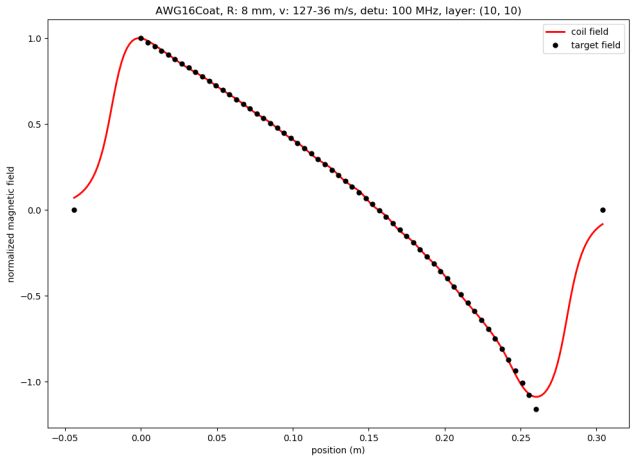

Figure B.2. Simulation of the Zeeman slower magnetic field.

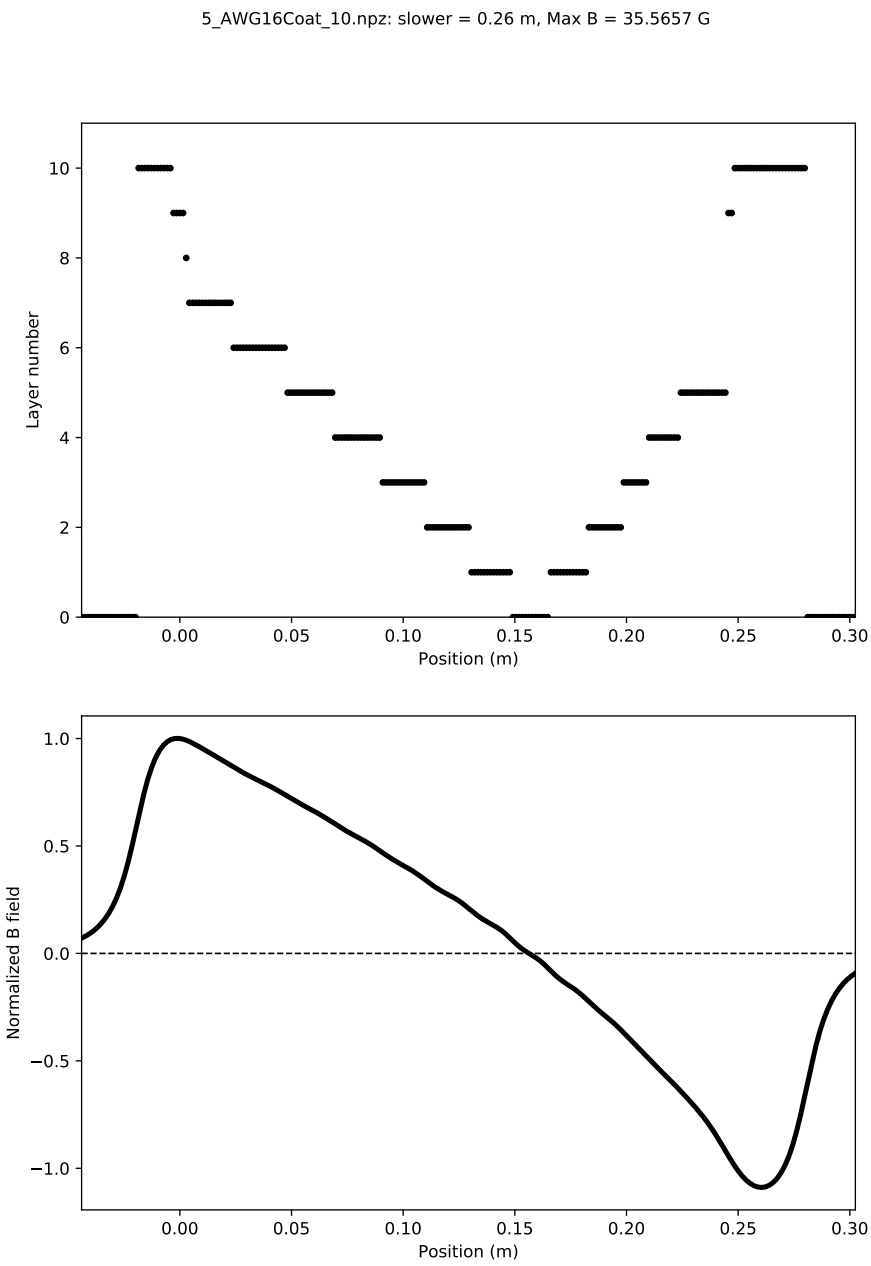

Figure B.3. Calculation of the Zeeman slower coil winding.

C. MAIN COIL DETAIL

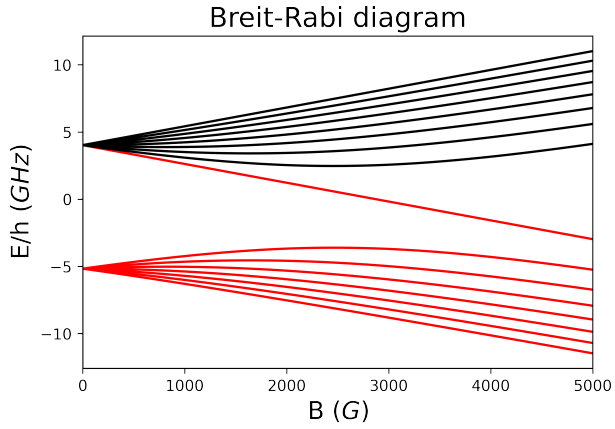

Figure C.1. Breit-Rabi diagram of cesium $6^2S_{1/2}$ ground state hyperfine structure $F = 4$ and $F = 3$.

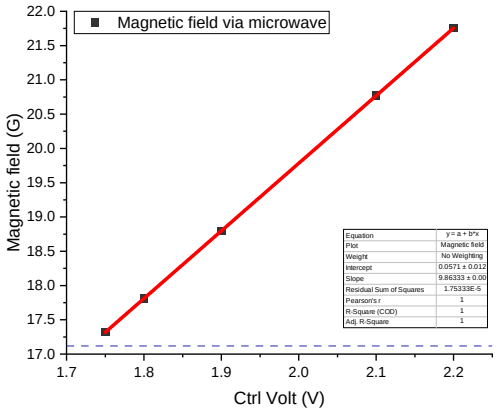

Figure C.2. Magnetic field calibration of the main coil by microwave spectroscopy. The horizontal axis is the voltage setpoint of the coil driver. The horizontal dash line indicates the zero crossing of cesium s-wave scattering length ≈ 17.2 G.

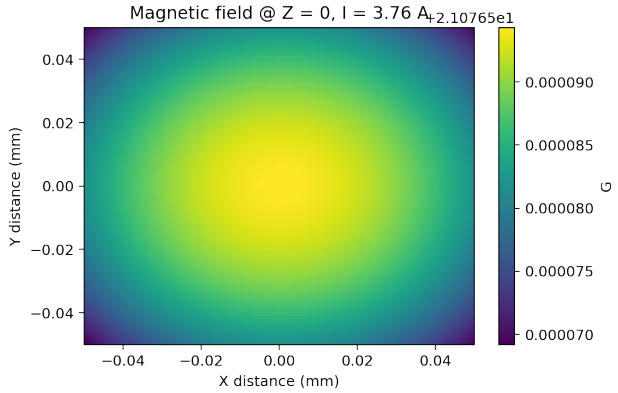

Figure C.3. Calculation of magnetic field from the main coil, Helmholtz configuration, showing weak magnetic trap at $x - y$ plane.

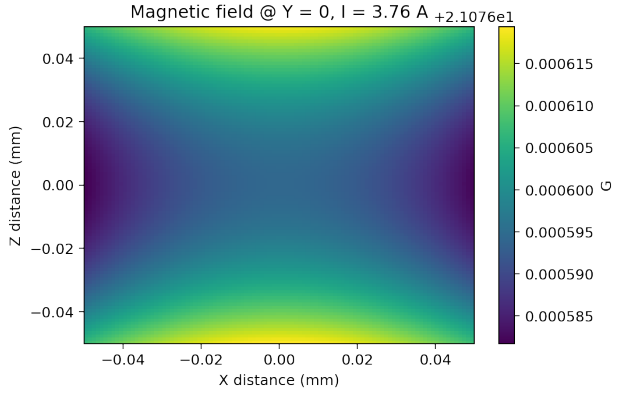

Figure C.4. Calculation of magnetic field from the main coil, Helmholtz configuration, showing weak magnetic anti-trap along z.

D. OPTICAL FESHBACH TUNING

Following Ref. [124], for a laser with intensity I, the total light shifts of atoms δE_a and molecules δE_m are

$$\delta E_a = (\alpha_a + \beta_a \mu_a) I \tag{D.1}$$

$$\delta E_m = (\alpha_m + \beta_m \mu_m) I \tag{D.2}$$

where α is the scalar polarizability and β is the vector polarizability, μ is the magnetic moment. The Feshbach molecular states are weakly bound, their polarizabilities are similar to free atoms: $\alpha_m = 2\alpha_a$ and $\beta_m \approx \beta_a \equiv \beta$. If the molecular and atomic magnetic moments are different: $\mu_m \neq 2\mu_a$, the fictitious magnetic field from the vector light shift can vary the energy of molecular bound states, hence introducing a light-induced Feshbach resonance.

We can choose a 'magic' wavelength λ_M whose atomic scalar light shift cancels vector light shift: $\alpha_a + \beta\mu_a = 0$, such that only the molecular light shift remains: $\delta E_m \approx \beta(\mu_m - 2\mu_a)I$. The vector polarizability on the Stark shift effectively manifests a light-induced fictitious magnetic field. The vector polarizability β can be calculated from [304]

$$\beta = \frac{(-1)^{J_\mathrm{i}}}{2\hbar\epsilon_0 c}\sqrt{\frac{6J_\mathrm{i}}{(J_\mathrm{i}+1)(2J_\mathrm{i}+1)}} \times \sum_f (-1)^{J_f} \begin{Bmatrix} 1 & 1 & 1 \\ J_\mathrm{i} & J_f & J_\mathrm{i} \end{Bmatrix} |\langle f||d||\mathrm{i}\rangle|^2 \times \left(\frac{1}{\omega_{f\mathrm{i}} - \omega} - \frac{1}{\omega_{f\mathrm{i}} + \omega}\right) \tag{D.3}$$

where $|f\rangle$ can be any excited state, c is the speed of light, ϵ is the vacuum permittivity, $\begin{Bmatrix} 1 & 1 & 1 \\ J_\mathrm{i} & J_f & J_\mathrm{i} \end{Bmatrix}$ is the Wigner 6-j symbol, $|\langle f||d||\mathrm{i}\rangle|$ and $\omega_{f\mathrm{i}}$ are the reduced dipole matrix element and resonance frequency for the transition from $|\mathrm{i}\rangle$ to $|f\rangle$, respectively, and ω is the laser frequency. The effective magnetic field becomes βI, where I is the laser intensity. On the other hand, the photon scattering rate $s(I)$ is

$$s(I) = \frac{I}{2\hbar^2\epsilon_0 c}\sum_f \frac{d_{f\mathrm{i}}^2 \Gamma_f}{(\omega_{f\mathrm{i}} - \omega)^2} \tag{D.4}$$

where Γ_f is the spontaneous emission rate of the excited state $|f\rangle$, $d_{\mathrm{fi}}^2 = C_{\mathrm{fi}}^{\pm}|\langle f||d||\mathrm{i}\rangle|^2$ is the squared dipole matrix elements, and $C_{\mathrm{fi}}^{\pm}$ is a numerical factor of the Clebsch-Gordan coefficients with beam polarization $\sigma_{\pm}$. Thus we can evaluate the shift of the molecular states in a fixed quantum gas lifetime from $M \equiv \frac{\beta I}{s(I)}$.

We can optimize M by using pure circular polarization. Figure D.1 shows M in different wavelengths and different polarizations. In the context of maximum fictitious magnetic field at magic wavelengths, one find that σ^+ with 870 nm and σ^- with 890 nm give us similar $|M| \approx 130$ mG·s and opposite sign. In our experiment, we can incorporate σ^- polarization and 890 nm laser for optical Feshbach resonance.

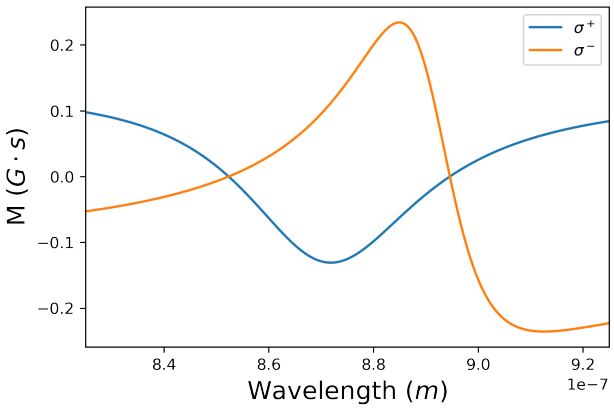

Figure D.1. The figure of merit $M \equiv \frac{\beta I}{s(I)}$ for choosing the wavelength and polarization of the laser, where βI is the effective field shift and $s(I)$ is the photon scattering rate.

E. SUPPLEMENTAL MATERIAL FOR UNIVERSAL QUENCH DYNAMICS AND TOWNES SOLITON FORMATION

E.1 Formation of a Townes soliton array

To fully demonstrate that Townes solitons can generally form from our quench recipe, we induce MI in another set of 2D samples initially confined and then released from a narrow rectangular wall potential as shown in Fig. E.1(a). We adjust the short side of the samples to be comparable to the MI length scale, so that a *single array* of solitons can form following the interaction quench. This avoids close proximity with many neighboring solitary waves or dispersing blobs, visible in large samples shown in Fig. 4.1(b). From these narrow samples, we clearly observe well-isolated solitary waves in almost every experiment repetition as shown in Fig. E.1(a) at hold time $\tau \geq 30$ ms. In these solitary waves, we find ubiquitous agreement with the Townes profiles [Fig. E.1(b-c)]. Together with Fig. 4.2, our observation confirms that Townes solitons can prevail from MI.

E.2 Quench-induced dynamics in the density power spectrum

In a 2D gas with uniform mean density distribution, the density power spectrum at finite k is essentially the density static structure factor, which is the Fourier transform of the density-density correlation function [221]. In the following, we discuss the quench evolution of the static structure factor (density power spectrum) measured in our samples, while neglecting density perturbations due to boundary effects.

E.2.1 Theory of density structure factor after an interaction quench to attractive

For a Bose superfluid with initial density n_i immediately following the interaction quench, we expect density waves with wavenumber $0 < k < \sqrt{4|g_f|n_\mathrm{i}}$ to growth unstably since the usual Bogoliubov dispersion becomes purely imaginary. There is no straightforward theory for evaluating quench evolution at all hold time τ. To gain insights, here we analytically evaluate the quench dynamics only in the very early stage when most of the atoms still

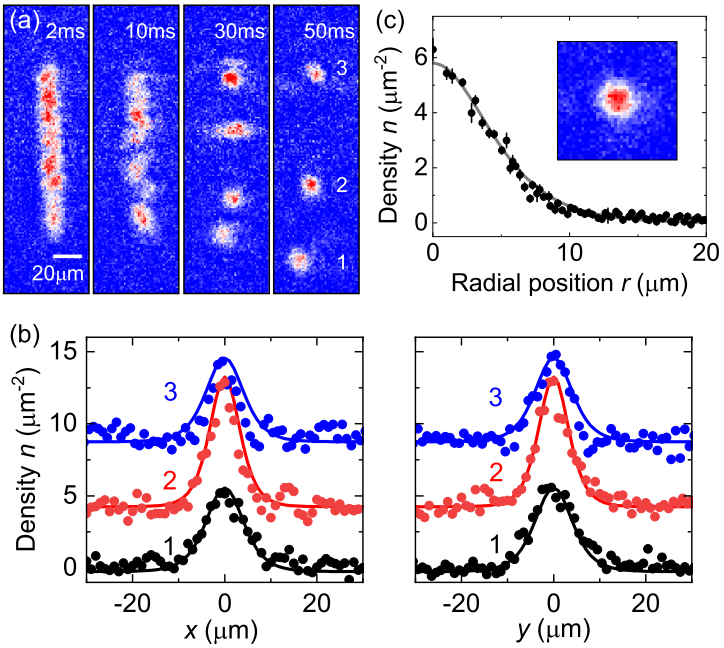

Figure E.1. Formation of a Townes soliton array. (a) Single-shot images of elongated samples quenched to $g_f = -0.0075$ and held for the labeled time τ. An array of fully isolated solitary waves become visible at $\tau \geq 30$ ms. (b) Density line cuts (solid circles) through the center of three solitary waves as numerically labeled in (a), each offset by $4.5/\mu\text{m}^2$ for viewing. Solid lines are the Townes profiles of $n_0 = 5.8/\mu\text{m}^2$ (for #1,#3) and $9/\mu\text{m}^2$ (for #2), respectively. (c) Mean density image of four randomly chosen solitons with $n_0 \approx 5.8/\mu\text{m}^2$ (inset: 40×40 μm^2) and the radial profile (solid circles), showing excellent agreement with theory (solid curve). Reprinted figure with permission from [200], Copyright 2021 by APS.

remain in the zero momentum state. We focus on the time-evolution of the static structure factor [202], [305]. Analytically, it can be evaluated as

$$S(\mathbf{k}) = \frac{1}{N}\sum_{\mathbf{q},\mathbf{q}'}\langle \hat{a}^\dagger_{\mathbf{q}+\mathbf{k}}\hat{a}_{\mathbf{q}}\hat{a}^\dagger_{\mathbf{q}'-\mathbf{k}}\hat{a}_{\mathbf{q}'}\rangle, \tag{E.1}$$

where $\hat{a}_{\mathbf{k}}(\hat{a}^\dagger_{\mathbf{k}})$ stands for the annihilation (creation) operator of a momentum state $|\mathbf{k}\rangle$ and N is the total atom number. At very short hold time $\tau \ll \gamma^{-1}$, the Bose gas is still primarily populated by ground state atoms ($\hat{a}_0^{(\dagger)} \approx \sqrt{N}$), where $\hbar\gamma = \hbar^2 n_{\text{i}}|g_f|/m$ is the interaction

energy, m is the atomic mass, and $\hbar$ is the reduced Planck constant. The structure factor reduces to

$$S(\mathbf{k}) = \langle \hat{a}^\dagger_{\mathbf{k}} \hat{a}_{\mathbf{k}} \rangle + \langle \hat{a}_{-\mathbf{k}} \hat{a}^\dagger_{-\mathbf{k}} \rangle + \langle \hat{a}^\dagger_{\mathbf{k}} \hat{a}^\dagger_{-\mathbf{k}} \rangle + \langle \hat{a}_{-\mathbf{k}} \hat{a}_{\mathbf{k}} \rangle. \tag{E.2}$$

We perform the following transformation for momentum state within the range $0 < |\mathbf{k}| < \sqrt{4|g_f|n_{\mathrm{i}}}$, expressing the momentum state operator with a set of bosonic mode operators $\hat{b}_{\mathbf{k}}$ ($\hat{b}^\dagger_{-\mathbf{k}}$) as

$$\begin{aligned} \hat{a}_{\mathbf{k}} &= \mathrm{i}\left[u_k \hat{b}_{\mathbf{k}} + v_k \hat{b}^\dagger_{-\mathbf{k}}\right] \\ \hat{a}^\dagger_{-\mathbf{k}} &= -\mathrm{i}\left[v_k \hat{b}_{\mathbf{k}} + u_k \hat{b}^\dagger_{-\mathbf{k}}\right]. \end{aligned} \tag{E.3}$$

Here, we set the coefficients $u_k = \sqrt{\frac{\hbar\gamma}{2\epsilon(k)} + \frac{1}{2}}$ and $v_k = \sqrt{\frac{\hbar\gamma}{2\epsilon(k)} - \frac{1}{2}}$, $\epsilon(k) = \sqrt{|\epsilon_k^2 - 2\epsilon_k \hbar\gamma|}$ is the imaginary part of the Bogoliubov energy, and $\epsilon_k = \hbar^2 k^2/2m$ is the single particle dispersion. $\hat{b}_{\mathbf{k}}$ ($\hat{b}^\dagger_{-\mathbf{k}}$) obeys the usual bosonic commutation relation. Using procedures similar to the standard Bogoliubov transformation, we can recast the weakly-interacting Hamiltonian into the following form

$$\hat{H} = \frac{N\mu}{2} + \sum_{\mathbf{k}\neq 0} \epsilon(k)(\hat{b}^\dagger_{\mathbf{k}} \hat{b}^\dagger_{-\mathbf{k}} + \hat{b}_{\mathbf{k}} \hat{b}_{-\mathbf{k}}) - \sum_{\mathbf{k}\neq 0} (\frac{\hbar^2 k^2}{2m} + \mu), \tag{E.4}$$

where the summation runs over half of momentum space and $\mu = -\hbar\gamma$ is the chemical potential. Note that, under this transformation, new excitations are generated (and also annihilated) in pairs as hold time increases. In the Heisenbeg picture, these operators obey a set of coupled equations of motion, $\dot{\hat{b}}_{\mathbf{k}} = \frac{\mathrm{i}}{\hbar}[\hat{H}, \hat{b}_{\mathbf{k}}] = -\frac{\mathrm{i}}{\hbar}\epsilon(k)\hat{b}^\dagger_{-\mathbf{k}}$ and its Hermitian conjugate, which lead to the following solution

$$\hat{b}_{\mathbf{k}} = \hat{b}_{0,\mathbf{k}} \cosh \tfrac{\epsilon(k)\tau}{\hbar} - \mathrm{i}\hat{b}^\dagger_{0,-\mathbf{k}} \sinh \tfrac{\epsilon(k)\tau}{\hbar} \tag{E.5}$$

$$\hat{b}^\dagger_{-\mathbf{k}} = \hat{b}^\dagger_{0,-\mathbf{k}} \cosh \tfrac{\epsilon(k)\tau}{\hbar} + \mathrm{i}\hat{b}_{0,\mathbf{k}} \sinh \tfrac{\epsilon(k)\tau}{\hbar}, \tag{E.6}$$

and $\hat{b}_{0,\mathbf{k}}(\hat{b}^\dagger_{0,-\mathbf{k}})$ is the bosonic mode operator at time $\tau = 0$ right after the interaction quench. Plugging this solution into Eq. (E.3) and evaluate the structure factor Eq. (E.2), we then find the following time-dependent evolution

$$\begin{aligned} S(\mathbf{k},\tau) \quad &= \frac{\epsilon_k}{\epsilon(k)}\Big[(\langle\hat{b}^\dagger_{0,\mathbf{k}}\hat{b}_{0,\mathbf{k}}\rangle + \langle\hat{b}_{0,-\mathbf{k}}\hat{b}^\dagger_{0,-\mathbf{k}}\rangle)\cosh 2\frac{\epsilon(k)\tau}{\hbar} \\ &-(\langle\hat{b}^\dagger_{0,\mathbf{k}}\hat{b}^\dagger_{0,-\mathbf{k}}\rangle + \langle\hat{b}_{0,-\mathbf{k}}\hat{b}_{0,\mathbf{k}}\rangle) \\ &-\mathrm{i}(\langle\hat{b}^\dagger_{0,\mathbf{k}}\hat{b}^\dagger_{0,-\mathbf{k}}\rangle - \langle\hat{b}_{0,-\mathbf{k}}\hat{b}_{0,\mathbf{k}}\rangle)\sinh 2\frac{\epsilon(k)\tau}{\hbar}\Big]. \end{aligned} \tag{E.7}$$

Here, the first line contains mode contributions that are seeded by the initial bosonic mode populations right after the quench. These modes grow 'hyperbolically' in the early stage of the quench dynamics. The second and third lines contain the contributions from mode populations that are generated or annihilated from the interaction quench, where the hyperbolic term is expected to vanish, leaving only the constant term (see below).

E.2.2 Amplification of density waves from density fluctuations prior to the quench

By using Eq. (E.3) and the Bogoliubov transformation, we can further relate the expectation values of the bosonic modes in Eq. (E.7) to those of the phonon modes before the interaction quench. We find

$$\langle\hat{b}^\dagger_{0,\mathbf{k}}\hat{b}_{0,\mathbf{k}}\rangle + \langle\hat{b}_{0,-\mathbf{k}}\hat{b}^\dagger_{0,-\mathbf{k}}\rangle = \epsilon_k\frac{\hbar(\gamma_\mathrm{i}+\gamma)}{\epsilon_\mathrm{i}(k)\epsilon(k)}\zeta \tag{E.8}$$

$$\langle\hat{b}^\dagger_{0,\mathbf{k}}\hat{b}^\dagger_{0,-\mathbf{k}}\rangle = \langle\hat{b}_{0,\mathbf{k}}\hat{b}_{0,-\mathbf{k}}\rangle = \frac{\epsilon_k^2 + \epsilon_k\hbar(\gamma_\mathrm{i}-\gamma)}{2\epsilon_\mathrm{i}(k)\epsilon(k)}\zeta, \tag{E.9}$$

and

$$\zeta = \langle\hat{c}^\dagger_{0,\mathbf{k}}\hat{c}_{0,\mathbf{k}}\rangle + \langle\hat{c}_{0,-\mathbf{k}}\hat{c}^\dagger_{0,-\mathbf{k}}\rangle. \tag{E.10}$$

Here, $\hat{c}_{0,\mathbf{k}}(\hat{c}^\dagger_{0,\mathbf{k}})$ is the phonon annihilation (creation) operator, $\epsilon_\mathrm{i}(k) = \sqrt{\epsilon_k^2 + 2\epsilon_k\hbar\gamma_\mathrm{i}}$ is the Bogoliubov dispersion at interaction $g_\mathrm{i} > 0$ prior to the quench, $\gamma_\mathrm{i} = \hbar n_\mathrm{i} g_\mathrm{i}/m$, and we have used $\langle\hat{c}^\dagger_{0,\mathbf{k}}\hat{c}^\dagger_{0,-\mathbf{k}}\rangle = \langle\hat{c}_{0,\mathbf{k}}\hat{c}_{0,-\mathbf{k}}\rangle = 0$ in the above relation since there is no source or sink for

phonons in our 2D gas. It is clear that the bosonic mode population Eqs. (E.8-E.9) is seeded by the initial thermal phonon population and zero-point fluctuations

$$\langle \hat{c}^\dagger_{0,\mathbf{k}} \hat{c}_{0,\mathbf{k}} \rangle + \langle \hat{c}_{0,-\mathbf{k}} \hat{c}^\dagger_{0,-\mathbf{k}} \rangle = \frac{2}{\mathrm{e}^{\epsilon_\mathrm{i}(k)/k_B T} - 1} + 1 = \coth \frac{\epsilon_\mathrm{i}(k)}{2k_B T}. \tag{E.11}$$

Using the above relations and keeping only the wavenumber k-dependence, Eq. (E.7) can now be simplified as

$$S(k,\tau) = S_0(k) \left[1 + \frac{2\epsilon_k \hbar(\gamma_\mathrm{i} + \gamma)}{\epsilon(k)^2} \sinh^2 \frac{\epsilon(k)\tau}{\hbar} \right], \tag{E.12}$$

where the overall factor

$$S_0(k) = \frac{\hbar^2 k^2}{2m\epsilon_\mathrm{i}(k)} \coth \frac{\epsilon_\mathrm{i}(k)}{2k_B T} \tag{E.13}$$

is exactly the equilibrium static structure factor [306] right before the interaction quench.

E.2.3 The scaling behavior

In Eq. (E.12), the second term in the bracket represents contributions from the MI-amplified density waves, suggesting density waves at wavenumber $k_p = \sqrt{2|g_f|n_\mathrm{i}}$ have the largest amplification rate $\epsilon(k_p)/\hbar = \gamma$. Thus, at short hold time $\tau \ll \gamma^{-1}$, we expect the growth of density power spectrum $\tilde{S}(k_p,\tau) \equiv S(k_p,\tau)/S(k_p,0)$ to obey the following scaling relation

$$\mathcal{S}(\tilde{\tau}) = \zeta \left[\tilde{S}(k_p,\tilde{\tau}) - 1 \right], \tag{E.14}$$

where $\tilde{\tau} = \gamma\tau$ is the scaled time, $\zeta = \frac{\gamma}{\gamma_\mathrm{i}+\gamma}$ is a dimensionless amplitude scaling factor, and $\mathcal{S}(\tilde{\tau})$ is the scaled spectrum; $\zeta \approx \gamma/\gamma_\mathrm{i}$ when $\gamma_\mathrm{i} \gg \gamma$. The scaled spectrum should display a universal hyperbolic growth at short hold time

$$\mathcal{S}(\tilde{\tau}) = 2\sinh^2(\tilde{\tau}). \tag{E.15}$$

E.2.4 Relationship with quench dynamics at repulsive

We note that the time-dependent density power spectrum Eq. (E.12) is essentially the analytical continuation of quench-induced Sakharov oscillations in the static structure factor at $g_f > 0$ [202],

$$S(k,\tau) = S_0(k)\Big[1 + \frac{\epsilon_{\rm i}(k)^2 - \epsilon^2(k)}{\epsilon(k)^2}\sin^2\frac{\epsilon(k)\tau}{\hbar}\Big], \tag{E.16}$$

where now a coherent, sinusoidal oscillation in the structure factor replaces the hyperbolic growth. The calculation is in principle valid for all hold time τ for $g_f > 0$, in contrast to the case of $g_f < 0$, provided no global trap effect or other effects set in.

E.2.5 Experimental test of the scaling behavior in the density power spectrum

We experimentally test the scaling behavior Eq. (E.14) over an extended time period. We have empirically searched for the best amplitude scaling relation ζ for a larger time range $0 < \tilde{\tau} < 5$. We find that the spectra scale the best with $\zeta \propto \gamma$, keeping explicit dependence on $n_{\rm i}|g_f|$. We adopt a simple amplitude scaling factor $\zeta = \gamma/\bar{\gamma}_{\rm i}$, using mean $\bar{\gamma}_{\rm i} = \hbar\bar{n}_{\rm i}g_{\rm i}/m = 306\ \mathrm{s}^{-1}$ evaluated from all samples (mean $\bar{n}_{\rm i} = 6/\mu\mathrm{m}^2$ and standard deviation $\delta n_{\rm i} = 1/\mu\mathrm{m}^2$). We note that an alternative amplitude scaling factor $\zeta = \gamma/(\bar{\gamma}_{\rm i} + \gamma)$ close to the exact form in Eq. (E.14) gives a similar data collapse.

E.3 Soliton collision dynamics

E.3.1 Soliton binary collision rate

Binary collisions between solitons can lead to merger [203], which makes soliton atom number $N_a > N_{\rm th}$ much greater than the Townes threshold and induces collapse and rapid atom loss. Soliton binary loss behavior can be effectively described by $\dot{N}_s/N_s = -\Gamma_s n_s$, where N_s is the number of solitons, $n_s = N_s/A$ is the surface density, and Γ_s is the 2D binary loss coefficient as discussed in the main text. For total atom number loss dominated by soliton binary collision loss, we should have $\dot{N}/N = -\Gamma_{\rm 2body}n$, where n is the atom number density. We convert the soliton number into total atom number N using $N_s = N/\bar{N}_a$ [185], [186] and assuming $\bar{N}_a$ is approximately constant over the experiment time. We find the simple

relation $\Gamma_s = \Gamma_{2\text{body}}\bar{N}_a$, relating the measured loss coefficient $\Gamma_{2\text{body}}$ to the binary collision coefficient Γ_s.

E.3.2 Collision lifetime of solitons

Following the determination of universal collision dynamics, we also obtain the collision lifetime of solitons right after the formation process near $\tilde{\tau} \approx \tilde{\tau}_c$. We calculate the lifetime $\Delta\tau_s = \frac{1}{\Gamma_s n_s} \approx \frac{m\bar{N}_a}{\eta\pi\hbar n_\text{i}} \approx \gamma^{-1}$, where we have used $n_s = n_\text{i}/\bar{N}_a$, the measured universal threshold $\bar{N}_a|g_f| = 6$ (Fig. 4.1), and the measured constant $\eta = 1.5$ (Fig. 4.4).

E.4 Collapse and expansion dynamics of an unstable Townes soliton

This section is dedicated for gaining further information about the evolution of unstable Townes solitons. We determine their collapse and expansion time scales by driving the atom number more than three times away from the Townes threshold via a second interaction quench.

E.4.1 Second interaction quench

We apply a second interaction quench after solitons form at a sufficiently long hold time $\tau = 50$ ms, hold for an additional time τ_2, and perform imaging. In a quench path labeled (i) in Fig. E.2(a) to a less attractive interaction, we induce immediate soliton expansion, during which $\bar{N}_a$ remains constant, as expected, but the number of solitons N_s observed from the ensemble measurements greatly reduces; see Fig. E.2(c) and inset. For a reversed quench path (ii) to a more attractive interaction, solitons collapse. In a short time scale $\gamma'^{-1} \sim 20$ ms corresponding to the interaction energy difference between the two quenches, we observe rapid reductions in both σ and $\bar{N}_a$.

In the collapse dynamics, we tentatively attribute the atom number loss within a soliton to few-body inelastic collisions that are primarily due to three-body recombination. However, in Fig. E.2(c), we obtain an unphysical loss coefficient that is five orders of magnitude larger than that measured in thermal samples [169]. A rapid three-body loss rate was also reported in the collapse within 1D solitons in a related experiment setting [185]. We believe that a

more likely explanation for the rapid loss may be due to a combination of three-body loss under higher local collapse density and collective matter-wave ejection out of the solitons during the collapse [172], [217], [307], [308], which is challenging to detect given limited image resolution and signal-to-noise. Interestingly, the collapse seemingly slows down as $\bar{N}_a$ drops to the new threshold value. We suspect either the atom loss has regulated the collapse, perhaps due to collective wave emission, or solitons with initial N_a close to the new threshold survive. From the inset of Fig. E.2(c), the observed continuing decrease of soliton number beyond $\tau_2 \geq 36$ ms may hint more of the latter case.

In either quench paths (i) and (ii), soliton evolution is clearly visible within the interaction time scale γ'^{-1}. For the dynamics after just a single quench, such rapid evolutions in mean atom number and soliton size are not observed. We therefore conclude that those surviving solitons formed by MI in a single quench are quasi-stationary within our experiment time < 200 ms as their norm are sufficiently close to the Townes threshold.

E.4.2 Fitting atom number loss during rapid soliton collapse

Following the second interaction quench in path (ii) as shown in Fig. E.2, mean atom number in a soliton $\bar{N}_a(\tau_2 = 0)$ exceeds the new Townes threshold by three-fold and solitons begin to collapse. From the linear fit in Fig. E.2(b), we obtain an approximate linear time-dependent size $\sigma(\tau_2) = \sigma_0 + \dot{\sigma}\tau_2$, where $\sigma_0 = 8.0$ μm and $\dot{\sigma} = -0.11$ mm/s. Here we consider a simple case where the atom number loss within a soliton is fully due to three-body recombination. Because the vertical oscillator length $l_z = 208$ nm far exceeds the magnitude of the 3D scattering length $|a| = 1.1$ nm, we expect the three-body loss behavior to be 3D in nature. To quantify the three-body loss rate, we develop a model that takes into account the shrinking soliton size in the 2D plane, while assuming that the vertical wave packet remains in the harmonic ground state. This is justified because the 2D density n needs to increase by ~ 170 times for the interaction energy to approach the vertical trap vibrational energy. Such dramatic increase in 2D density is not observed in our images,

where the soliton size remains larger than the image resolution during the time of collapse. We therefore adopt the standard three-body recombination loss model

$$\frac{d\bar{N}_a}{d\tau_2} = -\frac{L_3}{9\sqrt{3}\pi^3\sigma(\tau_2)^4 l_z^2}\bar{N}_a^3, \tag{E.17}$$

where L_3 is the three-body loss coefficient and we have used a Gaussian form to approximate the soliton 3D density profile. From the above equations and the approximate linear time-dependence in σ, we derive an analytical formula

$$\bar{N}_a(\tau_2) = \frac{\bar{N}_a(0)}{\sqrt{1 + \frac{2L_3\bar{N}_a(0)^2}{27\sqrt{3}\pi^3 l_z^2|\dot{\sigma}|}\left[\frac{1}{(\sigma_0+\dot{\sigma}\tau_2)^3} - \frac{1}{\sigma_0^3}\right]}}, \tag{E.18}$$

where L_3 is the fit parameter. This effective three-body loss model appears to fit our data except beyond $\tau_2 > 36$ ms when the atom number reaches the new Townes threshold. The fitted $L_3 = 1.1(1) \times 10^{-23}$ cm^6/s is nonetheless five orders of magnitude larger than that measured in a thermal sample [169], which we believe is not physical. To reconcile this discrepancy may require a different collapse dynamics that, for example, creates three-body loss under higher local collapse density beyond our image resolution and also rapidly ejects atoms out of a collapsing soliton [172], [217], [307], [308].

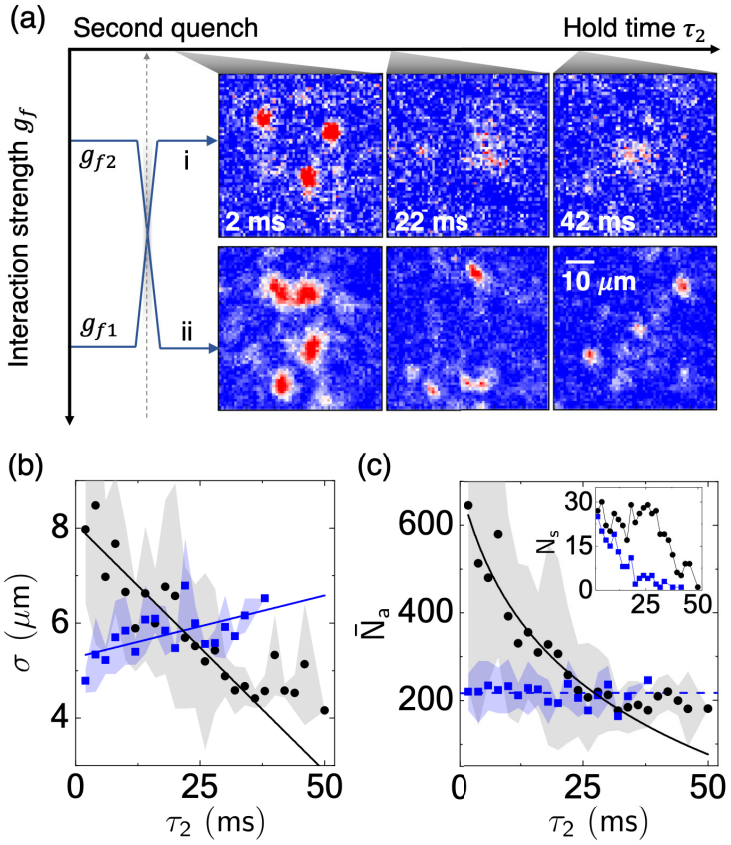

Figure E.2. Collapse and expansion dynamics following second interaction quenches. (a) Path i (ii): expansion (collapse) dynamics is initiated in solitons that are initially formed at $g_{f1} = -0.027$ (or $g_{f2} = -0.008$) followed by a second quench to g_{f2} (or g_{f1}). Single-shot sample images are recorded at the indicated hold time τ_2 after the second quench. (b-c) mean size σ and atom number $\bar{N}_a$ versus τ_2 for paths i (blue squares) and ii (black circles), respectively. In (b), solid lines are linear fits, giving a collapse (expansion) rate $\dot{\sigma}/\gamma' \approx -1.8$ μm (0.5 μm) normalized by the interaction energy unit $\gamma' = \hbar\bar{n}|g_{f2} - g_{f1}|/m \approx 55$ s^{-1} and $\bar{n} \approx 6/\mu$m^2 is mean initial peak density. In (c), blue dashed line marks the Townes threshold $N_{\rm th} = 5.85/|g_{f1}|$. Black solid line is a guide to the eye, given by a tentative three-body loss fit (see text). Inset shows the observed soliton number N_s from the ensemble measurements. Shaded bands represent standard errors. Reprinted figure with permission from [200], Copyright 2021 by APS.

F. SUPPLEMENTAL MATERIAL FOR SCALE INVARIANT TOWNES SOLITONS

F.1 Magnetic two-body interaction tuning

We tune the cesium scattering length by applying a uniform bias magnetic field perpendicular to the x-y plane to access a magnetic Feshbach resonance [59], [169]. We identify zero scattering length at the magnetic field $B = 17.120(6)$G, by minimizing superfluid in-situ size as well as the expansion rate in a 2D time-of-flight. We then adopt the formula [169] $a(B) = (1722 + 1.52B/G)\left(1 - \frac{\Delta B}{B/G - B_0}\right)$ for the scattering length conversion, where $\Delta B = 28.72$ and $B_0 = -11.60$ is adjusted to shift the zero-crossing to the measured value. The interaction strength is determined as $g = \sqrt{8\pi}a/l_z$, where $l_z = 184$ nm is the vertical harmonic oscillator length. The uncertainty ($\pm\delta g$) in g is primarily contributed by the uncertainty in the magnetic field at the scattering length zero-crossing. Within the range of our reported negative interaction strengths $-0.0075 \geq g \geq -0.022$, we have $\delta g \approx 0.0005$.

While we have calibrated the coupling constant g with relatively small uncertainty near zero-crossing, our measurement method does not distinguish a small offset contribution from the magnetic dipole-dipole interaction (MDDI). The 2D superfluid samples adopted in this calibration have in-situ widths of $w > 7$ μm much larger than the size $l_z = 184$ nm along the tightly confining axis. This large aspect ratio and our magnetic field orientation (perpendicular to the 2D plane) makes the mean field effect of the MDDI effectively a contact-like interaction, contributing to a shift in the calibrated coupling constant

$$g \approx g_c + 2g_{\mathrm{dd}} \tag{F.1}$$

where g_c is the bare coupling constant of the contact interaction and $g_{\mathrm{dd}} \approx 0.00087$ is the MDDI coupling constant of atomic cesium confined in the quasi-2D trap; see discussions below.

F.2 Scale-invariant 2D solitons

In the following sections, we evaluate the stationary 2D matter-wave density profile and consider the presence of a MDDI. We start by considering the Gross-Pitaevskii equation (GPE) with a coupling constant $g_c < 0$ for the contact interaction potential. Due to strong vertical confinement along the z-axis, the vibrational level spacing $\hbar\omega_z \gg \frac{\hbar^2}{m} n_p |g_c|$ is much larger than the absolute value of the interaction energy, where n_p is the peak density, $\hbar$ the reduced Planck constant, and m the atomic mass. The atomic wave function is frozen to the harmonic ground state along the z-axis. Integrating out the z-dependence in the GPE and assuming the wave function is isotropic in the x-y plane, we have

$$H\psi = -\frac{\hbar^2}{2m}\left(\frac{d^2\psi}{dr^2} + \frac{1}{r}\frac{d\psi}{dr}\right) + \frac{\hbar^2 g_c}{m}|\psi|^2\psi = \mu\psi\,, \tag{F.2}$$

where $\psi(\mathbf{r}) = \psi(r)$ is the wave function that only has a radial dependence and $n(r) = |\psi(r)|^2$ is the radial density profile. We rescale Eq. (F.2) using

$$\mathbf{R} = \sqrt{|g_c| n(0)}\mathbf{r}\,, \tag{F.3}$$

$$\frac{\psi(\mathbf{r})}{\sqrt{n(0)}} \to \phi(\mathbf{R})\,, \tag{F.4}$$

and arrive at a scale-invariant GPE

$$\tilde{H}\phi = -\frac{1}{2}\left(\frac{d^2\phi}{dR^2} + \frac{1}{R}\frac{d\phi}{dR}\right) - |\phi|^2\phi = \tilde{\mu}\phi\,. \tag{F.5}$$

The above equation can be numerically solved. The solution gives a chemical potential

$$\tilde{\mu} = \tilde{\mu}_{\rm ts} = -0.205\,. \tag{F.6}$$

We call the resulting scale-invariant solution, $|\phi_{\rm ts}(R)|^2$, the Townes profile. Assigning a peak density $n_p = n(0)$ and a coupling constant g_c, a Townes soliton must have the density profile

$$n(r) = n_p \left|\phi_{\rm ts}\left(\sqrt{n_p|g_c|}r\right)\right|^2\,. \tag{F.7}$$

F.3 Effect of the MDDI on 2D scale invariance

We now consider the impact on scale invariance with the addition of an MDDI term in the GPE

$$H_{\rm dd} = \int d\mathbf{r}' V_{\rm dd}(\mathbf{r}-\mathbf{r}')|\psi(\mathbf{r}')|^2\,, \tag{F.8}$$

where $V_{\rm dd}(r,\theta) = \frac{\mu_0\mu^2}{4\pi}(1-3\cos^2\theta)/r^3$ is the magnetic dipole-dipole potential, μ_0 is the vacuum permeability, $\mu \approx 0.75\mu_B$ is the magnetic moment of cesium near scattering length zero-crossing, and μ_B is the Bohr magneton. The above convolution integral can be expressed in the Fourier space, where the k_z dependence can be integrated out. We have

$$H_{\rm dd} = \frac{\hbar^2 g_{\rm dd}}{m}\int \frac{d\mathbf{k}}{(2\pi)^2} \mathrm{e}^{\mathrm{i}kr\cos\theta_k} h_{\rm dd}\left(\frac{kl_z}{\sqrt{2}}\right) n(\mathbf{k})\,, \tag{F.9}$$

where

$$g_{\rm dd} = \frac{m}{\hbar^2}\frac{\mu_0\mu^2}{3\sqrt{2\pi}l_z} \tag{F.10}$$

is the 2D MDDI coupling strength and $n(\mathbf{k})$ is the 2D Fourier transform of the density profile $|\psi(\mathbf{r})|^2$. The MDDI function reads [201], [226]

$$h_{\rm dd}(x) = (3\cos^2\alpha - 1) + 3\sqrt{\pi}x\mathrm{e}^{x^2}\mathrm{efrc}\,(x)\left(\sin^2\alpha\cos^2\theta_k - \cos^2\alpha\right)\,, \tag{F.11}$$

where $\mathrm{efrc}(x)$ is the complementary error function and α is the angle between the spin axis and the tight-confining z-axis. In our experimental setup, $\alpha = 0$ and $h_{\rm dd}$ simplifies to

$$h_{\rm dd}\left(\frac{kl_z}{\sqrt{2}}\right) = 2 - 3\sqrt{\pi}\left(\frac{kl_z}{\sqrt{2}}\right)\mathrm{e}^{k^2l_z^2/2}\mathrm{efrc}\left(\frac{kl_z}{\sqrt{2}}\right)\,. \tag{F.12}$$

We now express the full 2D Hamiltonian in the rescaled unit according to Eq. (F.4)

$$\left(\tilde{H}+\tilde{H}_{\rm dd}\right)\phi = -\frac{1}{2}\left(\frac{d^2\phi}{dR^2}+\frac{1}{R}\frac{d\phi}{dR}\right) - |\phi|^2\phi + \frac{g_{\rm dd}}{|g_c|}\int\frac{d\mathbf{k}}{(2\pi)^2}\mathrm{e}^{\mathrm{i}kR\cos\theta_k}h_{\rm dd}\left(\sqrt{\frac{n_p|g_c|}{2}}kl_z\right)\tilde{n}(\mathbf{k})\phi = \tilde{\mu}\phi\,, \tag{F.13}$$

where $\tilde{n}(\mathbf{k})$ is the dimensionless 2D Fourier transform of the rescaled density profile $|\phi(\mathbf{R})|^2$.

F.3.1 Scale invariance in deep 2D limit

We first consider the deep 2D limit with small $l_z \ll w$, where w is the characteristic horizontal size of the sample, and $\sqrt{n_p|g_c|}l_z \ll 1$. In this case, $\tilde{n}(\mathbf{k})$ is non-vanishing only when $k \lesssim O(2\pi/w\sqrt{n_p|g_c|})$, where $h_{\rm dd}(\sqrt{\frac{n_p|g_c|}{2}}kl_z) = 2$ remains a constant. The MDDI Hamiltoanian in Eq. (F.13) thus gives

$$\tilde{H}_{\rm dd} = 2\frac{g_{\rm dd}}{|g_c|}|\phi|^2\,, \tag{F.14}$$

which carries the same form of a contact interaction term. Equation (F.13) can thus be recast into the exact same form of Eq. (F.5) by rescaling using

$$\mathbf{R} = \sqrt{n_p|g|}\mathbf{r}\,, \tag{F.15}$$

where the bare coupling constant in Eq. (F.3) is replaces by

$$g = g_c + 2g_{\rm dd}\,. \tag{F.16}$$

The stationary solution of a 2D matter-wave with $g < 0$ remains to be that of a scale-invariant Townes profile. The solution has a chemical potential $\tilde{\mu}$ that relates to the solution $\tilde{\mu}_{\rm ts}$ of Eq. (F.5) as

$$\tilde{\mu} = \frac{g}{g_c}\tilde{\mu}_{\rm ts}\,. \tag{F.17}$$

F.4 Quasi-scale invariance

In the present experiment, we have $0.02 \lesssim \sqrt{n_g|g|}l_z \lesssim 0.15$ and $w \gtrsim 2$ μm$> l_z$ approximating the 2D limit. Here, we numerically confirm an effective scale-invariant scaling behavior (quasi-scale invariance) for stationary states realized in our experiment. To see if the scaling behavior is effectively preserved, we numerically solve for the soliton density profiles by finding the solutions to the integro-differential Eq. (F.13). Firstly, we obtain

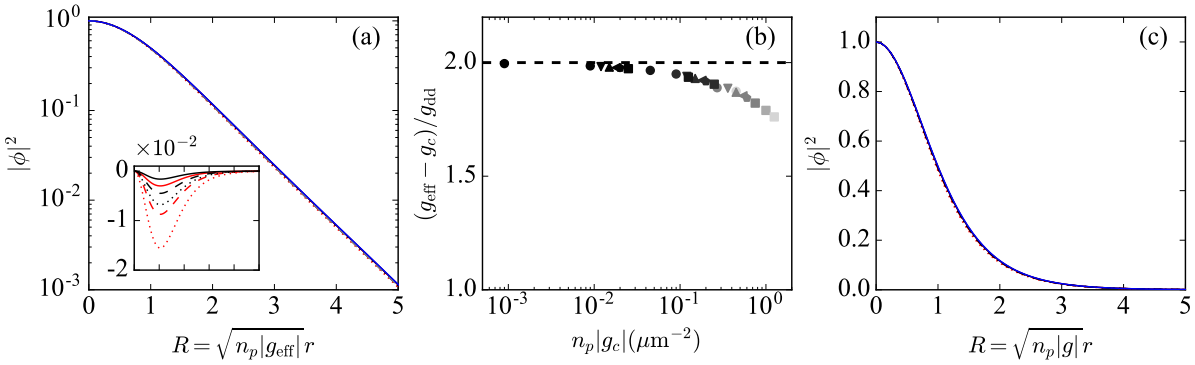

Figure F.1. Quasi-scale invariance in quasi-2D matter-wave solitons with the MDDI. (a) Scaled density profiles $|\phi(R)|^2$ evaluated using the full Hamiltonian Eq. (F.13) with $l_z = 184$ nm, bare coupling constants $g_c = -0.009$ (red curves), -0.025 (black curves), and with peak densities $n_p = 1/\mu\text{m}^2$ (solid), $10/\mu\text{m}^2$ (dashed), and $30/\mu\text{m}^2$ (dotted), respectively. Blue curve shows the Townes profile $|\phi_{\rm ts}(R)|^2$ without the MDDI. Inset plots the difference $|\phi(R)|^2 - |\phi_{\rm ts}(R)|^2$. (b) Filled symbols show the deviation of $g_{\rm eff}$ from the bare coupling constant g_c, normalized by $g_{\rm dd}$. Dashed line marks the 2D limit ($g - g_c = 2g_{\rm dd}$); $g_{\rm eff}$ is evaluated using $g_c = -0.009$ (circles), -0.012 (down triangles), -0.015 (up triangles), -0.018 (left triangles), -0.02 (pentagons), and -0.025 (squares), respectively, and at various peak densities $n_p = 0.1/\mu\text{m}^2 \sim 50/\mu\text{m}^2$ (dark to light gray). (c) Density profiles $|\phi(R)|^2$ as in (a), but with the radial coordinate rescaled using $g = g_c + 2g_{\rm dd}$ and plotted in linear scale. Reprinted figure with permission from [218], Copyright 2021 by APS.

the chemical potential $\tilde{\mu}$ and define the effective 2D coupling constant following the relation Eq. (F.17):

$$g_{\rm eff} = \frac{\tilde{\mu}}{\tilde{\mu}_{\rm ts}} g_c \,. \tag{F.18}$$

which should approach $g = g_c + 2g_{\rm dd}$ in the 2D limit. We then rescale the radial coordinate of the stationary density profile according to Eq. (F.15) using the effective coupling constant $g_{\rm eff}$. Figure F.1(a) plots the rescaled profiles $|\phi(R)|^2$ evaluated at various (n_p, g_c) around and beyond our experiment parameters. Indeed, the stationary profiles collapse very well to the universal Townes profile, with much less than $< 2\%$ deviation (relative to the peak density) over the entire density profile. In Fig. F.1(b), we calculate the shift in $g_{\rm eff}$ relative to the bare coupling constant g_c. The shift approaches the 2D limit ($2g_{\rm dd}$) quite well,

even after we increase the interaction parameter $n_p|g_c|$ by three orders of magnitude from $n_p|g_c| = 10^{-3}/\mu\text{m}^2$ up to $n_p|g_c| = 1/\mu\text{m}^2$, where only a small deviation $\Delta g \approx 0.25 g_{\text{dd}} \approx 0.00022 \ll g_{\text{eff}}$ occurs. In Fig. F.1(c), we plot the same density profiles $|\phi(R)|^2$ but with the radial coordinate R rescaled using $g = g_c + 2g_{\text{dd}}$, as this should be closer to the scaling performed in our experiment (see Fig. 5.4 and discussion in Sec. F.1). The Townes profile remains to be an excellent universal description for the rescaled density profiles.

G. SUPPLEMENTARY MATERIAL FOR QUASIPARTICLE PAIR-PRODUCTION AND QUANTUM ENTANGLEMENT

G.1 Calibration of the density noise power spectrum

It is known that the presence of image aberration can alter an imaging system's response to density fluctuations and correlations. In this section, we describe a procedure that calibrates and removes the effect of image aberrations in the measured density noise power spectrum. For detailed technical discussions, see also Ref. [221]. In brief, a recorded atomic density distribution $n_{\rm exp}(\mathbf{r})$ through an imaging apparatus is the measurement of a real atomic density distribution $n(\mathbf{r})$ convoluted with the point spread function $P(\mathbf{r})$ of the imaging system,

$$n_{\rm exp}(\mathbf{r}) = \int d\mathbf{r}' n(\mathbf{r}) P(\mathbf{r}-\mathbf{r}')\,. \tag{G.1}$$

By the convolution theorem, the Fourier transform of the density image is simply

$$n_{\rm exp}(\mathbf{k}) = n_{\mathbf{k}} P(\mathbf{k})\,, \tag{G.2}$$

which is the product of $n_{\mathbf{k}}$, the density distribution in Fourier space, and the optical transfer function $P(\mathbf{k})$, defined as the Fourier transform of the point spread function. The same relation holds for the measured density noise $\delta n_{\rm exp}(\mathbf{k}) = \delta n_{\mathbf{k}} P(\mathbf{k})$.

Through the above relationship, the density noise power spectrum $S(\mathbf{k}) \equiv \langle|\delta n_{\mathbf{k}}\rangle|^2/N$ can be obtained through dividing the image noise power spectrum $\langle|\delta n_{\rm exp}(\mathbf{k})|^2\rangle$ by $|P(\mathbf{k})|^2$. Here, N is total atom number and $\langle\cdots\rangle$ denotes ensemble averaging. Clearly, $S(\mathbf{k})$ can only be measured with nonzero $|P(\mathbf{k})|^2$. For an ideal, non-aberrated imaging system, $|P(\mathbf{k})|^2 = 1$ for all $k = |\mathbf{k}|$ within the resolution limit; with image aberration, $|P(\mathbf{k})|^2 \leq 1$ will be non-uniform and needs calibration.

For our superfluid samples, we expect $S(\mathbf{k})$ to be isotropic in the 2D Fourier space. Thus, we can find similar relation between the power spectrum and $|P(\mathbf{k})|^2$ under azimuthal averaging,

$$S(k) = \frac{\langle|\delta n_{\rm exp}(k)|^2\rangle}{NM^2(k)}\,, \tag{G.3}$$

where $\langle|\delta n_{\rm exp}(k)|^2\rangle$ is an azimuthally averaged spectrum at wavenumber k and $M^2(k) \equiv \int |P(\mathbf{k})|^2 d\theta_k$. We note that the equation holds within the resolution limit $k < \min(2\pi \mathrm{N.A.}/\lambda, 2\pi/l)$ where $M^2(k) \neq 0$. Here N.A. is the effective numerical aperture, λ is the wavelength of imaging light, and l is the image pixel size (in the atom plane). In our experiment, $(\mathrm{N.A.}, \lambda, l) \approx (0.35, 852\ \mathrm{nm}, 0.48\ \mu\mathrm{m})$ and the resolution is limited by finite numerical aperture. Once $M^2(k)$ is calibrated, the effect of aberration can be removed from the measurement using Eq. (G.3).

We calibrate $M^2(k)$ by measuring the density noise power spectra, $\langle|\delta n_{\rm exp}(k)|^2\rangle_{\rm th}$, of non-interacting thermal gases. With a sufficiently high temperature T, the density noise power spectrum for an ideal thermal gas, $S_{\rm th}(k)$, is known from a two-point correlation calculation [128]; $S_{\rm th}(k) = 1 + \int |g_1(z, \mathrm{e}^{-\pi r^2/\lambda_{\rm dB}^2})|^2 \mathrm{e}^{-i\mathbf{k}\cdot\mathbf{r}} d\mathbf{r}/g_1(z,1)\lambda_{\rm dB}^2$ would be approximately constant up to a spatial frequency $k \sim \lambda_{\rm dB}^{-1}$, where $\lambda_{\rm dB}$ is the thermal de Broglie wavelength, $z = \mathrm{e}^{\mu/k_B T}$ is the fugacity, μ is the chemical potential, k_B is Boltzmann constant, and $g_\gamma(x,y) = \sum_{k=1}^{\infty} x^k y^{1/k}/k^\gamma$ is the generalized Bose function. Within our resolution limit, a thermal gas essentially serves as a convenient source of atomic *white noise*, allowing us to calibrate $M^2(k)$ in a broad spatial frequency range.

To prepare for a thermal gas confined in the box potential, we first load a 2D superfluid sample using the standard loading procedure as described in [200]. We then quench the scattering length to a large and negative value at $a \approx -300\ a_0$, where a_0 is the Bohr radius, and hold for > 100 ms. During this time, the 2D sample suffers three-body recombination loss and heating, with $N \approx 7,000$ atoms remaining in the box and at a temperature up to $T = 170 \pm 15$ nK independently measured in time-of-flight measurements. We record the density fluctuations by quenching the scattering length back to a nearly non-interacting value followed by in situ absorption imaging. In our thermal samples, $\lambda_{\rm dB} < 0.5\ \mu$m is much smaller than the image resolution. The expected $S_{\rm th}(k) \approx S_{\rm th}(0) \approx 1.75$ is nearly a constant, with $\lesssim 3$ % decay for $k \lesssim 2.6/\mu$m. The normalized thermal noise power spectrum could thus give us an experimentally calibrated image response function

$$M^2(k) = \frac{\langle|\delta n_{\rm exp}(k)|^2\rangle_{\rm th}}{N S_{\rm th}(k)} \approx \frac{\langle|\delta n_{\rm exp}(k)|^2\rangle_{\rm th}}{\langle|\delta n_{\rm exp}(0)|^2\rangle_{\rm th}}\,. \tag{G.4}$$

Since we treat $S_{\rm th}(k)$ as a constant in the calibration Eq. (G.4), a small underestimation of $M^2(k)$ by $\lesssim 3\%$ may be present near large $k \sim 2.6/\mu$m. This suggests we could overestimate $S(k)$ by $\lesssim 3\%$ in later analyses.

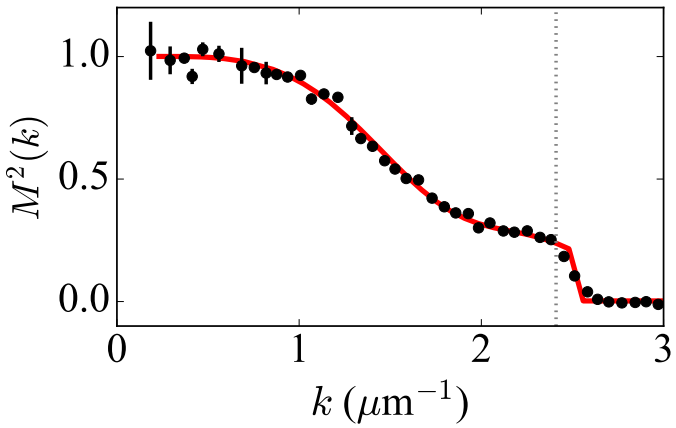

Figure G.1. Calibration of the imaging response function $M^2(k)$ using the measured thermal density noise power spectrum $\langle|\delta n_{\rm exp}(k)|^2\rangle_{\rm th}$ normalized by its asymptotic peak value. Solid curve is a theory fit $M^2_{\rm fit}(k)$. Vertical dotted line marks the boundary of $k \lesssim 2.4/\mu$m for entanglement analyses, where $M^2(k) \gtrsim 0.25$. Reprinted figure with permission from [261], Copyright 2021 by APS.

In Fig. G.1, we plot the measurement of $\langle|\delta n_{\rm exp}(k)|^2\rangle_{\rm th}$ normalized by the asymptotic peak value $\langle|\delta n_{\rm exp}(k_0)|^2\rangle_{\rm th} \approx 1.8$ at $k_0 \to 0$. By Eq. (G.4), this gives us experimentally calibrated $M^2(k)$. The response of our imaging system is smooth and finite until reaching the resolution limit $k \approx 2.6/\mu$m. Our $M^2(k)$ measurement result can also be well fitted by an analytical model based on standard aberration theory [221],

$$\mathcal{M}^2_{\rm fit}(k) = \frac{A^2(k)}{2} \sum_{n=-\infty}^{\infty} J_n^2(\eta k^2) + J_n(\eta k^2) J_{-n}(\eta k^2) \cos(2W(k)) \,. \tag{G.5}$$

where $A(k) = H(1-k/k_{\rm max})\mathrm{e}^{-\zeta k^4}$ models the transmittance function of imaging optics that terminates at $k = k_{\rm max} = 2\pi\mathrm{N.A.}/\lambda$, $H(x)$ is the Heaviside step function, $J_n(x)$ is the n-th order Bessel function of the first kind, and η is a coefficient of astigmatism; $\mathcal{M}^2_{\rm fit}(k)$ is evaluated by assuming simple aberration terms in the exit pupil function of the imaging

system, $p(k,\theta_k) = A(k)\exp\left[\mathrm{i}\eta k^2\cos 2\theta_k + \mathrm{i}W(k)\right]$, where the phase term $W(k) = \delta + fk^2 + Rk^4$ is parameterized by the coefficients of laser detuning (δ), defocus (f), and spherical aberration (R), respectively.

All the measured power spectra $S(k)$ are evaluated using Eq. (G.3) with experimentally calibrated $M^2(k)$ as shown in Fig. G.1. The power spectra $S(k)$ are presented within the range $k \lesssim 2.4/\mu$m, where $M^2(k) \gtrsim 0.25$ is sufficiently sensitive to density fluctuations and correlations in a 2D sample.

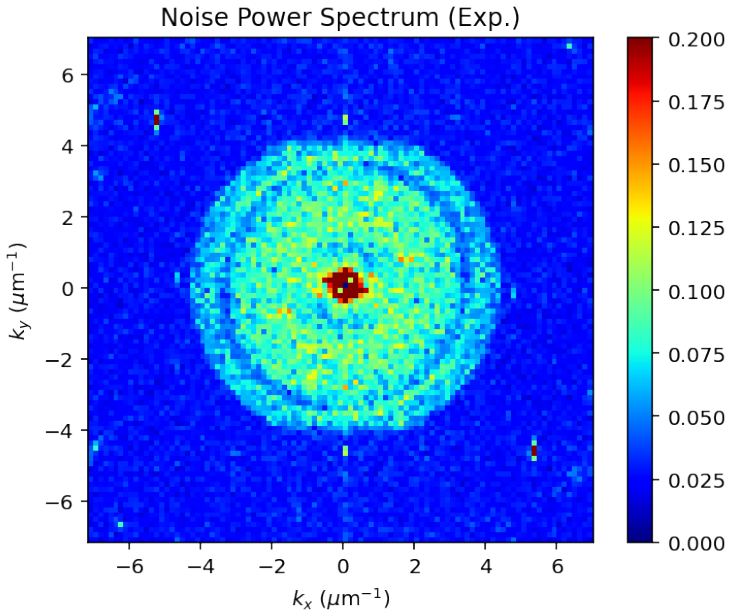

Figure G.2. Experimental density noise power spectrum of a 2D thermal gas with the new microscope objective (N.A. = 0.6). The dark ring shows the optical aberration of the microscope objective, dominated by the unexpected spherical aberration. This spherical aberration may be from viewport of the reflective optical element along the imaging path, it can be compensated using phase plates.

G.2 Separability criterion

In this section, we adapt the separability criterion for continuous variables obtained in Refs. [263], [264] to the case of counterpropagating quasiparticles in a superfluid and express the result in terms of the density noise power spectrum. The form of the criterion that we

use applies to the total variance of two commuting Hermitian operators $\hat{u}$ and $\hat{v}$ built out of the quadratures (coordinates and momenta) corresponding to two degrees of freedom. In our case, a natural choice is

$$\begin{aligned} \hat{u} &= \hat{x}_1 + \hat{x}_2 \\ \hat{v} &= \hat{p}_1 - \hat{p}_2, \end{aligned}$$

where the subscripts refer to two counterpropagating modes:

$$\begin{aligned} \hat{x}_1 &= \frac{1}{\sqrt{2}}(\hat{\alpha}_{\mathbf{k}} + \hat{\alpha}^\dagger_{\mathbf{k}}) \\ \hat{x}_2 &= \frac{1}{\sqrt{2}}(\hat{\alpha}_{-\mathbf{k}} + \hat{\alpha}^\dagger_{-\mathbf{k}}) \\ \hat{p}_1 &= \frac{\mathrm{i}}{\sqrt{2}}(\hat{\alpha}^\dagger_{\mathbf{k}} - \hat{\alpha}_{\mathbf{k}}) \\ \hat{p}_2 &= \frac{\mathrm{i}}{\sqrt{2}}(\hat{\alpha}^\dagger_{-\mathbf{k}} - \hat{\alpha}_{-\mathbf{k}}), \end{aligned}$$

and $\hat{\alpha}^\dagger_{\mathbf{k}}$, $\hat{\alpha}_{\mathbf{k}}$ as the quasiparticle creation and annihilation operators. We consider states that are on average uniform; in that case, the expectation values of $\hat{u}$ and $\hat{v}$ are zero, and their variances are simply $\langle \hat{u}^2 \rangle$ and $\langle \hat{v}^2 \rangle$. The total variance is

$$\langle \hat{u}^2 \rangle + \langle \hat{v}^2 \rangle = 2\langle \hat{\alpha}_{\mathbf{k}}\hat{\alpha}_{-\mathbf{k}} + \hat{\alpha}_{\mathbf{k}}\hat{\alpha}^\dagger_{\mathbf{k}} + \hat{\alpha}^\dagger_{-\mathbf{k}}\hat{\alpha}_{-\mathbf{k}} + \hat{\alpha}^\dagger_{-\mathbf{k}}\hat{\alpha}^\dagger_{\mathbf{k}} \rangle. \tag{G.6}$$

For a separable state of quasiparticles with momenta $\mathbf{k}$ and $-\mathbf{k}$, by the theorem proven in [263], [264], the total variance satisfies the following inequality:

$$[\langle \hat{u}^2 \rangle + \langle \hat{v}^2 \rangle]_{\mathrm{sep}} \geq 2. \tag{G.7}$$

For example, in a thermal state of $\hat{\alpha}_{\pm\mathbf{k}}$, $\hat{\alpha}^\dagger_{\pm\mathbf{k}}$, such as expected to result when a quenched superfluid has fully equilibrated, we have

$$[\langle \hat{u}^2 \rangle + \langle \hat{v}^2 \rangle]_{\mathrm{therm}} = 2(\langle \hat{\alpha}_{\mathbf{k}}\hat{\alpha}^\dagger_{\mathbf{k}} \rangle + \langle \hat{\alpha}^\dagger_{-\mathbf{k}}\hat{\alpha}_{-\mathbf{k}} \rangle) = 2(2n_B + 1) > 2,$$

satisfying the separability criterion. Here $n_B > 0$ is the Bose-Einstein distribution.

We now express the separability criterion Eq. (G.7) in terms of the density noise power spectrum $S(\mathbf{k})$. The density noise is calculated as $\delta n(\mathbf{x}, t) = n(\mathbf{x}, t) - \bar{n}$ at an arbitrary time t, where $\bar{n}$ is the average density of the superfluid, assumed uniform and time-independent. We define the Fourier components $\hat{n}_{\mathbf{k}}$ of the density noise operator as follows:

$$\delta\hat{n}(\mathbf{x}, t) = \frac{1}{V}\sum_{\mathbf{k}\neq 0} \hat{n}_{\mathbf{k}}(t)\mathrm{e}^{\mathrm{i}\mathbf{k}\cdot\mathbf{x}}, \tag{G.8}$$

where V is the volume of the gas. Note that we denote the noise operator $\hat{n}_{\mathbf{k}}$ here in place of $\delta\hat{n}_{\mathbf{k}}$ appeared in the main text. The Bogoliubov transformation expresses $\hat{n}_{\mathbf{k}}$ at an arbitrary moment of time in terms of the quasiparticle operators:

$$\hat{n}_{\mathbf{k}} = \sqrt{NC_k}(\hat{\alpha}_{\mathbf{k}} + \hat{\alpha}^\dagger_{-\mathbf{k}}), \tag{G.9}$$

where $N = \bar{n}V$ is the total particle number, assumed to be largely accounted for by ground state atoms, $C_k = \epsilon_k/\epsilon(k)$, $\epsilon(k) = \sqrt{\epsilon_k^2 + 2\frac{\hbar^2}{m}\bar{n}g\epsilon_k}$ is the Bogoliubov energy (at the interaction $g \geq 0$ when the measurement takes place), $\epsilon_k = \frac{\hbar^2|\mathbf{k}|^2}{2m}$ is the single particle energy, and m is the atomic mass.

Using Eq. (G.9), we can relate the density noise power spectrum to the variance (G.6):

$$S(\mathbf{k}) = \frac{\langle\hat{n}^\dagger_{\mathbf{k}}\hat{n}_{\mathbf{k}}\rangle}{N} = \frac{C_k}{2}\left[\langle u^2\rangle + \langle v^2\rangle\right]. \tag{G.10}$$

Thus, a necessary condition for separability is

$$S(\mathbf{k}) = \frac{\langle\hat{n}^\dagger_{\mathbf{k}}\hat{n}_{\mathbf{k}}\rangle_{\mathrm{sep}}}{N} \geq C_k, \tag{G.11}$$

where we have applied the inequality (G.7).